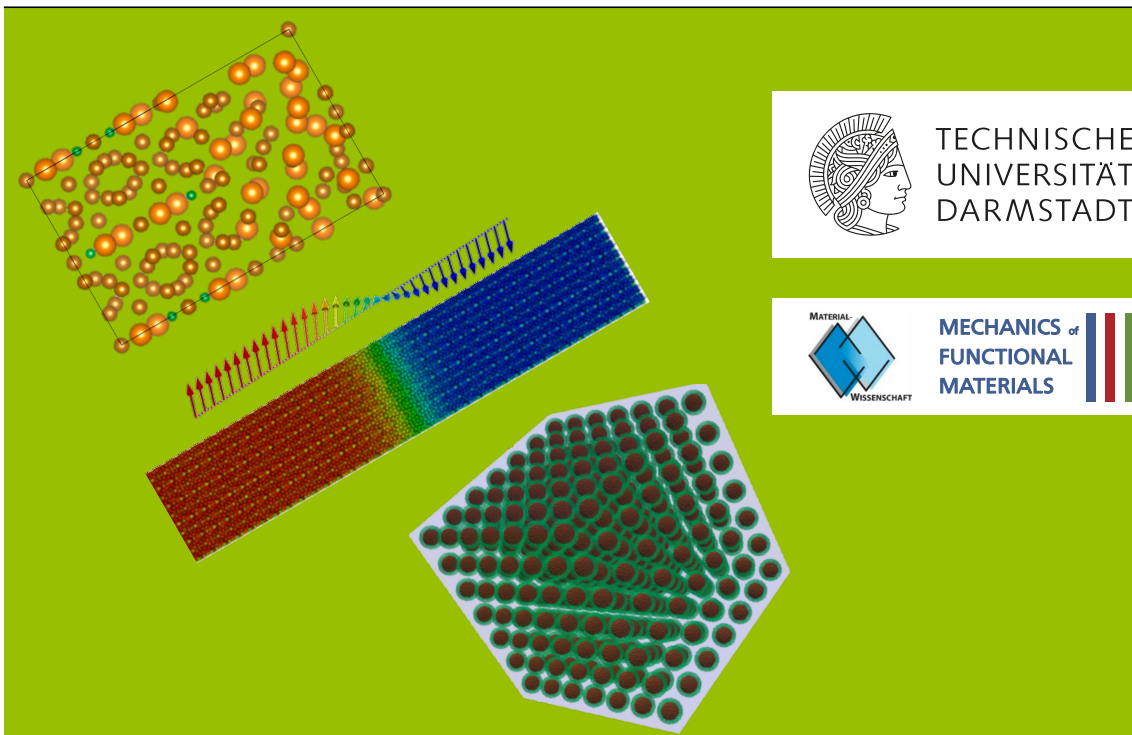# Multiscale Calculations of Intrinsic and Extrinsic Properties of Permanent Magnets

Multiskalenberechnungen der intrinsischen und extrinsischen Eigenschaften von Permanentmagneten
Zur Erlangung des akademischen Grades Doktor-Ingenieur (Dr.-Ing.)
genehmigte Dissertation von Qihua Gong aus Hunan, China
Tag der Einreichung: 22.04.2022, Tag der Prüfung: 04.07.2022

TECHNISCHE UNIVERSITÄT DARMSTADT

MATERIAL-WISSENSCHAFT
MECHANICS of FUNCTIONAL MATERIALS

Multiscale Calculations of Intrinsic and Extrinsic Properties of Permanent Magnets
Multiskalenberechnungen der intrinsischen und extrinsischen Eigenschaften von
Permanentmagneten

Doctoral thesis by Qihua Gong

1. Review: Prof. Dr. Bai-Xiang Xu
2. Review: Prof. Dr. Hongbin Zhang
3. Review: Prof. Dr. Thomas Schrefl
4. Review: Prof. Dr. Oliver Gutfleisch

Date of submission: 22.04.2022
Date of thesis defense: 04.07.2022

Darmstadt

Erklärungen laut Promotionsordnung

§8 Abs. 1 lit. c PromO

Ich versichere hiermit, dass die elektronische Version meiner Dissertation mit der schriftlichen Version übereinstimmt.

§8 Abs. 1 lit. d PromO

Ich versichere hiermit, dass zu einem vorherigen Zeitpunkt noch keine Promotion versucht wurde. In diesem Fall sind nähere Angaben über Zeitpunkt, Hochschule, Dissertationsthema und Ergebnis dieses Versuchs mitzuteilen.

§9 Abs. 1 PromO

Ich versichere hiermit, dass die vorliegende Dissertation selbstständig und nur unter Verwendung der angegebenen Quellen verfasst wurde.

§9 Abs. 2 PromO

Die Arbeit hat bisher noch nicht zu Prüfungszwecken gedient.

Darmstadt, 22.04.2022

_____

Qihua Gong

Erklärung zur Dissertation

Hiermit versichere ich, die vorliegende Dissertation ohne Hilfe Dritter und nur mit angegebenen Quellen und Hilfsmitteln angefertigt zu haben. Alle Stellen, die aus Quellen entnommen werden, sind als solche kenntlich gemacht. Diese Arbeit hat in gleicher oder ähnlicher Form noch keiner Prüfungsbehörde vorgelegen.

Darmstadt, den 22.04.2022

Qihua Gong

Acknowledgements

The thesis has finally been finished thanks to a tremendous help from my supervisor and colleagues in the group of Mechanics of Functional Materials at TU Darmstadt. Without these help from different sides, I can hardly image that I could complete this Ph.D project, topic of which seemed very far from my Master study and now interests me greatly.

First of all, I would like to express my heartful gratitude to my supervisor Prof. Bai-Xiang Xu, who gave me the chance to pursue my PhD degree and helped me a lot in both academic research and daily life. I will never forget her kindness, patience, smart ideas, timely supervision, and helpful suggestions when we discussed every small piece of my research issues and even a small term in an equation. I also appreciated that on one hand, she provided me a free academic environment to give me much freedom in the research activities. On the other hand, she convoyed me with timely and efficient instructions on all kinds of problems that I have encountered during my research. Her opening mind and foresight also made my PhD study as an eye-opening, unforgettable and wonderful experience in my whole life.

I am also very grateful to my colleagues with whom I had many discussions or exchanges on not only the scientific and technical aspects of my research issues, but also the shared beauty of life. Dr. Min Yi helped me a lot in the research ideas, simulation codes, material background, scientific paper writing, etc. Every time after discussing with Yangyang, Dominik and Mamun with whom I shared the office for a long time, I always had new passion and insight into the scientific and research world. Yang Bai and Peter Stein did me a favor in computer maintenance, Linux system repair, software/code compiling, network connection, etc. I did cherish the days I stayed at TU Darmstadt and was honored to be a member of the group of Mechanics of Functional Materials, which is like a big and warm family. My gratitude should also go to all colleagues from the group, including Peter Stein, Dagmar Eder-Goy, Habib Pouriayevali, Mamun Al-Siraj, Domink Ohmer, Christoph Reimuth, Yangbin Ma, Xiandong Zhou, Ying Zhao, Yang Bai, Ziqi Zhou, Yao Liu, Shuai Wang, Wei Liu, Binbin Lin, Maoyang Zhang, and Suxin Pan. They made me experience different cultures and a rich and colorful life. I wish to respectfully thank our secretory Maren Arnold, who helped me with some personal issues, contract matters, conference traveling, parental leave, defense preparation, etc.

Of course the German Research Foundation (DFG YI 165/1-1 and DFG XU 121/7-1) and the German federal state of Hessen through its excellence program LOEWE "RESPONSE"

Last but not least, I would like to thank my parents for their endless love and unconditionally support to my life. Also, I want to specifically thank my husband, who leaded me to Germany and brought me a totally different life. Without their help and support, I cannot achieve so much research outcome and cannot finish my PhD thesis so smoothly. I am also grateful to my two daughters, two-years-old QianQian and eight-months-old QingQing, who always accompany me and make me put my best effort to finish the thesis. The accomplishment of this thesis shaped a very start for my future career life and I have readily prepared for the following new challenges in my life. Currently I am pretty confident as the famous Chinese poem LI Bai said "Someday with my sail piercing the clouds, I will mount the wind, break the waves, and traverse the vast and rolling sea".

<div align="right">

Qihua Gong
November 1, 2021
@ Donghua Lakeside

</div>

Abstract

Permanent magnets with high coercivity H_c and maximum energy product $(BH)_{max}$ are indispensible for the modern technologies in which electric energy is efficiently converted to motion, or *vice versa*. Modelling and simulation play an important role in mechanism understanding and optimization of H_c and $(BH)_{max}$ and uncovering the associated coercivity mechanism. However, both H_c and $(BH)_{max}$ are extrinsic properties, i.e., they depend on not only the intrinsic magnetic properties of the constituent phases but also the microstructures across scales. Therefore, multiscale simulations are desirable for a mechanistic and predictive calculation of permanent magnets.

In this thesis, a multiscale simulation framework combining first-principles calculations, atomistic spin model (ASM) simulations, and micromagnetic simulations is demonstrated for the prediction of temperature-dependent intrinsic magnetic properties as well as the microstructure-related extrinsic properties in permanent magnets, with a focus on Nd-Fe-B and rare-earth free exchange-spring magnets. The main contents and results are summarized in the following.

(1) The intrinsic temperature-dependent magnetic properties of the main phase $Nd_2Fe_{14}B$ in Nd-Fe-B permanent magnets are calculated by *ab-initio* informed ASM simulations. The ASM Hamiltonian for $Nd_2Fe_{14}B$ is constructed by using the Heisenberg exchange of Fe–Fe and Fe–Nd atomic pairs, the uniaxial single-ion anisotropy of Fe atoms, and the Nd ion crystal-field energy. The calculated temperature-dependent saturation magnetization $M_s(T)$, effective magnetic anisotropy constants $K_{eff}^i(T)$ ($i = 1, 2, 3$), domain-wall width $\delta_w(T)$, and exchange stiffness constant $A_e(T)$ are found to agree well with the experimental results. This calculation framework enables a scale bridge between first-principles calculations and temperature-dependent micromagnetic simulations of permanent magnets.

(2) The intrinsic bulk exchange stiffness A_e in $Nd_2Fe_{14}B$ and the extrinsic interface exchange coupling strength J_{int} between $Nd_2Fe_{14}B$ and grain boundary (GB), as well as their influences on H_c, are explored by combining the first-principles calculations, ASM simulations, and micromagnetic simulations. Both A_e and J_{int} are found to be anisotropic. A_e is larger along crystallographic a/b axis than along c axis of $Nd_2Fe_{14}B$. "Double anisotropy" phenomenon regarding to GB is discovered, i.e., in addition to GB magnetization anisotropy, J_{int} is also strongly anisotropic even when GB possesses the same magnetization. It is found that J_{int} for (100) interface is much higher than that for (001) interface. The discovered

anisotropic exchange is shown to have profound influence on H_c. These findings allow new possibilities in designing Nd-Fe-B magnets by tuning exchange.

(3) H_c of Nd-Fe-B permanent magnets with featured microstructure are calculated by combining ASM and micromagnetic simulations. With the intrinsic properties from ASM results as input, finite-temperature micromagnetic simulations are performed to calculate the magnetic reversal and H_c at high temperatures. It is found that apart from the decrease of anisotropy field with increasing temperature, thermal fluctuations further reduce H_c by 5–10% and β (temperature coefficient of H_c) by 0.02–0.1% K^{-1} when a defect layer exists. Both H_c and β can be enhanced by adding the Dy-rich shell, but they saturate at a shell thickness (t_{sh}) around 6–8 nm after which further increasing t_{sh} or adding Dy into the core is not essential.

(4) The microstructural influence in rare-earth free permanent magnet candidates, in particular the α''-Fe$_{16}$N$_2$/SrAl$_2$Fe$_{10}$O$_{19}$ composite and MnBi/Fe$_x$Co$_{1-x}$ bilayer are investigated in collaboration with the experimental and theoretical partners. For the former, pure micromagnetic simulations show that the design criterion for the magnetically hard/soft-phase composite is invalid for the hard/semi-hard-phase composite. α''-Fe$_{16}$N$_2$ nanoparticle diameter less than 50 nm and an interface exchange in the order of 0.01–0.1 pJ/m enable the H_c enhancement, while less surface oxides and higher volume fraction of α''-Fe$_{16}$N$_2$ nanoparticles are decisive for enhancing the composite's $(BH)_{max}$. For the latter, DFT-informed micromagnetic simulations show that the interface roughness could deteriorate the interface exchange coupling and induce premature magnetic reversal in FeCo layer. A 1-nm thick FeCo layer and an interface exchange parameter around 2 pJ/m could improve $(BH)_{max}$ by 10% when compared to the pure MnBi layer.

The presented multiscale simulation framework across scales from the electronic level, atomistic classic spin to microstructure in this thesis is demonstrated to be of the capability towards a powerful and predicative computational design of high-performance permanent magnets, even though there is still a long way to go for its direct application to the real product design.

Abstract

Permanentmagnete mit hoher Koerzitivfeldstärke H_c und maximalem Energieprodukt $(BH)_{max}$ sind für moderne Technologien, in denen elektrische Energie effizient in Bewegung oder umgekehrt umgewandelt wird, unverzichtbar. Modellierung und Simulation spielen eine wichtige Rolle beim Mechanismusverständnis und der Optimierung von H_c und $(BH)_{max}$ und der Aufdeckung des damit verbundenen Koerzitivkraftmechanismus. Jedoch sind sowohl H_c als auch $(BH)_{max}$ extrinsische Eigenschaften, d. h. sie hängen nicht nur von den intrinsischen magnetischen Eigenschaften der konstituierenden Phasen ab, sondern auch von den Mikrostrukturen über Skalen hinweg. Daher sind Multiskalensimulationen für eine mechanistische und prädiktive Berechnung von Permanentmagneten wünschenswert.

In dieser Dissertation wird ein Multiskalen-Simulationsrahmen, der First-Principles-Berechnungen, Atomistic-Spin-Modell (ASM)-Simulationen und mikromagnetische Simulationen kombiniert, für die Vorhersage temperaturabhängiger intrinsischer magnetischer Eigenschaften sowie der mikrostrukturbezogenen extrinsischen Eigenschaften in Permanentmagneten verwendet, mit Fokus auf Nd-Fe-B und seltenerdfreie Wechselfedermagnete. Die wesentlichen Inhalte und Ergebnisse sind im Folgenden zusammengefasst.

(1) Die intrinsischen temperaturabhängigen magnetischen Eigenschaften der Hauptphase $Nd_2Fe_{14}B$ in Nd-Fe-B-Permanentmagneten werden durch *ab-initio* informierte ASM-Simulationen berechnet. Der ASM-Hamiltonian für $Nd_2Fe_{14}B$ wird konstruiert, indem der Heisenberg-Austausch von Fe-Fe- und Fe-Nd-Atompaaren, die uniaxiale Einzelionenanisotropie von Fe-Atomen und die Kristallfeldenergie der Nd-Ionen' verwendet werden. Die berechnete temperaturabhängige Sättigungsmagnetisierung $M_s(T)$, die effektive magnetische Anisotropiekonstanten $K_{eff}^i(T)$ ($i = 1, 2, 3$), die Domänenwandbreite $\delta_w(T)$ und die Austauschsteifigkeitskonstante $A_e(T)$ stimmen mit den experimentellen Ergebnissen gut überein. Dieser Berechnungsrahmen ermöglicht eine Maßstabsbrücke zwischen First-Principles-Berechnungen und temperaturabhängigen mikromagnetischen Simulationen von Permanentmagneten.

(2) Der Einfluss der intrinsischen Bulk-Austauschsteifigkeit A_e in $Nd_2Fe_{14}B$ und der extrinsischen Grenzflächenaustausch-Kopplungsstärke J_{int} zwischen $Nd_2Fe_{14}B$ und der Korngrenze (GB) wird durch die Kombination von First-Principles-Rechnungen, ASM-Simulationen und mikromagnetischen Simulationen untersucht. Sowohl A_e als auch J_{int} sind anisotrop. A_e ist entlang der kristallographischen a/b-Achse größer als entlang der

c-Achse von $Nd_2Fe_{14}B$. Das "doppelte Anisotropie"-Phänomen in Bezug auf GB wird entdeckt, d. h. zusätzlich zur GB-Magnetisierungsanisotropie ist J_{int} auch stark anisotrop, selbst wenn GB die gleiche Magnetisierung besitzt. Es zeigt sich, dass J_{int} für die (100)-Schnittstelle viel höher ist als für die (001)-Schnittstelle. Es wird gezeigt, dass der entdeckte anisotrope Austausch einen tiefgreifenden Einfluss auf H_c hat. Diese Erkenntnisse erlauben neue Möglichkeiten beim Design von Nd-Fe-B-Magneten durch Tuning-Austausch.

(3) H_c von Nd-Fe-B-Permanentmagneten mit gekennzeichneter Mikrostruktur werden durch die Kombination von ASM- und mikromagnetischen Simulationen berechnet. Mit den intrinsischen Eigenschaften aus ASM-Ergebnissen als Eingabe werden mikromagnetische Simulationen bei endlicher Temperatur durchgeführt, um die magnetische Umkehrung und H_c bei hohen Temperaturen zu berechnen. Es wurde festgestellt, dass neben der Abnahme des Anisotropiefeldes mit zunehmender Temperatur thermische Schwankungen H_c weiter um $5-10\%$ und β (Temperaturkoeffizient von H_c) um $0.02-0.1\%$ K^{-1} reduzieren, wenn eine Defektschicht vorhanden ist. Sowohl H_c als auch β können durch Hinzufügen der Dy-reichen Schale verbessert werden, aber bei einer Schalendicke (t_{sh}) von etwa 6-8 nm tritt eine Sättigung ein, wonach eine weitere Erhöhung von t_{sh} oder die Zugabe von Dy in den Kern nicht unbedingt erforderlich ist.

(4) Der mikrostrukturelle Einfluss in Seltenerd-freien Permanentmagnetkandidaten, im speziellen der α''-$Fe_{16}N_2$/$SrAl_2Fe_{10}O_{19}$ Komposit und die MnBi/Fe_xCo_{1-x} Doppelschicht, wird in Zusammenarbeit mit den experimentellen und theoretischen Partnern untersucht. Für ersteres zeigen reine mikromagnetische Simulationen, Auslegungskriterium für die magnetisch harte/weiche Phasen Komposite für harten/halbharte Phasen Komposite ungültig ist. Es wird vermutet, dass α''-$Fe_{16}N_2$ Nanopartikeldurchmesser von weniger als 50 nm und ein Grenzflächenaustausch in der Größenordnung von 0,01– 0,1 pJ/m die H_c-Verstärkung ermöglichen, während weniger Oberflächenoxide und ein höherer Volumenanteil von α''-$Fe_{16}N_2$ Nanopartikeln entscheidend für die Verbesserung des Komposit $(BH)_{max}$ Wertes sind. Für letzteres zeigen DFT-gestützte mikromagnetische Simulationen, dass die Grenzflächenrauigkeit die Grenzflächenaustauschkopplung verschlechtern und eine vorzeitige Magnetumkehr in der FeCo-Schicht induzieren könnte.

Eine 1 nm dicke FeCo-Schicht und ein Grenzflächenaustauschparameter von etwa 2 pJ/m könnten $(BH)_{max}$ im Vergleich zur reinen MnBi-Schicht um 10% verbessern.

Der in dieser Arbeit vorgestellte Multiskalen-Simulationsansatz über Skalen von der elektronischen Ebene über den atomaren Spin bis hin zur Mikrostruktur zeigt seine Fähigkeit zu einem leistungsstarken und prädiktiven rechnerischen Design von Hochleistungs-Permanentmagneten, auch wenn für die direkte Anwendung im tatsächlichen Produktdesign noch ein langer Weg erforderlich ist.

Contents

3 Temperature-dependent intrinsic properties of $Nd_2Fe_{14}B$ by *ab-initio* informed atomistic spin model simulations   73

4 Anisotropic exchange stiffness and interface exchange coupling in Nd-Fe-B permanent magnets by multiscale simulations   93

5 High-temperature coercivity of Nd-Fe-B permanent magnets by multiscale simulations   109

List of Figures

List of Tables

1 Introduction

1.1 Permanent magnets

1.1.1 Development history

As early as ca. 600 B.C., the Greek philosopher Thales of Miletus mentioned a hard magnetic material called loadstone [1]. This hard magnet was in fact a natural magnetic mineral, with a form of magnetic magnetite Fe_3O_4. Loadstone was then names as "magnes" since it was found in Magnesia, a district in Thessaly. In addition to this natural magnetic mineral, iron needles magnetized by touching the loadstone were the first artificial magnets. Following this idea, the first practical use of magnetism by human beings is the compass. In a French poem by Guyot de Provins, it was reported that around 1200 A.D. a touched needle of iron is supported by a floating straw [1]. In about 500 A.D., good magnet steel was available in China.

In addition to the above ancient records, William Gilbert seems to be the first one who presented the earliest systematic reporting of magnets in his scientific work in 1600 [2]. He showed the methodology of arming loadstones with soft iron pole tips to increase the attractive force. He also described how to magnetize pieces of iron or steel [1]. By 1867, it is recorded in German handbooks that nonmagnetic elements and magnetic materials (mainly iron) can be metallurgically integrated into ferromagnetic alloys. For example in 1901, Heusler alloy Cu_2MnAl, which had outstanding properties compared to previous magnets, were reported. The composition of a typical Heusler alloy reads 10 to 30% manganese and 15 to 19% aluminum.

After a long-history and slow development, high-carbon steels containing 1% carbon, which were later improved to tungsten steel, chromium steel [3] and finally KS (Kichizaemon-Sumitomo) steel [4], came out as the **first generation** of permanent magnets in the starting of 1900s. The coercivity of these magnetic alloys is attributed to the very fine microstructure generated by a martensitic phase transformation. The fine microstructure can hinder the domain wall movement and thus give rise to a higher coercivity and maximum energy product.

Along with the advancement of science and technology and the pursue of improved performance in permanent magnets, Alnico alloys appear as the **second generation** of permanent magnets in the 1930s. They were successfully developed owing to the previous

research experience of MK (Mitsujima ka) steel which is an alloy containing nickel and aluminum and was developed in 1931 by the Japanese metallurgist Tokuhichi Mishima [5]. MK steel is inexpensive, tough and durable. It can maintain strong magnetism at small scales. Also it can generate a stable magnetic force regardless of temperature changes or vibration. It possesses a coercivity of 32 kA/m, double that of the best magnet steels of the time. In fact, MK steel is similar to Alnico. Alnico is a family of iron alloys, which in addition to iron are composed primarily of aluminium (Al), nickel (Ni), and cobalt (Co). They also include small amount of other metals such as copper [6] and sometimes titanium. Typically , Alnico's composition is 8–12%Al, 15–26%Ni, 5–24%Co, up to 6%Cu, up to 1%Ti, and the balance is Fe. Alnico alloys have a high coercivity for resisting demagnetization and can be magnetised to produce strong magnetic fields, thus making them strong permanent magnets with a high Curie temperature around 800 °C, a remanence exceeding 1.2 T, a coercivity up to 80 kA/m, and a maximum energy product over 44 kJ/m^3. Alloys in this family also appear with the following trade names: Alni, Alcomax, Hycomax, Columax, and Ticonal. Indeed, before the rare-earth magnets appeared in the 1970s, they were the strongest permanent magnet. Their high performance is attributed to the special microstructure with formed two-phase constituents, which are a strongly magnetic α_1 phase (Fe-Co) and a very weakly magnetic α_2 phase (Ni-Al). The strong α_1 phase was embedded in a Ni-Al matrix which provides pinning sites to restrain the domain wall propagation. Meanwhile, the formation of long rod-shaped grains of Fe-Co gives rise to shape anisotropy, resulting in even much higher coercivity. The disadvantage of these alloys is that they are hard and brittle, making them be shaped only by casting or pressing and sintering of metal powder. Nevertheless, Alnico alloys are still welcome and widely used in industrial and consumer applications such as electric motors, electric guitar pickups, microphones, sensors, loudspeakers, magnetron tubes, cow magnets, etc.

Ferrite is another member of the second generation of permanent magnets. A ferrite is a ceramic material made by mixing and firing large proportions of iron(III) oxide (Fe$_2$O$_3$, rust) blended with small proportions of one or more additional metallic elements, such as strontium, barium, manganese, nickel, and zinc. In 1930s, Yogoro Kato and Takeshi Takei from the Tokyo Institute of Technology synthesized magnets made of powdered metallic oxides, which is the first ferrite compounds. This development was the forerunner of the modern ferrite. For example, barium and strontium ferrites were invented in the 1950s [7], expressed as MO×6(Fe$_2$O$_3$), where M is Ba, Sr, or Pb [8, 9]. Ferrites with high resistance to being demagnetized are hard and can be used to make permanent magnets for applications such as refrigerator magnets, loudspeakers, and small electric motors. They are ferrimagnetic and are not electrically conductive, making them useful in applications like magnetic cores for transformers to suppress eddy currents. Ferrites are often used to produce the so called plastic magnets by embedding the ferrite in a flexible plastic matrix. A ferrite has a higher coercive force than Alnicos, but at the same time has a lower remanence magnetic flux density and maximum energy product. Alnicos dominated the permanent
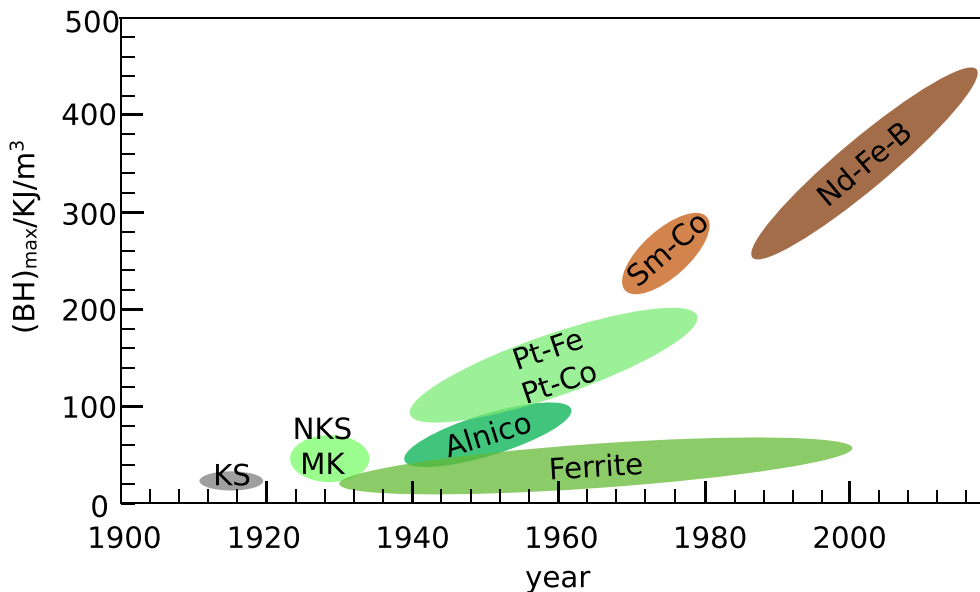
Figure 1.1: The improvement for the magnetic energy product shows four generations of permanent magnets since the turn of the century.

motors market between the mid 1940s and the late 1960s when ferrites became the most widely used materials [1]. Pt-Co and Pt-Fe were also developed in the late 1950s, but were no longer in commercial use due to its high cost.

Further concentrated efforts to explore new magnetic materials by alloying rare earth elements with the $3d$ transition metals bring forth the **third generation** of permanent magnets, mainly rare-earth magnets such as $SmCo_5$, Sm_2Co_{17}, $Nd_2Fe_{14}B$, etc. [10]. SmCo magnets were developed in the early 1960s based on work by Karl Strnat at Wright-Patterson Air Force Base and Alden Ray at the University of Dayton. In particular, Strnat and Ray developed the first formulation of $SmCo_5$. Benz and Martin used liquid phase sintering technique to make the commercial and large-scale production of fully dense and stable $SmCo_5$ magnets possible [11], which became the first generation of rare earth magnets. Latter in the mid 1970s, the development of Cu- and Zr-added $Sm(Co,Fe,Cu,Zr)_z$ alloys led to a $(BH)_{max}$ as high as 26–30 MGOe [12], resulting in the commercial success of the second generation of rare earth magnets. It was evidenced that the combination of Co with a high saturation magnetization and Sm with an extremely high magnetocrystalline anisotropy led to much higher coercivity and maximum energy product than those obtained in previous first and second generation of permanent magnetic materials. $SmCo_5$ and Sm_2Co_{17} were identified as high-performance permanent magnets, with a coercivity reaching 760 and 800 kA/m, respectively, and a maximum energy product reaching 150–200 kJ/m^3 and 260 kJ/m^3, respectively.

In the late 1970s and early 1980s, lots of efforts were made to further enhance the performance of SmCo magnets by replacing Sm with other rare earth elements (e.g., Nd,

Pr, etc.) and replacing Co with Fe. The idea behind these efforts is straightforward. On one hand, due to the intervention of economic circumstances in the early 1980s, there was an urgent need for new permanent magnetic material to replace Sm-Co. On the other hand, although a combination of rare-earth element R and transition metal T is shown to achieve the materials for high-performance permanent magnets, there is naturally one question that why R must be Sm and T must be Co. It is well known that Nd and Pr are very abundant rare-earth elements and cheaper than Sm and Co, and their magnetic moments are larger than Sm. Fe is almost inexhaustible, while Co is to some extent resource critical currently [13]. In addition, Fe in alloys typically possesses a larger magnetic moment than Co. Nevertheless, attempts to synthesize the binary Nd-Fe or Pr-Fe compounds with the magnetic properties required by a good permanent magnet never succeeded.

In an alternative way, these concerted efforts brought about the $Nd_2Fe_{14}B$-based rare earth magnets with superior magnetic performance at room temperature [14]. Specifically, Sagawa [14–17] and several researcher [18–21] developed ternary system $R_2Fe_{14}B$ with the addition of a small amount of boron. $Nd_2Fe_{14}B$ possesses a tetragonal crystal structure, breaking through the hexagonal system and rhombohedral system of permanent magnetic alloys of the first and second generations. It has extraordinary magnetic properties, with a world-record maximum energy product up to 500 kJ/^{3} [22], which has increased by almost an order of magnitude with respect to the best value for the transition metal based alloys, and by a factor of 100 with respect to the best steel magnets available before 1930s, as shown in Figure 1.1. Up to now, Nd-Fe-B magnets still have a strong priority in research interests. Since then, rare-earth permanent magnets Re-Fe-B were soon fast developed, and are highly efficient and suitable for applications such as computer hard disk drives, hybrid and electric vehicles, household electrical appliances, wind turbines, many small consumer electronic devices, etc. In order to increase the performance of $Nd_2Fe_{14}B$-based magnets at high temperature or obtain better thermal stability, heavy rare-earth elements such as Dy and Tb are essential ingredients to substitute Nd by 2–10w%. However, heavy rare-earth elements are extremely critical. Researchers around the world are making efforts to reduce the usage of heavy rare-earth elements or to substitute them by resource-rich elements [23].

In the late 1980s and 1990s, motivated by the discovery of $Nd_2Fe_{14}B$-based magnets, other novel magnets like the $ThMn_{12}$-type intermetallics with a general formula of $RFe_{12-x}M_x$ (M=Ti, V, Cr, Mo and Si) were designed [24]. It should be mentioned that $ThMn_{12}$, for example $NdFe_{12}$ and $SmFe_{12}$, are usually not stable without a stabilizing element such as Ti, Mo, Si, or V [25, 26]. They have intriguing properties. For instance, at 450 K the magnetic phase by $ThMn_{12}$ structure with Th as Nd and Sm possesses even higher magnetization and higher anisotropy field than $Nd_2Fe_{14}B$ [26, 27]. Moreover, the rare-earth content is much lower than that in $Nd_2Fe_{14}B$, thus reducing the rare earth usage and alleviating the rare-earth crisis. However, unlike $Nd_2Fe_{14}B$-based magnets, the grains in $ThMn_{12}$-type magnets are not isolated by a nonmagnetic or only weakly ferromagnetic grain boundary

phase [28]. As a consequence, there are still difficulties in large-scale production in terms of consistently superior magnets for commercial applications. In 1990s, extensive research on $Sm_2Fe_{17}N_x$ prevailed. However, the properties of $Sm_2Fe_{17}N_x$ are degraded at temperature beyond 600 °C, making it difficult to achieve a dense magnet.

The high performance of the above rare-earth permanent magnets are related to T-T interactions, the spin- orbit coupling in R, and R-T interactions (R is rare earth element and T is 3d transition metal). In these R-T based compounds, there are three important underlying mechanisms. On one hand, the strong T-T 3d-3d exchange interactions stabilize the magnetic ordering against thermal agitation at high temperatures and lead to a relatively high Curie temperature [29]. In addition, 3d metals contribute to a high spontaneous magnetization, thus making the magnets with a overall high saturation magnetization. The 3d metals (mostly Fe, Mn, Ni) are widely available, whereas the RE metals and Co are to some extent resource critical [13]. On the other hand, the single-electron spin-orbit coupling constant $\zeta \sim Z^2$ where Z is the atomic number, and rare-earth element usually possesses a very large Z. Therefore, the rare-earth element R can provide strong spin-orbit coupling for the realization of high magnetocrystalline anisotropy and thus the large magnetic hysteresis. Finally, the R-T 4f-3d magnetic interactions sustain the R-sublattice magnetization and consequently keep the strong 4f anisotropy well above room temperature. On the basis of these compounds, outstanding permanent magnetic properties are achievable.

In terms of the applications, permanent magnets offer the high energy product and are available in a wide range of shapes, sizes and grades. For instance, Nd-Fe-B magnets can be found in a variety of applications including high performance motors, information-storage devices, brushless DC motors, magnetic separation, magnetic resonance imaging, hybrid and electric vehicles, sensors, switches, loudspeakers, etc, [30], as illustrated in Figure 1.2. Among these, hybrid and electric vehicle are demanding a vast volume of high-performance permanent magnets [31, 32]. Permanent magnets, such as NdFeB, can also be used in DC motor. Kim [33] reported that the volume and weight are reduced by 50% with the application of NdFeB, compared to the conventional ferrite motor, without losing performance. The major driving force for the application to electromotor is the maximized energy densities. Most importantly, containing less Dy, NdFeB-type magnets could also remain temperature stability at around 450 K. While for a new generation of SmCo 2:17-type magnets, the working temperature could reach 670 K [34–36]. Unlike $Nd_2Fe_{14}B$, $Pr_2Fe_{14}B$ does not undergo a spin reorientation transition at low temperatures. At the operation temperature of the superconducting bearings, PrFeB magnets are more suitable than NdFeB magnets [37]. Film-type permanent magnets have vast applications in Micro-ElectroMechanical Systems (MEMS), such as micro-sized motors, actuator, mini-pumps, and other devices [38]. For MEMS applications, the permanent magnet films not only should possess high magnetic performance at the service temperatures, but also should be compatible to the integrated-circuit technologies. In this aspect, high-performance rare-

earth magnet films may be not the best choice, since their corrosion resistance is not so high. In contrast, PtFe or PtCo films may be more suitable for the future MEMS applications [38].
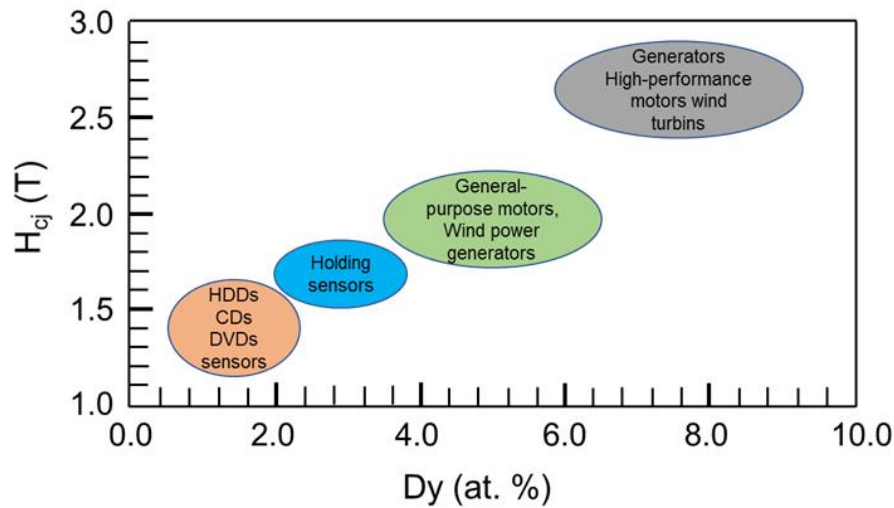
Figure 1.2: Applications of Nd-Fe-B permanent magnets [39].

1.1.2 Nd-Fe-B permanent magnets

At the moment, two families of permanent magnets are commercially produced on a large scale. The first family is ferrite, with the phases $BaFe_{12}O_{19}$ and $SrFe_{12}O_{19}$ of the hexagonal magnetoplumbite structure. The energy product of ferrite magnets is less than 38 kJ/m^3, but ferrites are cheap (less than \$5/kg) and relatively easy to produce in large scale. Ferrites occupy nearly about one-third of the permanent magnets market, with a yield of million tonnes each year [40].

The another family is Nd-Fe-B permanent magnets, which almost represent about two-thirds of the permanent magnets market and are based on $Nd_2Fe_{14}B$ which is an iron-rich tetragonal phase independently discovered in Japan [41] and in the USA [42] in 1982. Nd-Fe-B permanent magnets have been the most popular choice for the high-end applications, especially in the energy field such as wind turbines and electric vehicles [43].

In this thesis, our research on rare-earth permanent magnets is mainly based on $Nd_2Fe_{14}B$ phase, which possesses a tetragonal lattice with space group $P4_2/mnm$. Figure 1.3 displays the unit cell of $Nd_2Fe_{14}B$. Each unit cell contains four formula units, or 68 atoms with two different rare-earth positions, small $4f$ and big $4g$, six crystallographically distinct iron sites, Fe16($k1$), Fe16($k2$), Fe8($j1$), Fe8($j2$), Fe4(e), Fe4(c), and one boron site. The atomic coordinates and the interatomic distance are list in Table 1.1 and 1.2, respectively. With the synthesis of ternary $Nd_2Fe_{14}B$ permanent magnets, new research interest and
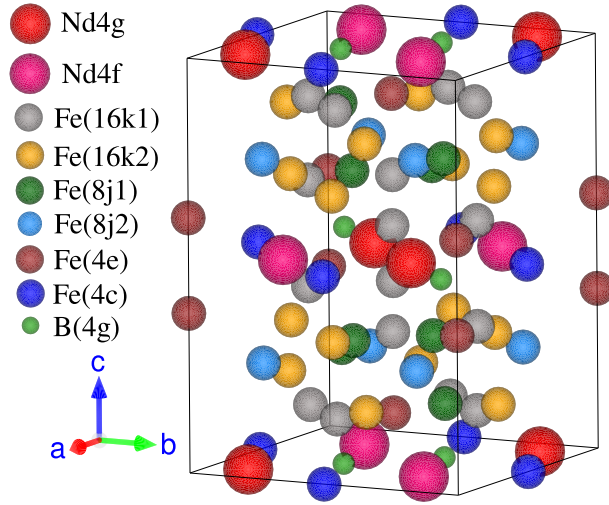
Figure 1.3: The prototypical structure of the $Nd_2Fe_{14}B$ compounds, which is a tetragonal unit cell.

technological application has been thrived. Pseudoternary based on $Nd_2Fe_{14}B$ has a prosper development, for example, $Nd_xCe_{(1-x)}Fe_{14}B$, $Nd_xDy_{(1-x)}Fe_{14}B$, $Nd_2Fe_xCo_{(1-x)}B$, etc. Most of pseudoternary either has a promotion on $(BH)_{max}$ or a much higher T_c, enabling more choices and wide applications in industry [44]. The crystal structure of other rare-earth, rare-earth-lean, and rare-earth-free permanent magnet candidates are shown in Figure 1.4.

Table 1.1: Crystallographically inequivalent atomic sites and fractional coordinates (x, y, z) in the $Nd_2Fe_{14}B$ unit cell with lattice constants of $a = 8.8$ Å, $c = 12.2$ Å at 295 K.

Atom	x	y	z
Nd($4f$)	0.268	0.268	0
Nd($4g$)	0.140	-0.140	0
Fe($16k_1$)	0.223	0.567	0. 127
Fe($16k_2$)	0.037	0.360	0. 176
Fe($8j_1$)	0.098	0.098	0. 204
Fe($8j_2$)	0.317	0.317	0. 246
Fe($4e$)	0.5	0.5	0. 114
Fe($4c$)	0	0.5	0
B($4g$)	0.371	-0.371	0

The magnetic properties of the Nd-Fe-B magnetic material are very sensitive to the metallurgical processing. Two principle methods of production have been devised, either by powdering and sintering, as in samarium-cobalt, or by rapidly quenching from the melt.

Table 1.2: Interatomic distances (Å) in $Nd_2Fe_{14}B$ from the coordinates in Table 1.1. All pairs of atoms separated by less than 4 Å are included.

Atom	Neighbors and distances		Atom	Neighbors and distances	
Nd(4f)	4 Fe(16k_2)	3.06	Fe(j_1)	2 Fe16(k_2)	2.39
	2 Fe(8j_2)	3.07		1 Fe(8j_1)	2.44
	4 Fe(8k_1)	3.08		1 Fe(4e)	2.53
	2 Fe(4c)	3.12		2 Fe(16k_1)	2.60
	2 Fe(4e)	3.21		2 Fe(8j_2)	2.65
	2 Fe(8j_1)	3.27		1 Fe(8j_2)	2.77
	2 B(4g)	3.30		1 Nd(4f)	3.27
	2 Nd(4g)	3.76		2 Nd(4g)	3.28
				1 B(4g)	3.62
Nd(4g)	1 B(4g)	2.87	Fe(j_2)	2 Fe16(k_2)	2.63
	4 Fe(16k_1)	3.09		2 Fe(8j_1)	2.65
	2 Fe(8j_2)	3.14		2 Fe(16k_2)	2.66
	4 Fe(8j_1)	3.28		2 Fe(16k_1)	2.70
	4 Fe(16k_2)	3.28		2 Fe(16k_1)	2.76
	2 Fe(4c	3.40		1 Fe(8j_1)	2.77
	1 Nd(16g)	3.49		1 Fe(4e)	2.80
	2 Nd(4f	3.76		1 Nd(4f)	3.07
				1 Nd(4g)	3.14
				1 B(4g)	3.88
Fe(16k_1)	1 B(4g)	2.10	Fe(4e)	2 B(4g)	2.12
	1 Fe(16k_2)	2.46		4 Fe(16k_1)	2.51
	1 Fe(4e)	2.51		2 Fe(8j_1)	2.53
	2 Fe(16k_2)	2.52		1 Fe(4e)	2.78
	1 Fe(4c)	2.57		2 Fe(8j_2)	2.80
	1 Fe(8j_1)	2.60		2 Nd(4f)	3.21
	1 Fe(16k_1)	2.60		4 Fe(16k_1)	3.86
	1 Fe(8j_2)	2.70			
	1 Fe(8j_2)	2.76	Fe(4c)	4 Fe(16k_2)	2.50
	1 Fe(4f)	3.08		4 Fe(16k_1)	2.57
	1 Fe(4g)	3.09		2 Nd(4f)	3.12
	1 Fe(16k_1)	3.11		2 Nd(4g)	3.40
	1 Fe(4e)	3.86		2 B(4g)	3.46
Fe(16k_2)	1 Fe(8j_1)	2.39	B(4g)	4 Fe(16k_1)	2.10
	1 Fe(16k_1)	2.46		2 Fe(4e)	2.12
	1 Fe(ec)	2.50		1 Nd(4g)	2.87
	2 Fe(16k_1)	2.52		1 B(4g)	3.21
	3 Fe(16k_2)	2.56		2 Nd(4f)	3.30
	1 Fe(8j_2)	2.63		2 Fe(4c)	3.46
	1 Fe(8j_2)	2.66		2 Fe(8j_1)	3.62
	1 Nd(4f)	3.06		2 Fe(8j_2)	3.88
	1 Nd(4g)	3.28			

Figure 1.4: The crystal structure of other rare-earth, rare-earth-lean, and rare-earth-free permanent magnet candidates.

In the powder sintering method developed by Sagawa et al. [14, 41], the constituents are induction melted in an alumina crucible under an inert atmosphere (argon for example) to prevent oxidation. The alloy is then milled into a powder with particles of diameter 3 μm. In order to obtain anisotropic permanent magnets with the highest possible $(BH)_{max}$ value, the powders are subsequently aligned in an external magnetic field of 800 kA/m, compacted under 200 MPa pressure, and then sintered in an argon atmosphere at a temperature in the range 1050–1250 °C. This process is followed by a post-sintering annealing. During annealing after sintering the microstructure of the material is optimized, thus considerably increasing the magnet coercivity. The rapid quenching process, known as "magnequench" was developed by Croat et al. [19, 20]. Constituents are arc melted together. Then the molten alloy in an argon atmosphere is ejected through a hole in the quartz crucible onto a rapidly rotating substrate. On the substrate, the metal cools rapidly to form ribbons. This gives a fine-grained microstructure of the equilibrium $Nd_2Fe_{14}B$ phase, with a particle size in the range of 20–80 nm. The ribbons are then processed by the following two procedures. One way is that they are bonded with epoxy to form a bonded magnet with intermediate maximum energy product typically of 72 kJ/m^3. Another way is that the ribbon fragments are vacuum hot pressed and vacuum die upset to form aligned magnets with a high maximum energy product up to 320 kJ/^{3} [45]. Up to know, plenty of investigations are still carried to optimize these two routes to improve the magnetic properties and examine the coercivty mechanism of Nd-Fe-B magnets.

Except for the metallurgical processing, magnetic properties are also very sensitive to the extrinsic microstructure such as grain size, grain shape, grain boundary composition, magnetic properties of grain boundary and intergranular phases, etc. The process combining hot-pressing and die-upsetting reported by [46] is shown to give a coercivity around 1.1 T with $(BH)_{max} = 320$ kJ/m^3. This performance is almost comparable to the that of sintered Nd-Fe-B magnets. In addition, Seelam [47] found that if a low melting temperature glass forming alloys could form in the intergranular regions, the coercivity can be improved up to 2.8 T. The minor addition of Cu and Al along with the post-sinter annealing can also enhance the coercivity [48, 49]. For example, Seeger et al. prepared sintered $Nd_2Fe_{14}B$ alloys with Ga and Nb additions [50]. Then Yan et al. followed this idea and added small amounts of W, Mo and Nb additives in sintered magnets, and found that the coercivity could be enhanced while the remanent magnetization did not change [51]. Furthermore, Sepehri-Amin found [52–56] that there exists Fe and Co in the grain boundary, so that the grain boundary is ferromagnetic and $Nd_2Fe_{14}B$ grains are ferromagnetically coupled. This finding in fact is against the result from previous work which demonstrates the Nd-rich grain boundary phase non-ferromagnetic [52, 57–61]. In order to make the grain boundary nonmagnetic and thus the $Nd_2Fe_{14}B$ grains magnetically isolated, Liu et al. gave a systematic study on the effect of Nd content on the microstructure and found that the excess Nd could lead to the formation of a thick distinct Nd-rich phase along the grain boundary and a coercivity enhanced to 1.79 T [58].

Grain boundary diffusion is currently widely explored to improve the performance of Nd-Fe-B magnets. By diffusing the Nd-rich phase from the powder surface to the grain boundary, an enhancement of the coercivity from 1.66 to 1.95 T was reported [62]. And using the Nd-Cu diffusion process, a large enhancement in the coercivity from 1.5 T to 2.3 T in hot-deformed magnets has been achieved [45, 63, 64]. A coercivity of 2.28 T has been obtained by adding 0.5 wt% Ga to $Nd_{16.5}Dy_{16}Fe_{53.45}Co_{13.0}B_{1.05}$ (wt%) alloys [65]. Moreover, if the diffuser contains heavy rare-earth elements, for instance Nd-Dy-Al compounds, the coercivity of a grain boundary diffused hot-deformed magnet could obtain a coercivity up to 2.75 T with a small sacrifice of remanence [66]. Other diffusion processes such as Dy [67] and Dy-Tb grain boundary diffusion in sintered Nd-Fe-B magnets [68] also significantly increase the coercivity.

The idea "smaller is stronger" is also testified in Nd-Fe-B magnets [69]. It is now well known that refining the crystalline size could increase the coercivity of Nd-Fe-B sintered magnets. Ramesh demonstrated that the coercivity increases as the grain size decreases [70, 71]. Critical grain size was also proposed and become a hot word for a decade, guiding people to find the mechanism of the domain reversal. It is found that the coercivity can exceed 2.5 T at room temperature when the grain size is reduced to 500 nm. The dependence of the coercivity of hot-deformed anisotropic Nd-Fe-B magnets on grain size has been examined to show that fine-grained magnets processed at lower temperature (700 °C) could realize higher coercivity [72]. As for the underlying mechanism, micromagnetic simulations of the exchange-coupled $Nd_2Fe_{14}B$ grains evidence that the local demagnetization factor decreases as the grain size is reduced, explaining the higher coercivity and the lower temperature dependence of coercivity in magnets with smaller grain sizes [73]. Besides, grain shape effects are also examined in details by micromagnetic simulations [74]. It was found that when the grain shape is changed from the triangular prism to the spheroid, the coercivity can be increased by a factor of ~2 [74].

Nd-Fe-B magnets, which are now produced in increasing quantities, have better room-temperature magnetic performance and are much cheaper than SmCo. But unfortunately they have a low Curie temperature around 350 °C, indicating that the magnetic properties will be strongly degraded if the temperature increases and the maximum service temperature is estimated to be around 250 °C. This is also one of the reasons that why Sm-Co magnets at some special cases, especially at wide temperature range and high temperature in aerospace engineering, still cannot be replaced by Nd-Fe-B magnets. Normally the coercivity of sintered magnets reach 1/3–1/5 of the theoretic value. So there is enough space to obtain a higher coercivity. Scientists exert many efforts in improving the coercivity and Curie temperature by advanced processing method, such as one element addition or combined additions on the main phase, grain boundary diffusion process [75]. It has been shown that Co addition can increase the Curie temperature and temperature stability [76]. Some research groups

found that coercivity in hot-deformed magnets can be improved due to the domain wall pinning in the grain boundary, and the domain wall energy barrier is temperature dependent [77]. In order to pin the domain wall at high temperatures, the surface nucleation of the hard magnets plays a critical role. It is expected that the suppression of nucleation at the surface would help increase the coercivity at high temperatures [78]. In hot-deformed Nd-Fe-B magnets, Yomogita found that the magnetization reversal process is governed by depinning in the thermal condition [79]. Liu [72] found that if one can achieve finer grains in hot-deformed magnets and thus the smaller local demagnetization, the temperature coefficient of coercivity (β) can be notably improved. It is found that a great advantage of the hot-deformed magnets is that its temperature coefficient of coercivity ($\beta \sim -0.45$ %/°C) is smaller than that of the sintered ones ($\beta \sim -0.60$ %/°C), thus better merit of thermal stability. It is now well accepted that adding heavy rare earth (Dy or Tb) into the main phase $Nd_2Fe_{14}B$ or the grain surface, can remarkably increase the coercivity and its temperature coefficient [66–68]. Alternatively, grain boundary diffusion of Nd-Cu [45] and Pr-Cu [80] alloys in the heavy rare earth free Nd-Fe-B magnets also enhances β.

1.1.3 Sm-Co permanent magnets

Even though the Nd-Fe-B magnets have almost occupied the two-thirds markets of permanent magnets, Sm-Co magnets are still required in some special application case such as aerospace engineering and defense technology where the performance stability at relatively high temperatures is the critical concern. Generally, Sm-Co magnets can be divided into $SmCo_5$ and Sm_2Co_{17} types [81, 82], which possess high magnetocrystalline anisotropy and Curie temperatures. Their standard commercial products could satisfy the applications with a temperature range from 50 to 250 °C.

Sm_2Co_{17} is observed as the rhombohedral (R) Th_2Zn_{17}-type structure in cast and homogenized alloys, with the lattice parameters $a \sim 8.395$ Å and $c \sim 12.216$ Å[83], as illustrated in Figure 1.4. It possesses high saturation magnetization M_s around 1.23 T, and a high Curie temperature T_c around 1,180 K, and an high magnetocrystalline anisotropy constant about 4 MJ/m^3 [84]. In contrast, the hexagonal (R) Th_2Ni_{17}-type structure is a high-temperature phase or is metastable over the entire temperature range and only obtained in splat-cooled samples [83]. $SmCo_5$ is a hexagonal intermetallic compound of a prototype $CaCu_5$, which is made up of alternating Co and Sm-Co layers, as shown in Figure 1.4. $SmCo_5$ combines a relatively high saturation magnetization M_s around 1.1 T, and a high Curie temperature T_c around 1,000 K, and an excellent magnetocrystalline anisotropy constant about 17–18 MJ/m^3 [81, 84, 85]. In $SmCo_5$, there exists Sm and Co sublattices which are coupled by moderately strong intersublattice exchange. The magnetocrystalline anisotropy of $SmCo_5$ is 3–4 times higher than that of Sm_2Co_{17}.

Sintered Sm-Co-type magnets based on the 2:17 R-type phase usually have a composition close to $Sm(Co,Fe,Cu,Zr)_{7.5}$, and the magnetic domain structure of SmCo 2:17-type magnets

is found to be very sensitive to details of the processing procedure [86]. The microstructure of this type magnets is found to be a diamond-shaped cellular structure, which consists of a cellular morphology with twinned rhombohedral 2:17 phase cell interiors as matrix phase, 1:5 phase cell boundaries surrounding the matrix of 2:17-type phase, and elongated thin platelets with a 1:3 structure oriented perpendicular to the c-axis [84, 87, 88]. Zr prefers go to the thin platelets and make them Zr rich. The role of Zr in developing the morphology and the chemical partitioning is very important [87]. The associated coercivity mechanism is pinning. The intersections of the Zr-rich platelet phase and the Cu-rich $SmCo_5$ boundary phase form the pinning sites, whose pinning strength is related to the large difference between the domain wall energies of the 1:5 phase and the Zr-rich platelet phase. Depending on the composition of the platelet phase, it is demonstrated to either have no direct influence on or notably contribute to the coercivity [84, 89]. Researchers also declare that the coercivity is dominated by the density and strength of the pinning sites in the 1:5 phase while modified by the Zr-rich platelet phase [88]. The Sm_2Co_{17}-based magnets was continuously investigated to increase the energy products throughout the 1970s. The optimized magnets $Sm(Co,Fe,CuZr)_{7-8}$ are shown to have a magnetic anisotropy of 4.2 MJ/m^3, a saturation magnetization of 0.97 MA/m, and a maximum energy product of 260 kJ/m^3 [90]. Their maximum working temperature is up to 300–350 °C.

For $SmCo_5$-based magnets, its synthesis process is simpler than Sm_2Co_{17}-based magnet, leading to lower production cost. $SmCo_5$-based magnets also have better corrosion resistance and temperature stability than Nd-Fe-B magnets [91]. The maximum energy product of $SmCo_5$-based magnet has reached 191 kJ/m^3 in 1972 [92] and is not remarkably increased afterwards. In $SmCo_5$-based magnets, the second phase is found to be either of composition close to Sm_3Co or SmCo. Sm_3Co is found to appear both at grain boundaries and within the $SmCo_5$ grains [93]. Recently, Zhang et al. declare that apart from the hexagonal $SmCo_5$ main phase, these exists hexagonal Sm_2Co_7 minor phase and a small amount of monoclinic Sm_2O_3 phase (about 100 nm) [91].

1.1.4 RFe_{12}-type potential rare earth-lean permanent magnets

RFe_{12}-type compounds (R denotes rare earth elements) with a tetragonal structure have been recognized as potential permanent magnets since the discovery of the $ThMn_{12}$-type compounds containing 75 and more at.% Fe in 1990s [94]. The major merit is that RFe_{12}-type compounds contain much less rare earth than the popular $Nd_2Fe_{14}B$ phase. So RFe_{12}-type compounds are promising candidate for the new classes of rare-earth-lean permanent magnets.

RFe_{12} are expected to have high magnetization as they have the highest Fe content of R-Fe compounds in the R-Fe system. However, they are unstable in R-Fe binary systems and have to be stabilized by replacing Fe with a third element M (M = Al, Cr, V, Ti, Mo, W, Si and Nb) to form $R(Fe_{1-x}M_x)_{12}$ [95]. In addition, interstitial nitrogen dissolution to form $RFe_{12}N_x$ is

demonstrated to enhance Curie temperature (T_c), saturation magnetization ($\mu_0 M_s$), and anisotropy field (H_a) [27]. After introducing nitrogen into R(Fe,M)$_{12}$, the average increase in T_c could be up to ~200 °C [96]. For example, T_c is increased from 274 °C for NdFe$_{11}$Ti to 467 °C for NdFe$_{11}$TiN [27, 97]. In terms of T_c, NdFe$_{11}$TiN is desirable as permanent magnets for the high-temperature applications such as traction motors in electric vehicles. Nevertheless, it only possesses a $\mu_0 M_s$ of 1.48 T which is smaller that that in Nd$_2$Fe$_{14}$B due to the substitution of nonmagnetic element Ti. For understanding the underlying mechanism, first-principle calculations show that Ti substation at the 8i site slightly increases the magnetocrystalline anisotropy, but decreases magnetization significantly [98]. Recently, it is found that even though there is no nitrogen, the SmFe$_{11}$V compound still can be stabilized into the ThMn$_{12}$-type structure to achieve $\mu_0 M_s$ around 1.12 T, H_a around 11 T, and T_c around 361 °C [99].

In order to achieve the NdFe$_{12}$N$_x$ phase without the substitution of M for Fe and thus realize a higher saturation magnetization while maintaining the magnetic hardness, NdFe$_{12}$N$_x$ films without any nonmagnetic element M are successfully grown. It is shown to possess T_c around 550 °C, $\mu_0 M_s$ around 1.7 T, and H_a around 6–8 T [27, 28]. Further more, T_c and $\mu_0 M_s$ for NdFe$_{12}$ is 282 °C, 1.64 T, respectively, and is remarkably increased to 586 °C and 1.78 T for SmFe$_{12}$N$_x$ [100]. H_a for both NdFe$_{12}$ and SmFe$_{12}$N$_x$ is around 12 T [28, 100].

In addition, the computational high-throughput screening approach is also applied to search for the intermetallic phases derived from the ThMn$_{12}$-type crystal structure. For instance, Körner et al. examined 1280 phases and found several promising phases like NdFe$_{12}$X or NdFe$_{11}$TiX (X = B, C, N) with energy products up to 600 kJ/m^3 and anisotropy fields up to 10 T. More interestingly, Ce containing compounds like CeFe$_{11}$TiX (X = B, C, N), CeFe$_{11}$CoX (X = B, N) CeFe$_8$Co$_4$X (X = B, C, N), or CeFe$_8$Ni$_4$N possess lower energy products, but have the advantage of being less resource-critical due to the avoidance of Nd and other heavy rare earth [101].

In spite of the above excellent magnetic performance, an optimum micro- or nanostructure has not yet been well developed for these alloys [23]. For example although SmFe$_{11}$Ti has high $\mu_0 M_s$ and magnetocrystalline anisotropy, its equilibrium phase diagrams do not offer neighboring phases with low melting points or decomposition reactions allowing precipitation hardening. This has prevented the production of these magnets in industry [23]. Moreover, the fabrication of dense three-dimensional magnets from RFe$_{12}$ is still in slow progress, and more efforts should be made in this aspect to realize the most advanced RFe$_{12}$-type compounds as high-performance permanent magnets for commercial or industrial applications [28].

1.1.5 Rare-earth free permanent magnets

Alnico as a typical Fe-based steel alloy is the primary permanent magnets in the first half of the twentieth century. In the beginning, Fe-based alloys usually possess a low $(BH)_{max}$ sig-

nificantly less than 8 kJ/m^3. In 1930s, the development of alnico contributed to a remarkable improvement in $(BH)_{\max}$ [102]. Since then, alnico forms the industry standard for high-end permanent magnet applications in mid-twentieth century. Alnico magnets are synthesized by the spinodal phase decomposition of high-temperature homogeneous compositiom into a two-phase nanocomposite which consists of ferromagnetic FeCo-rich and essentially non-magnetic NiAl-rich phases. The cubic FeCo phase possesses the highest known $\mu_0 M_s$ and a high T_c, but has cubic magnetocrystalline easy axes and thus magnetocrystalline anisotropy energy more than an order of magnitude smaller than that of the uniaxial Nd$_2$Fe$_{14}$B compound. Nevertheless, appreciable shape anisotropy can be obtained by processing FeCo phase to elongate as parallelepipeds. After a magnetic annealing procedure, alnico alloys referred to by their grades (alnico 5-7, alnico 8, and alnico 9) can achieve a $(BH)_{\max}$ up to 40–80 kJ/m^3 [102, 103]. Alnico magnets with columnar microstructure are highly required to make use of the shape anisotropy of FeCo phase to obtain higher coercivity. However, the shape anisotropy in this magnet is limited. Further analysis indicates that the currently realized coercivity does not make full use of the available magnetocrystalline anisotropy of FeCo phase owing to the nonoptimal nano/micro-structure. [104]. Therefore, optimizing the nano/micro-structure of alnico should further improve the coercivity.

Ferrites as a different class of permanent magnet are derived from a kind of oxides with a hexagonal crystal structure and were discovered in 1952 [105]. They are generally represented by the formula MO-6Fe$_2$O$_3$ or MO-2Fe$_2$O$_4$-6Fe$_2$O$_3$ with M as Ba, Sr, or Pb and O as oxygen. Pb is toxic and thus is not used for commercial ferrite magnets. The most successful permanent magnets based on ferrites contain Ba and thereby are well known as barium ferrite, barium hexaferrite or ceramic magnets. In terms of low or high magnetic coercivity, the different ferrites are generally classified as soft, semi-hard or hard. For example, manganese-zinc Mn$_x$Zn$_{1-x}$Fe$_2$O$_4$ and nickel-zinc Ni$_x$Zn$_{1-x}$Fe$_2$O$_4$ ferrites are often soft. Cobalt ferrites CoFe$_2$O$_4$ are often semi-hard. Strontium ferrite SrFe$_{12}$O$_{19}$ and Barium ferrite BaFe$_{12}$O$_{19}$ are often hard. T_c of ferrites is around 450 °C, but their overall magnetization is very sensitive to temperature ($\sim$–0.2%/K which is over 10 times that of alnico). The highest grade of ferrites possess a $(BH)_{\max}$ of 32 kJ/m^3 at room temperature. The significant merits of ferrites are that they are made with inexpensive elements, are easy to process, and have excellent corrosion stability for electric machine applications. The shortcoming is their low magnetization which requires large volumes of material to generate sufficient flux for machine operation [102].

FeNi (tetrataenite) with a lower-symmetry L1$_0$ structure has attracted much attention as a rare-earth free permanent magnet. The L1$_0$ structure consists of chemically ordered atomic layers of two Fe and Ni atoms which alternate along the tetragonal c-axis. In this way, L1$_0$ FeNi is shown to have a theoretically possible $(BH)_{\max}$ up to 446 kJ/m^3, large $\mu_0 M_s$ around 1.6 T, high T_c up to 550 °C, and large magnetocrystalline anisotropy constant around 1 MJ/m^3 [106, 107]. These intriguing magnetic properties are suitable for the

advanced permanent magnet applications. However, L1$_0$ structure is presently found to be only possible of forming the thin film state, prohibiting its utilization in bulk permanent magnets. The only minute quantities of L1$_0$ FeNi in the bulk form was found in the iron meteorites [108]. The artifcial synthesis of L1$_0$-FeNi has always remained as a challenge since its discovery in the 1960s [109]. Investigations are being carried to evaluate the fundamental properties and to develop artifcial synthesis routes for L1$_0$ FeNi [110, 111].

α''-**Fe$_{16}$N$_2$ (iron nitride)** is a metastable phase which was discovered in 1951 [112], which has been thought as one of the most promising rare-earth-free magnet candidates because of its use of environment-friendly raw materials [113]. It is confirmed to possess a giant $\mu_0 M_s$ around 2.9 T and a reasonably high magnetic anisotropy constant of 1.8 MJ/m^3. Also its temperature coefficient of coercivity is very small in the temperature range of 27–152 °C. But its Curie temperature is relatively low and can only be used at temperatures less than 150 °C. Another issue is the difficulty of fabricating α''-Fe$_{16}$N$_2$ bulk magnet. Up to know, the ion implantation method has be applied to fabricate the free-standing α''-Fe$_{16}$N$_2$ foils with magnetic energy product up to 160 KJ/m^3. A strained wire method is also newly proposed to fabricate the bulk anisotropic α''-Fe$_{16}$N$_2$ magnet and achieve a magnetic energy product around 70 KJ/m^3. Low-temperature nitridation method to fabricate iron nitride ribbons and foils provides another simplified way to fabricate a α''-Fe$_{16}$N$_2$ bulk magnet. Further optimization is underway to improve the energy product [113].

Mn-based compounds, such as ferromagnetic MnBi and MnAl, were considered as candidate materials for permanent magnets since 1960s. In compounds MnBi and MnAl, the Mn atoms are ferromagnetically coupled. But the total magnetization in these compounds is low, as the stoichiometry translates to a small volume fraction of magnetic atoms [102]. This will result in a low magnetic energy density. These compounds are demonstrated to deliver moderate $(BH)_{max}$ values around 50–100 kJ/m^3 [102] and are appropriate for applications where extremely high magnetic energy densities are not necessary. Most interestingly, the H_c of low-temperature MnBi phase increases with increasing temperature [114]. The highly anisotropic MnBi powders from arc-melting and low energy ball milling possess H_c around 1.17 T and $(BH)_{max}$ around 72 KJ/m^3. The bulk magnet fabricated from these powders shows $(BH)_{max}$ around 46 KJ/m^3 at room temperature and around 29 KJ/m^3 at 530 K, with T_c around 630 K [115, 116]. MnAl in the metastable τ-phase in the L1$_0$ structure is also a promising candidate for permanent magnets. Its room-temperature magnetocrystalline anisotropy is close to that of Nd2Fe$_{14}$B, but its $\mu_0 M_s$ is only $\sim 40\%$ of that of Nd2Fe$_{14}$B. These parameters yield a theoretical $(BH)_{max}$ around 100 KJ/m^3. Nevertheless, processing MnAl into permanent magnets is still difficult owing to the metastable nature of parent ϵ-phase MnAl at the τ-phase formation temperature and the competing decomposition reaction of the ferromagnetic τ-phase into two equilibrium paramagnetic phases [102, 117].

Theoretically predicted compounds such as $3d$-$5d$ transition metal compounds, Heusler alloys with interstitial doping, and MAB phases are also promising candidates for permanent

magnets. For instance, a high-throughput theoretical search focusing on $3d$-$5d$ transition metal compounds shows that the data-mining/data-filtering approach could identify Pt_2FeNi, Pt_2FeCu, and W_2FeB_2 as the most promising candidates for novel rare-earth free permanent magnets, with a magnetocrystalline anisotropy around 2.42, 5.83, and 1.07 MJ/m^3, respectively [118]. High-throughput density functional theory calculations considering the effect of light interstitial H, B, C, and N atoms on the magnetic properties of cubic Heusler alloys, demonstrate that interstitial doping yields 32 candidates with large uniaxial magnetocrystalline anisotropy (> 0.4 MJ/m^3) [119]. Similarly, in the MAB phase which is the ternary borides comprising stacked M–B layers (M: transition metal, B: boron) interleaved by monolayers of A atoms, 23 compounds with a uniaxial magnetocrystalline anisotropy greater than > 0.4 MJ/m^3 are also theoretically predicted [120]. These theoretically predicted compounds with moderate high uniaxial magnetocrystalline anisotropy could be intriguing for the gap between ferrite and rare-earth magnets with something cheap and effective. But they are still remained to be explored experimentally.

1.2 Intrinsic magnetic properties of permanent magnets

Permanent magnets are usually in the bulk type (or film state in some special applications) when they are used industries. In magnetism, there is a fundamental distinction between intrinsic and extrinsic properties. Intrinsic properties, such as the spontaneous magnetization M_s, the Curie temperature T_c, and magnetocrystalline anisotropy energy, are realized on the atomic length and time scales but described in infinite crystals representing the structure of main- and sub-phases in permanent magnets. Generally, they can be considered as equilibrium properties. For example, the magnetization of α-Fe single crystals, $\mu_0 M_s = 2.15$ T, is associated with body-centered cubic structure of elemental iron. By contrast, extrinsic magnetic properties, such as the coercivity H_c and the remanence M_r, reflect the magnet's real microstructure and are the overall exhibition of the interplay among different phases and structures. The strong microstructure dependence of extrinsic properties is seen, for example, from the fact that the coercivity of technical iron doubles by adding an extremely small amount of nitrogen (0.01 wt.%). By comparison, intrinsic properties are not sensitive to such as small concentration of defect or doping. Extrinsic properties are, in general, nonequilibrium phenomena, closely related to magnetic hysteresis and sensitive to microstructures.

Intrinsic magnetic properties refer to the atomic origin of magnetism and involve quantum phenomena such as exchange, crystal-field interaction, interatomic hopping, spin-orbit coupling, etc. The understanding of some problems of intrinsic magnetism, such as exchange, dates back to the very early days of quantum mechanics [121]. In contrast, the deciphering and exploitation of the large magnetic anisotropy of advanced magnetic materials is a comparatively recent event, with a focus on spin-orbit coupling and crystal-field interaction.

Intrinsic properties themselves are interesting figures of merit and play decisive roles in the design of magnets, but they also affect the hysteresis loop both experimentally and theoretically, for example, by entering the micromagnetic equations as parameters. In this section, I introduce shortly the magnetic dipole moment per atom, magnetic order, the spontaneous magnetization, the magnetocrystalline anisotropy, the interatomic exchange interaction, and the exchange stiffness as the intrinsic properties.

1.2.1 Magnetic moment

The magnetic moment of magnetic solids nearly exclusively originates from the partly filled inner electron shells of the transition-metal atoms. The most important ones are the iron-series transition-metal elements ($3d$ elements) such as Fe, Co and Ni, and the rare-earth or $4f$ elements such as Nd, Sm, Gd and Dy. In addition, palladium-series ($4d$), platinum-series ($5d$), and actinide ($5f$) elements, would also have a magnetic moment if they appear in a suitable crystalline or chemical environments. The inner-shell electrons give rise to a magnetic moment m, which is often measured in Bohr magneton $\mu = 9.274 \times 10^{-24}$ Am^2. An alternative way of characterizing a material's net moment is to consider the magnetization per volume $M_s = m/V$ in the unit of of A/m, or its flux-density equivalent $\mu_0 M_s$ in the unit of T. Here V is a small volume element which contains at least one unit cell.

From the quantum mechanics viewpoints, there are two sources of the atomic magnetic moment m, including the spin moment and orbital moment of the electrons, as illustrated in Figure 1.5. Currents associated with the orbital motion of the electrons (orbital moment) and the electron spin (spin moment as the intrinsic degree of freedom of electron) are the origins of the magnetic moment. The magnetism of free atoms or ions is governed by Hund's rules, which predict that the spin and orbital moments are a function of the number of inner-shell electrons [122]. Hund's rules are very well satisfied in rare-earth atoms, because the radius of the rare-earth $4f$ shells is much smaller than the atomic radius of the rare-earth atoms. The electrostatic field created by the crystalline environment is therefore largely screened, and the rare-earth $4f$ shells can be treated as quasi-free.
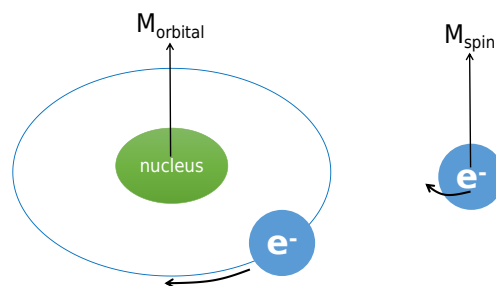
Figure 1.5: Illustration of the orbital moment and spin moment.

Table 1.3: Magnetic moment of rare-earth atom (R) in $R_2Fe_{14}B$ compounds at 4 K [44].

Compound	μ_R (μ_B)	gJ	J	L	S	g
$Pr_2Fe_{14}B$	3.1	3.2	4	5	1	4/5
$Nd_2Fe_{14}B$	3.2	3.3	9/2	6	3/2	8/11
$Sm_2Fe_{14}B$	1.0	0.7	5/2	5	5/2	2/7
$Gd_2Fe_{14}B$	−6.8	7	7/2	0	7/2	2
$Tb_2Fe_{14}B$	−9.1	9	6	3	3	3/2
$Dy_2Fe_{14}B$	−10.1	10	15/2	5	5/2	4/3
$Ho_2Fe_{14}B$	−10.1	10	8	6	2	5/4
$Er_2Fe_{14}B$	−9.3	9	15/2	6	3/2	6/5
$Tm_2Fe_{14}B$	−6.7	7	6	5	1	7/6
$Yb_2Fe_{14}B$	−4.2	4	7/2	3	1/2	8/7

The magnetic moment of iron-series transition-metal atoms in metals (Fe, Co, Ni, YCo_5) and nonmetals (Fe_3O_4, NiO) is primarily decided by the spin. So the moment, measured in μ_B, is equal to the number of unpaired spins. For example, Fe^{2+} (ferrous iron) has four unoccupied $3d\downarrow$ orbitals and thus the moment per ion is 4 μ_B. The orbital moment is very small, because the orbital motion of the electrons is suppressed or quenched by the electrostatic crystal field. In terms of elementary quantum mechanics, $3d$ wave functions of free atoms have a circular-current running-wave character and yield an orbital moment, but a crystalline environment forces the electrons to form standing waves with zero orbital moment. On the other hand, spin-orbital coupling competes with the crystal field and yields a small mixture of circular-current character, corresponding to a residual orbital moment in the order of 0.1 μ_B. The temperature dependence of the magnetization including the reorientation transition can be obtained from the Hamiltonian model [123]. In contrast to the iron-series transition-metals, the orbital moment in the rare-earth element is very large whereas the spin moment is small. The average magnetic moment per rare-earth atom (R) in $R_2Fe_{14}B$ compounds from the experimental magnetization data at 4 K is presented in Table 1.3, in which g is the Landé factor, J, L, and S are the total angular momentum, orbital momentum, and spin momentum in the Hund's-rule state of the $4f$ shell of the corresponding trivalent rare-earth ions, respectively [44]. Even though the spin moment of R is very small compared to the orbital moment, the total R moment and the R spin moment are antiparallel for the light-rare-earth ions and parallel for the heavy-rare-earth ions. The rare-earth $4f$ and iron $3d$ spin moments are always antiparallel, i.e., the $3d$-$4f$ exchange interaction is invariably antiferromagnetic. The negative μ_R in Table 1.3 means the antiferromagnetic coupling between R and Fe atoms. This is the reason that the net magnetic moment of $R_2Fe_{14}B$ with heavy-rare-earth R is much smaller than that with light-rare-earth R.
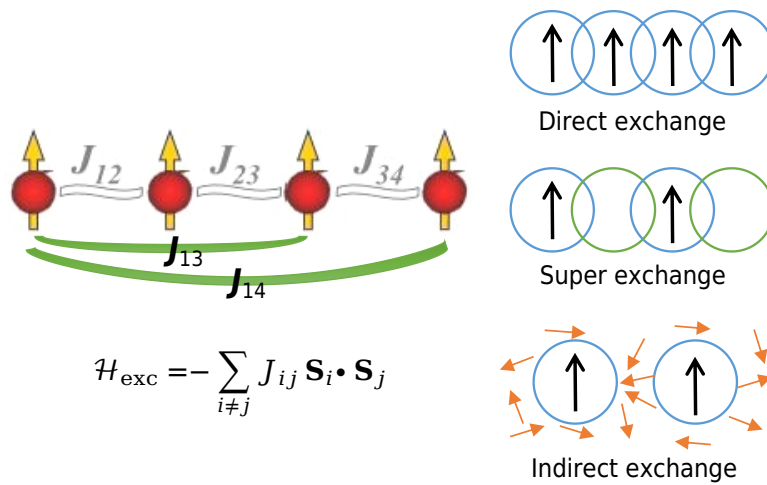
Figure 1.6: Illustration of interatomic exchange interactions J_{ij} and different exchange types.
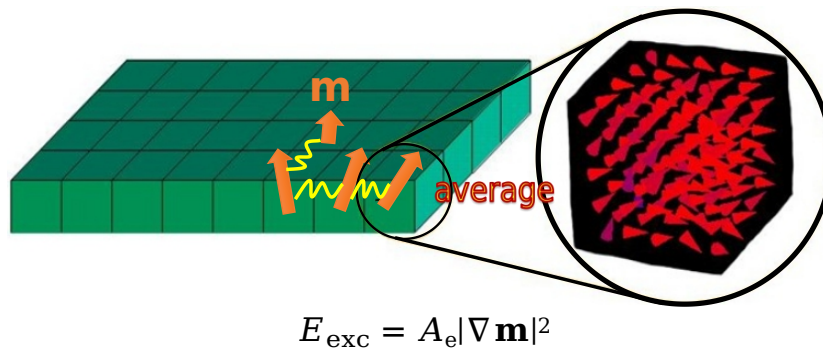
$$E_{\mathrm{exc}} = A_{\mathrm{e}}|\nabla \mathbf{m}|^2$$

Figure 1.7: Illustration of exchange stiffness A_{e} in terms of micromagnetics on the continuum level.

1.2.2 Interatomic exchange interaction and exchange stiffness

The net magnetic moment and spontaneous magnetization are realized by the exchange interaction between electrons. In a simple two-electron model, exchange gives rise to ⇈ (ferromagnetic) or ⇵ (antiferromagnetic) coupling between spins. In the quantum mechanics level, there are two main types of exchange. Firstly, atomic moments are determined by intra-atomic exchange. For example, the Fe atom has six $3d$ electrons and thus the intra-atomic exchange yields the schematic spin structure ↑↑↑↑↑↓. Secondly, there is an interatomic exchange J_{ij} between neighboring magnetic atoms. Interatomic exchange yields the long-range magnetic order observed in ferromagnets, ensures finite-temperature magnetocrystalline anisotropy, and is of importance in micromagnetism. Exchange is an

electrostatic many-body effect, caused by $1/|r - r'|$ Coulomb interactions between electrons located at sites r and r'. Physically, $\downarrow\uparrow$ electron pairs in an atomic orbital are allowed by the Pauli principle but unfavorable from the point of view of Coulomb repulsion. Parallel spin alignment $\uparrow\uparrow$ means that the two electrons are in different orbitals, which is electrostatically favorable. However, the corresponding gain in Coulomb energy competes against an increase in one-electron energies: only one electron benefits from the low ground-state energy, while the second electron must occupy an excited one-electron level. In agreement with Hund's rules, intra-atomic exchange favors parallel spin alignment. On the contrary, the sign of the interatomic exchange is more difficult to predict [121].

A widely-used approach to discuss interatomic exchange is the Heisenberg Hamiltonian $-\sum_{i \neq j} J_{ij} \mathbf{S}_i \cdot \mathbf{S}_j$ between neighboring spins $\mathbf{S}_i$ and $\mathbf{S}_j$, where J_{ij} is interatomic exchange interaction strength between site i and site j, as illustrated in Figure 5.1. The sign of exchange interaction strength is important for determining the magnetic order. $J_{ij} > 0$ indicates ferromagnetic materials in which neighboring spins are aligned in parallel. $J_{ij} < 0$ indicates antiferromagnetic materials in which the spins prefer to align antiparallel. The occurrence of Heisenberg exchange energy is due to the symmetry of the electron wave function and the Pauli exclusion principle. The orientation of electronic spins in overlapping electron orbitals is governed by the Pauli exclusion principle. There are generally three types of interatomic exchange interactions. As shown in Figure 5.1, the direct exchange indicates the overlapping of charge distribution in neighboring magnetic ions. The super exchange means that magnetic ions are interacted by charge overlap with the same non-magnetic ions between these two magnetic ions. The indirect exchange shows that the magnetic ions have interactions that are mediated by interaction with conduction electrons, which is called RKKY (Ruderman–Kittel–Kasuya–Yosida) interaction [124–126]. The RKKY interaction strength between local moments embedded in a free-electron gas of Fermi-wave vector k_{F} could be estimated as $J_{ij} \sim \cos(2k_F R)/R^3$ [127]. Interatomic exchange competes not only with finite-temperature disorder but also with micromagnetic magnetization inhomogenities such as domains.

On a continuum level, the Heisenberg exchange is translated into the micromagnetic exchange energy density, which is related to the so-called exchange stiffness A_{e} through $A_{\mathrm{e}}|\nabla\mathbf{m}|^2$ with $\mathbf{m}$ as the unit vector representing the magnetization direction. As illustrated in Figure 1.7, the atomic-scale spins are averaged over a volume to obtain $\mathbf{m}$ as a continuum variable in the macroscale. If one assumes that $\mathbf{m}$ slowly varies spatially, the exchange energy in the continnum level can be estimated as a function of the $\mathbf{m}$ gradient. A_{e} includes the atomic-level interactions with the micromagnetic formalism. The exchange energy density depending on A_{e} is tightly related to the domain wall energy and domain wall width. For a simple cubic lattice with a lattice constant of a, the exchange stiffness could be estimated as $A_{\mathrm{e}} = JS^2/a$ with J as the nearest neighbour exchange interaction and S as spin quantum number. In most general cases, there is no simple relationship between

macroscale A_e and interatomic J_{ij}. The determination of A_e from the atomic-scale J_{ij} is nontrivial, which will also be a issue to be thoroughly addressed for $Nd_2Fe_{14}B$ in this thesis. For typical ferromagnets, A_e is in the order of 10 pJ/m.

1.2.3 Magnetic order and spontaneous magnetization

The term magnetic order mainly refers to the atomic spin structure such as ferromagnetic, ferrimagnetic, antiferromagnetic, etc. It usually excludes the micromagnetic structure such as domains and domain walls. Interatomic exchange interaction with a positive and negative J_{ij} favors parallel or antiparallel alignment of neighboring spins, respectively. In ferromagnets, such as Fe, Co and $Nd_2Fe_{14}B$ (at temperature above the spin orientation temperature), all spins are parallel and the atomic moments are their summation. Ferrimagnets such as Fe_3O_4 and $BaFe_{12}O_{19}$, and antiferromagnets such as CoO and MnF_2, are characterized by two or more sublattices with opposite moments. If the moments of all sublattices with antiparallel spins do not totally cancel out, one gets the ferrimagnetic state. If they cancel out each other and the net moment is zero, it becomes antiferromagnetic state. Sublattice formation may be spontaneous as in typical antiferromagnets, or imposed by the atomic composition as in ferrimagnets. Competing exchange interactions in periodic crystals and in disordered magnets give rise to noncollinear spin arrangements. Examples are helimagnetic order in perfect crystals, which is caused by competing interactions between next and more distant neighbors, and spin-glass behavior in magnets with atomic-scale disorder [128]. Deviations from parallel or antiparallel spin alignment may also occur at surfaces and interface.

Another important issue is related to the distinction between zero-temperature magnetism and finite-temperature magnetic order. At finite temperatures, thermal fluctuations could make the spin disorder and thus overcome the interatomic exchange interactions. If the temperature is sufficiently high, the thermal disorder will dominate to result in the disappearance of spontaneous magnetization. This critical temperature is the well-known Curie temperature T_c. Generally, the total interatomic exchange per atom does not exceed about 0.1 eV. By contrast, from the ratio $k_\mathrm{B}/\mu_\mathrm{B} = 1.488$ T/K, one can estimate that 1 K could induce an equivalent magnetic field around 1.5 T. However, the typical magnetostatic field in solids is of the order of one Tesla, which cannot explain the magnetic order at temperatures above 1 K. From the mean-field approximation by Weiss, it is the Weiss effective field resulting from the exchange interaction that resists the thermal disorder.

The intra-atomic exchange, much larger than the interatomic exchange, is in the order of 1 eV. Therefore, the magnitude of atomic moment at T_c is close to their zero-temperature value. The high strength of the intra-atomic exchange interaction means that the typical magnetization changes in magnetic solids are caused by moment rotations rather than by changes in the moments' magnitude. This refers not only to the spontaneous magnetization but also to micromagnetic magnetization changes at a constant temperature.

Due to thermal excitations, the spontaneous magnetization M_s is temperature-dependent.

M_s (T) is often but not always smaller than the zero-temperature magnetization $M_s(0) = M_0$. The derivation of the spontaneous magnetization M_s of a solid from the corresponding Heisenberg Hamiltonian is a complicated problem. Since the spontaneous magnetization is an equilibrium quantity, the knowledge of the partition function $Z = \sum_\mu [\exp(-E_\mu/k_B T)]$ is sufficient to derive M_s, but the number of terms in Z increases exponentially with the size of the magnet, and only in a few cases there exist exact solutions [129].

The simplest finite-temperature approach is the spin $-1/2$ mean-field Ising model. It is defined in terms of the two energy levels $E_\pm = -hs_\pm$, where $s_\pm = \pm 1$ is the orientation of the atomic spin and $h = \mu_0 m H$ is an easy exercise to find the thermally averaged spin projection $\langle s \rangle = \tanh(h/k_B T)$. In the mean-field theory, $h = zJ\langle s \rangle$, where z is the number of nearest neighbors and J is the interatomic exchange. In this way,one has $\langle s \rangle = \tanh(zJ\langle s \rangle/k_B T)$. The temperature dependence of $M_s(T) = M_0\langle s \rangle$ is determined from this self-consistent equation, and the Curie temperature is equal to zJ/k_B. In contrast, the Heisenberg model, which takes into account the vector character of the quantum spins, has the mean-field Curie-temperature as $T_c = (S+1)zJ/3k_B S$, where S is the spin quantum number. The mean-field model could be easily generalized to two or more sublattices. For N sublattices (or N non-equivalent atomic sites), one will yield N coupled algebraic equations [130]. On the other hand, mean-field model does not work very well at low temperatures where M_s is determined by the cooperative spin waves [131], and also is not applicable close to T_c where long-range critical fluctuations interfere [129, 132, 133]. This could lead to the physically unreasonable prediction of ferromagnetism in one dimension [132, 133].

1.2.4 Magnetocrystalline anisotropy

The magnetocrystalline anisotropy is originate from the energy of a magnetic solid depending on the orientation of the magnetization with respect to the crystal axes. Permanent magnets need a high magnetocrystalline anisotropy energy in order to keep the magnetization in a desired or designed direction. The primary source of anisotropy is electrostatic crystal-field interaction and spin-orbit coupling (Figure 1.8), which means the magnitude of the anisotropy depends on the ratio of crystal-field energy and spin-orbit coupling. The crystal field reflects the local symmetry of the crystal or surface and acts on the orbits of the inner-shell d and f electrons. Rare-earth $4f$ electrons [134, 135] are close to the atomic core and exhibit a strong spin-orbit interaction. This leads to a rigid coupling between spin and orbital moment, and the magnetocrystalline anisotropy is given by the comparatively small electrostatic interaction of the unquenched $4f$ charge clouds with the crystal field [44, 136, 137]. However, due to the absence of quenching effects, the interaction with the crystal field is very effective, and the rare-earth single-ion anisotropy is much larger than the magnetic anisotropy of typical $3d$ element. It is basically the orbital motion of the electrons coupled with the crystal electric field that gives rise to the first order contribution to magnetocrystalline anisotropy. The second order arises due to the mutual interaction
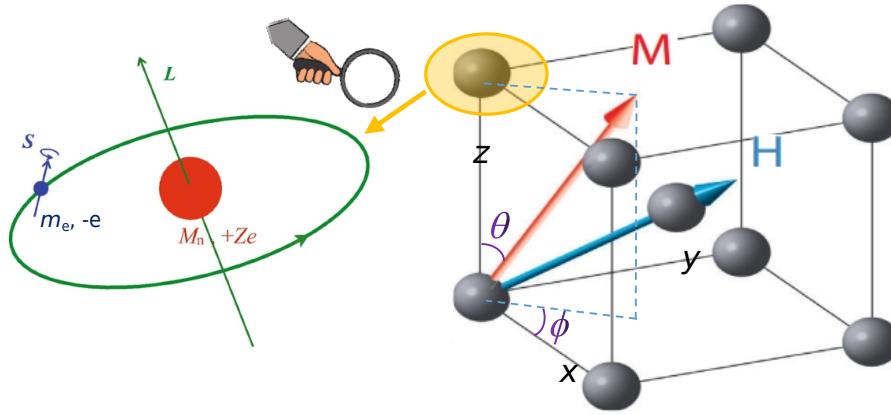
Figure 1.8: Illustration of spin-orbital coupling in a crystal.

of the magnetic dipoles. This effect is weak compared to the exchange interaction and is difficult to compute from first principles, although some successful computations have been reported [138].

The magnetocrystalline anisotropy is intimately linked to the crystal structure. Therefore only non-cubic crystal structures are interesting for permanent magnets. Mainly hexagonal and tetragonal crystals are used for the main phases of permanent magnets. A lot of crystal systems have a single axis of high symmetry (threefold, fourfold or sixfold), whose anisotropy is usually called uniaxial anisotropy. If the z axis is taken to be the main symmetry axis of the crystal, the lowest order term of the magnetocrystalline anisotropy energy density can be expressed as

$$E/V = K_1(\alpha^2 + \beta^2) = K_1(1 - \gamma^2) \tag{1.1}$$

The ratio E/V is an energy density (energy per unit volume). This can also be represented in the spherical polar coordinates with $\alpha = \cos\phi\sin\theta$, $\beta = \sin\phi\sin\theta$, and $\gamma = \cos\theta$, leading to

$$E/V = K_1\sin^2\theta \tag{1.2}$$

The parameter K_1, is often represented as K_u, has units of energy density and depends on composition and temperature, usually called uniaxial magnetocrystalline anisotropy constant. The minima in this energy with respect to θ satisfies

$$\partial E/\partial\theta = 0 \text{ and } \partial^2 E/\partial\theta^2 > 0 \tag{1.3}$$

If $K_1 > 0$, the directions of lowest energy are the $\pm z$ directions. The z axis is called the easy axis. If $K_1 < 0$, there is an easy plane perpendicular to the symmetry axis (the basel plane of the crystal). The typical values of K_1 in some magnetic crystals, some of which are the potential main phases for permanent magnets, at room temperature are given in Table 1.4. It

Table 1.4: Magnetocrystalline anisotropy constant and saturation magnetization of some typical magnetic crystals at room temperature [44, 139–147].

Compound	K_1 (MJ/m^3)	type	$\mu_0 M_s$ (T)
La$_2$Fe$_{14}$B	1.10	uniaxial	1.38
Ce$_2$Fe$_{14}$B	1.21	uniaxial	1.17
Pr$_2$Fe$_{14}$B	4.66	uniaxial	1.56
Nd$_2$Fe$_{14}$B	4.65	uniaxial	1.60
Sm$_2$Fe$_{14}$B	9.07	uniaxial	1.52
Gd$_2$Fe$_{14}$B	0.85	uniaxial	0.89
Tb$_2$Fe$_{14}$B	6.13	uniaxial	0.70
Dy$_2$Fe$_{14}$B	4.24	uniaxial	0.71
Ho$_2$Fe$_{14}$B	2.42	uniaxial	0.81
Er$_2$Fe$_{14}$B	0.29	uniaxial	0.90
Tm$_2$Fe$_{14}$B	0.37	uniaxial	1.15
Lu$_2$Fe$_{14}$B	1.21	uniaxial	1.17
Y$_2$Fe$_{14}$B	1.46	uniaxial	1.41
Th$_2$Fe$_{14}$B	1.46	uniaxial	1.41
SmCo$_5$	17.2	uniaxial	1.07
Sm$_2$Co$_{17}$	3.3	uniaxial	1.28
L1$_0$ CoPt	4.9	uniaxial	1.00
L1$_0$ FePt	6.6	uniaxial	1.43
α-Fe	0.05	cubic	2.15
Ni	-0.05	cubic	1.48
hcp-Co	0.53	uniaxial	1.81
FeO·Fe$_2$O$_3$ (magnetite)	-1.1	cubic	1.48
CoO·Fe$_2$O$_3$	0.35	cubic	0.58
NiO·Fe$_2$O$_3$	-0.04	cubic	0.37
MnO·Fe$_2$O$_3$	-0.038	cubic	0.50
MgO·Fe$_2$O$_3$	-0.025	cubic	0.14

can be found that the for the rare-earth compounds, such as Pr$_2$Fe$_{14}$B, Nd$_2$Fe$_{14}$B, Sm$_2$Fe$_{14}$B, Dy$_2$Fe$_{14}$B, Tb$_2$Fe$_{14}$B, and SmCo$_5$, a large K_1 exceeding 4.0 MJ/m^3 can be realized. L1$_0$ phase such as CoPt and FePt can also generate very large K_1 over 4.9 MJ/m^3. For the α-Fe, K_1 is as small as 0.05 MJ/m^3. For the nickel, manganese, and magnesium ferrites, K_1 is negative and its absolute value is less than 0.05 MJ/m^3, with diagonals as easy axes. Magnetite possesses a K_1 around –1.1 MJ/m^3. Only cobalt ferrites have a positive K_1 around 0.35 MJ/m^3 with three crystal axes (a, b, c) as easy axes.

Many models of magnetization represent the anisotropy as uniaxial and ignore higher order terms. However, if $K_1 < 0$, the lowest energy term does not determine the direction of the easy axis within the basal plane. For this, higher-order terms are needed, and these

depend on the crystal system (hexagonal, tetragonal or rhombohedral). For $Nd_2Fe_{14}B$ which is a tetragonal system, the magnetocrystalline anisotropy energy density can be expanded as

$$E/V = K_1\sin^2\theta + K_2\sin^4\theta + K_3\sin^4\theta\sin2\phi \qquad (1.4)$$

The K_3 term is the fourth order (same as the K_2 term) and makes the energy contribution from ϕ to be included in the magnetocrystalline anisotropy energy density, thus being applicable to the determination of the basal plane anisotropy.

For the cubic crystal, the simplest magnetocrystalline anisotropy energy density function reads

$$E/V = K_1(\alpha^2\beta^2 + \beta^2\gamma^2 + \gamma^2\alpha^2) \qquad (1.5)$$

in which positive K_1 determines the easy axes along the crystal axis a, b, and c of the cubic crystal (e.g. α-Fe), and negative K_1 determines the easy axes along the diagonals of the cubic crystal (e.g. Ni). A higher order term such as $K_2\alpha^2\beta^2\gamma^2$ can also be included, with which both K_1 and K_2 should be combined to figure out the easy axes or planes.

It should be noted that the magnetocrystalline anisotropy constants have a strong dependence on temperature. They generally decrease rapidly as the temperature approaches the Curie temperature when the crystal becomes effectively isotropic. In this thesis, I will comprehensively study the temperature dependent magnetocrystalline anisotropy constants of $Nd_2Fe_{14}B$.

1.3 Extrinsic magnetic properties of permanent magnets

Extrinsic properties not only depend on the above-mentioned intrinsic properties, but also highly depend on the processing history and the resultant microstructures of the sample. In fact, it is the extrinsic properties that determine the practical performance or value of a permanent magnet. The microstructure dependent extrinsic properties, which are affected by a lot of factor such as the size or the texture of the grains, the sub-phases, the grain boundaries, etc., are macroscopically reflected in the hysteresis loop. Continuous and persistent efforts are made in the area of optimizing the extrinsic properties, in order to produce and establish a practical permanent magnet after the initial optimistic finding of a new hard magnetic phase. The extrinsic properties can be modified by heat treatments, mechanical work, surface treatments, grain boundary diffusion, hot press, shape change of the alloy powders and of the finished magnets. In this section, I discuss briefly the magnetization curve, hysteresis loop, and energy product, coercivity, domain, domain walls, interface exchange coupling strength, reversed domain nucleation, and domain wall pinning as the extrinsic properties.

1.3.1 Magnetization curve, hysteresis loop, and energy product

Hysteresis loops show the nonlinear relationship between the magnetization M and the magnetic field H, or the magnetic induction B and the magnetic field H. We often use M–H curve when discussing about the problems on continuum theory of magnetization, while B–H is adopted when the research field related to engineering techniques and the maximum energy product $(BH)_{\max}$ is the focus.

Magnetization curve can be measured by experiments. A magnet can be magnetized when applying an external field. M firstly increases with the increasing external field, and then reaches a stable value M_{sat} (saturation magnetization) as H goes above a certain value, as shown the orange curve in Figure 1.9.

The M–H hysteresis loops are obtained by monitoring the magnetization M (volume-averaged magnetic moment, with the unit A/m) as a function of the external magnetic field H. Starting from a saturate state, M decreases with decreasing external field but will not go alone with the original curve. When H decreases to 0, there remains magnetization, which is called remnant magnetization M_{r}. If an reversed external field is applied to the
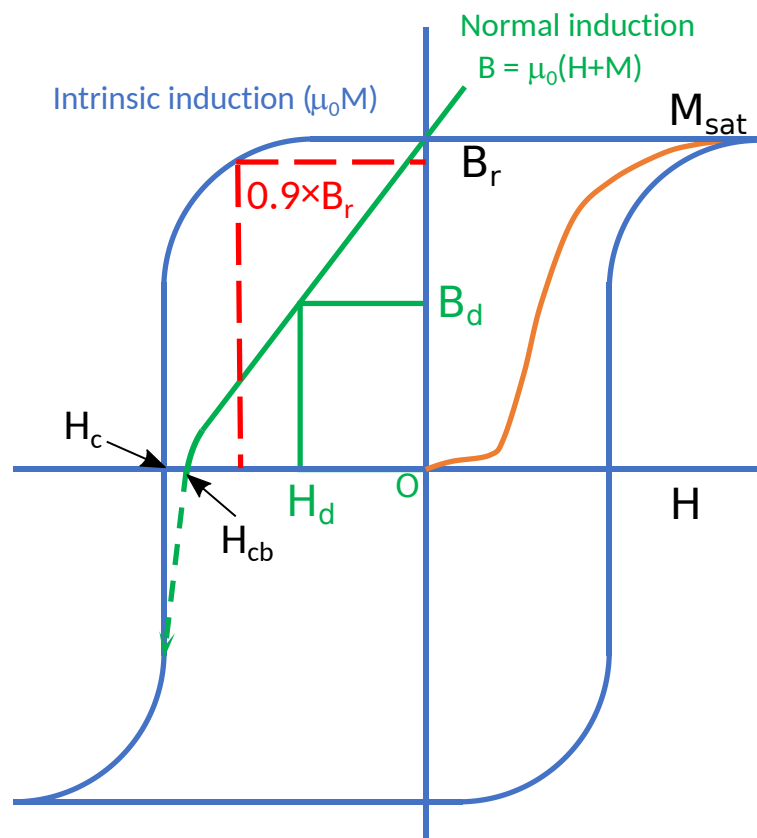
Figure 1.9: Typical hysteresis loop (schematic).

system, the magnetization will continue to decrease. At the point with $M = 0$, the value of the external field is called coercivity H_c or coercive force. The underlying physical meaning of this point is the magnetic ability to sustaining magnetization after being magnetized. Again, continuously increasing the reversed external field, the direction of M will rotate. And M will then reach $-M_{sat}$ at the end. Then repeat this procedure as mentioned before, and the M–H curve will follow the symmetry. Finally, a closed M–H curve was attained, which is called the hysteresis loop.

From the M–H loops, two very important extrinsic properties can be derived. One is coercivity H_c and another is remnant magnetization M_r. Micromagnetic problems are usually solved on a continuum level. For example, the magnetization M_s considered in micromagnetism is generally averaged over a few interatomic distances and can be regarded as a temperature-dependent but field-independent materials constant (micromagnetic parameter). The narrow-wall phenomena, which have been studied for example in rare-earth cobalt permanent magnets and at grain boundaries, involve individual atoms and atomic planes and lead to comparatively small corrections to the extrinsic behavior.

The B–H loop shows the flux density $B = \mu_0(H + M)$ as a function of H, which is used to determine the energy density stored in and outside the magnet. The green normal induction curve is a quarter of B–H loop, as shown in Figure 1.9, and $H_{cb} < H_c$. The energy product is a measurement for the amount of magnetic energy stored in a magnet, i.e., the product of B and H at each H point. The maximum energy product or $(BH)_{max}$ of a magnet is an energy density, which is equivalent to the area of the largest rectangle that can be inscribed under the normal induction curve as shown in Figure 1.9. At this operating point, one can define H_d and B_d. The unit of $(BH)_{max}$ is kJ/m^3 (Kilojoule per cubic meter) or MGOe (Mega-Gauss-Oersted).

1.3.2 Coercivity

The most intriguing aspect of hysteresis loops is the coercive force or coercivity. It describes the stability of the remnant state and gives rise to the classification of magnets into hard magnetic materials (permanent magnets), semihard material (storage media), and soft magnetic materials. The hardness of a magnet is described by the dimensionless parameter $\kappa = \sqrt{K_1/(\mu_0 M_s^2)}$ [148] , with K_1 as the above-mentioned uniaxial magnetocrystalline anisotropy constant. Magnetically very hard and very soft materials are characterized by $\kappa \gg 1$ and $\kappa \ll 1$, respectively. A widely-used phenomenological expression for the coercivity, with the consideration of both the microstructure and the thermal fluctuations, is

$$H_c = \alpha_k \frac{2K_1}{\mu_0 M_s} - N_{eff} M_s - \Delta H(T, \eta) \tag{1.6}$$

where α_K is the Kronmüller parameter [149, 150], N_{eff} is a magnetostatic interaction parameter (demagnetization effect), and ΔH is a fluctuation-field contribution caused by

thermal activation [151, 152]. The term ΔH is comparatively small at low temperatures, but makes the coercivity depend on the external field sweep rate $\eta = dH/dt$.

It should be noted that in Equation 1.6, $H_A = 2K_1/\mu_0 M_s$ is the so-called anisotropy field, which is the theoretically maximum coercivity that can be achieved. However, due to the microstructure in the real magnets, H_A is never achievable in experiments. The experimental coercivity H_c is usually one order of magnitude smaller than H_A. The concerns on an order of magnitude discrepancy between the micromagnetic or theoretical H_A and the experimental H_c are the well-known Brown's paradox [153, 154]. For instance, the theoretical nucleation field for an elongated iron specimen is around 50 mT, whereas the measured value for high-quality iron whiskers is about 0.01 mT [154]. Only in some rare cases of thin-film permanent magnets, a coercivity exceeding 20–30% of H_A is achieved. Only in an ideal case, it is possible to obtain a coercivity comparable to H_A. One example is the coherent-rotation or Stoner-Wohlfarth model [155]. However, it has been known for decades that neither the coercivity nor the loop shapes of real magnetic materials are reproduced by the Stoner-Wohlfarth theory. The Brown's paradox is basically ascribed to the presence of microstructures such as grain misorientation, metallurgical inhomogenities, surface irregularities, crystallographic defects of various kinds, grain boundaries, secondary phases, surface imperfections, intergrain exchange interactions, magnetic inhomogeneities, etc. These microstructural effects lead to local magnetic softening and reduce the anisotropy field H_A by a factor α, as shown in Equation 1.6, which is thought to correlate with the structural imperfections and spatial variation of intrinsic magnetic parameters such as M_s, K_1, A_e, etc. [149, 150]. Guided by the empirical expression in Equation 1.6, microstructure engineering is applied to design high-coercivity permanent magnets, but currently mostly limited to the following three aspects (taking Nd-Fe-B permanent magnets as example).

(1) **Tuning the effective demagnetization factor** N_{eff}. As shown in Equation 1.6 for H_c, the decrease of N_{eff} favors the enhancement of H_c. N_{eff} is the reflection of the average demagnetization field in a magnet, i.e., the reverse magnetic field generated by the magnetization itself [150]. It can be tuned by optimizing the grain size, shape, edges, and corners. At the sharp corners and edges of polyhedral $Nd_2Fe_{14}B$ grains, a large local demagnetizing stray field exits and usually leads to a premature magnetic reversal and thus a low coercivity. So the first way of tuning is to decrease the local demagnetization field by smoothing sharp grain corners, as shown by the enhanced coercivity predicted by micromagnetic simulations [74, 156]. The second way to tuning is the optimization of the $Nd_2Fe_{14}B$ grain shape (e.g., spheroid, circular prism, hexagonal prism, etc.), which can also increase coercivity by utilizing the shape anisotropy [153, 156, 157]. The third way is to refine the grain size, as shown by both experiments [72, 158] and theoretical studies [70, 73]; because the effective demagnetization field originating from magnetically reversed surface grains decreases with the average grain size. Nevertheless, experimental control of grain shape and corners is challenging. Grain size reduction usually has its own limit and is

accompanied with a decrease in remanence.

(2) **Tuning the anisotropy field in main phase $Nd_2Fe_{14}B$.** Increasing is intuitively a direct method to increase the coercivity of Nd-Fe-B magnets. One method is to directly dope the main phase $Nd_2Fe_{14}B$ by HRE (heavy rare earth), such as Dy and Tb. It is found that partial substitution of Nd by HRE (2–10 wt% of Nd) remarkably improves and thus gives higher coercivity and better thermal stability [44]. Since in this case HRE is distributed in the whole $Nd_2Fe_{14}B$ phase, this method suffers from a high usage of HRE whose supply is at risk. In order to reduce the usage amount of HRE, another method is to locally enhance and only distribute HRE near the surface of the $Nd_2Fe_{14}B$ grains. This is achieved by a grain boundary diffusion process of HRE. After diffusion heat treatment, a HRE-rich $R_2Fe_{14}B$ hard shell forms at the grain surface. It is shown that a shell thickness of a few nanometers is sufficient to enhance the coercivity [159–161]. This kind of strategy for tuning is intensively studied, but it cannot work without the usage of HRE. An alternative HRE-free approach is to manipulate of the Nd atoms in the interface or grain surface by investigating the surrounding chemical environment [162, 163] or strain/stress state [164, 165], with a focus on the theoretical calculations of crystal field parameters or magnetic anisotropy.

(3) **Tuning the saturation magnetization of the grain boundary (GB) phase.** Recently one of the mostly explored strategies for developing HRE-free Nd-Fe-B magnets is to decipher the magnetic properties of the GB phase with a focus on its M_s. The reduction of M_s of GB phase is thought to affect the coercivity by enhancing the GB pinning strength against the domain wall motion or decreasing the exchange interaction of the $Nd_2Fe_{14}B$ grains [166, 167]. In the sintered or melt-spun Nd-Fe-B magnets, it is found that the concentration of ferromagnetic elements (Fe,Co) in the thin GB layer is very high, corresponding to a GB M_s of 1 T [59]. More detailed studies show the anisotropic distribution of GB , i.e., GB parallel to the easy axis possesses much higher than that perpendicular to the easy axis [168]. These findings shed light on how to reduce GB M_s and increase coercivity. For instance, using the grain boundary diffusion of eutectic NdCu alloy to make the M_s of GB parallel to the easy axis almost zero, the coercivity of anisotropic hot-deformed Nd-Fe-B magnets was enhanced from 1.5 to 2.3 T [45]. In the Nd-rich Ga-doped Nd-Fe-B sintered magnet, optimal post-sinter annealing results in nonferromagnetic GB phases and thus an unusually high improvement in coercivity [54, 169].

1.3.3 Domain and domain walls

In large magnetic particles or magnets, the competition among the magnetocrystalline anisotropy energy, the exchange energy, and the magnetostatic self-interaction energy could lead to magnetization inhomogenities, i.e., multi-domain instead of single-domain state. For example, magnetostatic interactions tend to yield magnetic domains of opposite magnetization directions [170].

In terms of the magnetic charge density ($\nabla \cdot \mathbf{M}$), one can show that the self-interaction

energy is lowered by the absence of magnetic charges (poles) at the magnet's surface. Within a domain, the magnetization vectors are aligned in the same direction. Between two neighboring domains, there exists a smooth and thin transition zone, which is termed as domain wall. The reason is that the magnetization inside the domains tends to lie along the easy directions, whereas the transition between two easy magnetization directions involves energetically unfavorable spin orientations. As a consequence, magnetocrystalline anisotropy favors narrow domain walls. On the other hand, narrow walls correspond to large magnetization gradients and are unfavorable from the point of view of exchange energy which is related to $\nabla \cdot \mathbf{M}$.

Figure 1.10 shows the illustration of domains and two types of domain walls. For the Bloch wall in Figure 1.10(b) and (d), the magnetization components can be expressed as a function of the polar angle θ, i.e., $M_x = 0$, $M_y = M_s \sin \theta$, and $M_z = M_s \cos \theta$. Moreover, θ only changes with x and does not depend on y and z. In this case, the gradient of magnetization

$$\nabla \cdot \mathbf{M} = \frac{\partial M_x}{\partial x} + \frac{\partial M_y}{\partial y} + \frac{\partial M_z}{\partial z} = M_s \left(\cos \theta \frac{\partial \theta}{\partial y} - \sin \theta \frac{\partial \theta}{\partial z} \right) = 0 \qquad (1.7)$$

$\nabla \cdot \mathbf{M} = 0$ means that Bloch wall does not create magnetic charges or stray field within the crystal. Therefore, for a uniaxial magnet the total energy of the Bloch wall structure only includes the magnetocrystalline anisotropy energy and exchange energy, i.e.,

$$E_t = \int_{-\infty}^{+\infty} \left[A_e \left(\frac{\partial \theta}{\partial x} \right)^2 + K_1 \sin^2 \theta \right] \mathrm{d}x \qquad (1.8)$$

where x is the distance from central plane of the wall. Minimizing the functional in Equation 1.8 by variational principle, one yield the solution for θ as

$$\mathrm{d}x = \sqrt{\frac{A_e}{K_1}} \frac{1}{\sin \theta} \quad \Rightarrow \quad \theta(x) = 2\mathrm{atan} \left[\exp \left(\frac{x}{\sqrt{A_e/K_1}} \right) \right] \qquad (1.9)$$

Accordingly, the magnetization component M_z of Bloch wall in uniaxial magnets obeys

$$M_z(x) = M_s \cos \theta = -M_s \tanh \frac{x}{\sqrt{A_e/K_1}} \qquad (1.10)$$

There are several definitions of the domain wall width. The most commonly used definition is based on the slope of $\theta(x)$ at $x = 0$, as illustrated in Figure 1.10(e), in which the domain wall width is defined as

$$\delta_w = \pi \sqrt{\frac{A_e}{K_1}} \qquad (1.11)$$

and substituting Equation 1.9 into Equation 1.8 yields the associated domain wall energy

γ_w as

$$\gamma_w = 4\sqrt{A_e K_1} \tag{1.12}$$

If one uses M_z distribution and thus the slope of $\sin\theta$ at $x = 0$, the domain wall width will be $2\sqrt{A_e/K_1}$. One can also use the integral definition $\int_{-a}^{+a} \cos\theta(x)\mathrm{d}x$ with a as a parameter to define the domain wall width. This method is more reliable in experimental practice than the former two definitions which are based on a single point in a profile. For the case of Neél wall, $\nabla \cdot \mathbf{M} \neq 0$ and thus there exists stray field or magnetostatic energy. The solving procedure is similar to the case of the Bloch wall, but the solution is not analytic as Equation 1.9 and numerical methods should be utilized.

The domain-wall width can also be estimated from dimensional arguments. The domain-wall width is determined by the anisotropy constant K_1 and the exchange stiffness A_e, which are measured in J/m^3 and J/m, respectively. The only length and the only wall energy derivable from these parameters are the wall-width scale $\sqrt{A_e/K_1}$ and the wall-energy scale $\sqrt{A_e K_1}$, respectively. The typical domain wall width could be several nanometers for high-anisotropy materials and several micrometers for low-anisotropy materials. The domain wall width and energy for exemplary ferromagnetic materials are listed in Table 1.5.

There exists a critical diameter below which it is energetically more favorable for a particle to have a single domain state. Magnetostatic self-interaction favors domain formation to reduce the stray-field energy. Since the creation of domain wall costs energy, there are no walls if the reduction in magnetostatic energy is smaller than the increase in the wall energy. For a wall separating two semispherical domains in a spherical particle with a radius of R, the wall energy is $\gamma_w \pi R^2$. The competing loss in magnetostatic energy is roughly equal to half the single-domain energy, that is $\mu_0 M_s^2 V/12$. Therefore, from the equilibrium equation $\gamma_w \pi R^2 = \mu_0 M_s^2 V/12$, one can obtain that the domain formation is favorable for particles

Table 1.5: Domain wall width δ_w and energy γ_w for exemplary ferromagnetic materials [171, 172].

material	δ_w (nm)	γ_w (mJ/m^2)
Co	22.3	14.9
SmCo$_5$	2.64	57.1
Sm$_2$Co$_{17}$	5.74	30.7
Nd$_2$Fe$_{14}$B	3.82	22.4
Sm$_2$Fe$_{17}$N$_3$	3.36	40.6
BaFe$_{12}$O$_{19}$	13.94	5.7
Ni$_{80}$Fe$_{20}$	2000	0.1
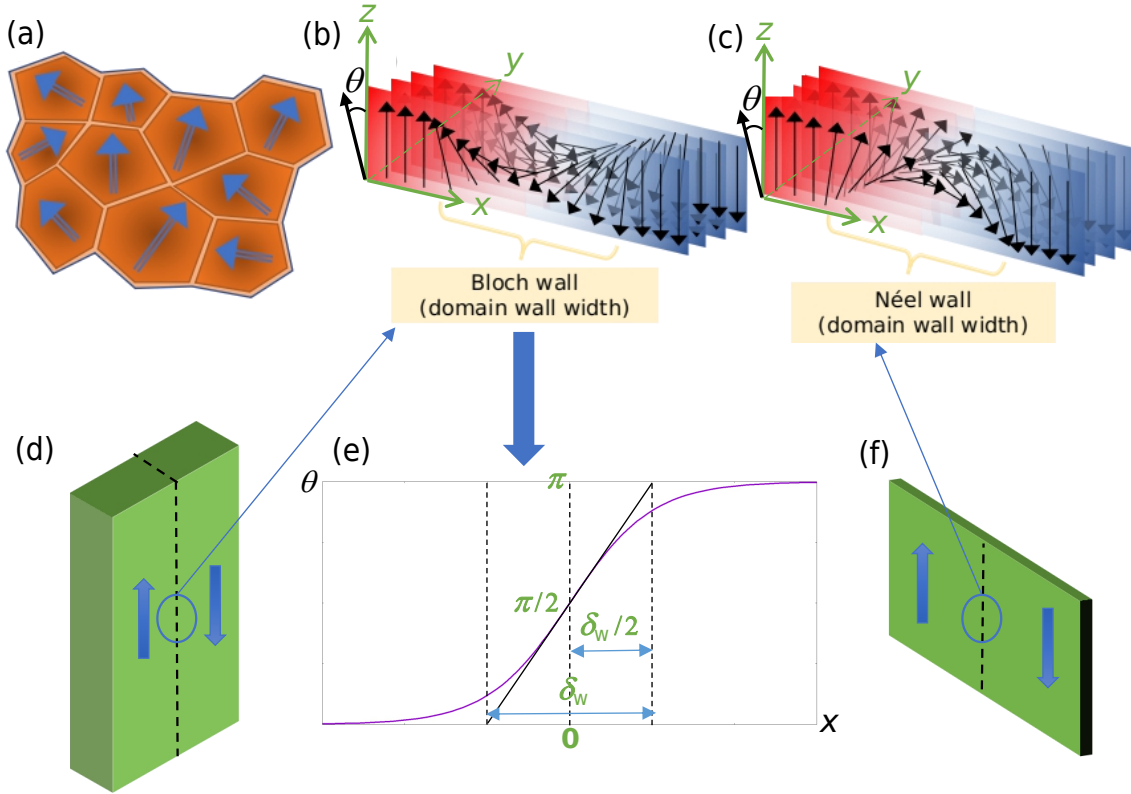
Figure 1.10: (a) Domain configuration. Crystals in each domain share the same magnetization direction. The domain wall exists between two neighboring domains. (b) (d) Bloch wall configuration. (c) (f) Néel wall configuration. (e) Polar angle θ distribution across the Bloch wall.

whose radius exceeds a critical single-domain radius

$$R_{\text{sd}} = \frac{9\gamma_{\text{w}}}{\mu_0 M_s^2} = \frac{36\sqrt{A_{\text{e}}K_1}}{\mu_0 M_s^2} \tag{1.13}$$

The single-domain critical radius R_{sd} of spherical particles of exemplary ferromagnetic materials is listed in Table 1.6. This R_{sd} value varies between a few nm in soft magnets and several hundreds nm in hard magnets. However, the critical single-domain size and the domain size in multidomain structures are strongly geometry-dependent. For example, typical domains in films with perpendicular anisotropy, often form meandering stripes. The domain size D_{d} is easily estimated by comparing the stray-field energy $\mu_0 M_s^2 D_{\text{d}} L^2$ where L^2 is the film area, with the wall energy $\gamma b L(L/D_{\text{d}})$ where b is the film thickness [170]. Minimizing the total energy with respect to D_{d} yields $D_{\text{d}} \approx \sqrt{\gamma b/\mu_0 M_s^2}$. In other words, the domain size exhibits a square-root dependence on the film thickness.

Table 1.6: Single-domain critical radius R_{sd} and domain-wall energy γ_w of spherical particles of exemplary ferromagnetic materials [171].

material	R_{sd} (nm)	γ_w (mJ/m^2)	$\mu_0 M_s^2$ (MJ/m^3)
α-Fe	4.9	2.1	3.82
Co	55.5	14.9	2.54
Ni	11.3	0.39	0.31
SmCo$_5$	585	57.1	0.88
Sm$_2$Co$_{17}$	210	30.7	1.33
Fe$_3$O$_4$	6.2	2.0	0.29
CrO$_2$	90	2.0	0.20
Nd$_2$Fe$_{14}$B	105	22.4	2.06
MnBi	240	12	0.45
BaFe$_{12}$O$_{19}$	31	5.7	0.183

It is important to keep in mind that the critical single-domain radius is largely unrelated to hysteresis. First, R_{sd} is a ground-state property, comparing free energies of single-domain and multidomain states. Whereas, hysteresis is a nonequilibrium phenomenon caused by free-energy barriers. As we will see in the next subsection, the onset of incoherent reversal in perfect ellipsoids of revolution is approximately governed by the exchange length

$$l_{ex} = \sqrt{\frac{2A_e}{\mu_0 M_s^2}} \tag{1.14}$$

This quantity is independent on magnetocrystalline anisotropy and in hard magnets is much smaller than R_{sd}. The popular but incorrect equating of single-domain magnetism and coherent rotation has its origin in the focus on soft and semihard magnets in the first half of the 20th century.

The exchange length Equation 1.14 can be interpreted as the length below which the atomic exchange interactions dominate the typical magnetostatic fields. It also determines the thickness of soft-magnetic films below which Néel walls are energetically more favorable than Bloch walls. From an atomic point of view, l_{ex} is proportional to $\alpha_0/\alpha = 7.52$ nm, where α_0 is the Bohr length and $\alpha \approx 1/137$ is Sommerfeld's fine-structure constant. Moreover, the region with a size smaller than the exchange length cannot be treated as a continuum, in which the atomistic spin model with the discrete nature should be utilized.

1.3.4 Nucleation and pinning

Coercivity mechanism is critical for analyzing and further designing high-performance permanent magnets. Generally, there are two main coercivity mechanisms: nucleation and

pinning, as illustrated in Figure 1.11.

Nucleation-controlled magnets are almost defect-free, and the coercivity is essentially given by the nucleation field, $H_c = H_N$. There are several types of nucleation: coherent rotation in very small particles, curling in large perfect ellipsoids of revolution, and localized nucleation in imperfect structures [173, 174]. In contrast to nucleation-type magnets, pinning-type magnets contain many defects or different phases with varying domain wall energy, which ensure coercivity by impeding the motion of the domain walls.

Nucleation means that the original magnetization state (remanent state) becomes unstable in a reverse magnetic field $H_z = H_N$. The nucleation field H_N is often a good estimate for the coercivity, particularly in nearly perfect magnets. The determination of the nucleation field amounts to an eigenmode analysis of the free energy. The coercivity reduction is accompanied by a localization of the nucleation mode. Localized nucleation corresponds to strongly inhomogeneous magnetization states and is therefore unfavorable from the point
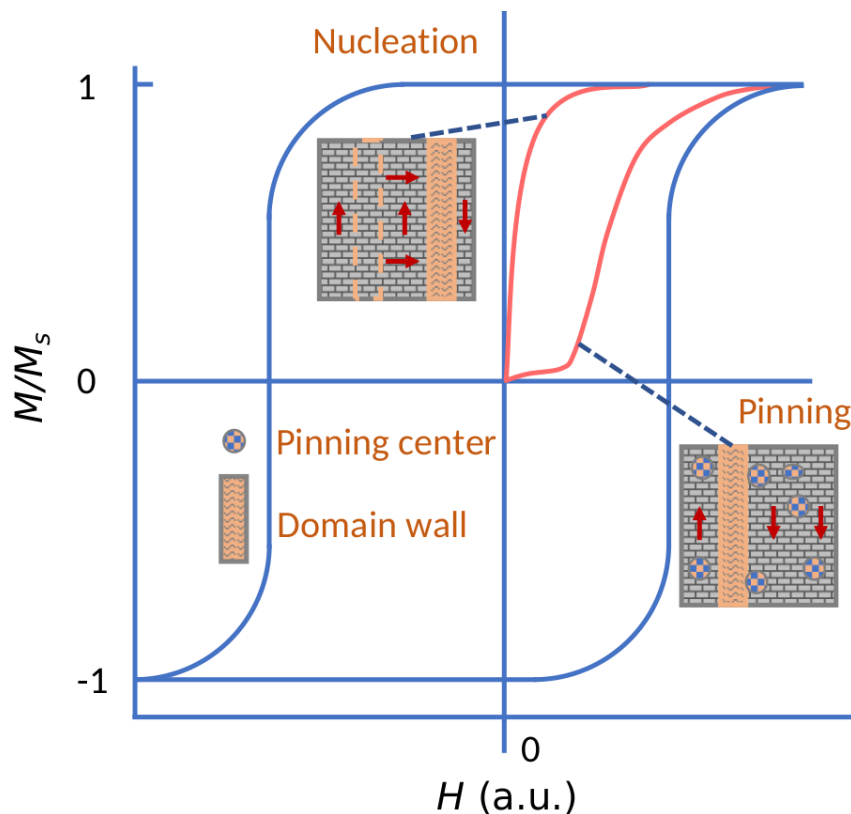
Figure 1.11: Illustration of nucleation and pinning mechanisms. In the case of nucleation, the coercivity relies on the absence of domains. Once reversal has started in nucleation-type magnets, the domain wall propagates nearly freely through the magnet.

of view of interatomic exchange. By contrast, the coherent-rotation and curling modes are delocalized, i.e., they extend throughout the magnet. On the other hand, localization is favorable from the point of view of magnetocrystalline anisotropy, because it exploits the local minima of magnetocrystalline anisotropy energy.

The pinning mechanism governs the magnetization reversal in strongly inhomogeneous magnets and means that the coercivity is determined by the interaction of domain walls with structural inhomogenities [175]. The trapping of walls by a small number of powerfull pinning centers is called strong pinning. A simple strong-pinning expression is $H_\mathrm{p} = [\mathrm{d}\gamma(x)/\mathrm{d}x]/(2\mu_0 M_\mathrm{s})$, where $\gamma(x)$ is the average domain-wall energy as a function of the wall position. By contrast, pinning caused by a large number of very small pinning centers, such as atomic defects, is called weak pinning. In the case of weak pinning, the wall energy is averaged over a distance in the order of δ_w, so that the density of pinning centers determines the overall pinning strength [176].

One typical pinning mechanism involves inhomogenities whose anisotropy constant is higher than that of the main phase; because high anisotropy yields high domain-wall energies and the penetration of the wall into the high-anisotropy regions is energetically unfavorable. This mechanism is known as repulsive pinning. Whereas the capturing of a wall in a low-anisotropy region is referred to as attractive pinning. The pinning energy barrier is, in a crude approximation, proportional to the anisotropy difference (if the exchange stiffness does not vary violently). By changing the critical chemical composition or the temperature [177], it is possible to adjust the anisotropy and to tune the pinning behavior.

The coercive field of minor hysteresis loops shows characteristic differences between pinning and nucleation hardened permanent magnets, as shown in Figure 1.11. In the case of a pinning hardened permanent magnet, the coercive field of a minor hysteresis loop is not larger than the maximum applied external field, whereas in the case of the nucleation hardened permanent magnet, the coercive field in general is larger than the applied external field if this is larger than the pinning coercive field which naturally also exists in the nucleation hardened permanent magnets. On approaching this critical field in nucleation hardened permanent magnets, an abrupt increase of H_c is observed which is considerably larger than the applied field. The coercive field exerted from nucleation mechanism can be several times larger than the applied external field. This cannot happen on pinning cases.

Larger coercive fields can be achieved either by domain wall pinning or by nucleation hardening. The nucleation mechanism has been found in Nd-Fe-B magnets. In a number of papers, the role of thermally activated nucleation and the expansion of the nuclei have been considered to be the leading coercivity mechanisms. Here it should be noted, however, that the effective field due to thermal fluctuations is only of the order of 0.1 T and therefore irrelevant for the interpretation of coercive fields of several tesla. For Nd-Fe-B magnets, previously it is widely accepted that their coercivity mechanism is nucleation. However,

recently it is declared that in conventional Nd-Fe-B sintered magnets in which the $Nd_2Fe_{14}B$ grains are exchange-coupled through ferromagnetic grain boundary phase, the coercivity is governed by domain wall pinning, not by nucleation. Only in the exchange-decoupled sintered magnets by tuning the chemical composition to a slightly Nd-rich and B-lean one with Ga-doping, the coercivity is governed by the nucleation mechanism and higher coercivity is achieved [178]. Deciphering the coercivity mechanism is still very important for the design or guidance of high-performance permanent magnets, and continues to attract persistent efforts from the research community, especially in terms of the latest discovered new magnets.

1.4 Outline of the thesis

1.4.1 Motivation of the thesis

As discussed in Sections 1.2 and 1.3, the performance of permanent magnets depends not only on the intrinsic properties of the main phases, but also the microstructure. The extrinsic magnetic properties are generally determined by the interplay of intrinsic magnetic properties of main- and sub-phases (the saturation magnetization, the magnetocrystalline anisotropy constant, and the exchange stiffness constant) and the microstructure. Therefore, there are two main thrusts towards new permanent-magnet materials, either by enhancing the intrinsic properties through the design of crystal structure and chemical composition of main- and sub-phases, or by improving the extrinsic properties via nanostructuring and microstructure optimization.

Theoretical study and simulation play an important role in the above thrusts, in terms of understanding and predicting the links between intrinsic magnetic properties, microstructure and extrinsic magnetic properties for the optimisation of magnetic performance. However, due to the huge gap between the different scales and the limitations of each theoretical methodology, there still remain challenges for a comprehensively theoretical simulation of permanent magnets across scales. For instance, the electronic-level calculations can yield the zero-temperature magnetic intrinsic properties, but can only handle magnetic systems of several hundreds of atoms. The commonly used micromagnetic simulations are suitable for exploring the influence of microstructure in permanent magnets, but have no direct access to the effect of the detailed interface structure at the atomic level and its effect on intrinsic magnetic properties. In fact, it has been verified that in Nd-Fe-B magnets, the coercivity is extremely sensitive to the atomic-scale or nanoscale local defect, sub-phase, or inter-granular phase. In addition, real magnets always work at finite temperatures. The intrinsic properties such as magnetocrystalline anisotropy, saturation magnetization and exchange stiffness constant must be temperature dependent. This is out of the ability of most electronic-level calculations. In the microscale and continuum scale, finite temperature will also induce thermal fluctuations that further notably influence the coercivity in addition
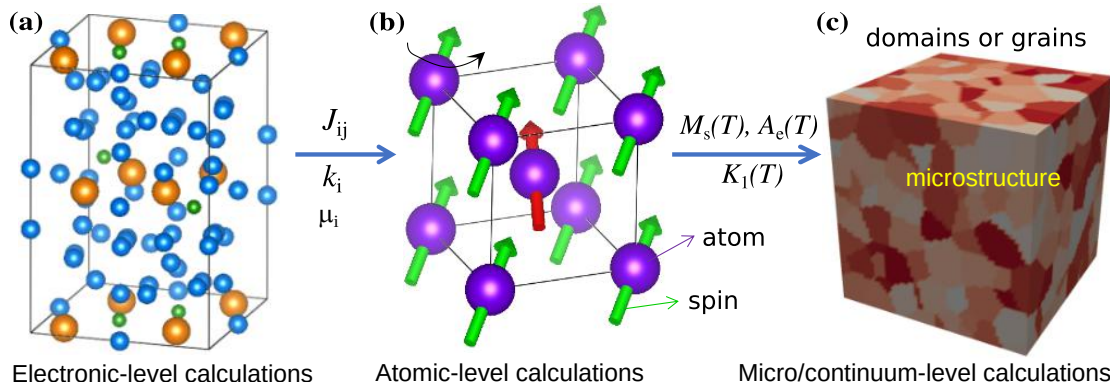
Figure 1.12: Schematics for a multiscale approach across the electronic, atomistic, and micro/continuum scales. (a) Electronic-level calculations for determining interatomic exchange parameters J_{ij}, atomic magnetocrystalline anisotropy energy k_i, and atomic magnetic moment μ_i at zero temperature. (b) Atomic-level calculations for determining temperature dependent intrinsic parameters, such as $M_{\mathsf{s}}(T), K_1(T), A_{\mathsf{e}}(T)$. (c) Micro/continuum-level calculations for obtaining extrinsic magnetic properties with the consideration of microstructure across scales.

to the microstructure itself.

Regarding to the above-mentioned dilemma in theoretical simulations bridging scales across intrinsic and extrinsic magnetic properties, the motivation of this thesis lies in the following three aspects.

(1) A theoretical and simulation methodology that is based on, but can go beyond the electronic-level calculations should be developed to calculate or predict the temperature dependent magnetic intrinsic parameters, which could be the basic input to micromagnetic models with microstructure taken into account.

(2) A multiscale approach across the electronic, atomistic, and micro/continuum scales should be established to link the calculation results from different scales, as illustrated in Figure 1.12. This is essentially important for the simulation of permanent magnets at finite temperatures with both the consideration of temperature dependent intrinsic parameters and thermal fluctuation effects at the micro/continuum level.

(3) Multiscale simulations should be essential to investigate the influence of local microstructure factors such as sub-phases, interfaces, or GB phases on the extrinsic magnetic properties. This is critical in terms of a multilevel understanding of interfacial effects on the coercivity at both the atomic level and microscopic level in permanent magnets.

1.4.2 Structure of the thesis

With in mind the motivations in Subsection 1.4.1, the thesis structure is arranged as follows.

In Chapter 1, the introduction of permanent magnets, the intrinsic magnetic parameters, and the extrinsic magnetic parameters are comprehensively reviewed. The motivation and structure of this thesis are also elucidated.

In Chapter 2, the theoretical backgrounds on multiscale simulations of magnetic materials are exhaustively introduced, including the spin-polarized density functional theory at the electronic level, the atomistic spin model at the atomic level, and the micromagnetic model at the micro/continuum level. Both the theory basis and the associated numerics are discussed in detail.

In Chapter 3, the intrinsic magnetic properties of the main phase $Nd_2Fe_{14}B$ in Nd-Fe-B permanent magnets and their temperature dependence are determined by *ab-initio* informed atomistic spin model simulations. This calculation framework provokes a scale bridge between first-principles calculations and temperature-dependent micromagnetic simulations of permanent magnets.

In Chapter 4, the influence of intrinsic bulk exchange stiffness in $Nd_2Fe_{14}B$ and the extrinsic interface exchange coupling strength between $Nd_2Fe_{14}B$ and grain boundary is investigated by the combined atomistic spin model simulations and micromagnetic simulations. The associated findings enable more freedom in designing Nd-Fe-B magnets by tuning exchange.

In Chapter 5, the extrinsic magnetic properties (e.g. coercivity) of Nd-Fe-B permanent magnets with microstructure features and their temperature dependence are explored by the integration of atomistic spin model simulations and finite-temperature micromagnetic simulations. The calculation scheme is essentially important for the simulation of permanent magnets at finite temperatures including thermal effects from different scales.

In Chapter 6, the microstructural influences in rare-earth free exchange-spring permanent magnet candidates, α''-$Fe_{16}N_2$/$SrAl_2Fe_{10}O_{19}$ composites and MnBi/FeCo bilayers, are uncovered by micromagnetic simulations. In collaboration with the experimental partners, the simulation results are useful for providing the correct direction to improve the performance of these two exchange-spring magnets by microstructure design.

In Chapter 7, the conclusions and outlook of this thesis are concisely summarized.

2 Theoretical backgrounds on multiscale simulations of magnetic materials

2.1 Spin-polarized density functional theory calculations

First-principles calculations based on quantum mechanics are capable of predicting the fundamental properties of materials or a given system without (or with less) artificial input parameters. For example, for a simple 2D square potential or a hydrogen atom, the Schrödinger equation can be exactly solved to obtain the wavefunction and then the allowed energy states of the system. However, it is impossible to exactly solve the Schrödinger equation for a many-body system. Therefore, some approximations must be made to make the Schrödinger equation solvable albeit tricky. There are lots of approximation methods, among which the density functional theory (DFT) is a typical method for obtaining an approximate solution to the Shrodinger equation of a many-body system. By using DFT, the properties of a many-electron system can be determined by using functionals, i.e., the spatially dependent electron density. Currently, DFT has been the most popular and versatile methods available in condensed-matter physics, computational physics, and computational chemistry, and has been widely used to investigate the structural, magnetic, and electronic, and optic properties of in particular atoms, molecules, and the condensed phases.

DFT was firstly put forward on the basis of the firm theoretical footing by Walter Kohn and Pierre Hohenberg in the framework of the two Hohenberg–Kohn (HK) theorems [179]. The original HK theorems only work for the non-degenerate ground states when there is no magnetic field. The first HK theorem indicates that an electron density $n(\mathbf{r})$ depending on only three spatial coordinates can uniquely determine the ground-state properties of a many-electron system. The second theorem expresses the system energy as a functional whose variational minimization is proved to give the ground-state electron density. Once the electron density distribution is solved, the other properties can be obtained. In work later by Walter Kohn and Lu Jeu Sham, the HK theorem was further developed to reach Kohn–Sham DFT (KS-DFT) [180]. Within the KS-DFT framework, the intractable many-electrons interacting problem in a static external potential is reduced to a tractable problem of noninteracting electrons moving in an effective potential. The KS equations of the tractable

noninteracting system can be derived as

$$\left[-\frac{\hbar^2}{2m}\nabla^2 + V_{\text{s}}(\mathbf{r}) \right] \varphi_i(\mathbf{r}) = \varepsilon_i \varphi_i(\mathbf{r}) \tag{2.1}$$

which yields the orbitals φ_i that reproduce the density $n(\mathbf{r})$ of the original many-body system as

$$n(\mathbf{r}) = \sum_{i=1}^{N} \left| \varphi_i(\mathbf{r}) \right|^2. \tag{2.2}$$

The effective single-particle potential V_{s} can be written as

$$V_{\text{s}}(\mathbf{r}) = V(\mathbf{r}) + \int \frac{n(\mathbf{r}')}{|\mathbf{r} - \mathbf{r}'|} \, \mathrm{d}^3\mathbf{r}' + V_{\text{XC}}[n(\mathbf{r})] \tag{2.3}$$

in which $V(\mathbf{r})$ is the external potential, the second term is the Hartree term related to the electron-electron Coulomb repulsion, and the last term V_{XC} is the exchange-correlation potential that includes all the many-particle interactions. It is clear that both the V_{XC} and Hartree term are dependent on $n(\mathbf{r})$ that depends on φ_i which in turn depends on V_{s}. Therefore, a self-consistent iterative procedure has to be carried out to solve the problem of KS equation. As a general routine, the calculation can be started with an initial guess for $n(\mathbf{r})$. Then the corresponding V_{s} is calculated and the KS equations are solved to obtain φ_i. From these φ_i, one can calculate a new density $n(\mathbf{r})$ and start the calculations again. This procedure is repeated until the convergence is reached (usually in terms of energy).

The exchange-correlation potential V_{XC} is difficult to determine, but is extremely crucial to the solving of KS equations. In general, approximations are applied to construct V_{XC}. The simplest approximation of V_{XC} is the local-density approximation (LDA), which is based upon exact exchange energy for a uniform electron gas. In order to account for the non-homogeneity of the true electron density, the gradient of the density is considered and thus generalized gradient approximations (GGA) are born. To further include the second derivative of the electron density, the meta-GGA functionals more accurate than the GGA functionals are developed. Other hybrid functionals [181], which incorporate a portion of exact exchange from Hartree–Fock theory with the rest of the exchange-correlation energy from other sources, are also proposed. For the system with strong on-site Coulomb interaction of localized electrons, the DFT+U method and the associated Hubbard Hamiltonian (for strongly correlated electronic states of d and f orbitals) are proposed [182]. The semiempirically tuned numerical parameter "U" is added to the local and semilocal density functionals, thus resulting in LDA+U and GGA+U computational operations.

If the spin or magnetism is considered, DFT is extended to spin-polarized DFT by Hedin and Rajagopal [183, 184]. If an electronic system is exposed to an external magnetic field, generally both the electron spin and the electronic orbital current are coupled to

the magnetic field. Spin-polarized DFT provides a framework for the description of spin coupling. Here, it is restricted to consider only the electron density and the spin density, and neglect the current and the small components of the Dirac spinors. In this case, the total energy $E = G[n(\mathbf{r}), \mathbf{s}(\mathbf{r})]$ is now a functional of the electron density and the spin density. $n(\mathbf{r})$ and $\mathbf{s}(\mathbf{r})$ are the scalar electronic density and the vector of the spin density, respectively. In the standard DFT literature the quantities $n(\mathbf{r})$ and $\mathbf{s(r)}$ are commonly written in terms of a compact object called the density matrix. Instead of these four variables, alternatively the 2×2 spin density matrix $n_{\alpha\beta}(\mathbf{r})$ can be used, i.e.,

$$n_{\alpha\beta}(\mathbf{r}) = \sum_{i=1}^{N} \varphi_i^*(\mathbf{r}; \alpha)\varphi_i(\mathbf{r}; \beta) \tag{2.4}$$

in which α and β can have two values, either + for spin-up majority spin or – for spin-down minority spin. In this way, the charge and spin densities which are related to the Pauli density matrix can be easily obtained as

$$n(\mathbf{r}) = \sum_{\alpha} n_{\alpha\alpha}(\mathbf{r}) \tag{2.5}$$

$$\mathbf{s}(\mathbf{r}) = \sum_{\alpha\beta} n_{\alpha\beta}(\mathbf{r})\sigma_{\alpha\beta} \tag{2.6}$$

where $\sigma_{\alpha\beta}$ indicate the (α, β) elements of the Pauli matrices. Using the newly defined density matrix $n_{\alpha\beta}(\mathbf{r})$, the most general statement of the spin-polarized DFT theory is that the total energy of the electrons in their ground state is a functional of the density matrix, i.e., $E = G[n_{\alpha\beta}(\mathbf{r})]$. At this point, the entire machinery of the KS formulation of DFT can be adapted to the case of spin-polarized DFT. In particular, KS equations can be derived by using the property that the density matrix in the ground state, $n_{\alpha\beta}^0$, minimizes the energy functional, i.e.,

$$\frac{\delta G[n_{\alpha\beta}]}{\delta n_{\alpha\beta}} = 0. \tag{2.7}$$

As shown by Barth and Hedin [183], this minimum principle leads to the KS equations in spin-polarized type. If one focuses on the simplest situation where there is no external magnetic field, then the spin-polarized DFT equation would be

$$[-\frac{\hbar^2}{2m}\nabla^2 + V_{\mathrm{n}}(\mathbf{r}) + V_{\mathrm{H}}(\mathbf{r}) + V_{\mathrm{xc}}(\mathbf{r}) + \mu_{\mathrm{B}}\sigma\mathbf{B}_{\mathrm{xc}}(\mathbf{r})]\mathbf{\Psi}_i(\mathbf{r}) = \varepsilon_i\mathbf{\Psi}_i(\mathbf{r}) \tag{2.8}$$

$$V_{\mathrm{xc}} = \frac{v_{11}^{\mathrm{xc}} + v_{22}^{\mathrm{xc}}}{2}, B_x^{\mathrm{xc}} = \frac{v_{12}^{\mathrm{xc}} + v_{21}^{\mathrm{xc}}}{2\mu_{\mathrm{B}}}, B_y^{\mathrm{xc}} = i\frac{v_{12}^{\mathrm{xc}} - v_{21}^{\mathrm{xc}}}{2\mu_{\mathrm{B}}}, B_z^{\mathrm{xc}} = \frac{v_{11}^{\mathrm{xc}} - v_{22}^{\mathrm{xc}}}{2\mu_{\mathrm{B}}}. \tag{2.9}$$

Here the presence of many electrons generates an effective magnetic field, $\mathbf{B}_{\mathrm{xc}}(\mathbf{r})$, called the exchange and correlation magnetic field. This extra field tends to align the spin of the

electrons and may drive magnetic order. One could think of this additional interaction as a conceptual tool for including spin density within the framework of DFT.

Spin-polarized DFT calculations have shown to be capable of predicting and understanding the ferromagnetism of Fe, Co, and Ni and the band magnetism itinerant and d electrons at zero temperature without adjustable parameters. However, for the strongly localized $4f$ electrons, normal DFT calculations cannot obtain the reasonable results. Even DFT+U calculations generally cannot yield the correct magnetic moment and magnetocrystalline anisotropy of rare-earth elements which contain $4f$ electrons in rare-earth permanent magnets.

In the light rare-earth magnetic system such as $Nd_2Fe_{14}B$, Nd^{3+} has an electronic basis/set of $4f^3$. According to the Pauli repulsion, the orbital momentum L and the spin momentum S are 6 and $3/2$, respectively. The super strong magnetic anisotropy originates from the $L-S$ coupling. According to Hund's law, the number of electrons less than half filled f orbital, total angular momentum $J = |L - S|$ is the energy minima for the Nd ions, and L and S are in the opposite direction, as illustrated in Figure 2.1(a). Campbell emphasizes the importance of the rare-earth $5d$ electrons and suggests that the $4f$ spins induce a positive and local $5d$ moment via ferromagnetic $4f - 5d$ exchange [185]. Then $3d - 5d$ exchange generates the indirect $3d - 4f$ interaction. The $3d - 5d$ interaction is expected to be negative and this was supported by the calculation of the self-consistent spin-polarized electronic structures by Jaswal [186]. The total Nd moment and the Nd spin moment are antiparallel for the light-rare-earth Nd ions. In (100) and (110) surface structures, the nearest-neighboring ion of an Fe is located just above the Nd ion. The exchange coupling mainly between the $5d$ valence electrons of the Nd ions and the $3d$ electrons of Fe makes $5d$ valence orbital slightly prolate distortion in the c direction. While in (001) surface structures, Nd ions can only hybridize with the orbitals in next-nearest B ions. Thus, the $5d$ valence electrons cloud turn to oblate.

In the heavy rare-earth magnetic system such as $Dy_2Fe_{14}B$, Dy^{3+} has an electronic basis/set (ground level) of $4f^9$ with $L = 5$, $S = 5/2$. According to Hund's law, the number of electrons more than half filled f orbital, total angular momentum $J = |L + S|$ is the energy minima for the Dy ions. Then, L and S are in the same direction, as illustrated in Figure 2.1(b). The total Dy moment and the Dy spin moment are parallel for the heavy-rare-earth Dy ions. Some people reported the shape of $4f$ in Dy [187]. There are only 9 electrons in the $4f$ orbital displaying asphericity among 63 electrons in Dy^{3+} and $4f$ are shielded by $4d$ and $4s$ electron cloud. The rest 54 electrons exhibit spherical cloud shell. The squashed structure of Dy^{3+} ion can be approximated as an ellipsoid under strong uniaxial anisotropy.

In fact, the total magnetic moments of the $4f$ shell of Nd and Dy atoms are 3.27 and $-10.0\ \mu_B$/atom, respectively. As far as one knows the direction of S and L in $4f$ orbital, it is easy to understand why the magnetic moment of the Nd $4f$ shell is added to the calculated total magnetic moment while the magnetic moment of the Dy $4f$ shell is subtracted from the
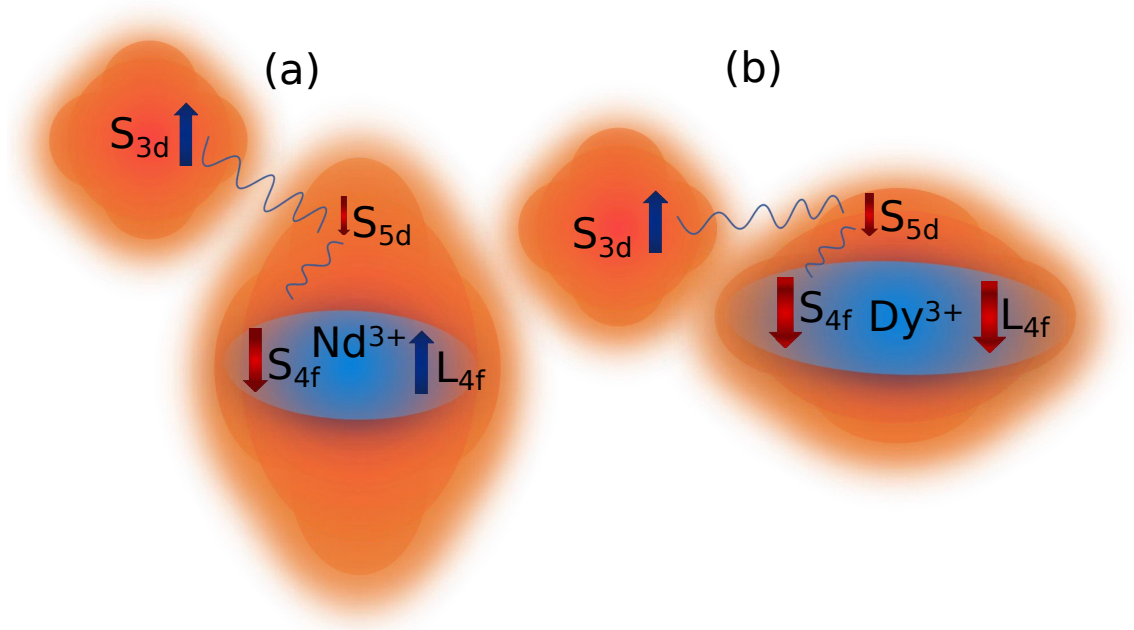
Figure 2.1: (a) Schematic diagram of a Nd ion and its nearest-neighboring Fe ion in the $Nd_2Fe_{14}B$ structure. The $5d$ valence clouds slightly extend to the Fe-direction, that is, almost to the c-axis direction due to the exchange coupling to the $3d$-electrons of the Fe ion. The $4f$ clouds tend to avoid to overlap with the distorted $5d$ clouds to reduce the electrostatic energy, and extends within the c-plane. (b) Schematic diagram of a Dy ion and its nearest-neighboring Fe ion in the $Dy_2Fe_{14}B$ structure.

Table 2.1: Basic specific parameters of $R_2Fe_{14}B$ compounds at 4 K [44].

Compound	T_C (K)	M_s (μ_B/f.u.)	H_a (kOe)	μ_R (μ_B)	Ground lever (R^{3+})	J	L	S
$Pr_2Fe_{14}B$	565	37.6	200	3.1	$[Xe]4f^2$	4	5	1
$Nd_2Fe_{14}B$	585	37.7	170	3.2	$[Xe]4f^3$	9/2	6	3/2
$Sm_2Fe_{14}B$	616	33.3	>200	1.0	$[Xe]4f^5$	5/2	5	5/2
$Gd_2Fe_{14}B$	661	17.9	19	-6.8	$[Xe]4f^7$	7/2	0	7/2
$Tb_2Fe_{14}B$	620	13.2	300	-9.1	$[Xe]4f^8$	6	3	3
$Dy_2Fe_{14}B$	598	11.3	170	-10.1	$[Xe]4f^9$	15/2	5	5/2
$Ho_2Fe_{14}B$	573	11.2	>100	-10.1	$[Xe]4f^{10}$	8	6	2
$Er_2Fe_{14}B$	554	12.9	260	-9.3	$[Xe]4f^{11}$	15/2	6	3/2
$Tm_2Fe_{14}B$	541	18.1	170	-6.7	$[Xe]4f^{12}$	6	5	1
$Yb_2Fe_{14}B$	524	23	—	-4.2	$[Xe]4f^{13}$	7/2	3	1/2

calculated total magnetic moment. For details on L, S, J, μ_R, M_s, H_a, and T_C for a series of $R_2Fe_{14}B$ rare-earth permanent magnet, the readers are referred to Table 2.1. Some remarks on the spin-polarized DFT calculation of atomic magnetic moment, magnetocrystalline anisotropy, and interatomic exchange interaction are given in the following.

2.1.1 Calculation of magnetic moment

DFT calculations can yield correct magnetic moment of Fe in $R_2Fe_{14}B$ permanent magnet. However, if one uses a pseudopotential for R with $4f$ electrons treated as valence electrons, the calculated orbital moment is usually too low and thus the total magnetic moment of rare-earth element R in $R_2Fe_{14}B$ is much lower than the values list in Table 2.1. An alternative way is to use an open-core pseudopotential for R atoms in which well-localized $4f$ electrons are treated as spin-polarized core electrons not as valence electrons. In this way, only the spin moment of R atoms are obtained. Then the magnetic moment of R list in Table 2.1 is added to the DFT calculated moments to obtain a total magnetic moment of the system, which agrees well with the experimental results. For instance, the Nd pseudopotential with $4f$ electrons as valence electrons gives rise to a spin and orbital moment of Nd around $-3.4\ \mu_B$ and $2.4\ \mu_B$ by VASP (Vienna Ab initio Simulation Package), respectively. So the total magnetic moment of Nd is $-1.0\ \mu_B$, which is apparently not correct since the experimental magnetic moment of Nd is $3.2\ \mu_B$ (Table 2.1). In contrast, the open-core Nd pseudopotential with $4f$ electrons as spin-polarized core electrons yields a spin moment of Nd as $-0.28\ \mu_B$ and neglectable orbital moment of Nd by VASP. With the addition of Nd magnetic moment around $3.2\ \mu_B$, the calculated total magnetic moment for $Nd_2Fe_{14}B$ is around $38.3\ \mu_B$/f.u., which matches well with the experimental value of approximately $37.7\ \mu_B$/f.u. [44].

2.1.2 Calculation of magnetocrystalline anisotropy

DFT calculations of magnetocrystalline anisotropy of crystals (mainly containing d electrons) usually rely on two methods, i.e., the total energy method and the force theorem [138, 188, 189]. For the total energy method, fully self-consistent calculations including spin-orbit coupling for all setups with different spin quantization axes $\mathbf{n}_i$ are performed to obtain the $\mathbf{n}_i$ dependent total energy $E^{tot}(\mathbf{n}_i)$. The magnetocrystalline anisotropy energy $K_{\mathbf{n}_i \to \mathbf{n}_j}$ between different $\mathbf{n}_i$ and $\mathbf{n}_j$ can be calculated as

$$K_{\mathbf{n}_i \to \mathbf{n}_j} = E^{tot}(\mathbf{n}_i) - E^{tot}(\mathbf{n}_j). \qquad (2.10)$$

This total energy method is suitable for small system in which the computation cost is not so high, but requires a huge amount of computation resources when the system contains a large number of atoms and valence electrons.

In order to reduce the computation cost, the so-called force theorem is proposed [138, 188,

189]. In the framework of force theorem, the spin-orbit coupling is treated as a perturbation and one only needs to perform a self-consistent calculation for a single setup. In general, self-consistent spin-polarized DFT calculations are firstly performed to obtain the converged spin and charge distributions. Then with the self-consistent charge and spin densities of the previous spin-polarized calculations as input, non-self-consistent DFT calculations with different spin quantization axes $\mathbf{n}_i$ are carried out by including spin-orbit coupling. The force theorem states that the spin-orbit coupling induced magnetocrystalline anisotropy energy is given by the difference in the fully relativistic band energies between two magnetization directions (e.g., $\mathbf{n}_i$ and $\mathbf{n}_j$) calculated with the same self-consistent scalar-relativistic charge and potential. In this way, the change in total energy with respect to $\mathbf{n}_i$ is given by the change in the eigenvalue sums over the occupied single-particle energies, i.e.,

$$K_{\mathbf{n}_i \to \mathbf{n}_j} = \sum_{I,\mathbf{k}}^{\text{occ}} \epsilon_I(\mathbf{n}_i, \mathbf{k}) - \sum_{I,\mathbf{k}}^{\text{occ}} \epsilon_I(\mathbf{n}_j, \mathbf{k}) \tag{2.11}$$

in which $\epsilon_I(\mathbf{n}_i, \mathbf{k})$ is the eigenvalue of the Ith band at the reciprocal point $\mathbf{k}$ when the magnetization is aligned along $\mathbf{n}_i$ direction.

However, for the rare-earth permanent magnets, the magnetocrystalline anisotropy energy is mainly originated from the $4f$ electrons of rare-earth elements. There are reports that Nd pseudopotential with $4f$ electrons as valence electrons in VASP can obtain the correct magnetocrystalline anisotropy energy of $Nd_2Fe_{14}B$ [165, 190]. But in most cases, pseudopotentials of rare-earth elements with $4f$ electrons as valence electrons can hardly yield correct magnetocrystalline anisotropy energy by DFT or DFT+U. Theoretically, there still remain problems and challenges to treat the $4f$ electrons of rare-earth elements in magnetic materials by DFT. Therefore, it is usually difficult to estimate the magnetocrystalline anisotropy energy of rare-earth permanent magnets by DFT calculations. It has been shown that crystal electric fields acting on the $4f$ electrons of rare-earth elements play a dominant role in determining the magnetocrystalline anisotropy energy of rare-earth magnets [191, 192]. The interactions between the crystal electric field of surrounding charges and the anisotropic $4f$ electronic clouds of rare-earth elements, together with the spin-orbit coupling, make the rare-earth magnetic moments aligned along a specific crystalline direction. Therefore, it is the crystal electric field that produces the large magnetocrystalline anisotropy energy of rare-earth magnets, which is due to the $4f$ aspherical charge cloud and can be expressed by the crystal electric field interaction Hamiltonian

$$\mathcal{H}_{\text{CEF}} = \sum_{l,m} \alpha_l A_l^m \left\langle r^l \right\rangle \hat{\Theta}_l^m \tag{2.12}$$

in which α_l is the Stevens factors and $\hat{\Theta}_l^m$ are the Stevens operator equivalents [193].

$A_l^m \langle r^l \rangle$ is given as [194–196]

$$A_l^m \langle r^l \rangle = C_{lm} \int_0^{R_c} r^2 |R_{4f}(r)|^2 V_l^m(r) \mathrm{d}r \tag{2.13}$$

with

$$\langle r^l \rangle = \int_0^{R_c} |R_{4f}(r)|^2 r^{l+2} \mathrm{d}r \tag{2.14}$$

in which $V_l^m(r)$ is the components of the total Coulomb potential of a rare-earth ion within an atomic sphere of radius R_c, $R_{4f}(r)$ is the radial part of the $4f$-orbital wave functions $(r^2|R_{4f}|^2$ as the radial distribution function), and C_{lm} is the conversion factors showing the relation between the symmetrized spherical harmonics and the real tesseral harmonics. a_{lm} transfers in the same way as $\hat{\Theta}_l^m$. For instance, $C_{20} = \sqrt{5/16\pi}$. If one only considers the lowest-order term with $l = 2$ and $m = 0$, the crystal electric field interaction energy can be simplified as

$$\mathcal{H}_{\mathrm{CEF},l=2,m=0} = \alpha_2 A_2^0 \langle r^2 \rangle \hat{\Theta}_2^0 \tag{2.15}$$

in which $\alpha_2 = -6.428 \times 10^{-3}$ and $\hat{\Theta}_2^0 = 3J_z^2 - J(J+1) = 3J^2 \cos\theta^2 - J(J+1)$ with θ as the angle between the magnetization direction and the z axis and J as the total angular momentum. Accordingly, the first-order anisotropy constant (K_1 for the uniaxial anisotropy energy $K_1 \sin^2\theta$) at zero temperature can be approximated as [162, 163, 197]

$$K_1 \approx -3J^2 \alpha_2 A_2^0 \langle r^2 \rangle \tag{2.16}$$

which indicates that positive A_2^0 leads to positive K_1 and thus uniaxial anisotropy along z axis. This suggests that the anisotropy constant can be indirectly determined by calculating the crystal field parameters A_2^0. As for the physical role of A_2^0, it reflects the electric field from the surrounding charge distribution acting on the $4f$ electrons whose spatial distribution is not spherical due to the strong spin-orbital coupling. For the higher-order anisotropy constants, $l = 2, 4, 6$ and $m = 0$ should be considered. The values of $\langle r^n \rangle$ and experimentally determined A_n^0 of R ions in $R_2\mathrm{Fe}_{14}\mathrm{B}$ compounds are list in Table 2.2 [198–200].

First-principles calculations have been tried to estimate the crystal electric field parameters of rare-earth ions in permanent magnets, despite the difficulties [192]. Taking the crystal electric field parameters of Nd in $\mathrm{Nd}_2\mathrm{Fe}_{14}\mathrm{B}$ as an example which are explored and calculated most frequently, Table 2.3 gives the calculated values of $A_2^0 \langle r^2 \rangle$ by different methods. It can be found that the calculated $A_2^0 \langle r^2 \rangle$ sometimes can be much higher than the experimental values, and possesses different values at g and f sites of Nd due the intrinsically different chemical environment of these sites. The full-potential linear muffin-tin orbital (FP-LMTO) method, as a specific implementation of density functional theory within the local density approximation, yields an average $A_2^0 \langle r^2 \rangle$ around 431 K [201]. If extracted from the one electron Hamiltonian expressed in the basis of Wannier functions, $A_2^0 \langle r^2 \rangle$ is averaged as

583 K [202]. By using LSDA+U in WIEN2k code, the average $A_2^0 \langle r^2 \rangle$ is calculated to be around 445 K [203]. VASP calculations with the generalized gradient approximations (GGA) and Nd 4f electrons as core electrons give an average $A_2^0 \langle r^2 \rangle$ around 297 K [163, 197], which agrees well with the experimental values. The full-potential linearized augmented plane wave plus local orbitals method (APW+lo) implemented in the WIEN2k code with the open-core treatment of $4f$ electrons of Nd gives an average $A_2^0 \langle r^2 \rangle$ around 410 K [195]. The same method also yields a high average $A_2^0 \langle r^2 \rangle$ up to 671 K [196], possibly due to the difference of the calculation parameters (e.g. muffin-tin sphere radius). By using open-core pseudopotential for Nd atoms, OpenMX gives $A_2^0 \langle r^2 \rangle$ around 316 K [162].

The substitution of Dy for Nd in $Nd_2Fe_{14}B$ and its influence on $A_2^0 \langle r^2 \rangle$ are also explored. It is found out that Dy substitution does not heavily change $A_2^0 \langle r^2 \rangle$, but the crystal field of the Dy ions is more insensitive to its crystallographic location than that of Nd ions possibly due to the more localized $4f$-electronic density $r^2 |R_{4f}(r)|^2$ of Dy [196]. The crystal electric field parameters of the Nd atoms located at surfaces are further calculated. It is found that the Nd atoms at $Nd_2Fe_{14}B$ (100) and (110) surfaces still possess a large positive $A_2^0 \langle r^2 \rangle$. But Nd atoms at $Nd_2Fe_{14}B$ (001) surface have a large negative $A_2^0 \langle r^2 \rangle$ between -292 and -422 K, which could induce the premature reversal of magnetization at the $Nd_2Fe_{14}B$ (001) surface.

Table 2.2: Crystal electrical field parameters A_n^0 (in units of K/a_0^n) and radial expectation values $\langle r^n \rangle$ (in units of a_0^n) of R ions in $R_2Fe_{14}B$ compounds [198−200]. $a_0 = 0.529$ Å is the Bohr radius.

	ref. [198]			ref. [200]			ref. [199]		
R	A_2^0 (K/a_0^2)	A_4^0 (K/a_0^4)	A_6^0 (K/a_0^6)	$\langle r^2 \rangle$ (a_0^2)	$\langle r^4 \rangle$ (a_0^4)	$\langle r^6 \rangle$ (a_0^6)	$\langle r^2 \rangle$ (a_0^2)	$\langle r^4 \rangle$ (a_0^4)	$\langle r^6 \rangle$ (a_0^6)
Pr	295	−12.3	−6.89	1.086	2.822	15.726			
Nd	295	−12.3	−1.84	1.001	2.401	12.396	1.114	2.910	15.03
Sm	297	−12.4	−7.95	0.883	1.897	8.775	0.974	2.260	10.55
Tb	300	−12.6	−0.96				0.822	1.651	6.852
Dy	302	−12.7	−0.97	0.726	1.322	5.102	0.7841	1.505	6.048
Ho	302	−12.7	−0.97				0.745	1.379	5.379
Er	303	−12.8	−0.98	0.666	1.126	3.978	0.711	1.270	4.816
Tm	303	−12.8	−0.98				0.680	1.174	4.340
Yb	303	−12.8	−0.98	0.613	0.960	3.104	0.652	1.089	3.932

Table 2.3: First-principles calculated and experimentally determined crystal electrical field parameters $A_2^0 \langle r^2 \rangle$ (in units of K) of Nd in $Nd_2Fe_{14}B$ compounds [162, 163, 195–198, 201–203]. FP-LMTO: full-potential linear-muffin-tin-orbital; LSDA: local spin density approximation; GGA: generalized gradient approximations; APW+lo: full-potential linearized augmented plane wave plus local orbitals; Dy→Nd(p): Dy is substituted for all of the Nd at p-sites (p=f and g).

$A_2^0 \langle r^2 \rangle$ (K) Nd(f)	$A_2^0 \langle r^2 \rangle$ (K) Nd(g)	methodology and remarks
323	540	FP-LMTO [201]
497	670	Wannier functions [202]
427	464	LSDA+U, WIEN2k [203]
385	209	GGA ($4f$ in core), VASP [163, 197]
358	463	APW+lo ($4f$ in core), WIEN2k [195]
552	790	APW+lo ($4f$ in core), WIEN2k [196]
507	Dy→Nd(g)	APW+lo ($4f$ in core), WIEN2k [196]
Dy→Nd(f)	736	APW+lo ($4f$ in core), WIEN2k [196]
316	316	GGA ($4f$ in core), OpenMX [162]
−413	−432	Nd at (001) surface, LSDA+U, WIEN2k [203]
−292	−292	Nd at (001) surface, GGA ($4f$ in core), VASP [163]
215	215	Nd at (110) surface, GGA ($4f$ in core), VASP [163]
432, 590	640, 479	Nd at (100) surface, APW+lo ($4f$ in core), WIEN2k [195]
295	295	experimental results [198]

2.1.3 Calculation of interatomic exchange interaction

The calculation of interatomic exchange interaction J_{ij} is not easy, especially for the rare-earth magnets. For a rough estimation, from the experimental results J_{ij} can be given by the mean-field expression

$$J_{ij} = \frac{3k_B T_c}{\epsilon z} \tag{2.17}$$

in which z is the number of the nearest neighbour interactions, k_B is the Boltzmann constant, T_c is the Curie temperature, and ϵ is a correction factor from the usual mean-field expression owing to spin waves in the 3D Heisenberg model [204, 205]. ϵ also depends on the crystal structure and coordination number. For example, Cobalt possesses a T_c of 1388 K and a hexagonal crystal structure with $z = 12$, thus resulting in a nearest neighbour exchange interaction $J_{ij} = 6.064 \times 10^{-21}$ J/link.

Theoretical calculations of J_{ij} mainly include three methods: DFT energy mapping onto a Heisenberg spin Hamiltonian to determine J_{ij} [206], extracting J_{ij} from DFT calculations of spin-spiral total energies [207], and local force theorem by the Liechtenstein formula [208–210].

The general procedure of calculating J_{ij} by mapping the DFT total energy onto the Heisenberg spin Hamiltonian is illustrated in Figure 2.2 that shows the determination of the first-, second-, and third-nearest-neighbor exchange parameters J_1, J_2, and J_3. According to the Heisenberg spin Hamiltonian formulation, one has to construct supercells and design different magnetic configurations including ferromagnetic state and different antiferromagnetic states. Then the total energy of these configurations are determined by DFT calculations. By inserting the DFT total energy into the expressions that describe the Heisenberg energies for different magnetic configurations, one can solve a group of linear equations to yield J_{ij}. This method is very convenient if only the nearest or second-nearest exchange parameters are considered. If long-distance exchange interactions are involved, the constructed supercells will be very large, making the DFT computation cost unacceptable. Another issue should be mentioned is that, this method seems to only work well for the semiconductor and insulator in which the localized electrons mainly contribute to the magnetism. For metallic systems

Heisenberg spin Hamiltonian (with the third nearest neighbor):

$$\mathcal{H} = E_0 - \frac{1}{2}J_1 \sum_N \mathbf{S}_i \cdot \mathbf{S}_j - \frac{1}{2}J_2 \sum_{NN} \mathbf{S}_i \cdot \mathbf{S}_j - \frac{1}{2}J_3 \sum_{NNN} \mathbf{S}_i \cdot \mathbf{S}_j$$

Different magentic configurations:

FM   stripy-AFM   zigzag-AFM   neél-AFM
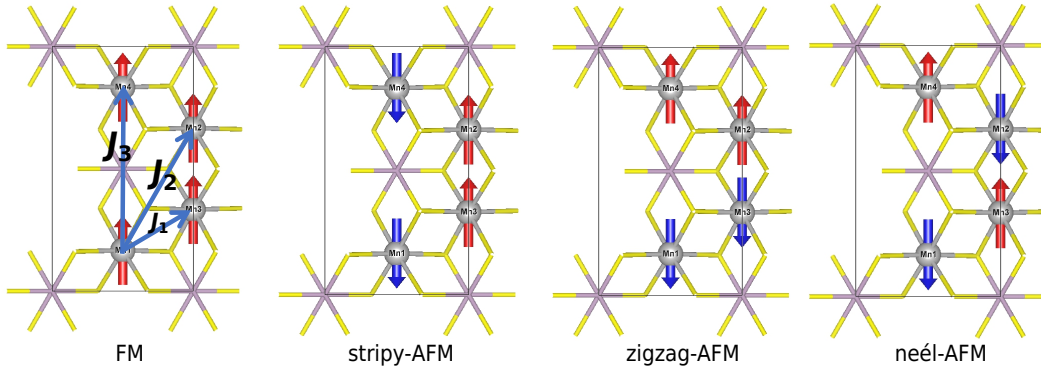
Expressions for total energy (can be calculated by DFT) of different magentic configurations:

$$E^{\mathrm{FM}} = E_0 - \frac{1}{2}(12J_1 + 24J_2 + 12J_3)|S|^2$$

$$E^{\mathrm{stripy\text{-}AFM}} = E_0 - \frac{1}{2}(-4J_1 - 8J_2 + 12J_3)|S|^2$$

$$E^{\mathrm{zigzag\text{-}AFM}} = E_0 - \frac{1}{2}(4J_1 - 8J_2 - 12J_3)|S|^2$$

$$E^{\mathrm{neel\text{-}AFM}} = E_0 - \frac{1}{2}(-12J_1 + 24J_2 - 12J_3)|S|^2$$

Figure 2.2: The schematic procedure for the calculation of interatomic exchange interaction J_{ij} by mapping DFT total energy onto the Heisenberg spin Hamiltonian.

which are featured by the itinerant electrons associated with the magnetism, this method is not reliable as expected. For instance, in metallic systems, it is found that the calculated magnitude of atomic spin moments in different magnetic configurations varies dramatically. This means that, apart from the atomic spin moment's direction change, its magnitude change will also contribute to the total energy change. Therefore, the calculated J_{ij} will not only depend on the changes in the directions of atomic spin moments, but also the changes in the magnitude of atomic spin moments. Therefore, a large deviation from the Heisenberg model exists.

The extraction of J_{ij} from DFT calculations of spin-spiral total energies is initiated by solving equations given by the Heisenberg Hamiltonian with the DFT-calculated total energies of the plane spin spirals at high symmetry $\mathbf{q}$ points ($\mathbf{q}_{\mathrm{hs}}$). Some typical spin-spiral structures are shown in Figure 2.3. For a classical Heisenberg model, atomic spin moments is located at atomic sites $\mathbf{R}_{n\alpha}$ which is defined by a lattice vector $\mathbf{R}_n$ and position vector τ_α of the magnetic Bravais lattice within a unit cell, i.e., $\mathbf{R}_{n\alpha} = \mathbf{R}_n + \tau_\alpha$. The unit vector defining the direction of atomic spin moments is expressed $\mathbf{e}_{n\alpha}$. n and α indicate the atomic spin moment located at which unit cell and which atom/position within the original unit cell, respectively. In this way, the interatomic exchange coupling parameters $J_{mn}^{\alpha\beta}$ can represent exchange interaction between atomic spins separated by any distance. Then the exchange Hamiltonian $\mathcal{H}_{\mathrm{ex}}$ is the sum over all pair interactions, expressed as

$$\mathcal{H}_{\mathrm{ex}} = -\frac{1}{2N} \sum_{mn\alpha\beta} J_{mn}^{\alpha\beta} \mathbf{e}_{m\alpha} \cdot \mathbf{e}_{n\beta} \tag{2.18}$$

where N is the number of unit cells in the magnetic crystal. The ground state of Hamiltonian $\mathcal{H}_{\mathrm{ex}}$ could be spin spirals, which are characterized by a wave vector $\mathbf{q}$ from the irreducible wedge of the Brillouin zone and by the angles θ between the spin and rotation axis along with a phase factor ϕ for all atoms belonging to the same magnetic Bravais lattice [207, 211]. For a spin spiral with $\mathbf{q}$, the unit vector of spin direction is given by

$$\mathbf{e}_{m\alpha} = \sin\theta \cos(\mathbf{q} \cdot \mathbf{R}_{m\alpha} + \phi_\alpha)\mathbf{e}_x + \sin\theta \sin(\mathbf{q} \cdot \mathbf{R}_{m\alpha} + \phi_\alpha)\mathbf{e}_y + \cos\theta\mathbf{e}_z. \tag{2.19}$$

Accordingly, the total exchange energies $E(\mathbf{q})$ of different collinear magnetic configurations, which are plane spin spirals for high symmetry $\mathbf{q}$ points ($\mathbf{q}_{hs}$), can be expressed as

$$E(\mathbf{q}) = -\frac{1}{2N} \sum_{mn\alpha\beta} J_{mn}^{\alpha\beta} \mathbf{e}_{m\alpha}(\mathbf{q}_{hs}) \cdot \mathbf{e}_{n\beta}(\mathbf{q}_{hs}). \tag{2.20}$$

If one designs cone spin spirals which have smaller perturbations, the problem that the magnitude of atomic spin moments change with the spin rotation will be overcome. Then it is possible to extract the exchange parameters by combining Equation 2.20 DFT-calculated energies, with the assumption of a maximum range of interactions. Based on this, least
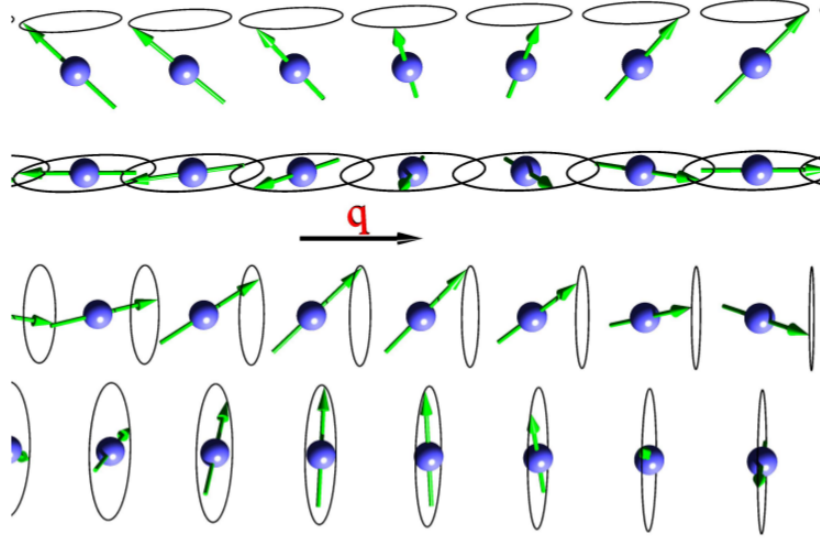
Figure 2.3: Four examples of spin spirals with spin-rotation axis perpendicular (upper two) and parallel (lower two) to the spin-spiral vector $\mathbf{q}$. For each case, two spirals with angles of $\pi/4$ and $\pi/2$ between the magnetic moment and the rotation axes are shown. [213].

square fitting approach [207] and reciprocal-space Fourier transforms approach in [212] have been developed to extract exchange parameters. Both approaches have been implemented in the full-potential linearized augmented plane-wave (FLAPW) method-based code FLEUR (www.flapw.de).

The local force theorem by the Liechtenstein formula [208–210] is another popular approach for the calculation of J_{ij}. In 1984, Liechtenstein et al. did a pioneering work and obtained the rigorous expression for the exchange parameters and the spin-wave stiffness constant of ferromagnetic metals using a local spin-density functional formalism and the muffin-tin potential model [208]. In their approach with the local spin-density functional (LSDF), according to the local forces theorem of Andersen [217], the total energy changes at small perturbations can be rigorously expressed through the variation of the sum of the one-particle energies determined with some fixed potential, i.e.,

$$\delta E = \int_{-\infty}^{E_{\mathrm{F}}} (E - E_{\mathrm{F}}) \delta N(E) \mathrm{d}E \tag{2.21}$$

in which E_{F} is the Fermi energy level and $\delta N(E)$ is the variation of the density of states. The change in the unit vector $\mathbf{s}_i$ of the ith atomic-spin moment can be derived from the change in the single-site scattering matrix $\mathbf{t}$ within the muffin-tin approximation, i.e.,

$$\mathbf{t}_i = \frac{1}{2}(\mathbf{t}_\uparrow + \mathbf{t}_\downarrow) + \frac{1}{2}(\mathbf{t}_\uparrow - \mathbf{t}_\downarrow)\boldsymbol{\sigma} \cdot \mathbf{s}_i \tag{2.22}$$

in which $\boldsymbol{\sigma}$ is the Pauli matrices. The scattering path operator $\mathbf{T}$ is given by multiple scattering theory as

$$\mathbf{T}^{-1} = \mathbf{t}^{-1} - \mathbf{G} \tag{2.23}$$

in which $\mathbf{G}$ is the structure Green function. With $\delta N(E)$ as the variation of the scattering path operators [218], Equation 2.21 can be converted to

$$\delta E = \frac{1}{\pi} \int_{-\infty}^{E_{\mathrm{F}}} \mathrm{Im\ Tr} \ln(1 - \Delta T) \mathrm{d}E \tag{2.24}$$

in which $\mathbf{T}$ matrix is defined for the ground state and $\Delta = \mathbf{t}_{\mathrm{old}}^{-1} - \mathbf{t}_{\mathrm{new}}^{-1}$. $\mathbf{t}$ and $\mathbf{T}$ are spinors and matrices in the orbital space, respectively. If a spin spiral with the wavevector $\mathbf{q}$ is considered, its energy variation can also be written as

$$\delta E = D_{\alpha\beta} q_\alpha q_\beta \tag{2.25}$$

with $D_{\alpha\beta}$ as the spin-wave stiffness tensor. Combining the expressions for $D_{\alpha\beta}$ and $\mathbf{s}_i$ being functions of $\mathbf{q}$ and lattice vectors $\mathbf{R}_{ij}$, J_{ij} can be derived from Equations 2.21 and 2.25 as [208]

$$J_{ij} = \frac{1}{4} \int_{-\infty}^{E_{\mathrm{F}}} \mathrm{Im\ Tr}_L (\mathbf{t}_\uparrow^{-1} - \mathbf{t}_\downarrow^{-1})^2 \mathbf{T}_\uparrow^{ij} \mathbf{T}_\downarrow^{ji} \mathrm{d}E \tag{2.26}$$

in which Tr_L is trace over the orbital states. In 1987, Liechtenstein et al. further derived a version of J_{ij} expression by using LSDF approach and Korringa–Kohn–Rostoker (KKR) Green functions formalism [209]. Now the Green's function representation of the well-established so-called Liechtenstein's approach has been implemented in several codes such as OpenMX
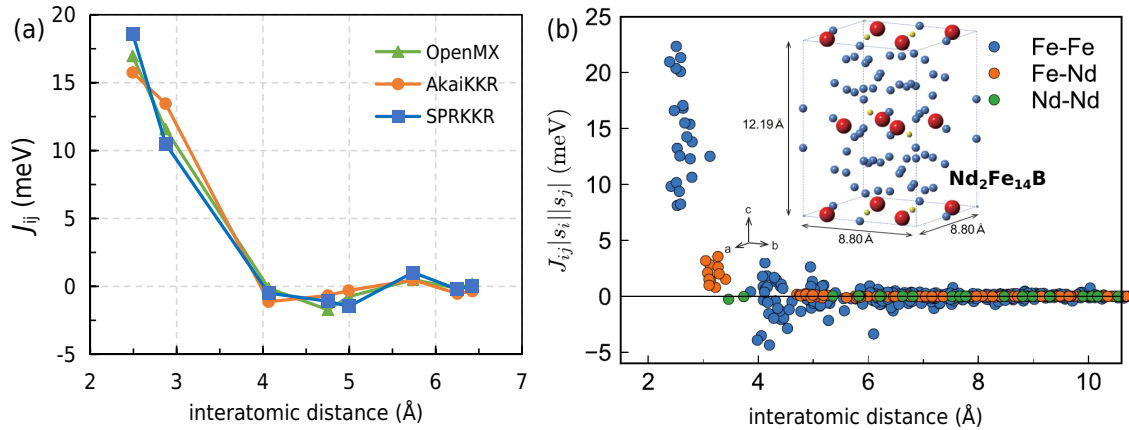
Figure 2.4: Calculated interatomic exchange parameters J_{ij} by Liechtenstein's approach. (a) J_{ij} for bcc Fe calculated by OpenMX, AkaiKKR, and SPRKKR [214, 215]. (b) J_{ij} for $Nd_2Fe_{14}B$ calculated by AkaiKKR [216].

(www.openmx-square.org) [214, 219, 220], SPRKKR (www.ebert.cup.uni-muenchen.de) [221] , AkaiKKR (http://kkr.issp.u-tokyo.ac.jp), etc. As an example, Figure 2.4 shows the calculated J_{ij} as a function of interatomic distance in bcc Fe and $Nd_2Fe_{14}B$ by using the Liechtenstein's approach in OpenMX, AkaiKKR, and SPRKKR [214–216]. It can be found that for bcc Fe, OpenMX, AkaiKKR, and SPRKKR almost yield the same J_{ij} results (Figure 2.4(a)) [214, 215]. As for the calculation of J_{ij} in $Nd_2Fe_{14}B$, standard muffin-tin-type potentials and the local density approximation are used, up to d-wave scatterings are considered in KKR, and the Nd $4f$ states are treated with open-core approximation [216]. As shown in Figure 2.4, the exchange couplings between Fe atoms have much larger values than those between Fe and Nd atoms. In addition, the exchange interaction between Nd atoms is negligible.

2.2 Atomistic spin model

The DFT computations are important for the determination of intrinsic magnetic parameters and unveil the related physical mechanism from the ground-state calculations at zero temperature. However, they are computationally powerless if the studied systems are too large, and are also difficult to consider the microstructural effects and calculate the finite-temperature parameters or properties and magnetization dynamics. For instance, the properties of magnetic materials are heavily influenced by thermal effects which are typically difficult to handle by standard DFT approaches. To appropriately take into account the temperature effect, one must use standard statistical mechanical methods with the canonical ensemble to handle the magnetic system. In contrast, atomistic spin model combines the quantum mechanical properties with robust thermodynamic formalism, and connects the electronic structure of magnetic materials and the finite-temperature parameters or properties and magnetization dynamics. It is an atomistic approach based on the quantum description of solids. It is capable of simulating larger magnetic systems which cannot be handled by DFT, and giving a much more accurate description of finite-temperature parameters and dynamic properties. Its most important ability is that it enables the bridging between DFT calculations and micromagnetic simulations, thus making it possible to computationally design the complex magnetic systems or structures by multiscale simulations across scales.

The atomistic spin model is physically based on the localization of unpaired electrons to atomic sites, i.e., an effective local atomic magnetic moment at each atomic site. However, since the magnetism is originated from the outer electrons that are theoretically loosely bound to the atoms, the degree of electron localization has historically been a controversial issue in $3d$ metals [222]. In 1984, Schwarz et al. did *ab initio* calculations of the electron density [223]. They found that even in ferromagnets with itinerant electrons, the spin polarization is still well-localized to the atomic sites. This indicates that the bonding electrons are unpolarized. So after excluding the bonding charge, the remaining d electrons form

a well-defined effective localized moment on the atomic sites [204]. This fact makes it possible to apply atomistic spin model for the study of magnetic materials.

2.2.1 Classical spin Hamiltonian

The energy of a magnetic system with interacting atomic moments at magnetic atom sites is given by a spin Hamiltonian as

$$\mathcal{H} = \mathcal{H}^{\mathrm{exc}} + \mathcal{H}^{\mathrm{ani}} + \mathcal{H}^{\mathrm{dip}} + \mathcal{H}^{\mathrm{app}} \tag{2.27}$$

in which $\mathcal{H}^{\mathrm{exc}}$ is the exchange interaction energy, $\mathcal{H}^{\mathrm{ani}}$ is the magnetocrystalline anisotropy energy, $\mathcal{H}^{\mathrm{dip}}$ is the dipolar interaction energy, and $\mathcal{H}^{\mathrm{app}}$ is the energy from the externally applied magnetic field. It should be mentioned that Equation 2.27 is in a classic version, in which the energy terms are expressed by classic parameters not by quantum operators. The classic spin Hamiltonian reflects the essential physics of a magnetic material at the atomic level and ignores the energy contribution from the non-magnetic effects.

$\mathcal{H}^{\mathrm{exc}}$ is originated from the electrostatic interactions, and thus its energy is very large (around 1–2 eV) which is up to 1,000 times larger than other contributions and could render magnetic ordering temperatures in the range 300–1300 K. $\mathcal{H}^{\mathrm{exc}}$ can be expressed as

$$\mathcal{H}^{\mathrm{exc}} = -\frac{1}{2} \sum_{i \neq j} J_{ij} \mathbf{s}_i \cdot \mathbf{s}_j \tag{2.28}$$

in which J_{ij} is the interatomic exchange parameters between atomic sites i and j that can be determined by DFT calculations in Subsection 2.1.3, and $\mathbf{s}_i$ is a unit vector denoting the local spin moment direction at the atomic site i. It is clear that in Equation 2.29 positive J_{ij} favors neighboring spins aligned in parallel, corresponding to a ferromagnetic material. Negative J_{ij} favors antiparallel alignment of neighboring spins, corresponding to an antiferromagnetic material. The calculation of Equation 2.29 is usually performed within a cutoff distance (sometimes only within the nearest neighbours), since J_{ij} is strongly dependent on the interatomic distance. It should be noted that scalar parameter J_{ij} in Equation 2.28 denotes the simplest isotropic exchange interactions, i.e., $\mathcal{H}^{\mathrm{exc}}$ only depends on the spins' relative orientation not their direction. In a more general case, J_{ij} could be anisotropic and thus $\mathcal{H}^{\mathrm{exc}}$ is expressed by

$$\mathcal{H}^{\mathrm{exc}} = -\frac{1}{2} \sum_{i \neq j} \mathbf{s}_i \cdot \mathbf{J}_{ij} \cdot \mathbf{s}_j \quad \text{with} \quad \mathbf{J}_{ij} = \begin{bmatrix} J_{xx} & J_{xy} & J_{xz} \\ J_{yx} & J_{yy} & J_{yz} \\ J_{zx} & J_{zy} & J_{zz} \end{bmatrix}. \tag{2.29}$$

The tensor $\mathbf{J}_{ij}$ can describe the anisotropic exchange interactions such as two-ion anisotropy. The Dzyaloshinskii–Moriya interaction can be described by the off-diagonal components of

the exchange tensor $\mathbf{J}_{ij}$.

For the simplest form of magnetocrystalline anisotropy in the single-ion uniaxial type, $\mathcal{H}^{\text{ani}}$ can be expressed as

$$\mathcal{H}^{\text{ani-uni}} = -\sum_i \left[k_{i,1}(\mathbf{s}_i \cdot \mathbf{e})^2 + k_{i,2}(\mathbf{s}_i \cdot \mathbf{e})^4 + k_{i,3}(\mathbf{s}_i \cdot \mathbf{e})^6 + \cdots \right] \tag{2.30}$$

where $k_{i,1}$, $k_{i,2}$, and $k_{i,3}$ are the second-, fourth-, and sixth-order anisotropy constants of the atomic site i. If the magnetic moments prefer to align along $\mathbf{e}$, then $\mathbf{e}$ is called as the magnetically easy axis. If the magnetic moments prefer to align in the plane perpendicular to $\mathbf{e}$, then plane perpendicular to $\mathbf{e}$ is called as the magnetically easy plane. In crystal lattice that is distorted along a single axis as in materials such as hexagonal Cobalt and L1$_0$ ordered FePt, uniaxial anisotropy exits. Achieving high uniaxial anisotropy energy is critical for the development of high-performance permanent magnets. But for the materials with a cubic crystal structure (e.g., Fe and Ni), there exists a different form of anisotropy called as cubic anisotropy. The associated energy can be expressed as

$$\mathcal{H}^{\text{ani-cub}} = \frac{k_c}{2} \sum_i (s_x^4 + s_y^4 + s_z^4) \tag{2.31}$$

in which k_c is the cubic anisotropy energy per atom. k_c is usually much smaller than the uniaxial anisotropy constant. Positive k_c gives a preferred easy axis orientation along the [001] directions, medium-hard along the [110] directions and hard along the [111] directions. Negative k_c gives a preferred easy direction along the [111] directions, medium-hard along the [110] directions and hard along the [100] directions.

When the interactions between the magnetic system and the external magnetic fields are considered (e.g. magnetic field induce reversal or dynamics of atomic magnetic moments), the associated energy $\mathcal{H}^{\text{app}}$ is simply expressed by

$$\mathcal{H}^{\text{app}} = \sum_i \mu_i \mathbf{s}_i \cdot \mathbf{H}_{\text{app}} \tag{2.32}$$

in which μ_i is the atomic magnetic moment of atomic site i and $\mathbf{H}_{\text{app}}$ is the external magnetic field.

The dipolar interaction energy $\mathcal{H}^{\text{dip}}$ originated from the interactions between atomic magnetic moments is expressed as [224]

$$\mathcal{H}^{\text{dip}} = -\frac{1}{2} \sum_{i \neq j} Q_{ij}^{\alpha\beta} \mu_i s_i^{\alpha} \mu_j s_j^{\beta} \tag{2.33}$$

where α and β are coordinate indices and $Q_{ij}^{\alpha\beta}$ is given by [224]

$$Q_{ij}^{\alpha\beta} = \frac{\mu_0}{4\pi}(3R_{ij}^{\alpha}R_{ij}^{\beta} - \delta_{\alpha\beta}R_{ij}^2)R_{ij}^{-5} \tag{2.34}$$

in which R_{ij} is the distance between atomic moments i and j. Dipolar interactions are long range and important for the long wavelength excitations. The interaction can be neglected in studies of short wavelength excitations [224].

In addition to the atomic structure of the magnetic material, each term in the spin Hamiltonian in Equation 2.27 has to be parameterized by the atomic-scale parameters that can be determined from experimental measurements or calculated by the methodology introduced in Section 2.1.

2.2.2 Atomistic stochastic Landau–Lifshitz equation

The spin Hamiltonian in Equation 2.27 only gives the energetics of the magnetic system, without information on the time evolution of atomic magnetic moment, the effect of thermal fluctuations, the dynamic path from the initially non-equilibrium state to the equilibrium state, etc. Therefore, the evolution equations governing the atomistic spin dynamics and the associated integration methods have to be developed.

The macroscopic time-dependent behaviour of the magnetization in a magnetic material is described by the equation initially derived by Landau and Lifshitz [225] as

$$\frac{\partial \mathbf{m}}{\partial t} = -\frac{\gamma}{1+\alpha^2}\left[\mathbf{m} \times \mathbf{H}_{\text{eff}} + \alpha\mathbf{m} \times (\mathbf{m} \times \mathbf{H}_{\text{eff}})\right] \tag{2.35}$$

in which $\mathbf{m}$ is a unit vector representing the direction of macroscopic magnetization, γ is the gyromagnetic ratio, $\mathbf{H}_{\text{eff}}$ is an effective magnetic field, and α is the phenomenological damping constant. The physical origin of the macroscopic Landau–Lifshitz (LL) equation contains two aspects. The first term in Equation 2.35 is related to the precession of the magnetization, due to the quantum mechanical interaction of an atomic spin with an applied field. The second term in Equation 2.35 denotes the relaxation of the magnetization, making the magnetization to align along the direction of $\mathbf{H}_{\text{eff}}$. The speed of the magnetization rotating towards $\mathbf{H}_{\text{eff}}$ depends on the damping constant. These two effects are illustrated in Figure 2.5.

For the atomistic spin moments, the evolution equation similar to Equation 2.35 can also be utilized. But the related physical mechanisms have to be understood in the atomistic level, in terms of atomic spins and direct angular momentum transfer between the spins and the heat bath. In addition, the damping parameter in the macroscopic and atomistic LL equations is physically different. In the macroscopic LL equation, the damping parameter α is an overall reflection of all kinds of contributions from intrinsic spin-lattice and spin-

electron interactions and extrinsic spin-spin interactions due to demagnetization fields, surface, defects, doping, temperature, etc. However, in the atomistic LL equation, the damping parameter only includes the local intrinsic contributions, and thus a microscopic damping parameter λ is introduced to show its difference with macroscopic α. With these considerations, the atomistic LL equation can be written as

$$\frac{\partial \mathbf{s}_i}{\partial t} = -\frac{\gamma}{1+\lambda^2} \left[\mathbf{s}_i \times \mathbf{H}_{\text{eff}}^i + \lambda \mathbf{s}_i \times (\mathbf{s}_i \times \mathbf{H}_{\text{eff}}^i) \right], \qquad (2.36)$$

in which $\mathbf{s}_i$ is a unit vector representing the direction of the magnetic spin moment of atomic site i, and $\mathbf{H}_{\text{eff}}^i$ is the effective magnetic field on each atomic spin. Similar to the case of macroscopic LL equation, $\mathbf{H}_{\text{eff}}^i$ can also be calculated by the variational derivative of the complete spin Hamiltonian as

$$\mathbf{H}_{\text{eff}}^i = -\frac{1}{\mu_i} \frac{\partial \mathcal{H}}{\partial \mathbf{s}_i}. \qquad (2.37)$$

It should be noted that even though the atomistic and macroscopic LL equations are with the similar form, the atomistic detail in the atomistic LL model allows for the calculation of the effective damping parameters including extrinsic effects for the macroscopic LL equation.

The atomistic LL equation in 2.36 is deterministic and can only be used for the calculations of atomistic spin dynamics at zero temperature. Its applicability to the finite-temperature calculations can be realized by using the Langevin dynamics [227]. Within the framework of Langevin dynamics, an effective thermal field is introduced into the atomistic LL equation as a white noise term to simulate the thermal effects. The finite-temperature induced thermal fluctuations at each atomic site are represented by a three-dimensional Gaussian stochastic distribution $\mathbf{\Gamma}(t, \mathbf{r}^i)$. $\mathbf{\Gamma}(t, \mathbf{r}^i)$ varies at each time step and each atomic site $\mathbf{r}^i$, and thus the
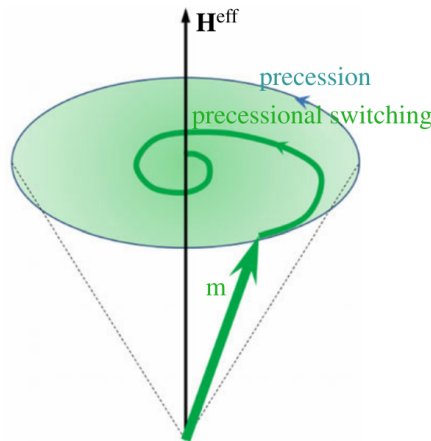
Figure 2.5: Illustration on precession and precessional switching of macroscopic magnetization [226].

thermal fluctuation field $\mathbf{H}_{\text{th}}^i$ can be expressed as

$$\mathbf{H}_{\text{th}}^i = \mathbf{\Gamma}(t, \mathbf{r}^i) \sqrt{\frac{2\lambda k_{\mathbf{B}} T}{\gamma \mu_i \Delta t}} \tag{2.38}$$

in which λ is the Gilbert damping parameter, $k_{\mathbf{B}}$ is the Boltzman constant, T is the material temperature, γ is the absolute value of the gyromagnetic ration, μ_i is the magnitude of the atomic magnetic moment at atomic site $\mathbf{r}^i$, and Δt is the integration time step [204]. The Gaussian stochastic process follows the statistical properties

$$\left\langle \Gamma_\alpha(t, \mathbf{r}^i) \right\rangle = 0 \tag{2.39}$$

and

$$\left\langle \Gamma_\alpha(t, \mathbf{r}^i) \Gamma_\beta(s, \mathbf{r}^j) \right\rangle = \delta_{\alpha\beta} \delta(t - s) \tag{2.40}$$

in which α and β are the Cartesian coordinates ranging from 1 to 3. Equation 2.39 states that the mean value of $\mathbf{\Gamma}$ over the whole sample at any time is zero. Equation 2.40 indicates that $\mathbf{\Gamma}$ are unrelated both in space and time. After including the thermal fluctuations, the total effective field appeared in the atomistic LL equation will be

$$\mathbf{H}_{\text{eff-tot}}^i = \mathbf{H}_{\text{eff}}^i + \mathbf{H}_{\text{th}}^i = -\frac{1}{\mu_i} \frac{\partial \mathcal{H}}{\partial \mathbf{s}_i} + \mathbf{H}_{\text{th}}^i \tag{2.41}$$

and then Equation 2.36 will be transferred into atomistic stochastic LL equation

$$\mathbf{s}_i = -\frac{\gamma}{1 + \lambda^2} \left\{ \mathbf{s}_i \times (\mathbf{H}_{\text{eff}}^i + \mathbf{H}_{\text{th}}^i) + \lambda \mathbf{s}_i \times \left[\mathbf{s}_i \times (\mathbf{H}_{\text{eff}}^i + \mathbf{H}_{\text{th}}^i) \right] \right\}. \tag{2.42}$$

2.2.3 Numerics for atomistic spin model simulations

With both the classic spin Hamiltonian (Equation 2.27) and the atomistic stochastic LL equation (Equation 2.42) at hand, numerical methodology has to be developed to obtain the simulation results. In general, two methodologies including time integration of stochastic LL Equation 2.42 and Monte Carlo method are available [224, 228–231].

Time integration of stochastic LL equation. If one is interested in the dynamic information about the magnetic properties or reversal processes for a magnetic system, the direct time integration of stochastic LL Equation 2.42 should be used. The integration solver must be suitable for the stochastic nature of the equations by ensuring the results converged to the Stratonovich solution [232, 233]. The essential requirement is that the solver preserves the magnitude of the atomistic spin either implicitly or by renormalization [234]. There are several time integration schemes available such as Euler's method, Heun method, midpoint method, modified predictor-corrector midpoint schemes, etc. Up to now, the Heun method is most commonly utilized, with the merit of larger time steps due to a predictor-corrector

algorithm within it [232]. In addition, it is relatively simple to be numerically implemented and is computationally efficient for the stochastic magnetization dynamics.

In the Heun method, at a given effective field $\mathbf{H}_{\text{eff-tot}}$, the new spin direction $\mathbf{s}'_i$ is calculated by performing a standard Euler integration step in the first or predictor step, i.e.,

$$\mathbf{s}'_i = \mathbf{s}_i + \Delta\mathbf{s}\Delta t \tag{2.43}$$

with

$$\Delta\mathbf{s} = -\frac{\gamma}{1+\lambda^2}\left[\mathbf{s_i} \times \mathbf{H}_{\text{eff-tot}} + \lambda\mathbf{s_i} \times (\mathbf{s_i} \times \mathbf{H}_{\text{eff-tot}})\right]. \tag{2.44}$$

Then $\mathbf{s}'_i$ is re-normalized as $\tilde{\mathbf{s}}'_i = \mathbf{s}'_i/|\mathbf{s}'_i|$ to ensure numerical stability and convergence to the Stratanovich solution. With known $\tilde{\mathbf{s}}'_i$, the new effective field is re-calculated as $\mathbf{H}^{i'}_{\text{eff-tot}}$. Then the second or corrector step is carried out to calculate the final atomic spin direction within the time step Δt as

$$\mathbf{s}^{t+\Delta t}_i = \mathbf{s}_i + \frac{1}{2}[\Delta\mathbf{s} + \Delta\mathbf{s}']\Delta t \tag{2.45}$$

with

$$\Delta\mathbf{s}' = -\frac{\gamma}{1+\lambda^2}\left[\tilde{\mathbf{s}}_i' \times \mathbf{H}^{i'}_{\text{eff-tot}} + \lambda\tilde{\mathbf{s}}_i' \times (\tilde{\mathbf{s}}_i' \times \mathbf{H}^{i'}_{\text{eff-tot}})\right]. \tag{2.46}$$

The re-normalized values $\tilde{\mathbf{s}}^{t+\Delta t}_i = \mathbf{s}^{t+\Delta t}_i/|\mathbf{s}^{t+\Delta t}_i|$ are the final results at time $t+\Delta t$. It should be noted that the random thermal field remains the same during one single Heun step. The procedure from Equations 2.43 to 2.46 is repeated many times to obtain the temporal and spatial evolution of the atomistic spin system until the specified total time or convergence criterion is satisfied.

Monte Carlo methods. If only the equilibrium magnetic properties are of interests, the Monte Carlo Metropolis algorithm [235] is a natural choice. The procedure is concisely presented here. Firstly, a atomic site i is randomly chosen and its initial spin direction $\mathbf{s}_i$ is varied randomly to a new trial position $\mathbf{s}'_i$. The change from $\mathbf{s}_i$ to $\mathbf{s}'_i$ is often called as trial move. The corresponding energy change is $\Delta E = E(\mathbf{s}'_i) - E(\mathbf{s}_i)$. The accept probability of this trial move is

$$P = \exp\left(-\frac{\Delta E}{k_{\text{B}}T}\right). \tag{2.47}$$

Comparing P with a uniform random number between 0 and 1 determines whether this trial move will be accepted or rejected. If P exceeds 1, the energy is decreased and this trial move is accepted unconditionally. The same procedure is repeated until N trial moves have been attempted, with N as the total number of spins. Each set of N trial moves constitute a single Monte Carlo step. Then specific statistical strategy is taken to calculate the temperature dependent magnetic properties of interests.

It is worthy that a constrained Monte Carlo method is specifically proposed to calculate the

temperature dependent magnetic anisotropy [236]. In the constrained Monte Carlo method, the random change of individual spin direction $\mathbf{s}_i$ is not completely free, but is constrained by the condition that the overall average magnetization direction of the system is fixed at a certain direction. In this way, the trial moves act on two spins at a time. As an example, here z axis is taken as the constrained direction of the overall average magnetization $\mathbf{m}$.

First, one chooses a primary spin $\mathbf{s}_i$ and a compensation spin $\mathbf{s}_j$.

Second, one displaces the primary spin as in the usual Monte Carlo method to yield a new spin $\mathbf{s}_i'$.

Third, $\mathbf{s}_j$ is adjusted to satisfy $m_x = m_y = 0$ by setting $s_{jx}' = s_{jx} + s_{ix} - s_{ix}'$ and $s_{jy}' = s_{jy} + s_{iy} - s_{iy}'$.

Fourth, the z component of $\mathbf{s}_j$ is corrected as $s_{jz}' = \mathrm{sgn}(s_{jz})\sqrt{1 - s_{jx}'^2 - s_{jy}'^2}$, in which if the square root is negative no trial move occurs.

Fifth, the new magnetization is calculated as $m_z' = m_z + s_{iz}' + s_{jz}' - s_{iz} - s_{jz}$. If m_z' is less than 0, no trial move occurs.

Sixth, the energy difference due to the allowable trial move is calculated as $\Delta E = E' - E$

Seventh, the acceptance probability P is calculated as

$$P = \min\left[1, \left(\frac{m_z'}{m_z}\right)^2 \frac{|s_{jz}|}{|s_{jz}'|} \exp(-\beta \Delta E) \right] \tag{2.48}$$

Eighth, the trial move is accepted with probability P or it does not occur with probability $1 - P$.

Repeating the above procedure until the total Monte Carlo steps or some specific criteria are satisfied.

2.3 Micromagnetic model

Different from the discrete and atomistic nature of the atomistic spin model in Section 2.2, the micromagnetic theory is a continuum model. It handles magnetization processes on a length scale that is small enough to resolve the transition of the magnetization within domain walls but large enough to replace the atomic magnetic moments by a continuous function of position [237, 238]. Unlike the atomistic spin model which describes the magnetic state by the discrete atomic spin moment at each atomic site, the state of the magnet in the micromagnetic model is described by the magnetization saturation M_s and the unit vector $\mathbf{m}$ that represents the magnetization direction and is spatially continuous functions of position.

The Micromagnetic theory is able to bridge the gap between the classic or continuum theory and the quantum theory for magnetic properties of materials. Lots of scientists made great contribution to this field [239–242]. The breakthrough toward micromagnetic theory

is the propose of LL equation in 1935 by Landau and Lifshitz [225]. The theory contains the continuum expression of exchange energy and gave a first interpretation of domain patterns. The emergence of the modern theory of magnetism is due to the publication of Brown's papers [243] which for the first time considered the effect of local perturbations of the direction of magnetization on the law of approach to ferromagnetic saturation. The micromagnetic theory is an approach to explain magnetization reversal and domain propagation of ferro- and ferri-magnetic materials at the length scale of nanometers. Micromagnetic modeling aims at simulating the domain structure on the nano-/micro-scale level and is very useful when studying the influence of microstructure (e.g., grain shape/size, grain boundary, intergranular phase, etc.) on the magnetization reversal process and the macroscopic properties of permanent magnets [73, 74, 157, 166, 238, 244–246].

Micromagnetic simulations based on micromagnetic model currently dominate the simulation market of understanding the mechanism of reversal domain coercivity [238, 247–252]. They have been widely applied to investigate the microstructural effects on the coercivity in Nd-Fe-B magnets. Especially for the influence of GB phase, based on the assumption of GB phase as defect layer with no magnetocrystalline anisotropy and the same or smaller saturation magnetization and exchange constant as in the main phase, micromagnetic simulation of both single-grain and multigrain Nd-Fe-B magnets were carried out to study the effect of the GB thickness, grain shape and grain size [74, 253–255]. By assuming different GB phase properties in different crystallographic planes, micromagnetic simulations showed that a reduction of exchange constant and saturation magnetization in the side GB phase parallel to the c-axis enhances the coercivity more efficiently than that parallel to the c-plane [256]. It should be noted that in these simulations the properties of GB phases are based on assumptions which are not directly connected to the experimental observations. In contrast, recently a combined nanoanalytical high-resolution TEM/STEM and micromagnetic study of the anisotropic nature of GB phase and coercivity in both anisotropically and isotropically oriented Nd-Fe-B magnets has been reported [168, 245, 246]. By using the experimental measurements of the geometry and magnetic properties of GB phase and its junctions as a direct input, micromagnetic simulations are demonstrated to perfectly predict the hysteretic properties of Nd-Fe-B magnets.

2.3.1 Free energy functional

For a magnet whose magnetic state can be described by the continuous function $\mathbf{m}(\mathbf{r})$ with the constraint of $|\mathbf{m}(\mathbf{r})| = 1$, the free energy functional of the magnet is

$$E(\mathbf{m}) = \int_{\Omega} \left[A_{\mathrm{e}}|\nabla\mathbf{m}|^2 + \tilde{e}^{\mathrm{ani}} - \frac{1}{2}\mu_0 M_{\mathrm{s}}\mathbf{m} \cdot \mathbf{H}_{\mathrm{d}} - \mu_0 M_{\mathrm{s}}\mathbf{m} \cdot \mathbf{H}_{\mathrm{ext}} \right] \mathrm{d}v \qquad (2.49)$$

with $\mathbf{m}$ as the unit vector that represents the magnetization direction and is continuous functions of spatial position $\mathbf{r}$, A_{e} as the exchange stiffness introduced in Subsection 1.2.2,

and M_s as the magnetization saturation that is assumed to be constant at a fixed temperature.

$\mathbf{H}_d$ in Equation 2.49 is the demagnetization field arising from the divergence of the magnetization. It is related to the self-energy depending on the current state of $\mathbf{m}$. There are magnetic charge distributed among the surface of a magnet, and it will produce a demagnetization field $\mathbf{H}_d$ in the body of the magnets. This is the main reason for the generation of magnetic domains. $\mathbf{H}_d$ can be calculated from the static Maxwell's equations. In the numerical solution of the magnetostatic boundary value problem for the magnetic scalar potential ϕ, the demagnetizing field can be derived as $\mathbf{H}_d = -\nabla\phi$.

$\tilde{e}^{\mathrm{ani}}$ in Equation 2.49 is the magnetocrystalline anisotropy energy density. Its expression depends on the anisotropy type of the magnetic materials of interests. For the uniaxial magnetic anisotropy, $\tilde{e}^{\mathrm{ani}}$ is expressed by

$$\tilde{e}^{\mathrm{ani}} = K_1 \left[1 - (\mathbf{m} \cdot \mathbf{e}^{\mathrm{easy}})^2 \right]. \tag{2.50}$$

If K_1 is positive in Equation 2.50, $\mathbf{e}^{\mathrm{easy}}$ is the magnetically easy axis, as shown the energy landscape in Figure 2.6(a). If K_1 is negative, the plane perpendicular to $\mathbf{e}^{\mathrm{easy}}$ is the magnetically easy plane, as shown the energy landscape in Figure 2.6(b).

For a cubic crystal, $\tilde{e}^{\mathrm{ani}}$ can be constructed as

$$\tilde{e}^{\mathrm{ani}} = K_1 \left(m_1^2 m_2^2 + m_2^2 m_3^2 + m_3^2 m_1^2 \right) + K_2 m_1^2 m_2^2 m_3^2. \tag{2.51}$$

If the second term in Equation 2.51 is neglected, i.e., $K_2 = 0$, the easy axes are the $\langle 100 \rangle$ axes (i.e., the $\pm x$, $\pm y$, and $\pm z$ directions) for $K_1 > 0$ and the $\langle 111 \rangle$ directions for $K_1 < 0$, as shown in Figure 2.6(c) and (d). If K_2 is nonzero, both K_1 and K_2 have to be considered to determine the easy axes, as shown in Tables 2.4 and 2.5. The hard axes mean the directions of the greatest energy. The intermediate axes corresponds to the direction at which the saddle points in the energy landscape are obtained.

| (a) | (b) | (c) | (d) |
| easy axis [001] | easy plane (001) | easy axis (100) | easy axis ⟨111⟩ |
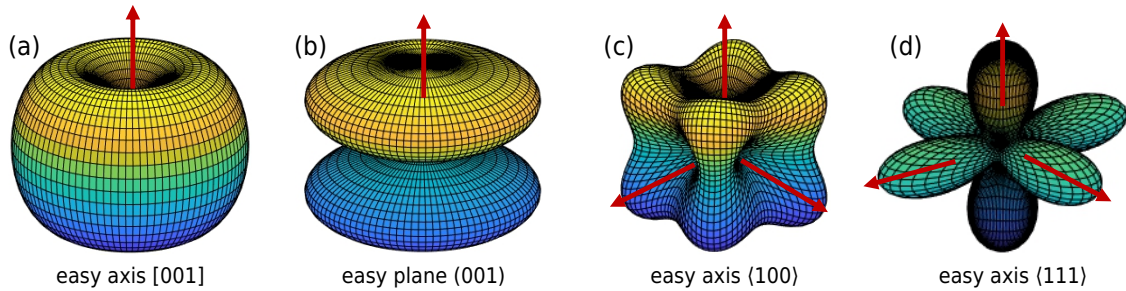
Figure 2.6: Illustration of landscape of magnetocrystalline anisotropy energy density $\tilde{e}^{\mathrm{ani}}$: uniaxial anisotropy with (a) $K_1 > 0$ and (b) $K_1 < 0$; cubic an-iostropy ($K_2 = 0$) with (c) $K_1 > 0$ and (d) $K_1 < 0$.

Table 2.4: Directions of easy, medium, and hard axes in a cubic crystal for $K_1 > 0$ [257].

Type of axis	$K_2 = +\infty$ to $-9K_1/4$	$K_2 = -9K_1/4$ to $-9K_1$	$K_2 = -9K_1$ to $-\infty$
Easy axis	$\langle 100 \rangle$	$\langle 100 \rangle$	$\langle 111 \rangle$
Medium axis	$\langle 110 \rangle$	$\langle 111 \rangle$	$\langle 100 \rangle$
Hard axis	$\langle 111 \rangle$	$\langle 110 \rangle$	$\langle 110 \rangle$

Table 2.5: Directions of easy, medium, and hard axes in a cubic crystal for $K_1 < 0$ [257].

Type of axis	$K_2 = -\infty$ to $9|K_1|/4$	$K_2 = 9|K_1|/4$ to $9|K_1|$	$K_2 = 9|K_1|$ to $+\infty$
Easy axis	$\langle 111 \rangle$	$\langle 110 \rangle$	$\langle 110 \rangle$
Medium axis	$\langle 110 \rangle$	$\langle 111 \rangle$	$\langle 100 \rangle$
Hard axis	$\langle 100 \rangle$	$\langle 100 \rangle$	$\langle 111 \rangle$

2.3.2 Macroscopic Landau–Lifshitz equation

Minimizing the total energy in Equation 2.49 with respect to the magnetization unit vector $\mathbf{m}$ could yield a stable equilibrium state of the magnetic structure. However, the physical path which the magnetic system follows towards equilibrium is described by the Landau–Lifshitz (LL) equation [225]

$$\dot{\mathbf{m}} = -\frac{\gamma}{1+\alpha^2} \left[\mathbf{m} \times \mathbf{H}_{\text{eff}} + \alpha \mathbf{m} \times (\mathbf{m} \times \mathbf{H}_{\text{eff}}) \right] \tag{2.52}$$

or the Landau–Lifshitz–Gilbert (LLG) equation [226, 258]

$$\dot{\mathbf{m}} = -\gamma \mathbf{m} \times \mathbf{H}_{\text{eff}} + \alpha \left(\mathbf{m} \times \dot{\mathbf{m}} \right) \tag{2.53}$$

in which γ denotes the gyromagnetic ratio, α is the dimensionless Gilbert damping parameter, and the effective field is derived as

$$\mathbf{H}_{\text{eff}} = -\frac{1}{M_{\text{s}}} \frac{\delta E(\mathbf{m})}{\delta \mathbf{m}} = \frac{2A_{\text{e}} \nabla^2 \mathbf{m}}{M_{\text{s}}} + \mathbf{H}_{\text{eff-other}} \tag{2.54}$$

in which the first term corresponds to the exchange field that will introduce numerical difficulty, and $\mathbf{H}_{\text{eff-other}}$ denotes the effective field contributed by the energy apart from the exchange energy. It should be noted that $\mathbf{H}_{\text{eff-other}}$ does not contain the derivatives of $\mathbf{m}$ ($\nabla \mathbf{m}$ and $\nabla^2 \mathbf{m}$).

If the damping parameter α is known, Equations 2.52 and 2.53 can be used to obtain

the time evolution of the magnetization. In general, α is not a constant and could depend nonlinearly on the magnetization. α is usually assumed to be in the range of 0.01 to 0.1 for numerical convenience and reduced computation time. α also governs the rate of magnetization approaching to equilibrium state. The physical origin of the damping process is very complicated. Here, in terms of the phenomenological description of micromagnetics, all the effect from the microscopic physical processes are included in the single parameter α. Due to the phenomenological nature of α and the continuum assumption of the magnetization, Equation 2.52 here is called as macroscopic LL equation, in order to distinguish it from the atomistic version in Equation 2.36.

The finite temperature effects in micromagnetics is modelled by adding a fluctuating thermal field $\mathbf{H}_{\text{therm}}$ into $\mathbf{H}_{\text{eff}}$, so that a macroscopic stochastic LL equation is obtained. According to Brown [227], the thermal field can be expressed as

$$\mathbf{H}_{\text{therm}} = \boldsymbol{\eta} \sqrt{\frac{2\alpha k_{\text{B}} T}{M_{\text{s}}(T)\gamma \Delta V \Delta t}} \tag{2.55}$$

in which $\boldsymbol{\eta}$ is a random vector from a standard normal distribution and is regenerated at every mesh node/grid after every time step. ΔV is the single mesh/cell volume and Δt is the time step. In general, $\mathbf{H}_{\text{therm}}$ has zero mean value and is uncorrelated both in time and space, which means randomly changes between time steps. It should be mentioned that the atomic-scale thermal field in Equation 2.41 is independent of the mesh/cell volume, but the macroscopic thermal field in Equation 5.3 highly depends on the mesh/cell volume. This is also the intrinsic difference between the atomistic and macroscopic models.

In the framework of macroscopic stochastic LL equation, it is possible to study the magnetic properties at finite temperatures by micromagnetic simulations [228, 259, 260], if the temperature dependence of the micromagnetic input parameters, such as magnetization [261–264] , exchange stiffness [264–269], anisotropy constant [236, 270–274] are readily available.

2.3.3 Numerics for micromagnetic simulations

There are several numerical methodologies available to implement the micromagnetic model to study both the equilibrium and dynamic properties of magnetic materials with microstructure information taken into account. The basis is that the computation requires the discretization of Equation 2.49 by either finite element method [275] and finite difference method [276, 277]. Based on the FEM or FDM discretization, several energy minimization methods are applied to obtain the equilibrium results and several time integration methods for LL and LLG equations are used to calculate the dynamic properties.

Finite element method. In the finite element method, the weak forms of the LLG equation 2.53 and the Maxwell's equations $\nabla \cdot \mathbf{B} = 0$ with $\mathbf{B} = \mu_0(-\nabla\phi + M_s\mathbf{m})$ are usually the

starting point. The degrees of freedom are $\mathbf{m}$ and ϕ (magnetic scalar potential). With the test functions $\boldsymbol{\psi}_m$ for LLG equation and ψ_ϕ for the Maxwell's equations, one obtains the weak forms as

$$\int_\Omega \left[\dot{\mathbf{m}} + \gamma \mathbf{m} \times \left(\frac{2A_\mathrm{e} \nabla^2 \mathbf{m}}{M_\mathrm{s}} + \mathbf{H}_\text{eff-other} \right) - \alpha \left(\mathbf{m} \times \dot{\mathbf{m}} \right) \right] \cdot \boldsymbol{\psi}_m \mathrm{d}v = 0 \tag{2.56}$$

and

$$\int_\Omega \nabla \cdot \mathbf{B}\, \psi_\phi \mathrm{d}v = 0. \tag{2.57}$$

The term $\mathbf{m} \times \nabla^2 \mathbf{m}$ contains the second order derivative of $\mathbf{m}$. To lower the order, one makes use of the partial integration. Rewriting the integrand yields

$$\left(\mathbf{m} \times \nabla^2 \mathbf{m} \right) \cdot \boldsymbol{\psi}_m = \left[(\mathbf{m} \times \mathbf{e}_i) \cdot \boldsymbol{\psi}_m \right] \nabla^2 m_i = \left[(\boldsymbol{\psi}_m \times \mathbf{m}) \cdot \mathbf{e}_i \right] \nabla^2 m_i \tag{2.58}$$

in which $\mathbf{e}_i$ is the unit vector of Cartesian coordinates ($i = 1, 2, 3$). By using the divergence theorem and integrating over the magnetic volume, the weak form for the exchange field term in Equation 2.58 is derived as

$$\int_\Omega \left(\mathbf{m} \times \nabla^2 \mathbf{m} \right) \cdot \boldsymbol{\psi}_m \mathrm{d}v = \int_{\partial\Omega} \left[(\mathbf{m} \times \mathbf{e}_i) \cdot \boldsymbol{\psi}_m \right] \nabla m_i \cdot \mathbf{n}\, \mathrm{d}s - \int_\Omega \nabla \left[(\boldsymbol{\psi}_m \times \mathbf{m}) \cdot \mathbf{e}_i \right] \cdot \nabla m_i \mathrm{d}v$$

$$= \int_{\partial\Omega} \left[(\mathbf{m} \times \mathbf{e}_i) \cdot \boldsymbol{\psi}_m \right] \nabla m_i \cdot \mathbf{n}\, \mathrm{d}s - \int_\Omega (\mathbf{m} \times \mathbf{m}_{,i}) \cdot \boldsymbol{\psi}_{m,i} \mathrm{d}v. \tag{2.59}$$

If the constraint $|\mathbf{m}| = 1$ is not satisfied by the artificial renormalization in each time step, an additional functional Π_c and its variation have to be considered, i.e.,

$$\Pi_c = \int_\Omega \lambda_c \left(|\mathbf{m}|^2 - 1 \right) \mathrm{d}v - \int_\Omega \frac{\lambda_c^2}{2k_c} \mathrm{d}v \tag{2.60}$$

and

$$\delta\Pi_c = \int_\Omega \left(|\mathbf{m}|^2 - 1 - \frac{\lambda_c}{k_c} \right) \delta\lambda_c\, \mathrm{d}v + \int_\Omega 2\lambda_c \mathbf{m} \cdot \delta\mathbf{m}\, \mathrm{d}v \tag{2.61}$$

in which λ_c is the Lagrange multiplier and k_c is a sufficiently large constant to make the diagonal of the iterative matrix nonzero.

Considering the additional variation in Equation 2.61, the degrees of freedom will be $[\mathbf{m}, \phi, \lambda_c]$ and thus the weak forms can be rewritten as

$$\int_\Omega \left[\dot{\mathbf{m}} + \gamma \mathbf{m} \times \mathbf{H}_\text{eff-other} - \alpha \left(\mathbf{m} \times \dot{\mathbf{m}} \right) + 2\lambda_c \mathbf{m} \right] \cdot \boldsymbol{\psi}_m \mathrm{d}v$$

$$- \frac{2\gamma A_\mathrm{e}}{M_\mathrm{s}} \int_\Omega (\mathbf{m} \times \mathbf{m}_{,i}) \cdot \boldsymbol{\psi}_{m,i} \mathrm{d}v + \frac{2\gamma A_\mathrm{e}}{M_\mathrm{s}} \int_{\partial\Omega} \left[(\mathbf{m} \times \mathbf{e}_i) \cdot \boldsymbol{\psi}_m \right] \nabla m_i \cdot \mathbf{n}\, \mathrm{d}s = 0, \tag{2.62}$$

$$\int_\Omega \mu_0(-\nabla\phi + M_\mathbf{s}\mathbf{m}) \cdot \nabla\psi_\phi \, \mathrm{d}v - \int_{\partial\Omega} \mathbf{B} \cdot \mathbf{n}\psi_\phi \, \mathrm{d}s = 0, \tag{2.63}$$

and

$$\int_\Omega \left(|\mathbf{m}|^2 - 1 - \frac{\lambda_c}{k_c}\right)\psi_{\lambda_c} \, \mathrm{d}v = 0, \tag{2.64}$$

In the finite element discretization with the Galerkin type, both the degree of freedom and the test function are discretized by the same shape function, i.e.,

$$\begin{aligned}
\mathbf{m} &= N^I \mathbf{m}^I, \ \phi = N^I \phi^I, \ \lambda_c = N^I \lambda_c^I \\
\boldsymbol{\psi}_m &= N^I \boldsymbol{\psi}_m^I, \ \psi_\phi = N^I \psi_\phi^I, \ \psi_{\lambda_c} = N^I \psi_{\lambda_c}^I
\end{aligned} \tag{2.65}$$

in which I is the finite-element node number and $N^I(\mathbf{r})$ is the shape function of the node I. After inserting the disctetization Equation 2.65 into the weak forms in Equations 2.62 to 2.64, one can get the elemental residuals as

$$\begin{aligned}
\mathbf{R}_m^I &= \int_\Omega \left[\dot{\mathbf{m}} + \gamma\mathbf{m} \times \mathbf{H}_{\text{eff-other}} - \alpha\left(\mathbf{m} \times \dot{\mathbf{m}}\right) + 2\lambda_c\mathbf{m}\right] N^I \mathrm{d}v \\
&\quad - \frac{2\gamma A_\mathrm{e}}{M_\mathrm{s}} \int_\Omega (\mathbf{m} \times \mathbf{m}_{,i}) N_{,i}^I \mathrm{d}v + \frac{2\gamma A_\mathrm{e}}{M_\mathrm{s}} \int_{\partial\Omega} N^I(\mathbf{m} \times \mathbf{e}_i)(\nabla m_i \cdot \mathbf{n}) \, \mathrm{d}s, \\
\mathrm{R}_\phi^I &= \int_\Omega \mu_0(-\nabla\phi + M_\mathrm{s}\mathbf{m}) \cdot \nabla N^I \, \mathrm{d}v - \int_{\partial\Omega} N^I(\mathbf{B} \cdot \mathbf{n}) \, \mathrm{d}s, \\
\mathrm{R}_{\lambda_c}^I &= \int_\Omega \left(|\mathbf{m}|^2 - 1 - \frac{\lambda_c}{k_c}\right) N^I \mathrm{d}v.
\end{aligned} \tag{2.66}$$

The backward Euler method can be used for the time discretization of $\mathbf{m}$. Then the iterative matrix including damping matrix and stiffness matrix can be calculated by the derivative of residuals in Equation 2.66 with respect to the degrees of freedom at node J. Currently, several open source finite-element codes, such as finmag (github.com/fangohr/finmag), feeLL-Good (feellgood.neel.cnrs.fr), Nmag (nmag-project.github.io/) [249], magpar (www.magpar.net) [247], Commics (geras.asc.tuwien.ac.at/cpfeiler/commics) [278] etc., and commercial finite-element codes, such as FEMME and magnum.fe (www.suessco.com/simulations/) [279], TetraMag [277], Fastmag [252], etc., are available [280].

Finite difference method. The basic idea of the finite difference method is approximating the partial derivatives of a function $f(\mathbf{r}, t)$ by finite difference quotients Δx, Δy, Δz and Δt. For instance,

$$f(x + \Delta x, y, z, t) = f(x, y, z, t) + \Delta x \frac{\partial f}{\partial x} + \frac{(\Delta x)^2}{2} \frac{\partial^2 f}{\partial x^2} + \cdots \tag{2.67}$$

In other words, the finite difference discretization is a process of replacing partial derivatives

by finite-difference quotients, which is much more straightforward than the finite element discretization. After the discretization, partial differential equations can be changed to a system of algebraic equations, which is solved numerically by an iterative process to obtain an approximate solution.

The most important discretization in the finite difference method for micromagnetic simulations is the effective field term $\mathbf{H}_\text{eff}$ in Equations 2.52 and 2.53. $\mathbf{H}_\text{eff}$ is usually divided into several parts including exchange field $\mathbf{H}_\text{exch}$, magnetocrystalline anisotropy field $\mathbf{H}_\text{ani}$, and demagnetization field $\mathbf{H}_\text{demag}$. $\mathbf{H}_\text{exch}$, the effective field due to the exchange interaction, is evaluated using a 6-neighbor small-angle approximation [281, 282], i.e.,

$$\mathbf{H}_\text{exch} = \frac{2A_\text{e}}{M_\text{s}} \sum_{i \in \text{NN}} \frac{\mathbf{m}_i - \mathbf{m}}{\Delta x_i^2} \tag{2.68}$$

in which NN stands for the indices of the nearest neighbours, i ranges over the six nearest neighbors of the central cell with magnetization $\mathbf{m}$, and Δx_i is the cell size in the direction of neighbor i. For the case of exchange interaction between different materials with different material parameters A_e1, A_e2 and M_s1, M_s2, a simple harmonic mean gives rise to [250]

$$\mathbf{H_\text{exch}} = 4S \frac{A_\text{e1}}{M_\text{s1}} \frac{A_\text{e2}}{M_\text{s2}} \left(\frac{A_\text{e1}}{M_\text{s1}} + \frac{A_\text{e2}}{M_\text{s2}} \right)^{-1} \sum_{i \in \text{NN}} \frac{(\mathbf{m}_i - \mathbf{m})}{\Delta x_i^2} \tag{2.69}$$

where S is an arbitrary scaling factor for adjusting the exchange coupling strength between regions.

The contributions by the magnetocrystalline anisotropy to the effective field are straightforward and for the uniaxial anisotropy, one has

$$\mathbf{H}_\text{ani} = \frac{2K_1}{M_\text{s}} (\mathbf{m} \cdot \mathbf{e}^\text{easy}) \mathbf{m} \tag{2.70}$$

The calculation of demagnetizing field $\mathbf{H}_\text{demag}$ is computationally most expensive. Two approximation methods are available for calculating $\mathbf{H}_\text{demag}$. The approximation of the demagnetization field of each computational cell by the dipole field in the center of the cell i with the magnetic moment $\Delta V M_\text{s}$ can be given as [248, 283]

$$\mathbf{H}_\text{demag} = -\frac{\Delta V M_\text{s}}{4\pi} \sum_{i \neq j} \left[\frac{\mathbf{m}_i}{r_{ij}^3} - 3 \frac{(\mathbf{m}_i \cdot \mathbf{r}_{ij}) \mathbf{r}_{ij}}{r_{ij}^5} \right] \tag{2.71}$$

in which ΔV is the volume of cell i, $\mathbf{r}_{ij}$ is the vector pointing from cell i to cell j, and r_{ij} is the distance between cell i and j. Another method to calculate the demagnetization field is

the (discrete) convolution of the magnetization with a demagnetizing kernel $\hat{\mathbf{K}}$ [250], i.e.,

$$\mathbf{H}_{\text{demag}} = M_{\text{s}}\hat{\mathbf{K}} \cdot \mathbf{m}_j \tag{2.72}$$

which is FFT-accelerated based on the well-known convolution theorem. $\hat{\mathbf{K}}$ is calculated by assuming constant magnetization in each finite difference cell [284]. The resulting $\mathbf{H}_{\text{demag}}$ is averaged over the cell volumes. The integration is done numerically with the number of integration points automatically chosen based on the distance between source and destination cells and their aspect ratios [250].

For the time integration of the LL equation, a number of explicit Runge–Kutta methods are available, such as Dormand–Prince method, Bogacki–Shampine method, Heun's method, Euler's method, Runge–Kutta–Fehlberg, etc [250, 285]. In the case of stochastic LL equation to calculate the finite-temperature properties, it is found that the relative performance of Dormand–Prince and Runge–Kutta–Fehlberg solver is comparable. The Dormand–Prince solver is shown to be faster at higher simulated temperatures, while the Runge–Kutta–Fehlberg solver is faster at low temperatures. Both Dormand–Prince and Runge–Kutta–Fehlberg solvers can use adaptively time stepping, obtaining a twenty fold speedup compared to the commonly best practice of using the Heun's solver with a small fixed time step [285].

For energy minimization to obtain the equilibrium magnetic properties, variants of the steepest-descent method, the non-linear conjugate gradient method, and the quasi-Newton method are most widely used in micromagnetics for permanent magnets [238]. There are several finite difference method based open-source codes, such as OOMMF (math.nist.gov/oommf) [286], MuMax3 (mumax.github.io) [250], magnum.fd (micro-magnetics.org/magnum.fd), fidimag (fidimag.readthedocs.io) [287], etc., and commercial codes, such as LLG (llgmicro.home. mindspring.com), GPMagnet (www.goparallel.net) [288], etc., available [280].

For the calculation of thermally activated coercivity or thermal fluctuation induced coercivity reduction, apart from the direction integration of stochastic LL equation, the combination of equilibrium calculation and energy barrier calculation is widely used, as illustrated in Figure 2.7. The underlying physics is that if there exits thermal activation, the magnetic system can hop over a finite energy barrier, resulting in a reduction in the coercivity or switching field. Firstly, the demagnetization curve of the magnet is calculated by using a standard micromagnetic solver, from which the static coercive field $H_{\text{c,static}}$ with no thermal fluctuation effects and the magnetic configurations at each external field H are obtained (Figure 2.7(a)). Then the intermediate magnetization configurations at H (not fully reversed) close to the switching field will taken as an initial guess. With this initial guess and the final fully reversed configuration, the climbing image nudged elastic band method [253, 289, 291] or the modified string method [253, 289, 292] can be applied to compute the minimum energy path and the associated energy barrier ΔE (Figure 2.7(b)). The nudged
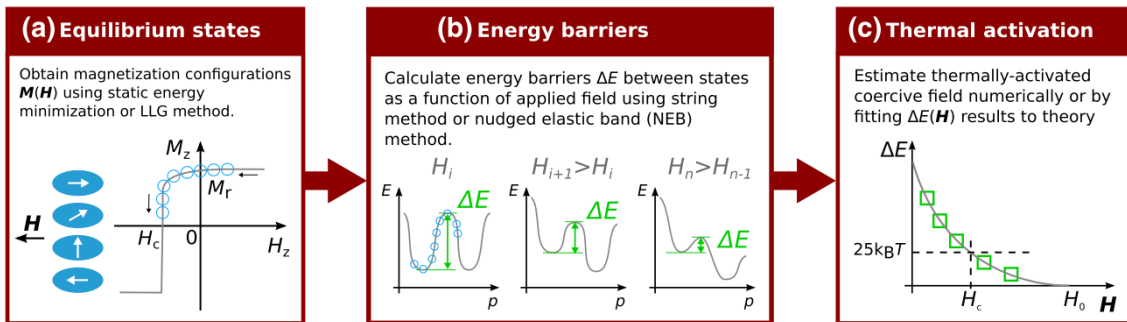
Figure 2.7: Illustrative procedure for calculating thermally activated coercivity using numerical micromagnetics: (a) equilibrium states calculation; (b) energy barriers calculation; (c) energy barrier fitting to a critical value $25 k_\mathrm{B} T$ [289].

elastic band method is an algorithm to find minimum energy transitions between equilibrium states and has been implemented for numerical micromagnetics in the open-source code fidimag (fidimag.readthedocs.io) [287]. As shown in Figure 2.7(c), this process is repeated as a function of applied field H and the resulting energy barriers are fitted to an
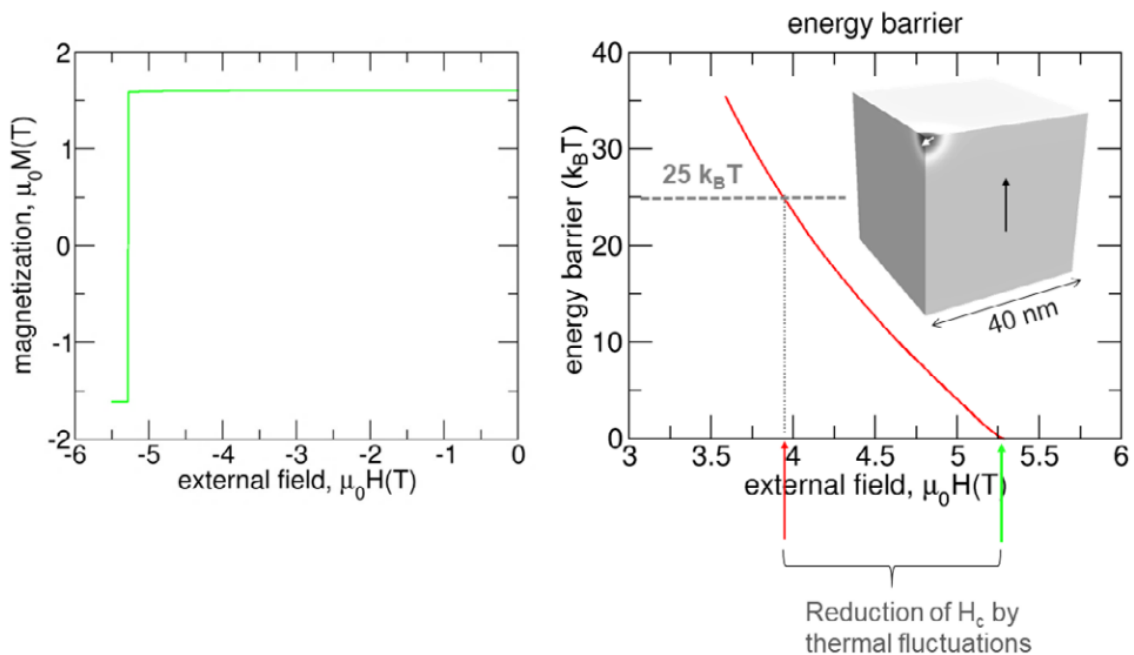
Figure 2.8: Thermally induced magnetization reversal in a $Nd_2Fe_{14}B$ cube. Left: demagnetization curve with thermal fluctuations. Right: energy barrier as a function of the external field. The inset shows the saddle point configuration of the magnetization [238, 290].

effective energy barrier function [253]

$$\Delta E = \Delta E_0 \left(1 - \frac{H}{H_{\text{c,static}}} \right)^n \tag{2.73}$$

with ΔE_0 and n as fitting parameters. ΔE_0 is the energy barrier when there is no external field. The relaxation time τ characterizing the process of the thermal activation of the magnetization over an energy barrier E_B is given by the Arrhenius–Néel law $\tau = f_0^{-1} \exp[E_B/(k_B T)]$. The attempt frequency is in the order of $10^{11}\ s^{-1}$ [293] and the relaxation time is in the order of 1 s, corresponding to an energy barrier around $25k_B T$ [294]. Therefore, with the fitting parameters in Equation 2.73 and setting ΔE as $25k_B T$, one can determine the coercivity at a fixed temperature. Figure 2.8 shows the the coercive field of a $Nd_2Fe_{14}B$ cube with an edge length of 40 nm obtained by classical micromagnetic simulations and computing energy barriers [238, 290]. It can be seen that the room temperature $T = 300$ K induced thermal fluctuations reduce the coercivity by more than 1.25 T.

3 Temperature-dependent intrinsic properties of Nd$_2$Fe$_{14}$B by *ab-initio* informed atomistic spin model simulations

3.1 Introduction

Nd-Fe-B permanent magnets are critical for the key components of energy-related technologies, such as wind turbines and electro-mobility. They are also important in robotics, automatisation, sensors, actuators, and information technology [23, 43, 178]. Since there is increasing demand in high-end technology for permanent magnets used at finite or elevated temperatures, the temperature-dependent properties of Nd$_2$Fe$_{14}$B, as the main phase of Nd-Fe-B magnets, are of great interest. For example, these magnets are exposed to elevated temperatures in many applications such as the motors inside hybrid vehicles where the operating temperature can approach 450 K.

Modelling and simulation play an important role in the design of permanent magnets for applications at elevated temperatures. Currently, first-principles calculations and micromagnetic simulations dominate the modelling of permanent magnets. The first-principle calculations help to understand and evaluate the intrinsic magnetic properties on the electronic-level, e.g. magnetic moment, crystal field parameter, etc.) at zero temperature [162, 163, 165, 195, 197, 295]. However, first-principles calculations become very challenging at finite temperature. Micromagnetic model aims at simulating the domain structure on the nano/microscale level, and is very useful when one is interested in the influence of microstructure (e.g., grain shape/size, grain boundary, intergranular phase, etc.) on the magnetization reversal process and the mesoscopic properties of permanent magnets [73, 74, 157, 166, 238, 244–246, 248, 296]. The thermal activation of nucleation at finite temperatures and its effect on the decay of coercive field in Nd-Fe-B magnets were addressed by micromagnetic simulations [253, 289]. However, for such purposes, the temperature-dependent intrinsic properties have to be known or determined beforehand. In addition, it is well known that the micromagnetic model is essentially a continuum approximation and assumes the magnetization to be a continuous function of position. This approximation is only valid, when the considered length scales are sufficiently large so the atomic structure can be ignored [248, 297]. However, when the region of interest is at the same scale as

the exchange length, this approximation would fail. For example, in Nd-Fe-B magnets, the amorphous grain boundary is often found to be around 2 nm (close to the micromagnetic exchange length of $Nd_2Fe_{14}B$). The validity of micromagnetic representation of this 2-nm region with homogenized parameters remains as an issue.

A scale bridge between these two methodologies for modeling Nd-Fe-B magnets is desired. Moreover, the evaluation of temperature-dependent macroscopic parameters for micromagnetic simulations is highly nontrivial. In this aspect, there are recent attempts to study temperature-dependent effective magnetic anisotropy, saturation magnetization, and reversal process in $Nd_2Fe_{14}B$ by using atomistic spin model simulations [123, 216, 231, 298, 299], based on which the concept of a multiscale model approach for the design of advanced permanent magnets is proposed [230]. In general, an atomistic spin model is capable of calculating magnetic properties at different temperatures [204, 224, 300], in which the temperature effects can be taken into account by either the Langevin-like spin dynamics or Monte Carlo simulations. Its application to permanent magnets, or more especially rare-earth permanent magnets, is still at its early stage. More efforts have to be made e.g. revealing the gap between model simulations and experimental measurements or predicting parameters over a broad range of temperatures, in order to establish the atomistic spin model as a readily available methodology for designing Nd-Fe-B magnets.

In this work, following the similar framework in [216, 269, 299], we not only calculate the Curie temperature and the temperature dependent magnetization, magnetocrystalline anisotropy and domain wall width, but also add some additional new knowledge into the community of Nd-Fe-B magnets in terms of atomistic spin model simulations and temperature dependent intrinsic parameters. For example, considering the different description of spin states in the classical and quantum manner, such as the different availability of spin states in the classical atomistic spin model simulations and experiments, we determine the temperature rescaling parameter for $Nd_2Fe_{14}B$ and reveal the difference between simulation and experimental temperatures. In this way, the calculated magnetization *vs* temperature curve shows a better agreement with the experimental one, in comparison with the literature [216]. In addition, except for the domain wall width at temperatures higher than the spin reorientation temperature, we also carefully examine various types of domain wall configurations and their width at temperatures lower than the spin reorientation temperature. Moreover, linking the simulation results with the micromagnetic theory, we determine the exchange stiffness for a wide range of temperatures and identify the scaling law.

The chapter presents an *ab-initio* informed atomistic spin model for $Nd_2Fe_{14}B$, and applied for the theoretical calculation of the Curie temperature, spin-reorientation temperature, and magnetic properties, such as saturation magnetization $M_s(T)$, effective magnetic anisotropy constants $K_i(T)$ ($i = 1, 2, 3$), domain wall width $\delta_w(T)$, and exchange stiffness constant $A_e(T)$ at temperatures both higher and lower than the spin reorientation temperature. In detail, the atomistic spin model Hamiltonian for $Nd_2Fe_{14}B$ is constructed by using the

Heisenberg exchange of Fe−Fe and Fe−Nd atomic pairs, the uniaxial single-ion anisotropy of Fe atoms, and the crystal-field energy of Nd ions which is approximately expanded into an energy formula featured by the second, fourth, and sixth-order phenomenological anisotropy constants. After applying a temperature rescaling strategy, it is shown that the calculated Curie temperature, spin-reorientation phenomenon, $M_s(T)$, $\delta_w(T)$, and $K_i^{\text{eff}}(T)$ agree well with the experimental results. $A_e(T)$ is estimated through a general continuum description of the domain wall profile by mapping atomistic magnetic moments to the macroscopic magnetization. A_e is found to decrease more slowly than K_1^{eff} with increasing temperature, and approximately scale with normalized magnetization as $A_e(T) \sim m^{1.2}$. Especially, the possible domain wall configurations at temperatures below the spin-reorientation temperature and the associated δ_w and A_e are identified.

The calculation results show good agreement with the experimental results. This work presents a scale bridge between *ab-initio* calculations and temperature-dependent micromagnetic simulations of Nd-Fe-B permanent magnets, and will be useful for revealing the atomic-scale magnetic behavior in Nd-Fe-B magnets.

3.2 Atomistic spin model for Nd$_2$Fe$_{14}$B

For calculating the temperature-dependent magnetic properties, the atomistic spin mode treating each atom as a classic spin is used [204, 224, 300]. For Nd$_2$Fe$_{14}$B, the atomistic spin Hamiltonian can be written as

$$\mathcal{H} = -\frac{1}{2} \sum_{\substack{i \neq j}}^{i,j \in \text{Fe}} J_{ij}^{\text{Fe-Fe}} \mathbf{s}_i \cdot \mathbf{s}_j - \frac{1}{2} \sum_{i \in \text{Fe}}^{j \in \text{Nd}} J_{ij}^{\text{Fe-Nd}} \mathbf{s}_i \cdot \mathbf{s}_j - \sum_{i \in \text{Fe}} k_i^{\text{Fe}} (\mathbf{s}_i \cdot \mathbf{e}^z)^2 + \mathcal{H}_{\text{Nd}}^{\text{cf}}. \tag{3.1}$$

It should be noted that in Equation 3.1 the energy terms associated with the external magnetic field and the dipole interaction between atomic spin moments are not included, since here we only focus on the calculation of intrinsic properties. $\mathbf{s}_i$ is a unit vector denoting the local spin moment direction. The first two terms in Equation 3.1 correspond to the Heisenberg exchange energy. They only contain the exchange interactions in Fe-Fe ($J_{ij}^{\text{Fe-Fe}}$) and Fe-Nd ($J_{ij}^{\text{Fe-Nd}}$) atomic pairs, owing to the fact that B sites are usually taken to be nonmagnetic and the interaction between Nd sites can be negligible [216, 230, 299, 301]. The third term in Equation 3.1 represents the uniaxial magnetic anisotropy energy of Fe atoms, with k_i^{Fe} being the anisotropy energy per Fe atom and $\mathbf{e}^z$ the z-axis unit vector. The fourth term in Equation 3.1 denotes the crystal-field (CF) Hamiltonian of Nd ions, which is the main source of large magnetic anisotropy in Nd$_2$Fe$_{14}$B and can be approximated as [198, 216, 299]

$$\mathcal{H}_{\text{Nd}}^{\text{cf}} = \sum_{i \in \text{Nd}} \sum_{n=2,4,6} \alpha_n \langle r^n \rangle_{4f,i} A_{n,i}^0 \hat{\Theta}_{n,i}^0, \tag{3.2}$$

in which α_n is the Stevens factors, $\langle r^n \rangle_{4f,i}$ the $4f$ radial expectation value of r^n at the respective Nd site i, $A_{n,i}^0$ the CF parameters, and $\hat{\Theta}_{n,i}^0$ the Stevens operator equivalents. For Nd^{+3} ions, $\alpha_2 = -6.428 \times 10^{-3}$, $\alpha_4 = -2.911 \times 10^{-4}$, and $\alpha_6 = -3.799 \times 10^{-5}$ [302]. $\langle r^n \rangle$ values of Nd^{+3} ions can be calculated as $\langle r^2 \rangle = 1.001 a_0^2$, $\langle r^4 \rangle = 2.401 a_0^4$, and $\langle r^6 \rangle = 12.396 a_0^6$ in which a_0 is the Bohr radius [200]. The Stevens operator equivalents are expressed as [302]

$$
\begin{aligned}
\hat{\Theta}_2^0 =& 3J_z^2 - \mathcal{J} \\
\hat{\Theta}_4^0 =& 35J_z^4 - 30\mathcal{J}J_z^2 + 25J_z^2 - 6\mathcal{J} + 3\mathcal{J}^2 \\
\hat{\Theta}_6^0 =& 231J_z^6 - 315\mathcal{J}J_z^4 + 735J_z^4 + 105\mathcal{J}^2J_z^2 \\
& - 525\mathcal{J}J_z^2 + 294J_z^2 - 5\mathcal{J}^3 + 40\mathcal{J}^2 - 60\mathcal{J}.
\end{aligned}
\tag{3.3}
$$

$J_z = J(\mathbf{s} \cdot \mathbf{e}^z)$ denotes the z-component of the total angular momentum J which is $9/2$ for Nd ions [302]. $\mathcal{J} = J^2$ instead of $\mathcal{J} = J(J+1)$ is used in the classical manner [216]. The reliable first-principles calculation of high-order CF parameters in Nd$_2$Fe$_{14}$B is still challenging. Here the A_n^0 values which are determined from the experiment results [198] are taken, i.e., $A_2^0 = 295$ K/a_0^2, $A_4^0 = -12.3$ K/a_0^4, and $A_6^0 = -1.84$ K/a_0^6. All Nd ions with the same CF parameters are set approximately. In this way, combining Equation 3.2, Equation 3.3, and $J_{i,z} = J(\mathbf{s}_i \cdot \mathbf{e}^z)$ yields the CF energy as

$$
\mathcal{H}_{\mathrm{Nd}}^{\mathrm{cf}} = -\sum_{i \in \mathrm{Nd}} \left[k_{i,1}^{\mathrm{Nd}}(\mathbf{s}_i \cdot \mathbf{e}^z)^2 + k_{i,2}^{\mathrm{Nd}}(\mathbf{s}_i \cdot \mathbf{e}^z)^4 + k_{i,3}^{\mathrm{Nd}}(\mathbf{s}_i \cdot \mathbf{e}^z)^6 \right],
\tag{3.4}
$$

in which the parameters $k_{i,1}^{\mathrm{Nd}}$, $k_{i,2}^{\mathrm{Nd}}$, and $k_{i,3}^{\mathrm{Nd}}$ are listed in Table 3.1. The constant term in $\mathcal{H}_{\mathrm{Nd}}^{\mathrm{cf}}$ is less important and thus not presented in Equation 3.4. The magnetocrystalline anisotropy energy of the Fe sublattice and the magnetic moments of each atom, as listed in Table 3.1, are taken from the previous first-principles calculations [216, 303].

The exchange parameters $J_{ij}^{\mathrm{Fe\text{-}Fe}}$ and $J_{ij}^{\mathrm{Fe\text{-}Nd}}$ in Equation 3.1 are evaluated in the relaxed unit cell (lattice parameters are kept constant as $a = b = 8.76$ Å, $c = 12.13$ Å and the thermal expansion is not considered) by using OpenMX [209, 214, 219, 304, 305]. The calculation of the Heisenberg exchange parameters J_{ij} between two different atomic sites i and j is implemented in OpenMX by using the magnetic-force theorem (follow the original formalism by Liechtenstein et al. [209]) and its extension to the nonorthogonal LCPAO (linear combination of pseudoatomic orbitals) method [219]. In detail, J_{ij} is estimated as a response to small spin tiltings (as a perturbation) from the given converged solution, as shown by the detailed formulation in [209, 219, 304]. More application examples of OpenMX in calculating Heisenberg exchange parameters are reported by the OpenMX's developers in the literature [214, 219, 304–306].

An open-core pseudopotential for Nd is used, with the $4f$ electrons in the core and not

Table 3.1: Magnetic moments and atomic-site resolved magnetic anistropy energy of each crystallographically equivalent atom.

Atom	μ_i (μ_B)	k_i $(\times 10^{-21}$ J$)$
Nd($4g$)	2.860	$k_{i,1}^{\text{Nd}} = -4.935$
Nd($4f$)	2.871	$k_{i,2}^{\text{Nd}} = 25.98$
		$k_{i,3}^{\text{Nd}} = -22.94$
Fe($4c$)	2.531	-0.342
Fe($4e$)	1.874	-0.0048
Fe($8j_2$)	2.629	0.093
Fe($8j_1$)	2.298	0.171
Fe($16k_2$)	2.206	0.0608
Fe($16k_1$)	2.063	0.0880

as valence electrons. For the many local-orbital-based methods in OpenMX, the basis set of each atom should be chosen. A notation of $sN_s pN_p dN_d fN_f$ is used to represent the basis-set choice for a given atom. For example, $s1p2d3$ denotes that one s, two p, and three d orbitals are taken as a basis set. According to the previous work [162], the basis sets for Nd, Fe, and B atoms are chosen as $s2p2d2$, $s2p2d2$, and $s2p2$, with cutoff radii of 8.0, 6.0, and 7.0 a.u., respectively. A $5 \times 5 \times 4$ k-point mesh, and a 500-Ry cutoff energy is used. The convergence criteria for the self-consistent calculation is 10^{-6} Hartree.

In fact, the unit cell here is already very large and thus the lattice translation vectors have negligible influence on the calculated J_{ij}. Indeed, our additional calculations of the $2 \times 1 \times 1$ and $2 \times 2 \times 1$ supercells show that the influence of the adopted cell size on the calculated J_{ij} can be ignored, as shown in Figure 3.1. Therefore, the calculated J_{ij} here can be used in the Heisenberg spin model and the Monte Carlo simulations. The calculated exchange parameters are further calibrated (interactions of Fe–Fe and Fe–Nd are rescaled by 2 and 0.9, respectively) by checking the results from the atomistic spin model simulation of $Nd_2Fe_{14}B$, and are shown in Figure 3.1. It can be found that the total magnetic moment of Nd ions is ferromagnetically coupled to Fe moments, and the exchange of Fe-Fe pairs is $3-10$ times stronger as that of Fe-Nd pairs.

It should be noted that the non-collinearity of the magnetic configuration is shown to significantly influence the exchange parameters, as reported in [307, 308]. However, in our case of $Nd_2Fe_{14}B$ here, it has been verified that the angle difference between the total magnetization and the Fe/Nd magnetization is very small over the entire temperature range [309], especially in temperature higher than 300 K considered here. Thus, the non-collinearity effect here is negligibly small. Therefore, calculating J_{ij} (Figure 5.1) in

Nd$_2$Fe$_{14}$B by assuming the collinearity is reasonable.

Previous studies have shown that the cutoff radius (within which exchange parameters are calculated) affect the magnetization at higher temperatures [216]. In order to reduce the computational cost, in this Chapter only the exchange parameters within the nearest-neighbor approximation is calculated. The effect from longer-range exchange interactions is not included. For the Nd$_2$Fe$_{14}$B system, the nearest-neighbor exchange interactions dominate while the longer-range ones are less important. In the following it will show that the calculated macroscopic properties from this simplification are in line with the previous work [216] and the experimental report [15, 310, 311], without significant disparity. It should be noted that the micromagnetic exchange length is evaluated from the micromagnetic model in the framework of continuum theory without information from the atomistic spin at each atomic site. The micromagnetic exchange length governs the width of the transition between magnetic domains. In contrast, the exchange parameters describe the interaction between each pair of atomistic spins at specific atomic sites. They are in the framework of discrete picture in the atomistic spin scale. Thus, the micromagnetic exchange is not
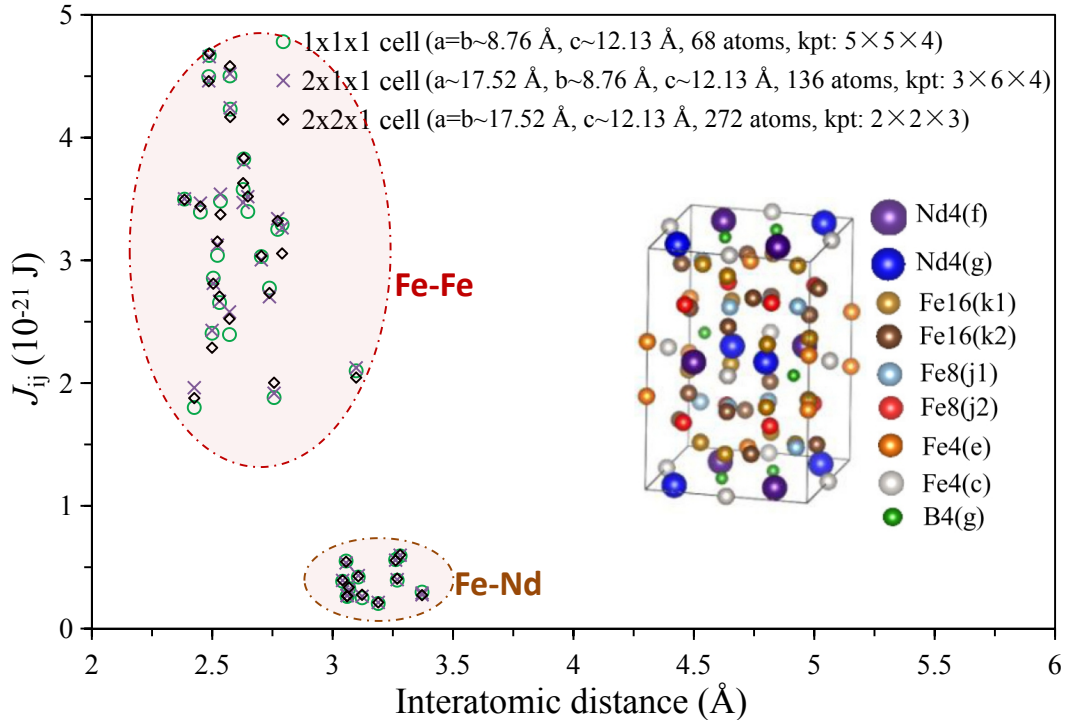
Figure 3.1: Exchange parameters J_{ij} as a function of interatomic distance, with the nearest neighbor considered. Inset: unit cell of Nd$_2$Fe$_{14}$B showing different kinds of crystallographically equivalent atoms. The results of $2 \times 1 \times 1$ and $2 \times 2 \times 1$ supercell are also presented to show the independence of J_{ij} on the calculated cell size. kpt: K points.
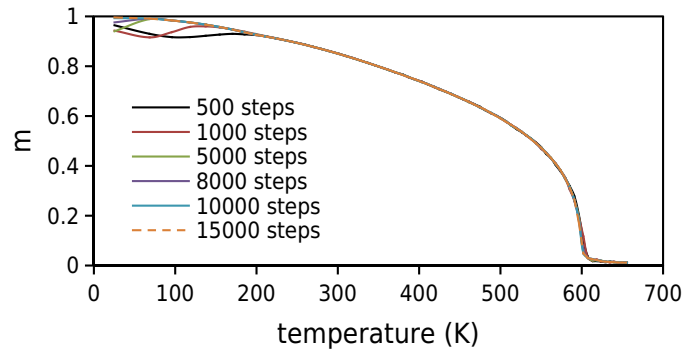
Figure 3.2: Calculated m-temperature curves when different Monte Carlo steps for equilibration and averaging are used.

a direct indicator for the cutoff radius of the exchange interaction in the atomistic spin model.

After parameterization, the atomistic spin model in Equation 3.1 is implemented in VAMPIRE [204]. For calculating the Curie temperature and temperature-dependent magnetization, the Monte Carlo Metropolis method is adopted, using a sample with $10 \times 10 \times 10$ unit cells and periodic boundary conditions in all three directions. After performing 10,000 Monte Carlo steps at each temperature, the equilibrium properties of the system are calculated by averaging the magnetic moments over a further 10,000 steps. It should be noted that by performing calculations at different steps, the results are found to remain the same after Monte Carlo steps exceed 10,000, as shown the dependence of magnetization-temperature curves on Monte Carlo steps in Figure 3.2. For the calculation of effective magnetic anisotropy constants at different temperatures, the constrained Monte-Carlo method is applied [204, 236]. The direction of the global magnetization is constrained at a fixed polar angle (θ) while allow the individual spins to vary. In this way, the restoring torque acting on the magnetization can be calculated as a function of θ, from which the effective magnetic anisotropy constants can be obtained by data-fitting. When calculating domain wall width, the spin dynamics approach and the Heun integration scheme are utilized. A sharp Bloch-like domain wall (wall plane perpendicular to the x axis) in the middle of the sample with $N_x \times N_y \times N_z$ unit cells is set as the initial condition. The system with the demagnetizing field included further relaxes from this initial condition by 100,000 steps with a time step of 1 fs. The final domain configuration is determined by averaging the magnetic moment distribution of 100 states at 90.1, 90.2, 90.3, ..., 100 ps.

3.3 Curie temperature and saturation magnetization

The calculated temperature-dependent magnetization curve for $Nd_2Fe_{14}B$ is shown in Figure 3.3(a). For a classical spin model, the simulated magnetization can be related to temperature
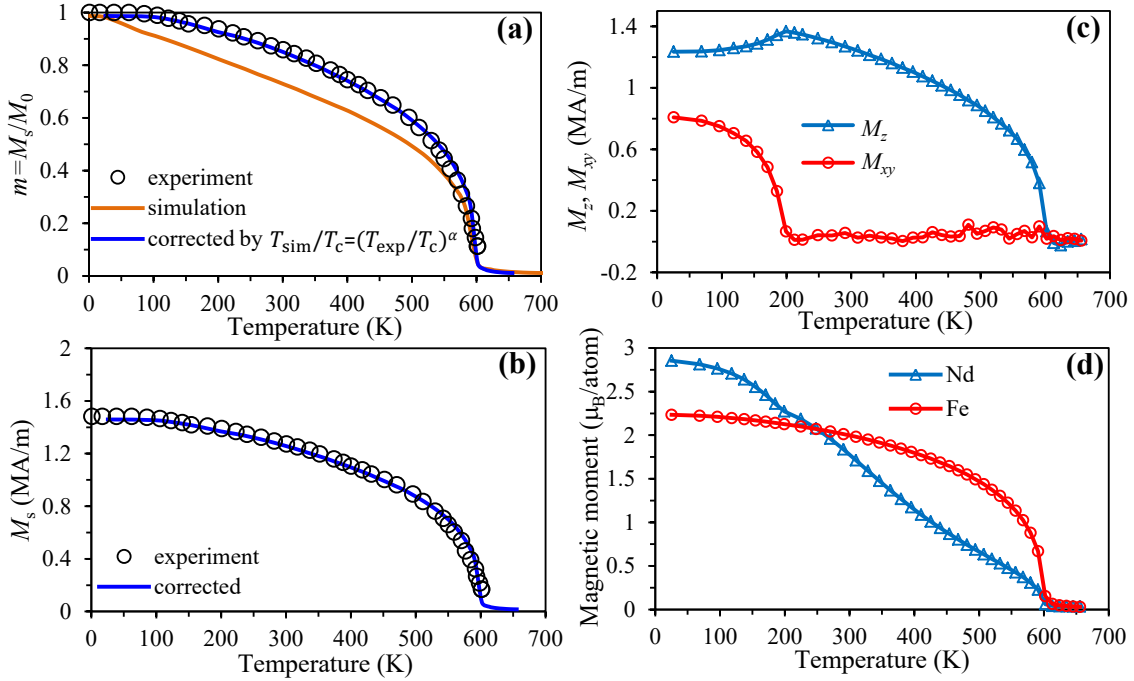
Figure 3.3: Temperature dependence of (a) (b) the magnetization amplitude, (c) the magnetization components M_z and M_{xy}, and (d) the magnetic moment per atom in Nd and Fe sublattices. The corrected curves are plotted by $\alpha = 1.802$. The experimental results are taken from [15].

through the function [204]

$$m = M_s(T)/M_0 = (1 - T/T_c)^\beta, \tag{3.5}$$

in which $M_s(T)$ is the temperature dependent saturation magnetization, M_0 denotes the saturation magnetization at zero temperature, T_c is the Curie temperature, and β is an exponent. Direct fitting the simulation data by Equation 3.5 yields $T_c = 602$ K and $\beta = 0.418$. The calculated T_c matches well with the experimental data [15].

However, it can be found from Figure 3.3(a) that only the simulation results around the Curie temperature agree with the experimental measurement. This disparity could be related to the following two aspects. Firstly, the exchange parameters could vary when temperature changes, as the case for Fe shown in [312]. At high temperatures, there may exist disordered local moment (DLM) state [313] and thus different exchange parameters and magnetization. However, the calculation of temperature dependent exchange parameters by first-principles methods is still challenging for the complicated $Nd_2Fe_{14}B$. Nevertheless, using the constant exchange parameters, the Curie temperature of $Nd_2Fe_{14}B$ is well predicted in Figure 3.3(a). Apart from the possible reason related to temperature or
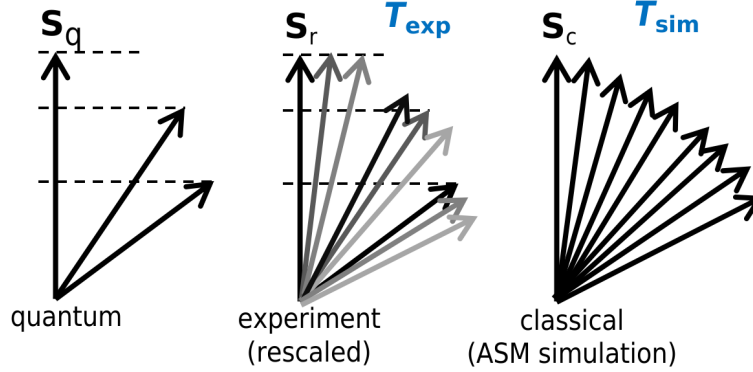
Figure 3.4: Illustration for the different behaviors among quantum, experimental, and classical atomistic spin model (ASM) simulation. For instance, one obtains $m_{\mathrm{c}} = \langle \mathbf{S}_{\mathrm{c}} \rangle$ at the ASM simulation temperature T_{sim}. However, this m_{c} corresponds to a higher experimental temperature T_{exp} ($T_{\mathrm{exp}} > T_{\mathrm{sim}}$); because the available states are less in experiments at the same T_{sim}, and only increasing temperature (i.e. $T_{\mathrm{exp}} > T_{\mathrm{sim}}$) favors more available states to achieve the same $m_{\mathrm{c}} = m_{\mathrm{r}} = \langle \mathbf{S}_{\mathrm{r}} \rangle$.

DLM-state dependent exchange parameters, the distinction between the quantum model and the classical model should also contribute to the deviation in Figure 3.3(a), as thoroughly discussed in [314] and illustrated in Figure 3.4.

Atomistic spin model is a classical model which considers localized classical atomic spins $\mathbf{S}_i = \mu_i \mathbf{s}_i$, where the spin operator $\mathbf{S}_i$ at each lattice site takes unrestricted values on the unit sphere surface $|\mathbf{s}_i| = 1$. In contrast, it is restricted to its particular eigenvalues in the quantum case. A direct consequence of the distinction between classical and quantum models manifests in the particular statistical properties of each approach. For example, in the limit of low temperatures, $m(T) = M(T)/M(0)$ can be calculated as $m = 1 - \rho(T)$, where $\rho(T)$ is the sum over the wave vector $\mathbf{k}$ of the spin-wave occupation number in the Brillouin zone [314, 315]. $\rho(T)$ at low temperatures for both quantum and classical statistics is well known [315]. For the classical statistics,

$$m_{\mathrm{classical}}(T) \approx 1 - \frac{1}{3}\frac{T}{T_{\mathrm{c}}} \tag{3.6}$$

in which T_{c} is the Curie temperature. In contrast, for the quantum statistics, one obtains

$$m_{\mathrm{quantum}} = 1 - \frac{1}{3}s\left(\frac{T}{T_{\mathrm{c}}}\right)^{\frac{3}{2}} \tag{3.7}$$

in which s is a slope factor. From Equations 3.6 and 3.7, one can see that even at low temperatures, $m(T)$ expression by the quantum model is different from that by the classical

model.

In short, atomistic spin model is a classical model which considers localized classical atomistic spins with unrestricted and continuous values. In contrast, the experimental measurement spontaneously includes the manifestation of a quantum system which only allows particular eigenvalues. It indicates more available states in the classical model than in experiments, as illustrated in Figure 3.4. The macroscopic magnetization obtained at simulation temperature T_{sim} should be achieved at higher temperature T_{exp} in experiments. For this reason, there should be a mapping between T_{sim} and T_{exp}. Here the temperature rescaling method is adopted to determine this mapping, as proposed in the previous work [314]. The (internal) simulation temperature T_{sim} is rescaled so that the equilibrium magnetization at the input experimental (external) temperature T_{exp} agrees with the experimental result, i.e.,

$$T_{sim}/T_c = \left(T_{exp}/T_c\right)^{\alpha}, \tag{3.8}$$

in which α is the rescaling parameter which can be fitted. The physical interpretation of the rescaling is that at low temperatures the allowed spin fluctuations in the classical limit are overestimated, and so this corresponds to a higher effective temperature than given in the simulation (i.e. $T_{exp} > T_{sim}$) [314]. The physical origin of α may be relate to the different availability of spin states in the classical atomistic spin model simulation and the experiment. However, it would be interesting to apply detailed first-principles calculations to delineate the origin. For detailed discussion on the temperature rescaling, the readers are referred to [314]. Applying the temperature rescaling Equation 3.8 to the simulation data and directly comparing the rescaled data with the experimental data, the parameter α is fitted as 1.802. After these operations, it can be seen in Figure 3.3(a) that the corrected simulation data show excellent agreement with the experimental one, and both can be described by the Curie–Bloch equation

$$m = M_s(T)/M_0 = [1 - (T/T_c)^{\alpha}]^{\beta} \tag{3.9}$$

with the fitted parameters $\alpha = 1.802$ and $\beta = 0.418$.

Calculating the total magnetic moments per volume, then the temperature dependent saturation magnetization $M_s(T)$ from the corrected simulation data is obtained. $M_s(T)$ agrees well with the experimental data [15], as shown in Figure 3.3(b). The spin reorientation phenomenon can also be captured by atomistic spin simulations, as shown in Figure 3.3(c). The simulated M_z in Figure 3.3(c) firstly increases and then decreases with the increasing temperature. By comparing M_z in Figure 3.3(c) to M_s in Figure 3.3(b), it can be estimated that the tilting angle of the magnetization direction away from the z-axis is around 32° at $T = 25$ K. The simulated spin reorientation temperature is around 180 K, higher than the experimental value around 150 K. This deviation may be related to the low quality of the temperature rescaling at low temperature. Nevertheless, the results on spin

reorientation are in line with the experimental observations [15, 198, 311]. Meanwhile, it can be seen from Figure 3.3(d) that as temperature increases, the magnetization of Nd sublattice decreases faster than that of Fe sublattice. This is due to the strong exchange coupling in Fe sublattice and indicates that Fe sublattice is responsible for the magnetic order.

3.4 Effective magnetic anisotropy

In order to determine the effective magnetic anisotropy constants, the system energy when the global magnetization is aligned along different directions have to be calculated. This can be done through the calculation of torque. In the constrained Monte Carlo scheme, the azimuthal angle is fixed at zero degree and the polar angle is gradually changed from 0 to 90 degree, i.e., the global magnetization is rotated in the z-x plane and only the torque component T_y is nonzero. The total internal torque T_y is calculated from the thermodynamic average and transferred into the energy per volume, as shown in Figure 3.5(a). It can be seen that at low temperature (e.g., 25 and 100 K) T_y is positive when θ is close to the the $z/[001]$ axis, indicating a spontaneous deviation of the global magnetization from the $z/[001]$ axis. This result is in line with the easy-cone type of anisotropy and the spin tilting away from $z/[001]$ axis (Figure 3.3(c)) at low temperature. At high temperature, T_y is always negative and thus there is a revert torque for driving the global magnetization towards the $z/[001]$ axis, implying an easy-axis type of anisotropy.

After obtaining the temperature dependent T_y, the free energy (F) of the magnetic system can be related to the work done by the torque acting on the whole system, i.e.,

$$F(\theta, T) = -\int_0^\theta T_y(\Theta, T)\mathrm{d}\Theta. \tag{3.10}$$

Integrating the data in Figure 3.5(a) through Equation 3.10 gives the free-energy curves in Figure 3.5(b). It can be seen that at 25 K, F shows a local minimum at $\theta \approx 32°$, reflecting the spin tilting away from $z/[001]$ axis. The effective magnetic anisotropy constants can be determined through the fitting of F curves by the phenomenological six-order formula

$$F(\theta, T) = K_1^{\mathrm{eff}}(T)\sin^2\theta + K_2^{\mathrm{eff}}(T)\sin^4\theta + K_3^{\mathrm{eff}}(T)\sin^6\theta, \tag{3.11}$$

in which K_1^{eff}, K_2^{eff}, and K_3^{eff} are the macroscopically effective second-, fourth-, and sixth-order anisotropy constants, respectively. The fitting results are presented in Figure 3.5(c) and compared to the experimental measurement [310]. It can be seen that below 150 K, K_1^{eff} is negative and both K_2^{eff} and K_3^{eff} play a critical role, agreeing with the cone-type anistropy of $Nd_2Fe_{14}B$ at low temperature. After 250 K, K_1^{eff} dominates and K_2^{eff} and K_3^{eff} are relatively small. At 300 K, our calculated results are: $K_1^{\mathrm{eff}} = 4.26$ MJ/m^3, $K_2^{\mathrm{eff}} = 0.15$ MJ/m^3, and $K_3^{\mathrm{eff}} = -0.10$ MJ/m^3. At higher temperature, K_2^{eff} and K_3^{eff} almost vanish.
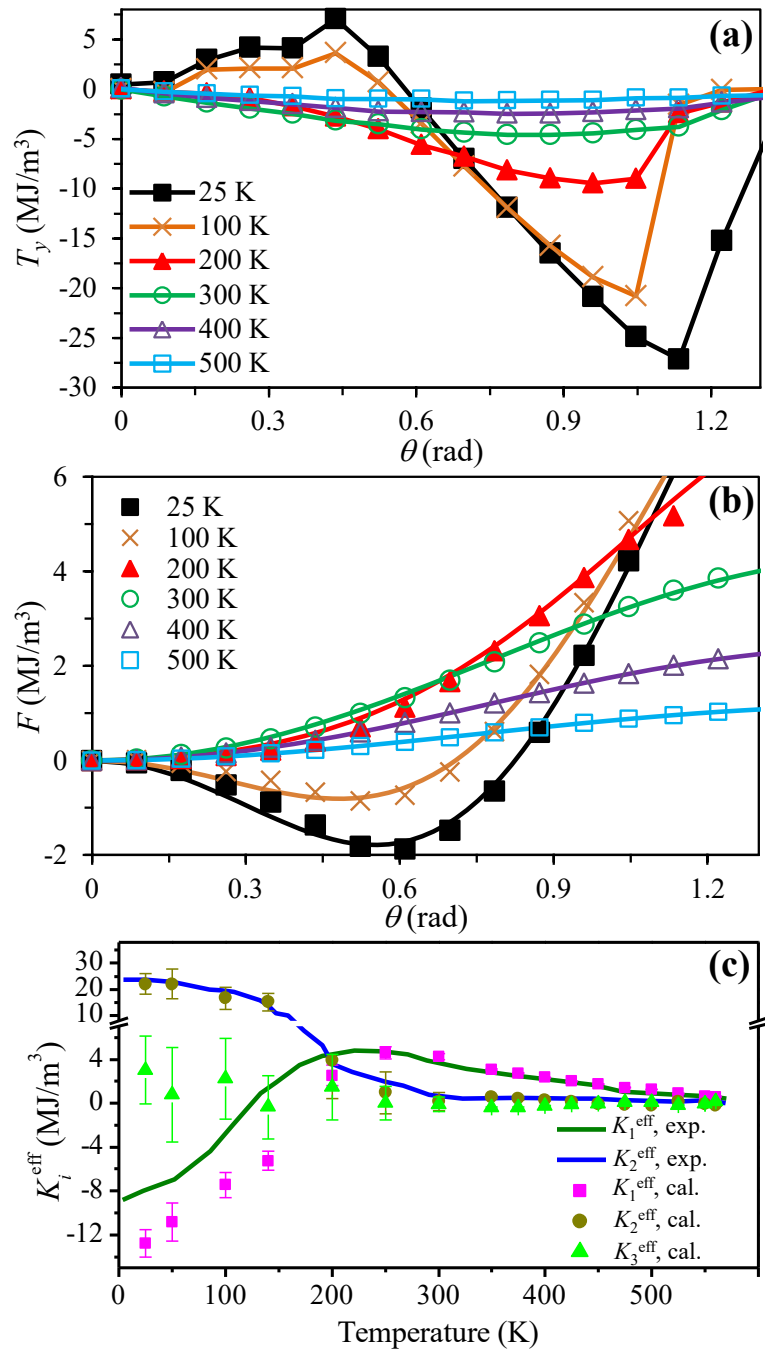
Figure 3.5: (a) Internal torque density $T_y(\theta)$ and (b) free energy density $F(\theta)$ at different temperatures. (c) Temperature dependent experimental and calculated effective magnetic anisotropy constants K_i^{eff} ($i = 1,\ 2,\ 3$).
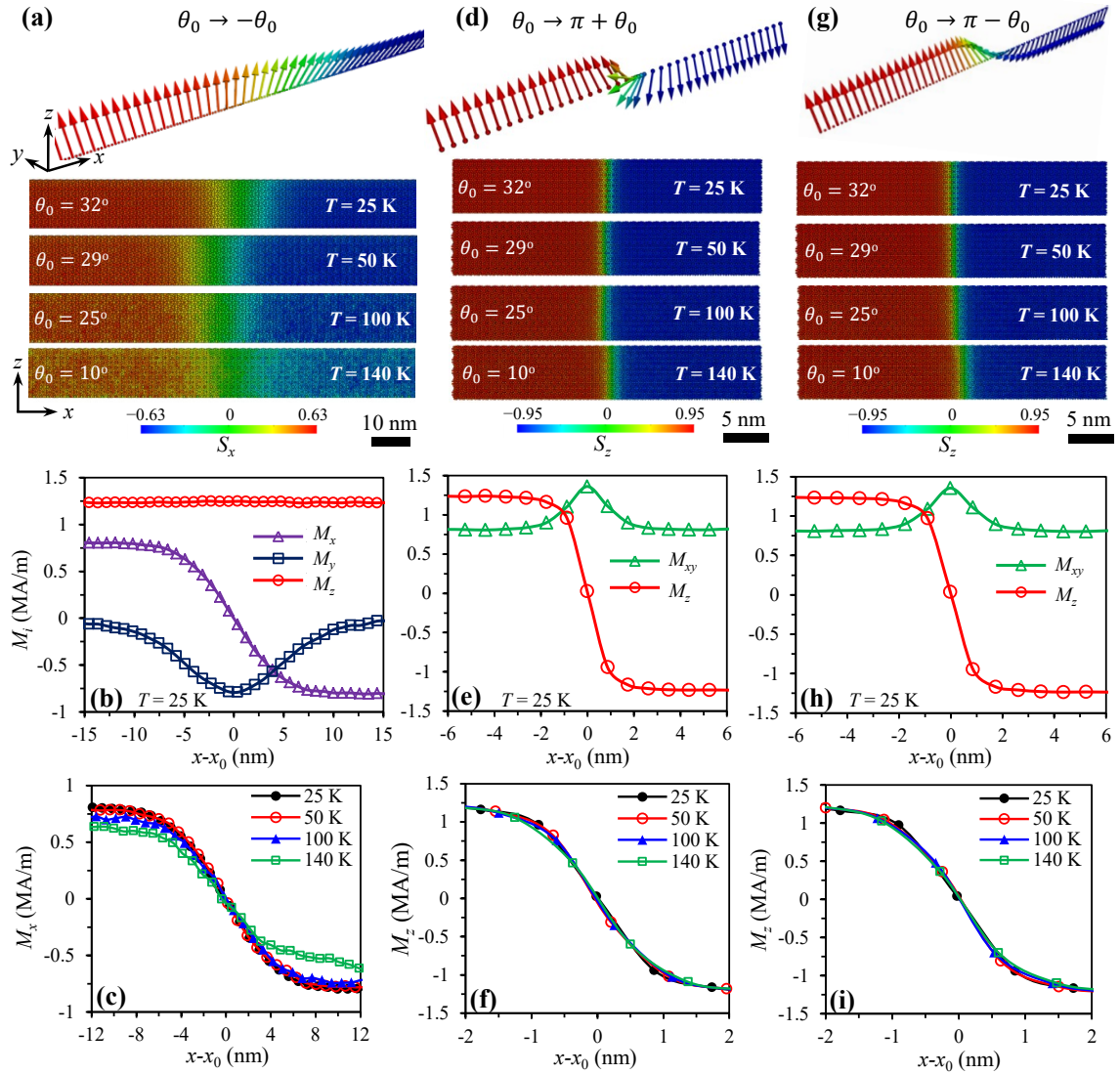
Figure 3.6: (a) (d) (g) Three types of possible low-temperature (easy axis tilted from z-axis with angle θ_0) domain wall configuration displayed by the distribution of atomistic magnetic moments. The distribution of macroscopic magnetization components along x axis in the case of (b) (c) domain wall $\theta_0 \to -\theta_0$, (e) (f) domain wall $\theta_0 \to \pi + \theta_0$, and (h) (i) domain wall $\theta_0 \to \pi - \theta_0$.

The calculated temperature dependence of K_i^{eff} in Figure 3.5(c) agrees reasonably with the previous experimental measurement [15, 310, 316] and theoretical calculations [216, 274].

3.5 Domain wall configurations

Due to the different anisotropy types at low temperature (cone-type anisotropy) and high temperature (easy-axis anisotropy) in $Nd_2Fe_{14}B$, the domain wall will also be distinct. At temperatures lower than the spin reorientation temperature, a number of possible variants of domain-wall types have been observed due to the cone-type anisotropy [317, 318]. For hard materials (Nd-Fe-B permanent magnets here) with dominant magnetocrystalline anisotropy, the typical domain wall profile is of the Bloch type, i.e. the magnetization is parallel to the easy axis (z or c axis for $Nd_2Fe_{14}B$) in the two domains separated by a domain
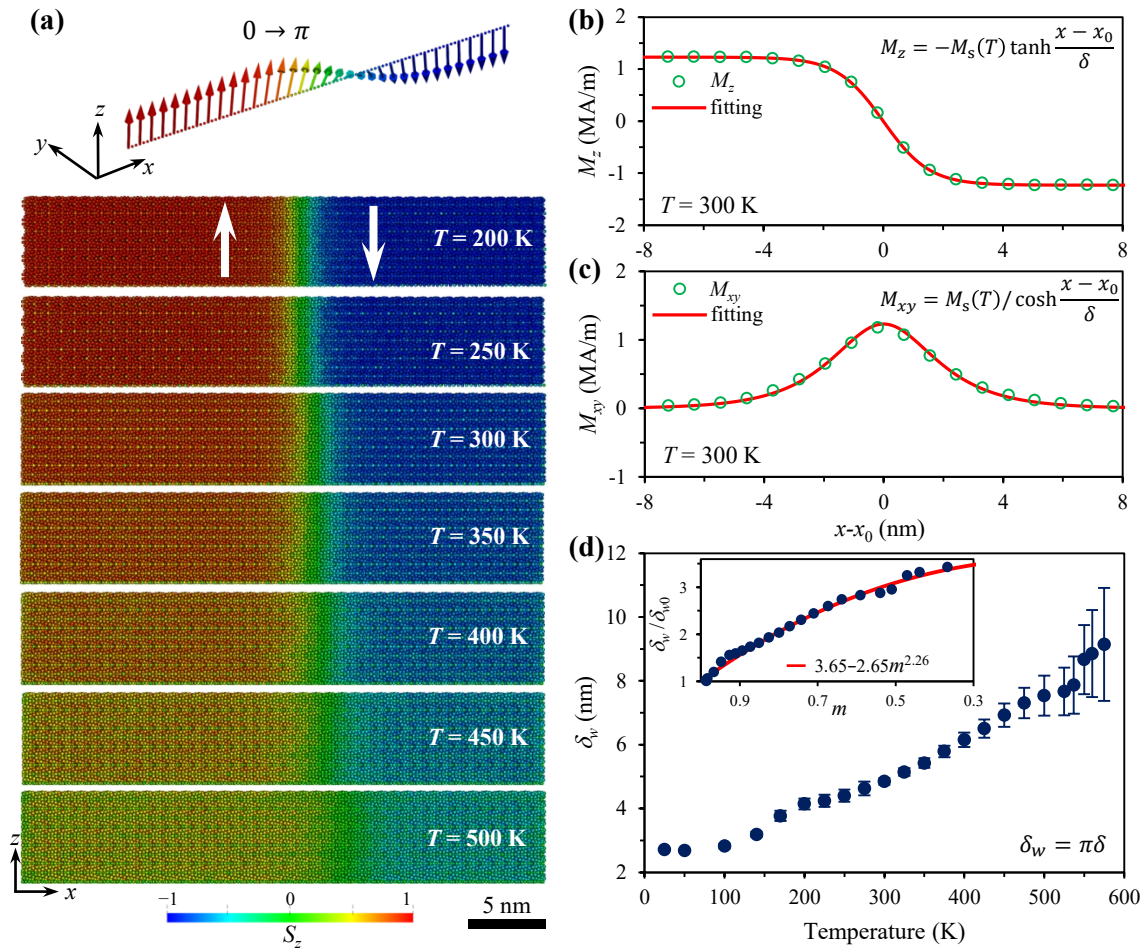
Figure 3.7: (a) High-temperature (easy axis along z-axis) domain wall configuration displayed by the distribution of atomistic magnetic moments. Macroscopic (b) M_z and (c) M_{xy} distribution along x axis at $T = 300$ K. (d) Domain wall width δ_w at different temperatures. Inset in (d): δ_w scaling with magnetization as a function of $m^{2.92}$. δ_{w0} is the wall width at zero temperature.

wall perpendicular to x (a) axis. Hence, the Bloch-like domain walls are studied, with the wall plane perpendicular to x axis, as shown in Figures 3.6 and 3.7. Three types of Bloch-like domain walls at low temperatures in Figure 3.6 are considered. More complicated domain walls with the wall plane perpendicular to different crystallographic axes will be investigated in our next work. The three wall modes are described as the polar angle changing from θ_0 to $-\theta_0$ in Figure 3.6(a), θ_0 to $\pi + \theta_0$ in Figure 3.6(d), and θ_0 to $\pi - \theta_0$ in Figure 3.6(g), with the angle through the wall as $2\theta_0$, π, and $\pi - 2\theta_0$, respectively. At temperatures higher than the spin reorientation temperature, the $180°$ Bloch-like domain wall with the polar angle changing from 0 to π is considered, as shown in Figure 3.7(a).

For calculating the domain wall, the magnetic moment direction is set in the $y - z$ plane with a polar angle as θ_0 (i.e. tilting angle) and $-\theta_0$ (or $\pi \pm \theta_0$) in the upward and downward domain, respectively. The system is then relaxed to attain the distribution of magnetic moments around the domain wall, as shown in Figure 3.6(a)(d)(g) and Figure 3.7(a). It can be seen that at low temperature (e.g. below 200 K) the magnetic moments are uniformly distributed within the domain, and a clear transition of magnetic moment distribution from the domain wall to the domain is visually observable. In contrast, at higher temperatures (e.g. above 400 K), the effect of thermal fluctuations is stronger, so that there are some randomly distributed magnetic moments even in the domain and no obvious transition between the domain wall and domain can be intuitively identified.

In order to determine the domain wall width, the continuum description of domain wall or diffusive interface is utilized. For mapping the atomistic magnetic moments to the continuum magnetization, the simulation sample with $N_x \times N_y \times N_z = 40 \times 5 \times 5$ unit cells is divided into N_x parts along x axis. For the case of $2\theta_0$ domain wall in Figure 3.6(a), the wall is very wide and thus a simulation sample with $N_x \times N_y \times N_z = 120 \times 5 \times 5$ unit cells is used. Each part (with an index of l_x, $1 \leq l_x \leq N_x$) represents $1 \times 5 \times 5$ unit cells, with its x coordinate set in its center. The magnetization of each part is calculated by dividing its total magnetic moments by its volume. In this way, the magnetization components $M_i(x)$ and $M_{jk}(x)$ are attained for each part l_x from the atomistic results in Figures 3.6 and 3.7, i.e.,

$$M_i(x) = \sum_{I \in l_x} \frac{\mu_I s_I^i}{V_{l_x}} \tag{3.12}$$

and

$$M_{jk}(x) = \sum_{I \in l_x} \frac{\mu_I \sqrt{(s_I^j)^2 + (s_I^k)^2}}{V_{l_x}} \tag{3.13}$$

at $x = 0.5 + (l_x - 1)a$, in which μ_I is the magnetic moment of atom I in the part l_x, s_I^i $(i = x, y, z)$ the spin direction components of atom I, V_{l_x} the volume of part l_x, and $a = 8.76$ Å the in-plane lattice parameter. Following the mapping in Equation 3.12, one obtains the scattered data to describe the domain wall configuration, as shown in Figures 3.6 and 3.7.

In the continuum model, the domain wall or diffusive interface can be described by the hyperbolic functions [171, 319, 320] through

$$M_i(x) = -M_{\mathrm{s}}(T) \tanh \frac{x - x_0}{\delta} \qquad (3.14)$$

or

$$M_{jk}(x) = M_{\mathrm{s}}(T) / \cosh \frac{x - x_0}{\delta}, \qquad (3.15)$$

in which x_0 is for shifting the domain wall to the center and δ is the parameter related to domain wall width δ_w by $\delta_w = \pi\delta$.

The domain wall profile at temperature lower than the spin reorientation temperature is presented in Figure 3.6. For the $2\theta_0$ domain wall in Figure 3.6(a), the domain wall width is quiet large. It can be found from Figure 3.6(b) and (c) that M_z does not change along x axis, whereas M_x can be described by Equation 3.14. So this wall does not satisfy the condition of constant normal component of the magnetization along the wall axis, i.e. not a Bloch-like wall. Moreover, the uniform M_z indicates constant magnetic anisotropy energy according to Equation 3.11 and thus the domain wall cannot exist; because the formation of domain wall is a result of the competition between variable exchange energy and magnetic anisotropy energy. One possible explanation for the wide domain wall in Figure 3.6(a) is that, the azimuthal angle also takes effects in the magnetic anisotropy energy and could contribute to the domain wall formation. The role of azimuthal angle in determining the easy direction of $Nd_2Fe_{14}B$ at low temperatures has also been addressed before [318]. However, in Equation 3.11 the azimuth-angle dependence is neglected, which has to be taken into account in the following work. Here the Bloch-like wall is the focus and no emphasis will be put on the wide domain wall in Figure 3.6(a) as well as its width. In contrast, the π and $\pi - 2\theta_0$ domain walls are Bloch-like and narrow, and M_z can be well described by Equation 3.14, as shown in Figure 3.6(e), (f), (h) and (i). The domain wall becomes slightly wider as the temperature increases from 25 K to 140 K. In addition, the wall profiles in π and $\pi - 2\theta_0$ domain walls are almost the same at a specific temperature. In the following, the wall profile in $\pi - 2\theta_0$ domain wall will be taken to calculate the domain wall width and exchange stiffness at low temperatures.

At temperatures higher than the spin reorientation temperature, 180 degree Bloch-like domain walls clearly form, as shown in Figure 3.7(a). Fitting the scattered data associated with the domain wall configuration by Equation 3.14 or 3.15 can give δ and thus the domain wall width. Typical fitting results at 300 K are presented in Figure 3.7(b) and (c), with $\delta = 1.55$ nm and $\delta_w = 4.87$ nm. It should be noted that at 300 K, the exchange stiffness A_{e} is often taken as 6.6–12 pJ/m [171, 310, 321] and K_1^{eff} as 4.2–4.5 MJ/m^3 [171, 310] in the literature, corresponding to an estimated $\delta_w = \pi(A_{\mathrm{e}}/K_1^{\mathrm{eff}})^{1/2}$ as 3.63–5.31 nm. Our calculated δ_w at 300 K falls well in the range of δ_w estimated from the literature. The measured δ_w by electron microscopy is more widely distributed, ranging from 1 to 10 nm
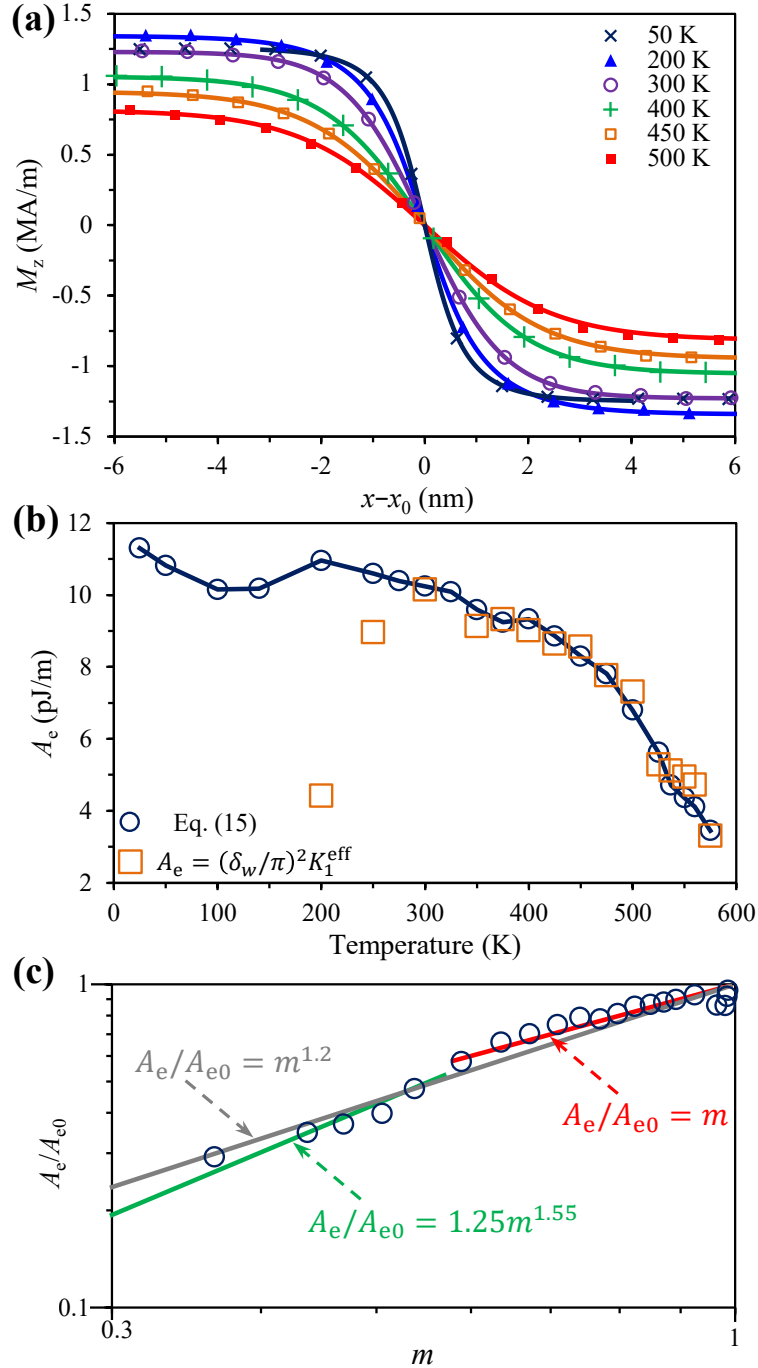
Figure 3.8: (a) M_z distribution along x axis at different temperatures. (b) Calculated temperature-dependent exchange stiffness. (c) Scaling behavior of the exchange stiffness, with the solid lines showing the scaling law with normalized magnetization. A_{e0} is the exchange stiffness at 0 K.

[322–324]. The calculated domain wall width at different temperatures are summarized in Figure 3.7(d). It can be found that domain wall becomes wider as the temperature increases, from $\delta_w = 2.72$ nm at 25 K to $\delta_w = 8.67$ nm at 550 K. The large standard deviation of δ_w at higher temperature is attributed to the stronger thermal fluctuations. These results are also consistent with the previous simulation results [299]. In addition, the dimensionless wall width δ_w/δ_{w0} (δ_{w0}: wall width at 0 K) can be fitted as a function of the power of dimensionless magnetization, i.e., δ_w/δ_{w0} linearly varies with $m^{2.26}$, as shown in the inset of Figure 3.7(d). This is different from the low-temperature power-law scaling behavior of $m^{-0.59}$ as found in cobalt [268], possibly due to the complicated and intrinsically different crystal structure of $Nd_2Fe_{14}B$.

3.6 Exchange stiffness

The determination of temperature-dependent exchange stiffness constant $A_e(T)$ is nontrivial. At 300 K, spin-wave dispersion measurements in Nd-Fe-B magnets reveal A_e as 6.6 pJ/m [321]. In the case of uniaxial anisotropy with positive K_1^{eff} and zero K_2^{eff} and K_3^{eff}, the domain wall width can be calculated as $\delta_w = \pi(A_e/K_1^{\text{eff}})^{1/2}$, from which A_e is estimated around 7–12 pJ/m at 300 K [171, 310]. However, when K_1^{eff} is negative or K_2^{eff} and K_3^{eff} cannot be neglected, e.g. at low temperatures, the expression $\delta_w = \pi(A_e/K_1^{\text{eff}})^{1/2}$ does not work. It should be mentioned that if all K_i^{eff} are taken into account, there is no analytic solution for the Bloch wall profile [320]. In the general case, the Bloch wall profile is governed by [320]

$$\mathrm{d}x = \mathrm{d}\theta\sqrt{A_e(T)/\left[F(\theta,T) - F(\theta_0,T)\right]} \tag{3.16}$$

and thus

$$x(\theta,T) = \sqrt{A_e(T)}\int_{\theta_0}^{\theta}\frac{\mathrm{d}\Theta}{\sqrt{F(\Theta,T) - F(\theta_0,T)}}, \tag{3.17}$$

in which $F(\theta,T)$ is taken from Equation 3.11.

Since x is a monotonic function of θ in Equation 3.17, there exists an inverse function $\theta(x,T)$. Therefore, after numerical integration of Equation 3.17 with various $A_e(T)$, a series of theoretical curves with x as a function of $M_z = M_s(T)\cos(\theta(x,T))$ are attained. Then $A_e(T)$ is optimized through the least-square method by comparing the simulation data to the theoretical curves. In Figure 3.8(a), both the simulation data points and the theoretical curves (solid lines) with the optimum $A_e(T)$ are plotted. It can be found that the theoretical curves by Equation 3.17 match well with the fitting results by Equation 3.14. But there is intrinsic difference, i.e., Equation 3.14 only gives domain wall width which can be used to estimate A_e indirectly through $\delta_w = \pi(A_e/K_1^{\text{eff}})^{1/2}$ when K_1^{eff} is positive, whereas Equation 3.17 directly gives A_e without the constraint on K_i^{eff}. The optimum $A_e(T)$ as a function of temperature is presented in Figure 3.8(b). It can be seen that $A_e = (\delta_w/\pi)^2 K_1^{\text{eff}}$ yields

reasonable results only above 300 K. In general, $A_{\mathrm{e}}(T)$ shows a decreasing trend as the temperature increases. Below the spin reorientation temperature, $A_{\mathrm{e}}(T)$ slowly decreases from 11.3 pJ/m at 25 K to 10.2 pJ/m at 140 K. After 200 K, $A_{\mathrm{e}}(T)$ decreases much faster, from 11 pJ/m at 200 K to 3.5 pJ/m at 575 K. $A_{\mathrm{e}} = 10.2$ pJ/m at 300 K is also consistent with the literature. However, A_{e} decreases more slowly than K_1^{eff} with increasing temperature. For instance, from 300 to 500 K, A_{e} is reduced by 34% while K_1^{eff} by 85%. This explains the wider domain wall at higher temperature in Figure 3.7(d).

The scaling behavior of $A_{\mathrm{e}}(T)$ is presented in Figure 3.8(c). It is found that at temperatures lower than 500 K, a scaling behavior $A_{\mathrm{e}}(T) \sim m$ exists. The power exponent of 1 for $\mathrm{Nd_2Fe_{14}B}$ is much lower than 2 in the mean-field approximation (MFA), 1.66 for a simple cubic lattice, and 1.76 for FePt [266]. At temperatures close to T_{c}, the high-temperature behavior deviates far away from this power scaling law. In addition, fitting the data after 500 K reveals that $A_{\mathrm{e}}(T)$ approximately follows the scaling law of $m^{1.55}$. Fitting all the data together with low quality gives a scaling law of $m^{1.2}$. The underlying physical reason of this distinct scaling behavior in $\mathrm{Nd_2Fe_{14}B}$ has to be uncovered theoretically in the near future. It should be mentioned that the classical spectral density method has been attempted towards a deep theoretical understanding of the scaling behavior of exchange stiffness for simple cubic, body-centered cubic, and face-centered cubic systems [266, 325], but its application to the complex rare-earth based $\mathrm{Nd_2Fe_{14}B}$ system remains to be further explored.

3.7 Summary

In summary, *ab-initio* informed atomistic spin model simulations have been carried out to predict the temperature-dependent intrinsic properties of $\mathrm{Nd_2Fe_{14}B}$ permanent magnets. The results are relevant for temperature-dependent micromagnetic simulations of Nd-Fe-B magnets. The main conclusions are summarized as follows.

(1) The Hamiltonian of the atomistic spin model for $\mathrm{Nd_2Fe_{14}B}$ includes contributions from the Heisenberg exchange of Fe-Fe and Fe-Nd atomic pairs, the uniaxial single-ion anisotropy energy of Fe atoms, and the crystal-field energy of Nd ions. Specially, the crystal-field Hamiltonian of Nd ions are approximately expanded into an energy formula featured by second, fourth, and sixth-order phenomenological anisotropy constants.

(2) Monte Carlo simulations of the atomistic spin model readily capture the Curie temperature T_{c} of $\mathrm{Nd_2Fe_{14}B}$. After applying the temperature rescaling strategy and the fitted rescaling parameter $\alpha = 1.802$, it is shown that the calculated temperature dependence of saturation magnetization $M_{\mathrm{s}}(T)$ agrees well with the experimental results, and the spin reorientation phenomenon at low temperature is well predicted.

(3) Constrained Monte Carlo simulations give the temperature-dependent total internal torque, from which the macroscopically effective second-, fourth-, and sixth-order anisotropy constants are calculated, which match well with the experimental measurements. The cal-

culated values at 300 K shows good consistency with literature reports, with K_1^{eff}, K_2^{eff}, and K_3^{eff} as 4.26, 0.15, and -0.10 MJ/m^3, respectively.

(4) Mapping the atomistic magnetic moments to the continuum magnetization leads to the domain wall profile, which can be further fitted by hyperbolic functions to evaluate the domain wall width δ_w. Different domain wall configurations at low temperatures are identified. The calculated δ_w and its variance increases with temperature, and its value at 300 K is consistent with experimental observation. δ_w is found to scale with magnetization as a function of $m^{2.26}$.

(5) By using a general continuum formula with the exchange stiffness constant $A_e(T)$ as a parameter to describe the domain wall profile, $A_e(T)$ is readily determined. A_e is found to decrease more slowly than K_1^{eff} with increasing temperature. The scaling behavior of the exchange stiffness with the normalized magnetization is found to be $A_e(T) \sim m$ at temperatures below 500 K and $A_e(T) \sim m^{1.55}$ at temperatures close to T_c.

4 Anisotropic exchange stiffness and interface exchange coupling in Nd-Fe-B permanent magnets by multiscale simulations

4.1 Introduction

High-coercivity permanent magnets are indisputably one of the critical materials indispensible for modern technologies in which electrical energy is converted to mechanical energy with a high efficiency, or *vice versa* [43, 326–328]. Among all the available permanent magnets, nowadays Nd-Fe-B (neodymium-iron-boron) is the most powerful and commercially important magnet. However, for certain applications such as hybrid/electric vehicles where the increased operating temperatures of 120-160 °C are common, the coercivity of sintered Nd-Fe-B magnets ($\sim$1.2 T) is too low. Improving the coercivity of Nd-Fe-B magnets without the usage of heavy rare earth elements (e.g., Dy and Tb) and without sacrificing remanence is still of great importance [23, 178, 297].

Coercivity is an extrinsic property. In Nd-Fe-B magnets, it is determined by the interplay of intrinsic magnetic properties of $Nd_2Fe_{14}B$ phase (the saturation magnetization M_s, magnetocrystalline anisotropy constant K_1, and the exchange stiffness A_e) and the microstructure including grain boundary (GB) and intergranular phases [23, 165, 178, 244, 297]. Microstructure engineering has been explored to design high-coercivity Nd-Fe-B magnets, e.g. optimizing the grain shape and reducing the grain size to decrease the local effective demagnetization factor N_{eff} [72–74, 156, 157], doping $Nd_2Fe_{14}B$ grain or its surface with Dy or Tb to increase the anisotropy field H_A [296, 329–331], deceasing M_s of GB to make $Nd_2Fe_{14}B$ grains exchange decoupled by GB diffusion [56, 160, 332], etc.

Based on the micromagnetic theory, the coercivity of Nd-Fe-B magnets can be tailored by controlling the distribution of three parameters, i.e., M_s, K_1, and A_e whose spatial variation represents the magnet microstructure. In contrast to the efforts on tuning N_{eff}, H_A, and GB M_s, the critical role of exchange (A_e) is not fully explored for sintered and hot-pressed magnets, in contrast to the situation of exchange-spring magnets [130, 333, 334]. The associated challenge is mainly attributed to the difficulty of measuring exchange

experimentally, including bulk exchange stiffness and interface exchange coupling strength, in Nd-Fe-B magnets. The experimental determination of M_s and K_1 is much easier [15, 310, 311, 335]. Even though the decrease of GB M_s to improve coercivity is qualitatively explained by the exchange decoupling [56, 160, 332], the underlying quantitative interface exchange behavior still remains to be explored.

The exchange is critical for designing high-performance Nd-Fe-B permanent magnets. A_e in $Nd_2Fe_{14}B$ phase is estimated as 7.7 pJ/m by using K_1 and the domain wall energy which is calculated from the measured M_s and domain width through the Bodenberger–Hubert formula [310]. This value is widely adopted and hardly questioned. As for the interface exchange, both first-principles calculations and experiments suggest that the exchange coupling is positive in $Nd_2Fe_{14}B(001)/\alpha$-Fe interface, while negative in $Nd_2Fe_{14}B(100)/\alpha$-Fe interface [336–339]. But the favorable and extremely thin (several nanometers) GB phase in sintered and hot-pressed Nd-Fe-B magnets is often amorphous, resulting in the local atomic arrangements different from α-Fe and thus possibly distinct interface exchange behavior. In addition, electron microscopic analysis has confirmed that GB composition is
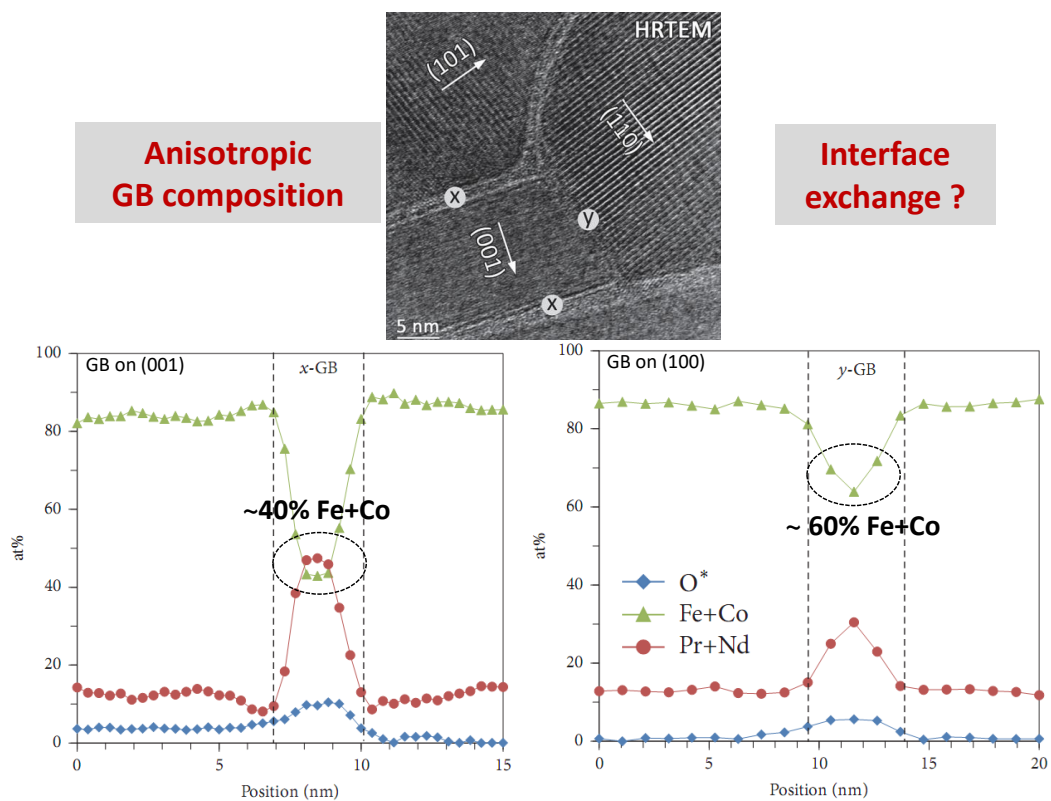
Figure 4.1: Transmission electron microscopy analysis shows the significant difference in the chemical composition (Fe+Co) of GB located at (001) surface and GB located at the surface perpendicular to (001) surface [246].

anisotropic, i.e., GB phase parallel to the c-plane contains lower concentration of Fe+Co than that perpendicular to the c-plane [45, 168, 246], as shown in Figure 4.1. This means the anisotropic GB composition depending on where the GB located. One would naturally raise the question that will the interface exchange coupling between $Nd_2Fe_{14}B$ main phase and GB also exhibit the similar anisotropic behavior ? However, whether and how the $Nd_2Fe_{14}B$/GB interface orientation and GB composition anisotropy will influence the interface exchange coupling is yet unknown quantitatively.

In this chapter, through first-principles calculations and atomistic spin model (ASM) simulations, the hitherto missing information is provided on the quantitative exchange anisotropy in Nd-Fe-B permanent magnets. Specifically, the strong anisotropy in the exchange stiffness of $Nd_2Fe_{14}B$ phase and the interface exchange coupling strength between $Nd_2Fe_{14}B$ and GB are demonstrated. The "double anisotropy" phenomenon related to GB is discovered. More exactly, in addition to the experimentally confirmed GB magnetization anisotropy, the $Nd_2Fe_{14}B$/GB interface exchange coupling is also anisotropic. In detail, ASM simulations of $Nd_2Fe_{14}B$ are performed to calculate the temperature dependent exchange stiffness along different crystallographic axes. Moreover, first-principles calculations are carried out to relax the $Nd_2Fe_{14}B$/GB interface structure and unravel the interface orientation dependent exchange coupling strength. The influence of exchange anisotropy on coercivity is revealed by micromagnetic simulations. More generally, these discoveries may enable more freedom in the design of Nd-Fe-B magnets by tuning exchange.

4.2 Multiscale methodology

The temperature dependent A_e of $Nd_2Fe_{14}B$ is evaluated through ASM simulation by using VAMPIRE [204] based on the atomistic spin Hamiltonian which is proposed and parameterized previously [216, 269, 299, 340, 341]. Detailed formulations for the ASM of $Nd_2Fe_{14}B$ are the same as in Section 3.2. The spin dynamics approach and the Heun integration scheme in VAMPIRE [204] is utilized to calculate the domain-wall width. A sharp Bloch-like domain wall (wall plane perpendicular to x axis) and Néel-like domain wall (wall plane perpendicular to z axis) in the middle of the sample with $N_x \times N_y \times N_z = 40 \times 5 \times 5$ and $N_x \times N_y \times N_z = 5 \times 5 \times 40$ unit cells is set as the initial condition, respectively. With the demagnetizing field included in the ASM simulations, the system is relaxed from this initial condition by 100,000 steps (time step: 1 fs). The final domain configuration is obtained by averaging the magnetic moment distribution of 100 states at 90.1, 90.2, 90.3, ... , 100 ps.

First-principles calculations were carried out by using VASP (Vienna *Ab-initio* Simulation Package). According to previous studies [162, 163, 197, 216, 337, 339], an open-core pseudopotential for Nd is used, with the $4f$ electrons in the core and not as valence electrons. The cutoff energy is set as 500 eV. Based on the energy convergence test, a $3 \times 3 \times 1$ and $1 \times 3 \times 2$ k-point mesh is used for $Nd_2Fe_{14}B(001)/Fe_xNd_{1-x}$ and $Nd_2Fe_{14}B(100)/Fe_xNd_{1-x}$,

respectively. For the relaxation of $Nd_2Fe_{14}B/Fe_xNd_{1-x}$, the convergence criteria for the maximum force on each atom and the total energy are 0.03 eV/Å and 0.05 meV, respectively. In the self-consistent calculations of the total energy, an energy convergence criteria of 0.01 meV is used.

Micromagnetic simulations are performed by using MuMax3 [250]. There are four kinds of energy considered in micromagnetics, which are exchange energy, anisotropy energy, Zeeman energy, demagnetization energy. The cell size is set as 1 nm, which is smaller than the exchange length and thus reasonable. The reversed curves are calculated by using the conjugate gradient method to find the energy minimum. The external field (H_{ex}) along z axis is applied as a stepwise field with a step of 0.01 T.
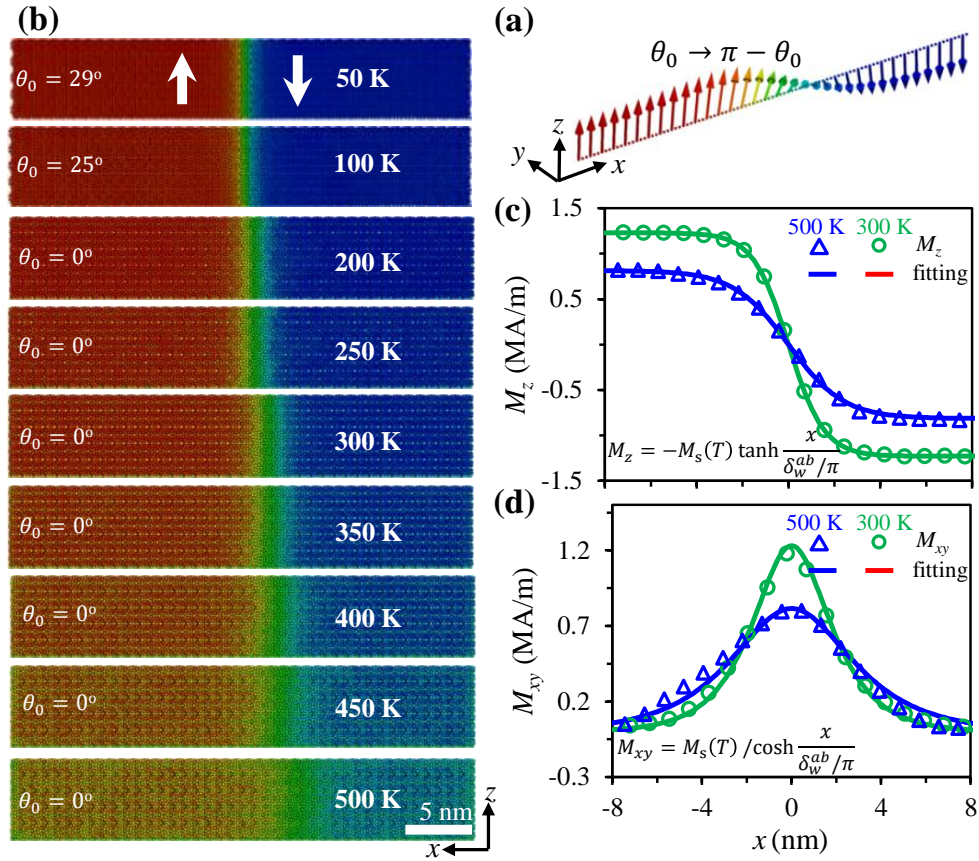
Figure 4.2: ASM simulated temperature-dependent Bloch-like domain wall. (a) Schematics of Bloch-like wall with easy axis tilted from z-axis with a angle θ_0. (b) Domain wall configurations displayed by the distribution of atomistic magnetic moments. Distribution of macroscopic magnetization components (c) M_z and (d) M_{xy} along x axis and their fitting by hyperbolic functions.
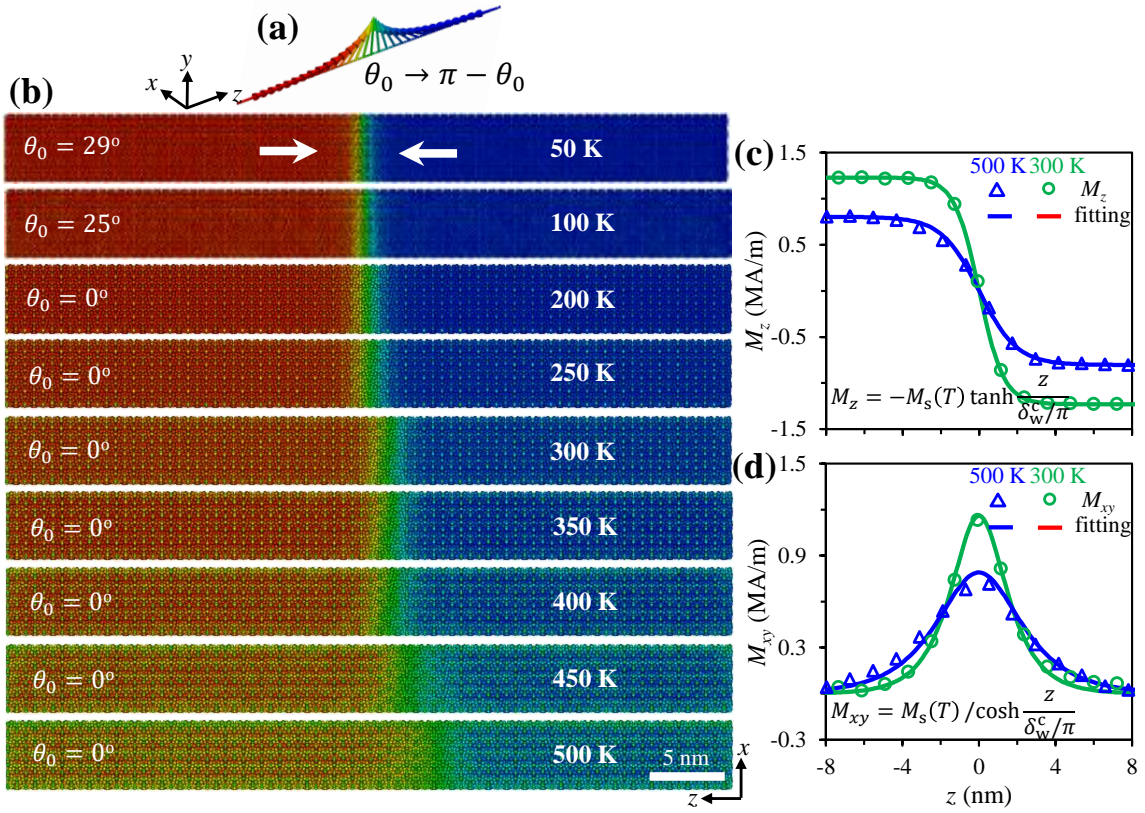
Figure 4.3: ASM simulated temperature-dependent Néel-like domain wall. (a) Schematics of Néel-like wall with easy axis tilted from z-axis with a angle θ_0. (b) Domain wall configurations displayed by the distribution of atomistic magnetic moments. Distribution of macroscopic magnetization components (c) M_z and (d) M_{xy} along z axis and their fitting by hyperbolic functions.

4.3 Anisotropic domain wall width and exchange stiffness in Nd$_2$Fe$_{14}$B

Since the exchange stiffness is highly related to the domain wall, the domain wall profile is firstly calculated. The ASM simulated Bloch- and Néel-like configurations at different temperatures are shown in Figures 4.2(b) and 4.3(b), respectively. Different from the previous work [269, 299], domain walls with the tilting angle θ_0 at low temperatures is also calculated. It is obvious that both walls become wider when the temperature increases. The atomistic magnetic moments in Figures 4.2(b) and 4.3(b) can be mapped to the continuum magnetization by hyperbolic functions [171]

$$M_z = -M_\text{s}(T)\tanh\frac{x}{\delta_\text{w}^i/\pi} \quad \text{or} \quad M_{xy} = M_\text{s}(T)/\cosh\frac{x}{\delta_\text{w}^i/\pi} \tag{4.1}$$
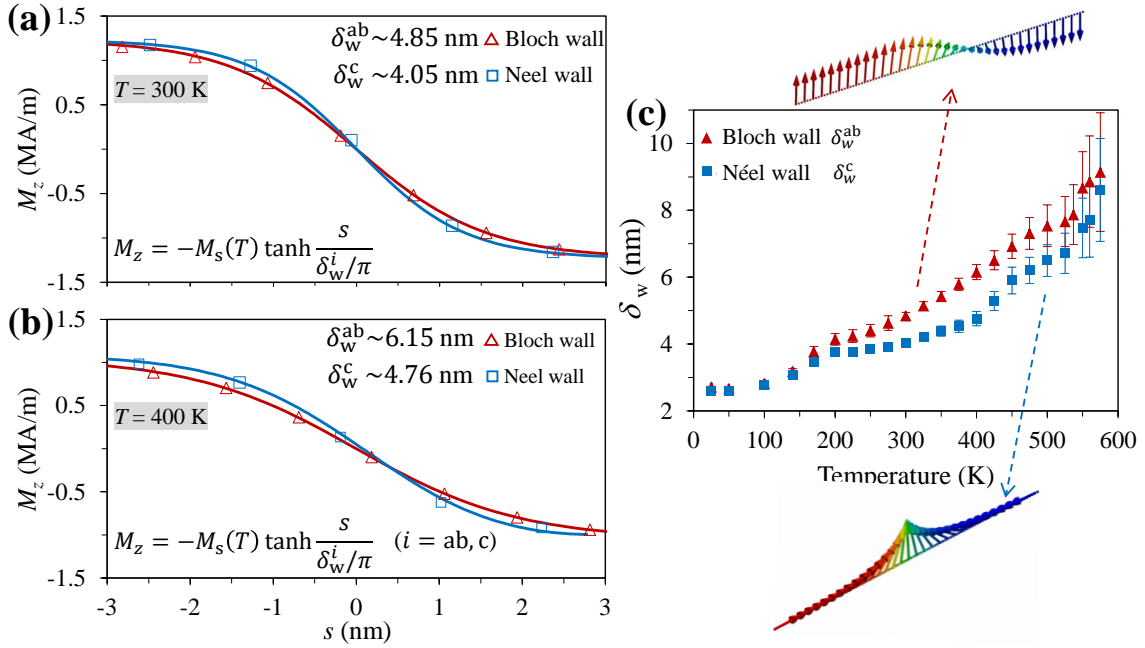
Figure 4.4: Distribution of macroscopic magnetization component (M_z) in Bloch and Néel walls at (a) 300 K and (b) 400 K. (c) Domain wall width δ_w^i at different temperatures.

in which $M_s(T)$ is the temperature dependent saturation magnetization, i denotes ab for Bloch wall and c for Néel wall, and δ_w^i is the domain wall width. The fitted domain wall configurations at 300 and 500 K are plotted in Figure 4.2(c)(d) for the Bloch wall and in Figure 4.3(c)(d) for the Néel wall. It is apparent that the fitting quality is quite well for both Bloch and Néel walls.

Figure 4.4(a) and (b) compares the Bloch and Néel wall configurations at 300 and 400 K. It is clear that the Bloch wall is much more diffusive than the Néel wall. For example, at 400 K δ_w^{ab} is approximately 6.15 nm, much larger than δ_w^c around 4.76 nm. With the fitting data from Figures 4.2(c)(d) and 4.3(c)(d), the temperature dependent domain wall width δ_w^i can be determined and summarized in Figure 4.4(c). It should be noted that at 300 K, the exchange stiffness A_e [171, 310, 321] and K_1 [171, 310] in the literature corresponds to an estimated $\delta_w^i = \pi\sqrt{A_e/K_1}$ as 3.63–5.31 nm. Our calculated δ_w^i at 300 K falls well in this range. It can be seen from Figure 4.4(c) that after the spin reorientation temperature around 150 K, both the Bloch wall width (δ_w^{ab}) and the Néel wall width (δ_w^c) increase with temperature. However, δ_w^{ab} is larger than δ_w^c, indicating the anisotropic nature of domain wall width in $Nd_2Fe_{14}B$.

According to the continuum micromagnetic theory [171], the domain wall profile is
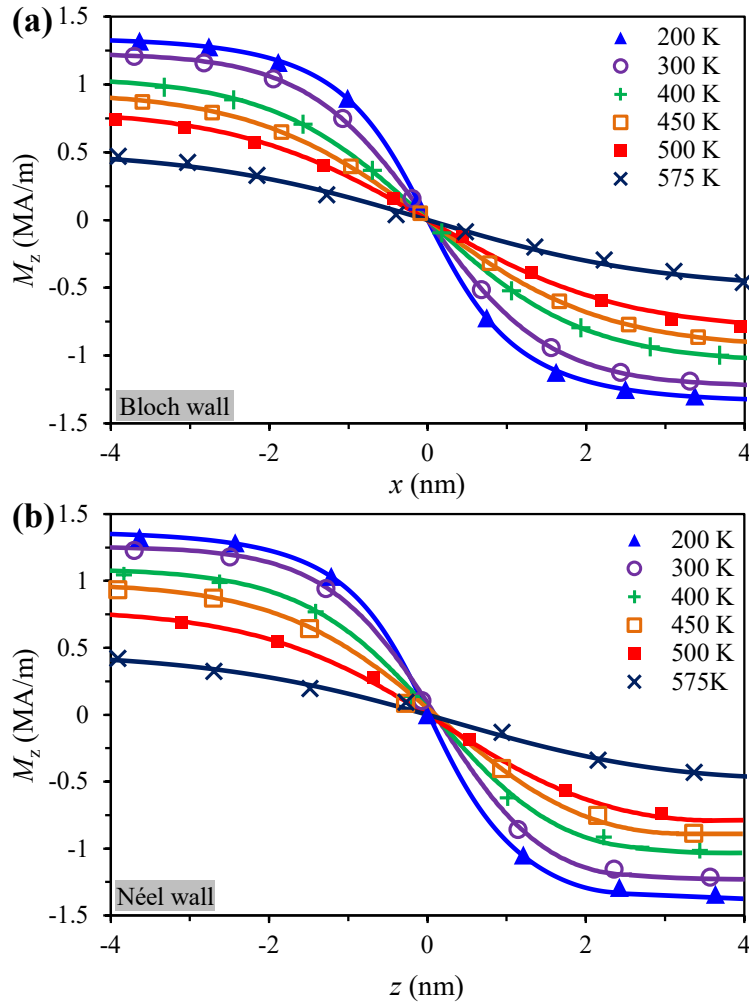
Figure 4.5: M_z distribution for (a) Bloch wall and (b) Néel wall at different temperatures. The scattered points are from ASM simulation results. The solid lines are calculated from Equations 4.2 and 4.3 by using the optimized A_{e} values.

generally governed by

$$x(\theta, T) = \sqrt{A_{\mathrm{e}}^{ab}(T)} \int_{\theta_0}^{\theta} [F(\Theta, T) - F(\theta_0, T)]^{-\frac{1}{2}} \, \mathrm{d}\Theta, \tag{4.2}$$

and

$$z(\theta, T) = \sqrt{A_{\mathrm{e}}^{c}(T)} \int_{\theta_0}^{\theta} [F(\Theta, T) - F(\theta_0, T) + 0.5\mu_0 M_s^2(T)(\cos\Theta - 1)\cos\Theta]^{-\frac{1}{2}} \mathrm{d}\Theta, \tag{4.3}$$
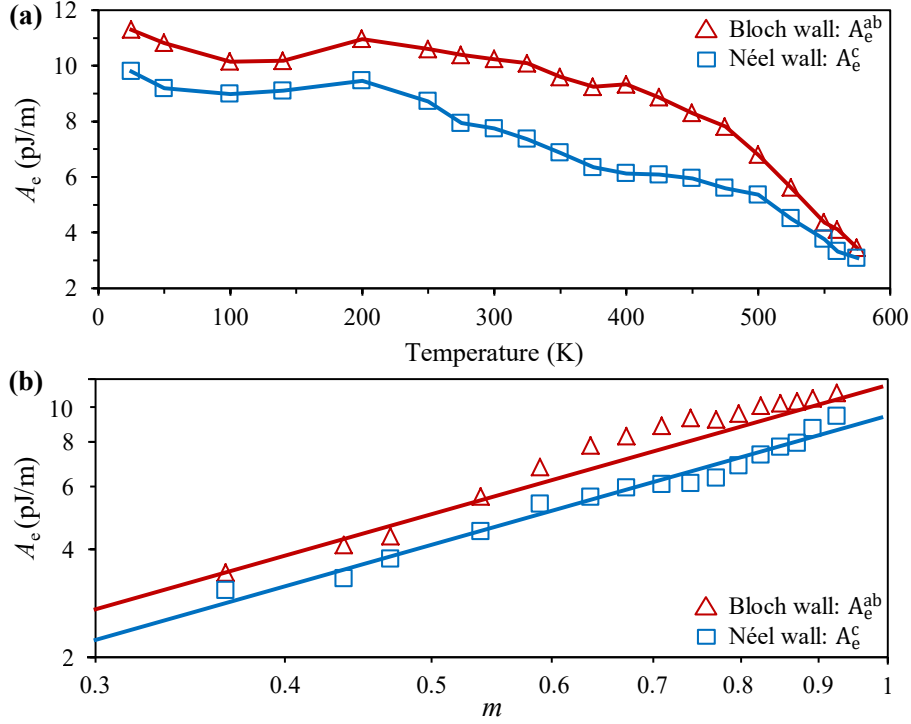
Figure 4.6: Exchange stiffness (A_e) of $Nd_2Fe_{14}B$ calculated by ASM simulation: A_e as a function of (a) temperature T and (b) normalized magnetization $m = M_s(T)/M_s(T=0)$. The fitting lines in (b) $\propto m^{1.2}$.

for Bloch walls and Néel walls, respectively. $F(\Theta, T)$ is the temperature dependent magnetocrystalline anisotropy energy as a function of the polar angle Θ. $M_s(T)$ is the temperature dependent saturation magnetization. Both $F(\Theta, T)$ and $M_s(T)$ have been determined previously [216, 340]. In Equation 4.3, the additional term regarding to M_s is originated from the demagnetization energy in the Néel wall. In most cases, there is no analytic solution for Equations 4.2 and 4.3. Since x and z are monotonic functions of θ in Equations 4.2 and 4.3, there exists an inverse function $\theta(x, T)$. Therefore, after numerical integration of Equations 4.2 and 4.3 with various $A_e^{ab}(T)$ or $A_e^c(T)$, a series of theoretical curves with s (s: x or z) as a function of $M_z = M_s(T) \cos(\theta(x, T))$ are obtained. Then $A_e^{ab}(T)$ and $A_e^c(T)$ are optimized through the least-square method by comparing the simulation data to the theoretical curves. In Figure 4.5, both the simulation data points and the theoretical curves (solid lines) with the optimum $A_e^{ab}(T)$ and $A_e^c(T)$ are plotted. The fitted curves coincide well with the scatter points from ASM simulations, indicating the method to determine A_e by least-square fitting of Equations 4.2 and 4.3 is reliable.

The calculated exchange stiffness is summarized in Figure 4.6(a). It is obvious that $A_e^{ab}(T)$ is higher than $A_e^c(T)$, indicating the anisotropic exchange stiffness in $Nd_2Fe_{14}B$ and

agreeing with the previous report [269]. This anisotropic A_e is intrinsically attributed to the tetragonal crystal structure of $Nd_2Fe_{14}B$. At 300 K, $A_e^{ab}(T)$ and $A_e^c(T)$ are estimated as 10.2 and 7.7 pJ/m, respectively. These values are in accordance with those used in micromagnetic simulations and experimentally determined ones [171, 310]. A_e is found to decrease much faster at higher temperatures. The scaling behavior of $A_e(T)$ with respect to the normalized magnetization m is presented in Figure 4.6(b). It is found that fitting the data gives a scaling law $A_e(T) \propto m^{1.2}$.

4.4 Anisotropic interface exchange coupling with grain boundary

Another important exchange-related phenomenon that has to be explored is the interface exchange coupling strength (J_{int}) between GB phase and $Nd_2Fe_{14}B$, which should play a critical role in the determination of coercivity of Nd-Fe-B magnets.

In this section, first-principles calculations are performed to estimate J_{int}. Following the experimental observation [52, 59, 168, 246, 342], Fe_xNd_{1-x} with different Fe content is taken as the model GB. The $Nd_2Fe_{14}B$/GB interface is set as (001) and (100) surface of $Nd_2Fe_{14}B$, as shown in Figure 4.7. Nd atoms in Fe_xNd_{1-x} are initially randomly distributed
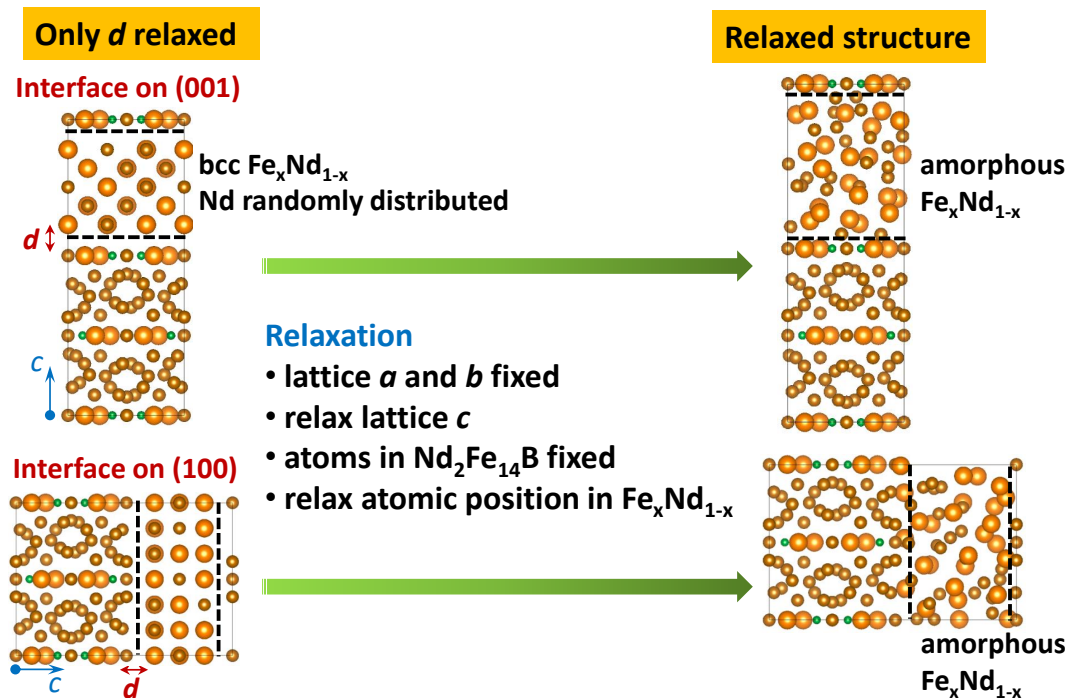
Figure 4.7: Illustrative procedures for the first-principles relaxation of $Nd_2Fe_{14}B$/GB interface structures with amorphous-like GB phase Fe_xNd_{1-x} with different contents of Fe.

$$J_{\text{int}} = \frac{E^{\text{AFM}} - E^{\text{FM}}}{2A}$$

AFM   FM
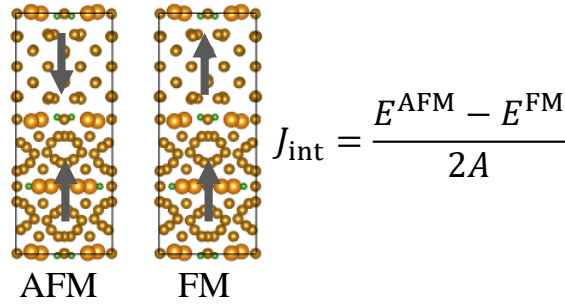
Figure 4.8: Illustration for the evaluation of interface exchange coupling strength J_{int}, with A as the interface area and E^{AFM} and E^{FM} as the total energy of the antiferromagnetic and ferromagnetic configuration, respectively.
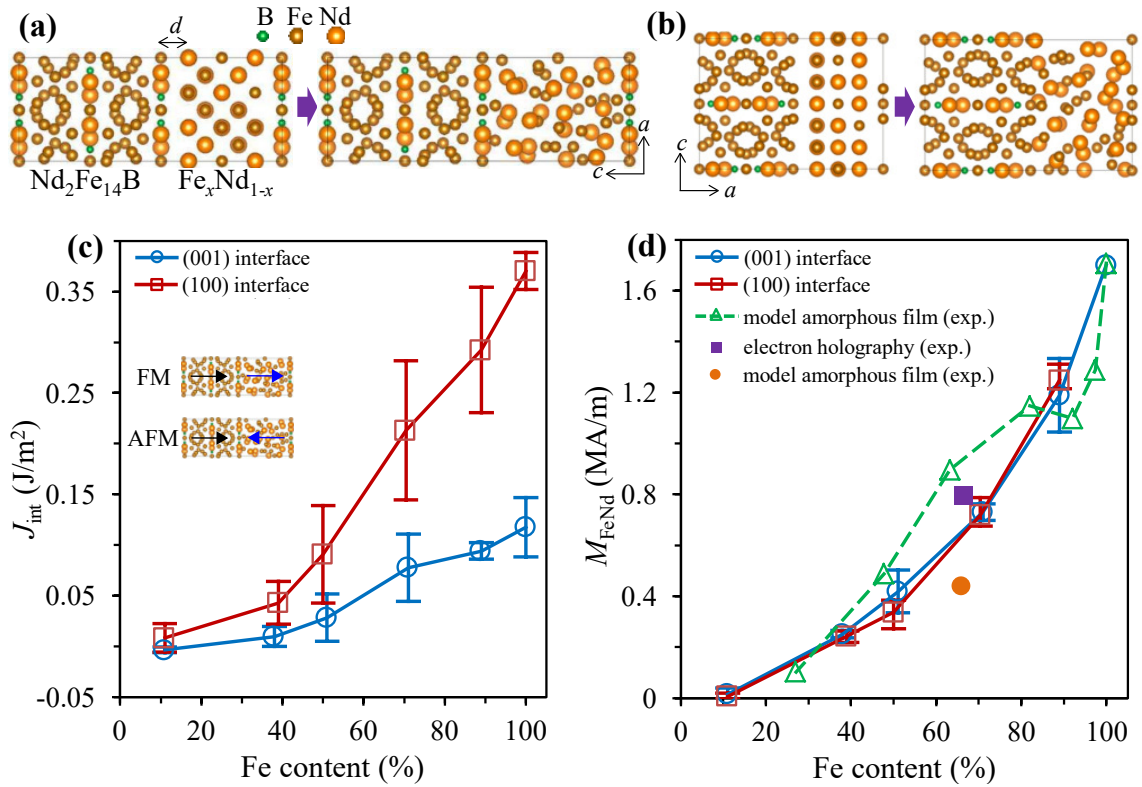
Figure 4.9: Interface exchange coupling strength (J_{int}) in $Nd_2Fe_{14}B$/GB evaluated by first-principles calculation. Unrelaxed and relaxed structure of $Nd_2Fe_{14}B$/Fe_xNd_{1-x} system with interface located at (a) (001) plane and (b) (100) plane. (c) J_{int} and (d) magnetization of Fe_xNd_{1-x} (M_{FeNd}) as a function of Fe content x for both (001) and (100) interfaces. The experimental data in (d) are taken from the literature [52, 59, 342].

in a bcc Fe structure. Five different random distributions are calculated and the associated results are averaged. The procedures for the first-principles relaxation of $Nd_2Fe_{14}B$/GB interface structures to obtain the amorphous-like GB phase Fe_xNd_{1-x} with different contents of Fe is illustrated in Figure 4.7. In detail, the system lattice parameters in the plane parallel to the interface, as well as the atom position and lattice parameters of $Nd_2Fe_{14}B$, is fixed. The structure of GB Fe_xNd_{1-x} is relaxed by two steps. Firstly, only the distance between $Nd_2Fe_{14}B$ and Fe_xNd_{1-x} is relaxed (d in Figure 4.9(a)). Then both the atomic position and the lattice parameter along the axis perpendicular to the interface are fully relaxed. The typical relaxed structure is shown in Figure 4.9(a) and (b). It can be seen that after relaxation, Fe_xNd_{1-x} becomes amorphous-like, in accordance with the experimental observation of thin amorphous GB in Nd-Fe-B magnets [45].

After obtaining the relaxed structure, J_{int} between $Nd_2Fe_{14}B$ and GB Fe_xNd_{1-x} is estimated by comparing the energy difference between the ferromagnetic (E^{FM}) and antiferromagnetic (E^{AFM}) configurations as illustrated in Figure 4.8, i.e., $J_{int} = (E^{AFM} - E^{FM})/2A$ with A as the interface area. The calculated J_{int} for both (001) and (100) interfaces is summarized in Figure 4.9(c). It is found that J_{int} is positive for both interfaces, indicating ferromagnetic coupling between GB Fe_xNd_{1-x} and $Nd_2Fe_{14}B$. It should be noted that in the case of (100) interface, if the GB phase is kept as α-Fe or not fully relaxed to be amorphous-like [336–339], J_{int} is negative and the antiferromagnetic coupling dominates. In contrast, our results here reveal that if GB is amorphous-like (i.e., the experimental case when GB is as thin as several nanometers), ferromagnetic coupling between $Nd_2Fe_{14}B$ and GB still remains for the (100) interface. Most importantly, even when the Fe content is the same, J_{int} is much higher for (100) interface than for (001) interface, indicating strong anisotropy in the interface exchange coupling.
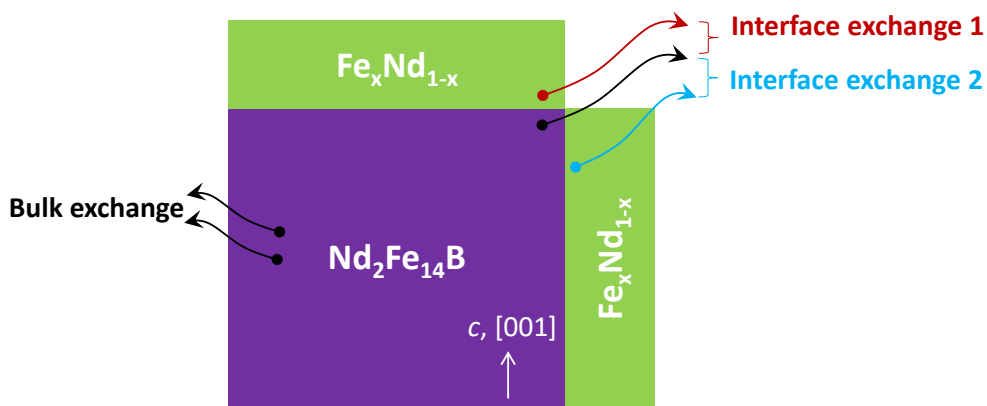
Figure 4.10: Illustration of different types of exchange coupling in micromagnetic simulations, including bulk exchange stiffness in $Nd_2Fe_{14}B$ and interface exchange between $Nd_2Fe_{14}B$ and GB located at different surfaces.

Previous experiments have confirmed that the Nd-containing GB in the (100) surface of $Nd_2Fe_{14}B$ grain contains much higher Fe (i.e., higher magnetization) than those in the (001) surface [45, 168, 246]. Therefore, if the anisotropy in GB magnetization is considered, J_{int} will be even more anisotropic due to the increasing J_{int} with Fe content. This GB/$Nd_2Fe_{14}B$ interface orientation induced "double anisotropy" (i.e., anisotropy in both magnetization and J_{int}) is expected to have a remarkable influence on the coercivity of Nd-Fe-B magnets. The magnetization of Fe_xNd_{1-x} GB phase (M_{FeNd}) as a function of Fe content is also calculated and shown in Figure 4.9(d). The calculated M_{FeNd} agrees well with the experimental reports [52, 59, 342]. It can be also seen that regardless of the interface orientation, M_{FeNd} only depends on the Fe content.

4.5 Influence of anisotropic exchange on coercivity

Different types of exchange coupling should affect the coercivity of Nd-Fe-B magnets. As illustrated in Figure 4.10, in terms of micromagnetic simulations, there exist bulk exchange stiffness A_e in the $Nd_2Fe_{14}B$ main phase and different interface exchange coupling between $Nd_2Fe_{14}B$ and FeNd GB phase located at different surfaces. Previous micromagnetic studies usually assume isotropic exchange stiffness in $Nd_2Fe_{14}B$ and isotropic interface exchange coupling strength.

In order to evaluate the influence of the above anisotropy (i.e., exchange anisotropy in A_e and J_{int}, and GB composition anisotropy) on the coercivity ($\mu_0 H_c$) of Nd-Fe-B magnets, micromagnetic simulations of model microstructures are further carried out by using MuMax3 [250], as shown in Figure 4.11. For the exchange anisotropy, the effective field due to the bulk exchange within the $Nd_2Fe_{14}B$ grain is reformulated (using a 6-neighbor small-angle approximation) as

$$\mathbf{B}_{exch}^{B} = 2\frac{A_e^{ab}}{M_s} \sum_{i \in a \, or \, b} \boldsymbol{\mathcal{M}}_i + 2\frac{A_e^{c}}{M_s} \sum_{i \in c} \boldsymbol{\mathcal{M}}_i, \tag{4.4}$$

in which $\boldsymbol{\mathcal{M}}_i = (\mathbf{m}_i - \mathbf{m})/\Delta_i^2$ with Δ_i as the mesh size along i direction, $\mathbf{m}$ as the magnetization unit vector of the current cell, and $\mathbf{m}_i$ as the magnetization unit vector of the neighbor cell along i direction. Similarly, the effective field (due to the exchange interaction between $Nd_2Fe_{14}B$ and GB) which is exerted on $Nd_2Fe_{14}B$ can be reformulated as

$$\mathbf{B}_{exch}^{Int} = 2\frac{A_{int}^{ab}}{M_s} \sum_{i \in a \, or \, b}^{\mathbf{m}_i \, in \, GB} \boldsymbol{\mathcal{M}}_i \text{ and } 2\frac{A_{int}^{c}}{M_s} \sum_{i \in c}^{\mathbf{m}_i \, in \, GB} \boldsymbol{\mathcal{M}}_i \tag{4.5}$$

for the (100) and (001) interface, respectively. A_{int} is the inter-region exchange parameter as defined in MuMax3 [250], which is an indicator of J_{int} in Figure 4.9(c). Since the current version of MuMax3 [250] does not have the functionality of doing micromagnetic simulations with anisotropic exchange constants, additional codes regarding to Equations
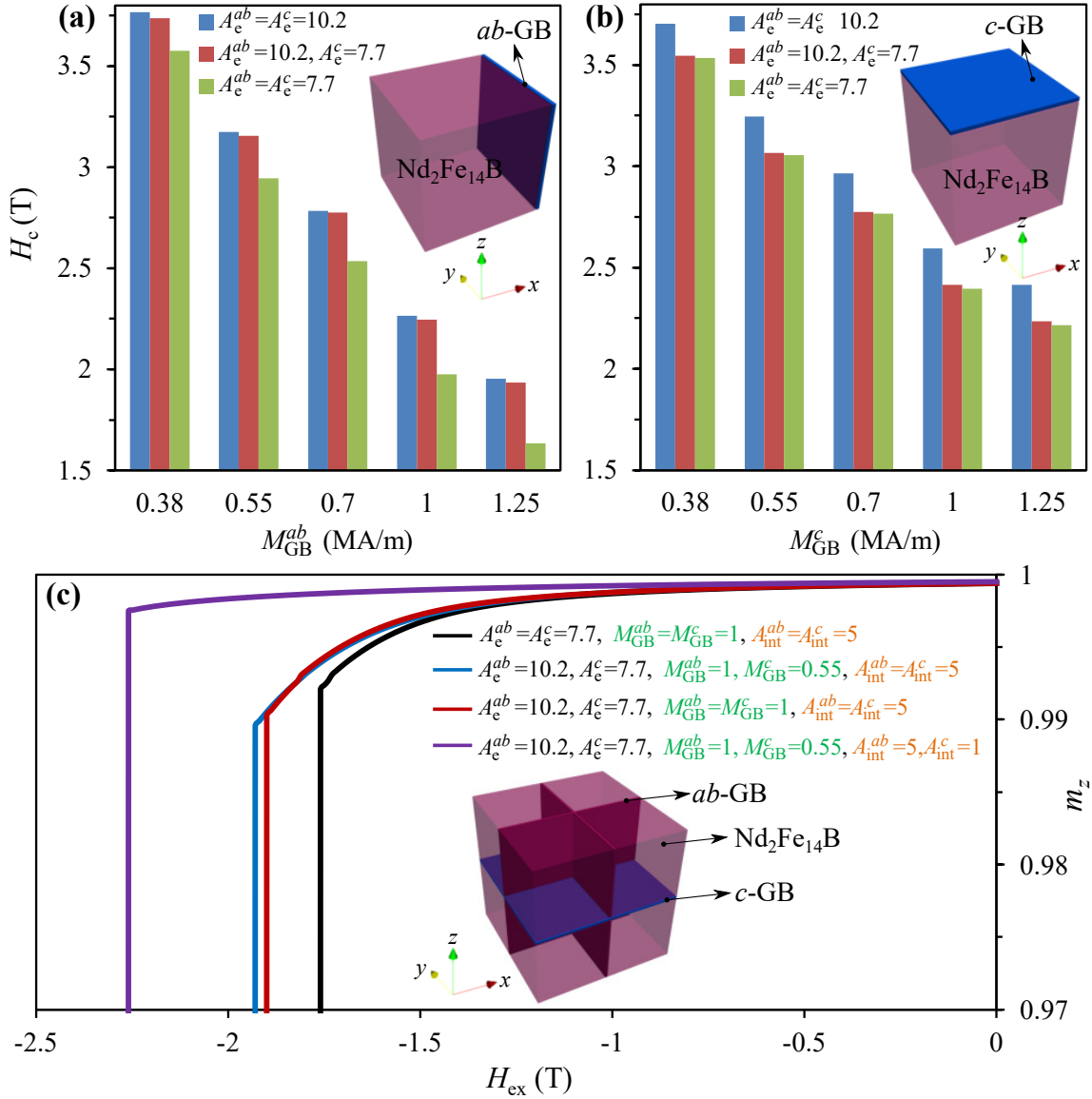
Figure 4.11: Dependency of coercivity on anisotropic exchange. Effect of anisotropic exchange stiffness of $Nd_2Fe_{14}B$ (A_e) in single grain with GB at (a) a surface and (b) c surface ($A_{int} = 5$ pJ/m). (c) Effect of A_e, GB composition anisotropy, and anisotropic exchange coupling between two regions (A_{int}) in multigrain Nd-Fe-B. A_e and A_{int}: pJ/m. M_{GB}: MA/m. Grain size: 100 nm. GB thickness: 4 nm. The external field in applied along z axis.

4.4 and 4.5 are written in the open-source MuMax3. The bulk exchange of GB phase is isotropic and estimated as $A_e^{GB} \sim \epsilon(\mu_0 M_{GB})^2$ with $\epsilon = 5.41$ pJm^{-1}T^{-2} [246].

The effect of anisotropic A_e in $Nd_2Fe_{14}B$ is explored in a single grain model with GB at different surfaces, as shown in Figure 4.11(a) and (b). It can be seen that for GB on the (100) interface, the anisotropic exchange $A_e^{ab} = 10.2$ pJ/m and $A_e^c = 7.7$ pJ/m results in much higher coercivity than the isotropic case $A_e = 7.7$ pJ/m. In contrast, for GB on the (001) surface, the anisotropic exchange leads to much lower coercivity than the isotropic case $A_e = 10.2$ pJ/m. These results indicate that the anisotropic exchange stiffness of $Nd_2Fe_{14}B$ has obvious influence on the coercivity, and the influence also depends on the $Nd_2Fe_{14}B$/GB interface orientation.

The determination of A_{int} in micromagnetics is nontrivial. In most literature on micromagnetic simulations of exchange-coupled behavior, A_{int} is chosen as the same as the bulk value, or is artificially tuned to study its influence. Skomski presented a continuum method to estimate the effective exchange between grains [130]. However, in the case of interface, the methodology for transferring first-principles results (J_{int}) to the continuum micromagnetic interface parameters (A_{int}) is unattainable at present. Here, A_{int} is assumed to be proportional to J_{int}, and its value along a or b axis is set as $A_{int}^{ab} = 5$ pJ/m for ab-GB with 80% Fe ($M_{GB}^{ab} = 1$ MA/m). The c-GB contains less Fe, i.e., 60% Fe ($M_{GB}^c = 0.55$ MA/m). According to J_{int} in Figure 4.9(c), A_{int}^c is estimated as one fifth of A_{int}^{ab}, i.e., 1 pJ/m. The influence of anisotropy in exchange (A_e and J_{int}) and GB composition on the coercivity in an 8-grain microstructure is summarized in Figure 4.11(c). It can be found that A_e anisotropy alone increases $\mu_0 H_c$ by 0.17 T when compared to the case of isotropic $A_e = 7.7$ pJ/m. GB anisotropy alone slightly improves $\mu_0 H_c$ by 0.03 T. When both the anisotropy in A_e and GB composition have been taken into account, the additional consideration of interface exchange anisotropy can remarkably enhance $\mu_0 H_c$ by 0.33 T. These results imply that the aforementioned exchange anisotropy has profound influence on the coercivity. It is thus necessary for the community of micromagnetic simulations to include these anisotropies in order to realize a reasonable design or prediction.

4.6 Summary

In short, the exchange anisotropy and its influence on the coercivity of Nd-Fe-B magnets have been identified by using multiscale simulations. The bulk exchange stiffness in $Nd_2Fe_{14}B$ phase is found to be intrinsically anisotropic (i.e., depend on the crystallographic axis) and its value along c axis is lower than along a/b axis.

The "double anisotropy" phenomenon regarding to GB is discovered, i.e., in addition to the experimentally determined anisotropy in GB composition or magnetization, the interface exchange coupling strength between $Nd_2Fe_{14}B$ and GB is also confirmed to be strongly anisotropic. Even when the GB Fe_xNd_{1-x} has the same composition, J_{int} for (100) interface is much higher than that for (001) interface. Due to this "double anisotropy", the ferromagnetic exchange coupling for (001) interface is much weaker than that for (100) interface.

The coercivity of Nd-Fe-B magnets is demonstrated to be obviously influenced by the exchange anisotropy, suggesting the necessity of including exchange anisotropy in order to realize a reasonable design or prediction by micromagnetic simulations.

Overall, these findings in this chapter not only provide comprehensive understanding of exchange in Nd-Fe-B magnets, but also are useful in deciphering coercivity mechanism and inspiring a strategy of tailoring exchange for the design of high-performance Nd-Fe-B permanent magnets.

5 High-temperature coercivity of Nd-Fe-B permanent magnets by multiscale simulations

5.1 Introduction

Nd-Fe-B permanent magnets are required to remain its functionality at high temperatures in many applications. For example, the operating temperature of Nd-Fe-B magnets can approach 350 K and 450 K in the wind turbines and motors inside electric/hybrid vehicles, respectively. Therefore, increasing thermal stability and understanding/predicting the temperature dependence of magnetic properties is of great significance in the design of Nd-Fe-B permanent magnets for the applications at high temperatures.

In order to increase the thermal stability of Nd-Fe-B permanent magnets, diverse methods have been attempted. The effects of the alloying elements Co, Dy, Al, Nb, Zr, Cu, Gd, etc. on the high-temperature properties of sintered Nd-Fe-B magnets have been explored [343, 344]. The most efficient way to increase thermal stability is the partial substitution of Nd with heavy rare earth (HRE) such as Dy and Tb [345, 346], since $(Nd,HRE)_2Fe_{14}B$ possesses a higher intrinsic anisotropy field. However, due to the limited supply and high cost of HRE, the community of permanent magnets makes great efforts to reduce the usage amount of HRE or totally remove HRE. In this aspect, hot deformation is shown to achieve an improved temperature coefficient of coercivity (β) in HRE-free Nd-Fe-B magnets, owing to the finer grains and thus smaller local demagnetization field [72]. Alternatively, grain boundary diffusion of Nd-Cu [45] and Pr-Cu alloys [80] in HRE-free Nd-Fe-B magnets also enhances β. However, for high-end applications such as electro-mobility where temperature can approach 450 K, the addition of HRE is still necessary. In order to reduce the HRE usage amount, HRE is not added to the main phase during the alloying step, but is diffused along the grain boundary of Nd-Fe-B magnets to form a thin HRE-rich hard shell around the main phase $Nd_2Fe_{14}B$ [53, 68, 160, 347]. Nevertheless, the tasks toward HRE-free Nd-Fe-B magnets with excellent performance at high temperatures have not yet been accomplished. .

Apart from the experimental efforts to enhance the high-temperature performance of Nd-Fe-B magnets, theoretical model and computational methodology are very helpful in

terms of reducing the research cost and accelerating the design process. Up to know, three modelling and simulation techniques are available for the theoretical and computational study of Nd-Fe-B magnets. First-principles calculations are important for the prediction of intrinsic magnetic parameters of $Nd_2Fe_{14}B$ phase and some subphases in Nd-Fe-B magnets at 0 K and the associated physical mechanism at electronic level [162, 163, 165, 195, 197, 295]. But it is still challenging to directly apply first-principles for the calculation of finite-temperature properties of Nd-Fe-B magnets. Recently atomistic spin model (ASM) have been utilized to calculate the temperature-dependent intrinsic parameters of $Nd_2Fe_{14}B$ by considering temperature effects via Langevin-like spin dynamics or Monte Carlo scheme [123, 204, 216, 224, 230, 231, 269, 298–300, 340]. In the analysis of the experimental hysteresis and the simulation of magnetic domain reversal and microstructural influences, micromagnetic model plays an important role and is already widely used [73, 74, 157, 166, 238, 244–246, 248, 253, 289, 296].

Based on the micromagentic nucleation model, the coercivity of Nd-Fe-B magnets is often expressed as: $H_c(T) = \alpha_k H_k(T) - N_{eff} M_s(T) - H_{th}(T)$ [150], where the coefficients α_k represents the microstructural influence on the anisotropy field and N_{eff} is related to the effect of the microstructure-sensitive local demagnetization factor. Efforts on tuning the microstructure such as grain boundary, hard shell, intergranular phase, and texture contribute to the increase of α_k [45, 53, 68, 73, 80, 160, 166, 238, 244–246, 296, 347, 348]. The work on grain size or shape is actually related to the tailoring of N_{eff} [69, 71–74, 157, 158, 349, 350]. $H_{th}(T)$ gives the reduction of coercivity by the temperature induced thermal fluctuations. It should be noted that this thermal fluctuation related to $H_{th}(T)$ is exerted on the macrospin or magnetization vector in terms of micromagnetic theory. Whereas, the thermal fluctuation in ASM is exerted on the atomistic spin. According to the above expression for $H_c(T)$, the temperature-dependent H_k, M_s, and H_{th} play a decisive role in the coercivity of Nd-Fe-B magnets at finite temperatures.

As mentioned above, experimental results or first-principles informed ASM provides a feasible way for calculating temperature-dependent H_k and M_s. But the application of ASM to permanent magnets, or more specifically rare-earth permanent magnets, is still in its infancy. For the estimation of H_{th} influence, micromagnetic simulations are indispensable and there are two different choices depending on how the temperature induced thermal fluctuations are taken into account. One choice is to compute the energy barrier as a function of the applied field by micromagnetic simulations without the consideration of thermal fluctuations. When the energy barrier equals to the thermal energy $25k_BT$, the corresponding external magnetic field is defined as the thermal coercivity at temperature T. For the calculation of energy barrier, the elastic band method [291, 351, 352] or the string method [292, 353–355] is often utilized. Recently, Schrefl *et al.* has applied this method to calculate the temperature dependent coercivity and thermal activation of magnetic reversal in Nd-Fe-B permanent magnets [238, 253, 289, 290]. The alternative choice for dealing

with the temperature influence and thermal activation in the magnetic reversal process is to add a stochastic term into the effective magnetic field in the Landau–Lifshitz (LL) equation, leading to the stochastic LL equation [227]. The strength of the stochastic term is related to temperature. Numerical implementation of the stochastic LL equation makes it possible to study the thermally activated magnetization reversal and the temperature influence on switching dynamics by micromagnetic simulations [356–361]. But its application to rare-earth permanent magnets is still rare.

From the viewpoint of modelling and simulation, no individual methodology is applicable for simultaneously calculating all the three terms H_k, M_s, and H_{th} at different temperatures to evaluate the temperature dependent coercivity of Nd-Fe-B magnets. To this end, in this chapter a multiscale scheme by combining ASM and micromagnetic simulations is proposed for the computational prediction of coercivity of Nd-Fe-B permanent magnets at high temperatures. Following the work in Chapter 3, the ASM Hamiltonian for $Nd_2Fe_{14}B$ is constructed and the temperature-dependent intrinsic material parameters of $Nd_2Fe_{14}B$ are calculated, including the saturated magnetization (M_s), the magnetocrystalline anisotropy (K_1), and the exchange stiffness constant (A_e). Taking the calculated $M_s(T)$, $K_1(T)$, and $A_e(T)$ as input, micromagnetic simulations based on the stochastic LL equation are performed to reveal the temperature influence on the coercivity of Nd-Fe-B magnets. The representative microstructural features including surface defect and Dy-rich hard shell are also explored to reveal their influences on the coercivity at high temperatures. The thermal fluctuations induced coercivity reduction, the thermal activation volume, the temperature coefficient of coercivity, and the role of Dy-containing hard shell are thoroughly discussed.

5.2 Simulation methodology

5.2.1 Atomistic spin model simulation

The atomistic spin model for calculating the temperature-dependent intrinsic magnetic parameters of $Nd_2Fe_{14}B$ and the associated simulation parameters and numerical schemes are the same as those in Section 3.2. The only difference is that here only the temperatures beyond 300 K are considered and then only the second-order magnetocrystalline anisotropy constant K_1 is calculated. Moreover, in contrast to the Section 3.2 that only calculates J_{ij} within the nearest neighbor for simplicity, here J_{ij} in both cases of nearest neighbor and 9-Å cutoff is calculated from a comparison, as shown in Figure 5.1. It can be found that beyond the nearest neighbor, the Fe–Nd exchange indeed almost vanishes, while the Fe–Fe exchange is small and oscillates. The long-range behavior of Fe–Fe exchange is also reported in [362]. In order to reduce computational costs, as a simplification, sometimes only the exchange parameters within the nearest neighbor is used, as also shown in Section 3.2. In the case here for $Nd_2Fe_{14}B$, it is shown in the following that the calculated intrinsic parameters from this simplification agree well with the experimental report (Figure 5.3)
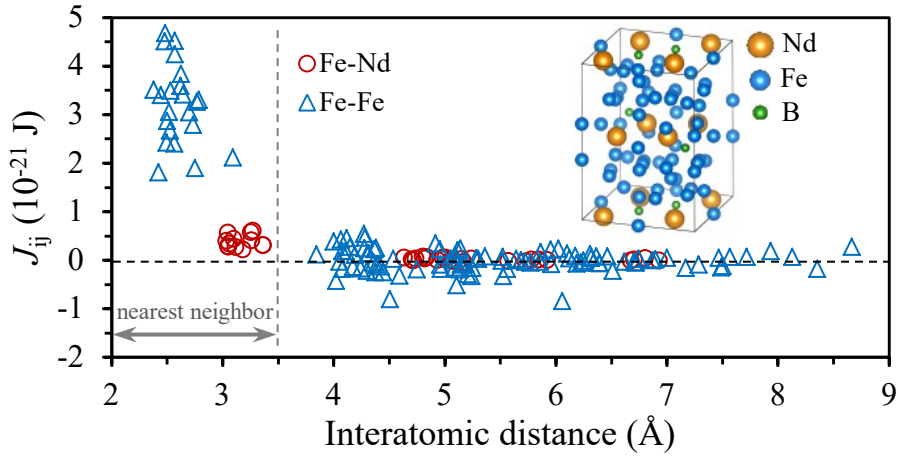
Figure 5.1: Exchange parameters J_{ij} as a function of interatomic distance, with the nearest-neighbor range marked. Inset: unit cell of $Nd_2Fe_{14}B$.

[15, 310, 311], and the disparity between using nearest-neighbor and 9-Å-cutoff J_{ij} is small (Figures 5.3 and 5.4).

5.2.2 Micromagnetic simulation

In contrast to the ASM at the atomistic spin scale, micromagnetic model is a continuum theory that disentangles the magnetization process on the length scale of magnetic domain and domain walls [237]. The magnetic state is described by the magnetization $\mathbf{M} = \mathbf{m}M_s$ with $\mathbf{m}$ as the unit vector for the magnetization direction. For Nd-Fe-B magnets with the unixial magnetic anisotropy, the magnetic Gibbs energy is expressed as

$$E(\mathbf{m}, T) = \int_{\Omega} \left\{ A_e(T) \|\nabla \mathbf{m}\|^2 + K_1(T)[1 - (\mathbf{m} \cdot \mathbf{e}^z)^2] \right.$$
$$\left. - \frac{1}{2}\mu_0 M_s(T)\mathbf{m} \cdot \mathbf{H}_d - \mu_0 M_s(T)\mathbf{m} \cdot \mathbf{H}_{ext} \right\} dv. \tag{5.1}$$

The spatial distribution of temperature dependent exchange stiffness $A_e(T)$, magnetocrystalline anisotropy $K_1(T)$, and magnetization saturation $M_s(T)$ represents the microstructure of Nd-Fe-B magnets. In micromagnetic simulations, the demagnetization field is included. $\mathbf{H}_d$ and $\mathbf{H}_{ext}$ denote the demagnetization field and external magnetic field, respectively.

The magnetization dynamics are described by LL equation [226, 258]

$$\dot{\mathbf{m}} = -\frac{\gamma}{1 + \alpha^2} \left[\mathbf{m} \times \mathbf{H}_{eff} + \alpha \mathbf{m} \times (\mathbf{m} \times \mathbf{H}_{eff}) \right], \tag{5.2}$$

where γ denotes the gyromagnetic ratio, α the dimensionless Gilbert damping parameter, and $\mathbf{H}_{eff} = -\frac{1}{M_s}\frac{\delta E}{\delta \mathbf{m}}$ the effective field. The finite temperature effect is modelled by adding
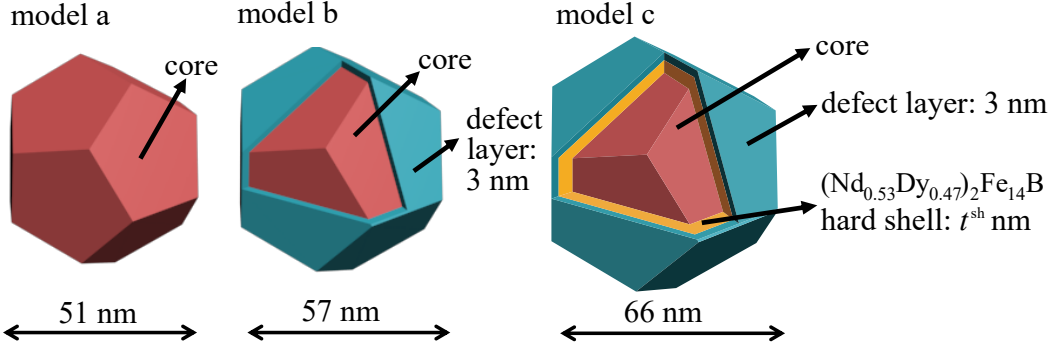
Figure 5.2: Three kinds of models for micromagnetic simulations. (a) $Nd_2Fe_{14}B$ dodecahedral grain with a diameter of 51 nm. (b) $Nd_2Fe_{14}B$ grain covered with a 3-nm defect layer. (c) $Nd_2Fe_{14}B$ grain covered with $(Nd_{0.53}Dy_{0.47})_2Fe_{14}B$ hard shell (thickness t^{sh}) and 3-nm outer defect layer.

a fluctuating thermal field $\mathbf{H}_{therm}$ into $\mathbf{H}_{eff}$, so that a stochastic LL equation is obtained. According to Brown [227], the thermal field can be expressed as

$$\mathbf{H}_{therm} = \boldsymbol{\eta}\sqrt{\frac{2\alpha k_B T}{M_s(T)\gamma\Delta V\Delta t}},$$ (5.3)

in which $\boldsymbol{\eta}$ is a random vector from a standard normal distribution and is regenerated after every time step. ΔV is the single cell volume and Δt is the time step. In general, $\mathbf{H}_{therm}$ has zero average and is uncorrelated both in time and space. The stochastic LL equation is solved in MuMax3 [250, 285] by using the Heun integration method and a fixed time step which will be optimized in the following to reduce the computation cost. Therefore, there are five kinds of energy being considered in micromagnetics, which are exchange energy, anisotropy energy, zeeman energy, demagnetization energy and thermal engergy. For the calculation of magnetic reversal curves, $\mathbf{H}_{ext}$ is applied as a stepwise field.

Dodecahedral grain model, as an approximation of the polyhedral geometry of grains observed in actual Nd-Fe-B permanent magnets, is used in this work. For the single dodecahedral, an open boundary condition is used, not a periodic boundary condition. In the current work, the single grain the focus. Since there are already previous micromagnetic studies on the similar single grain [253, 289], it is convenient for us to compare our micromagnetic results with previous ones and thus verify our method. The single grain is not realistic here, but a model to verify the proposed multiscale scheme. Multigrain case will be studied later. Typical microstructures such as magnetically soft grain-boundary phase (modeled as defect layer) and grain boundary diffused Dy-rich layer (modeled as hard shell) are also considered. They provide the possibility of improving the coercivity of Nd-Fe-B permanent magnets by microstructure engineering, while alleviating the risk of heavy-rare-earth crisis.

Namely, three kinds of models based on single dodecahedral grain are built here: (a) a pure $Nd_2Fe_{14}B$ grain without neither defect nor hard shell; (b) a $Nd_2Fe_{14}B$ grain covered with a 3 nm thick defect layer; (c) a $Nd_2Fe_{14}B$ core with a hard $(Nd_{0.53}Dy_{0.47})_2Fe_{14}B$ shell and a outer defect layer of 3 nm, as shown in Figure 5.2. The diameter of $Nd_2Fe_{14}B$ core is kept constant at 51 nm. The hard shell thickness (t^{sh}) is varied to investigate its effectiveness in enhancing coercivity.

According to the ASM results on the temperature dependent intrinsic parameters in the following, the exchange length $l_{ex}(T) = \sqrt{2A_e(T)/[\mu_0 M_s^2(T)]}$ and the Bloch parameter $\delta_w(T)/\pi = \sqrt{A_e(T)/K_1(T)}$ at 300–550 K can be estimated and their minimum value is found to be around 1.6 nm. The finite-difference cell size should be smaller than $l_{ex}(T)$ and $\delta_w(T)/\pi$ [363] and thus is chosen to be 1.5 nm. It should be noted that in the thermal micromagnetic problems, the cell size is suggested to satisfy an additional criteria, i.e., it should be not larger than the thermal exchange length $l_{th}(T) = \sqrt{2A_e(T)/[M_s(T)\|\mathbf{H}_{therm}(T)\|]}$ [359]. Here, in the case of Gilbert damping parameter 0.1, cell size 1.5 nm, and time step 50 fs, the minimum $l_{th}(T)$ at 300–550 K is estimated as 1.5 nm, indicating a cell size of 1.5 nm is reasonable. Recently, there is a report which normalizes or rescales the micromagnetic parameters as a function of mesh size, in order to achieve the mesh-size independent results or avoid unphysical mesh-size dependence [364].

The temperature dependent M_s and K_1 of the $(Nd_{1-x}Dy_x)_2Fe_{14}B$ hard shell (model c Figure 5.2) are obtained by using the experimental data [365]. $A_e(T)$ of the hard shell is taken the same as that of $Nd_2Fe_{14}B$. Direct calculation of these intrinsic magnetic parameters of $(Nd_{1-x}Dy_x)Fe_{14}B$ by ASM simulations is still challenging and will be explored in the near future. In the following calculations, $(Nd_{1-x}Dy_x)_2Fe_{14}B$ with $x = 0.47$ is chosen as the hard shell.

5.3 Intrinsic parameters at high temperature

The temperature dependent magnetization calculated by ASM simulations is shown in Figure 5.3(a). The ASM simulation results show excellent agreement with the experimental one [15]. Fitting the data in Figure 5.3(a) by the Curie–Bloch equation $M_s(T) = M_0 [1 - (T/T_c)^{\alpha_1}]^{\alpha_2}$ yields the Curie temperature $T_c = 602$ K, parameter $\alpha_1 = 1.802$, and parameter $\alpha_2 = 0.418$.

The magnetocrystalline anisotropy is determined by calculating the system energy when the global magnetization is aligned along different directions at different temperatures. The energy density F at different temperatures is estimated by the constrained Monte Carlo method, in which the azimuthal angle is fixed at zero degree and the polar angle is gradually changed from 0 to 90 degree. The ASM simulation results on temperature dependent F are shown in Figure 5.3(b) and can be well fitted by $F = K_1 \sin^2 \theta$, from which the magnetocrystalline anisotropy constant K_1 is attained. As presented in Figure
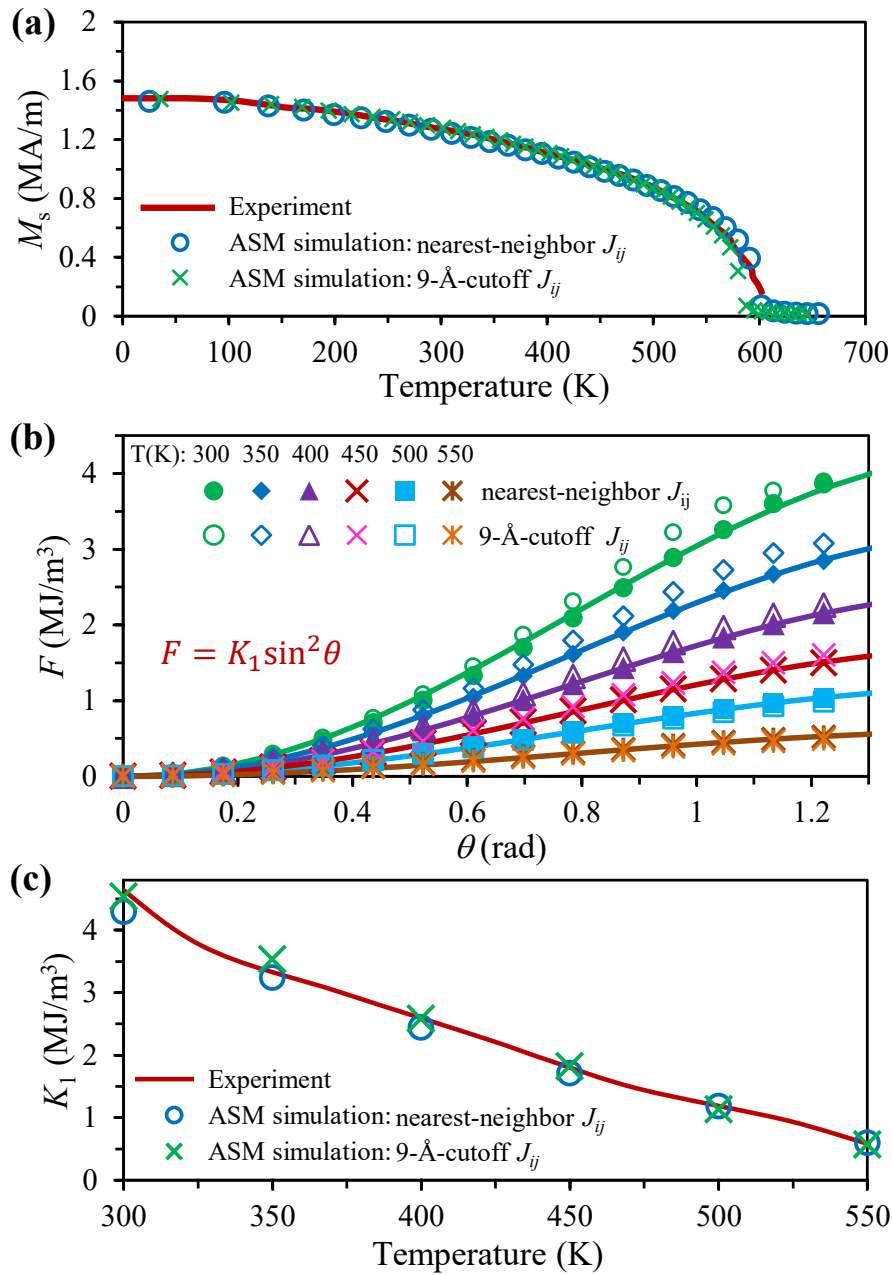
Figure 5.3: ASM simulation results on (a) temperature dependent magnetization saturation M_s, (b) free energy density as a function of polar angle θ at high temperatures, and (c) magnetocrystalline anisotropy $K_1(T)$. The experimental results in (a) and (c) are taken from Refs. [15] and [310]. Results for both nearest-neighbor and 9-Å-cutoff J_{ij} are shown and compared.
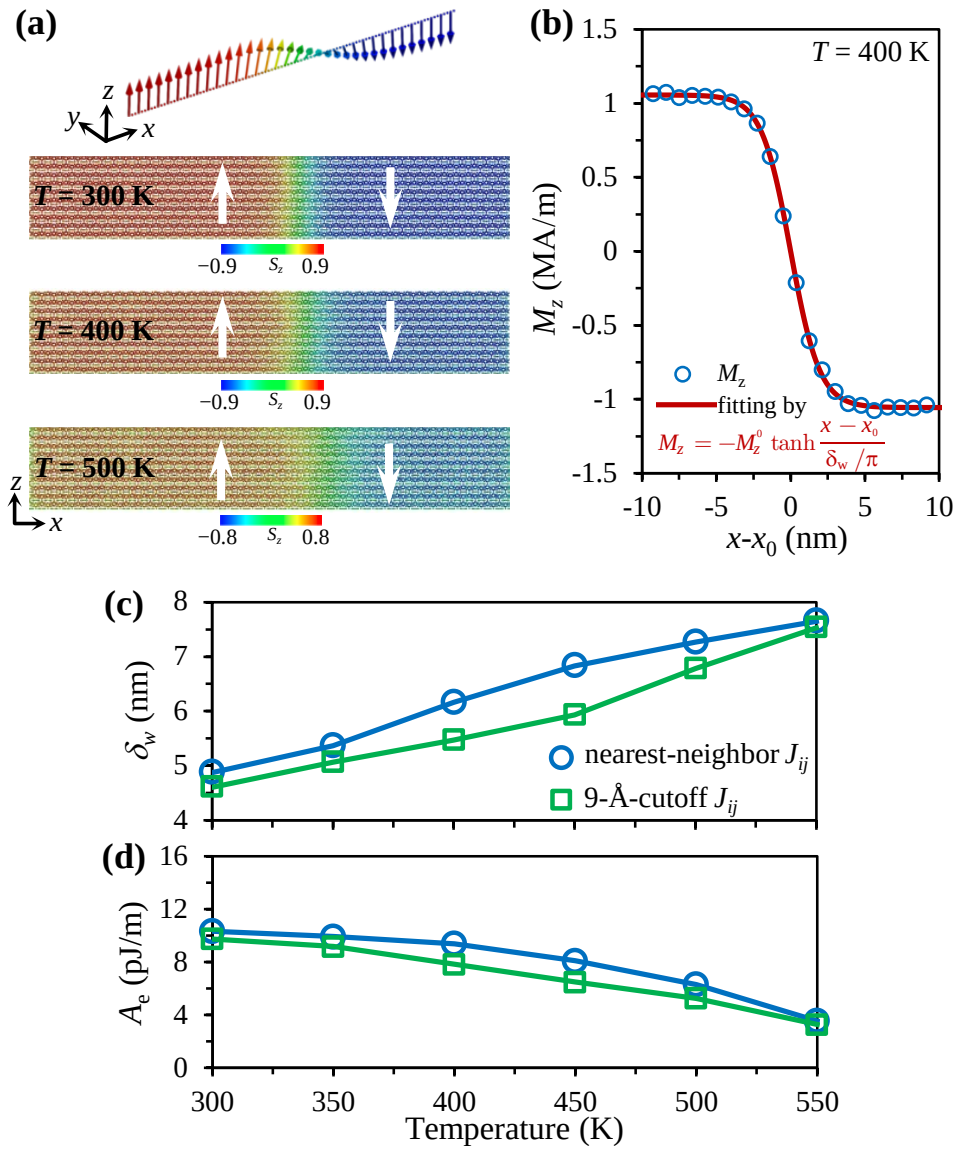
Figure 5.4: ASM simulations results on (a) temperature-dependent domain wall configuration presented by the distribution of atomistic magnetic moments, (b) M_z distribution along x axis at $T = 400$ K, (c) domain wall width and (d) exchange stiffness at high temperature. Results for both nearest-neighbor and 9-Å-cutoff J_{ij} are shown and compared in (c) and (d).

5.3(c), the fitted K_1 is well in line with the experimental measurement [310].

In order to calculate the exchange stiffness A_e at high temperatures, the domain wall width δ_w is firstly determined. For the calculation of δ_w, the magnetic moment direction is set in the y-z plane with a polar angle as 0 and 180° in the upward and downward

domain, respectively. Then the system is relaxed to obtain the Bloch domain wall configuration represented by the atomistic magnetic moments, as shown in Figure 5.4(a). The domain wall is observable. As the temperature increases, the effect of thermal fluctuations is stronger and the domain wall becomes wider. In order to compute δ_w, the magnetization distribution along x axis in Figure 5.4(a) is fitted by the continuum description of domain wall or diffusive interface, i.e., $M_z = -M_z^0 \tanh\left[(x - x_0)/(\delta_\mathrm{w}/\pi)\right]$ [171]. The parameter M_z^0 is determined by fitting the M_z data points over the x axis. The fitted M_z^0 is found to agree well with the values in Figure 5.3(a) at high temperatures. The typical fitting results at 400 K are shown in Figure 5.4(b), from which δ_w is readily attained. The fitted δ_w as a function of temperature is presented in Figure 5.4(c). Finally, the combination of δ_w in Figure 5.4(c), K_1 in Figure 5.3(c), and the relationship $\delta_\mathrm{w} = \pi\sqrt{A_\mathrm{e}/K_1}$ [171] yields temperature dependent A_e, as shown in Figure 5.4(d). It can be found that A_e decreases with the increasing temperature. $A_\mathrm{e} = 10.3$ pJ/m at 300 K is also consistent with the literature report [171]. With these temperature dependent intrinsic parameters at hand, micromagnetic simulations including the microstructure features are feasible.

It should be mentioned that the main objective of this work is to demonstrate the proof of concept, i.e., the feasibility of multiscale simulations combing atomistic spin model (ASM) and micromagnetics to calculate the coercivity of permanent magnets at high temperatures. As a preliminary step, Nd-Fe-B is taken as an example whose intrinsic parameters (M_s, K_1, and A_e) are experimentally available so that the feasibility of multiscale simulations can be verified. In the near future, the multiscale simulation methodology in this work will be extended to other set of materials whose properties are not experimentally available and thus the predictive power of the methodology will be further explored.

5.4 Temperature dependent coercivity

5.4.1 Influence of stepwise external field and step time

In order to calculate the magnetic hysteresis and thus the coercivity, a stepwise external field is applied. The stepwise field is characterized by two parameters ΔB_ex and t_rB, as illustrated in Figure 5.5(a). ΔB_ex is the increment step of the external field. t_rB indicates the duration of each external field, i.e., how long an external field is kept until it is decreased by ΔB_ex. According to Equation 5.3, it is obvious that thermal fluctuation field is strongly influenced by the cell volume (ΔV) and the integration time step (Δt) for solving the stochastic LL equation. Here the cell size is fixed as 1.5 nm and thus ΔV as 1.5^3 nm^3, as mentioned in Subsection 5.2.2. In principle, smaller Δt and larger t_rB favor the reliable calculation of coercivity, but takes more computation time. Hereby, in order to make the calculated coercivity H_c at high temperatures convincing and at the same time save the computation cost, the influence of ΔB_ex, t_rB, and Δt for the three models is evaluated, as shown in Figure 5.2.
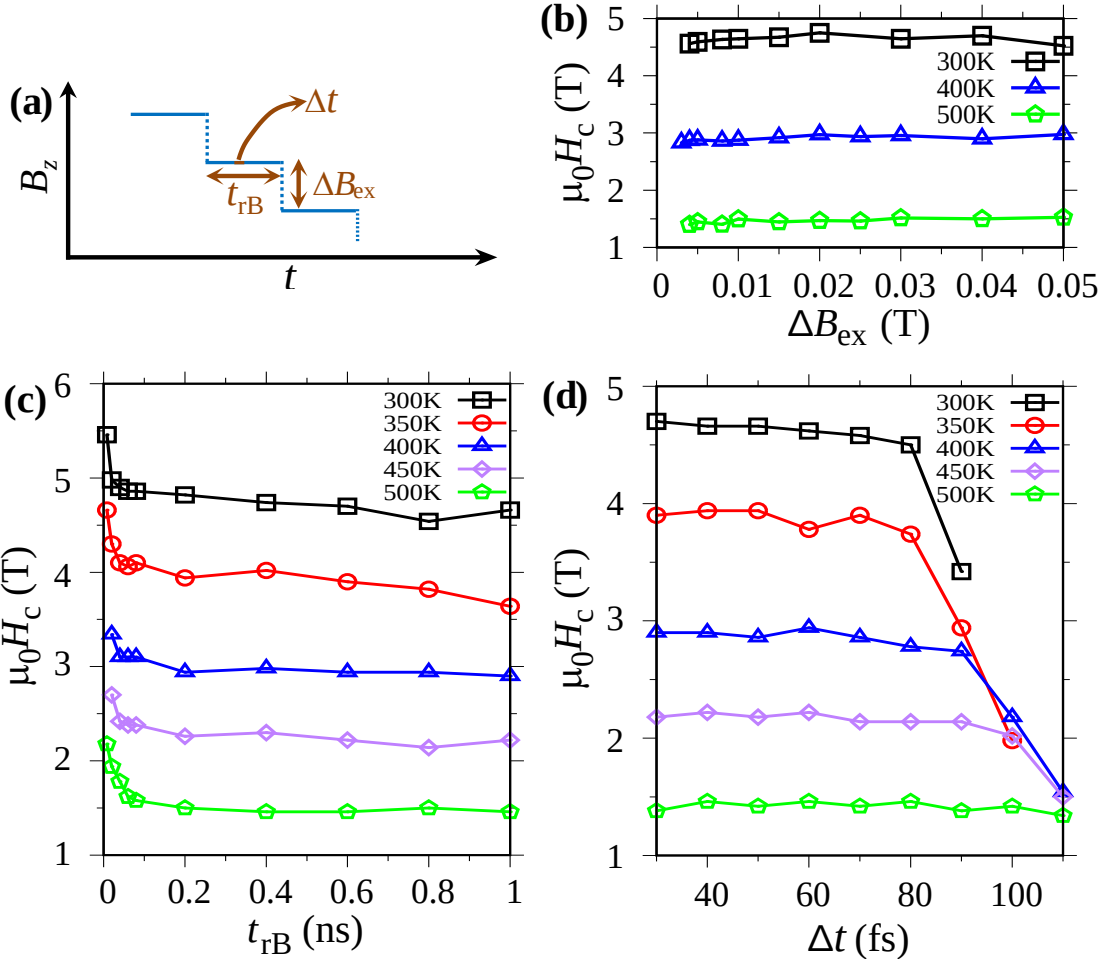
Figure 5.5: (a) Schematics of applying stepwise external field for the coercivity calculation. ΔB_{ex}: increment step of the external field; Δt: step time for solving stochastic LL equation; t_{rB}: duration of applying a constant external field. Temperature dependent coercivity of model a (Figure 5.2) as a function of (b) ΔB_{ex} with fixed $t_{rB} = 0.4$ ns and $\Delta t = 50$ fs, (c) t_{rB} with fixed $B_{ex} = 0.01$ T and $\Delta t = 50$ fs, and (d) Δt with fixed $\Delta B_{ex} = 0.01$ T and $t_{rB} = 0.4$ ns.

Figures 5.5(b)–(d) shows the typical results for the case of model a) defined in the subsection 5.2.2. It can be seen from Figure 5.5(b) that the H_c vs ΔB_{ex} curves present very weak increasing trends when ΔB_{ex} is changed by one order of magnitude (ranging from 0.004 to 0.05 T). This indicates H_c is not strongly influenced by ΔB_{ex}. For the following calculations, $\Delta B_{ex} = 0.01$ T is chosen. In contrast, as shown in Figure 5.5(c), H_c is found to firstly decrease with the increasing t_{rB} and then nearly saturate at $t_{rB} = 0.2 - 0.4$ ns. Similarly, in Figure 5.5(d), H_c decreases with the increasing Δt when Δt is above 70 fs. H_c

almost saturates when Δt is reduced from 60 fs at 300–500 K. Similar results are also found for the cases of models b and c. Ideally, t_{rB} should be in the scale of second which is the typical experimental time scale for the coercivity measurement. However, t_{rB} in the order of second makes the computational cost unacceptable. Seeing that the saturation behavior of H_c with respect to both t_{rB} and Δt appears in Figs. 5.5(c) and (d), $\Delta t = 50$ fs and $t_{rB} = 0.4$ ns are taken for the following micromagnetic simulations.
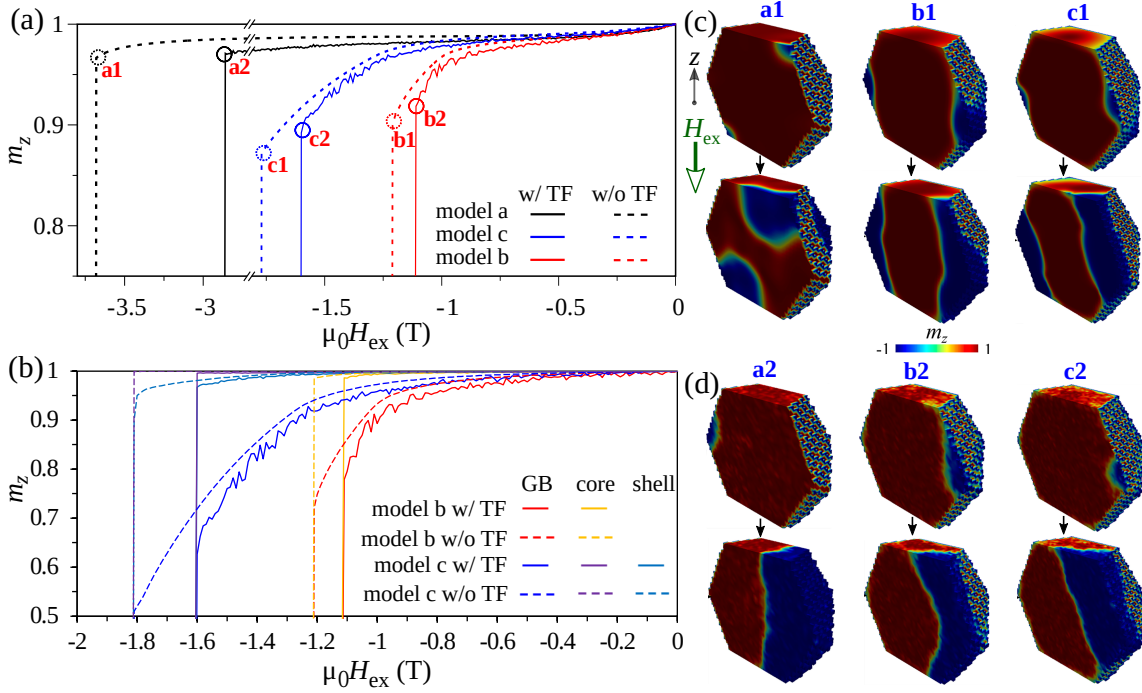
Figure 5.6: (a) Total magnetization reversal curves and (b) magnetization curves with separate contributions from the core ($Nd_2Fe_{14}B$), GB, and shell at 400 K with and without thermal fluctuations (TF). The z-component magnetization in (a) and (b) is normalized with respect to its remanent value. Magnetization states and their evolution at the points marked in Figure 5.6(a): (c) without TF; (d) with TF. 4.5-nm-thick hard shell in model c. 3-nm-thick defect layer: $\mu_0 M_s^d = 1$ T, $A_e^d = 6.2$ pJ/m, $K_1^d = 0$ MJ/m^3 [246].

5.4.2 Influence of thermal fluctuations

At finite temperatures, the thermal activation will induce the premature nucleation and thus influence the coercivity. In micromagnetic simulations, the temperature effects should be attributed to not only the temperature dependent intrinsic parameters, but also the finite temperature induced thermal fluctuations.

In order to investigate the effect of thermal fluctuations, the geometry, composition, and

magnetic properties of the defect layer and hard shell are kept unchanged. As shown in model b (Figure 5.2), the $Nd_2Fe_{14}B$ grain surface is assumed to be covered by a 3-nm-thick soft defect layer whose magnetic properties are set as $\mu_0 M_s^d = 1$ T, $A_e^d = 6.2$ pJ/m, and $K_1^d = 0$ MJ/m^3. These values for M_s^d, A_e^d, and K_1^d of the defect layer are chosen according
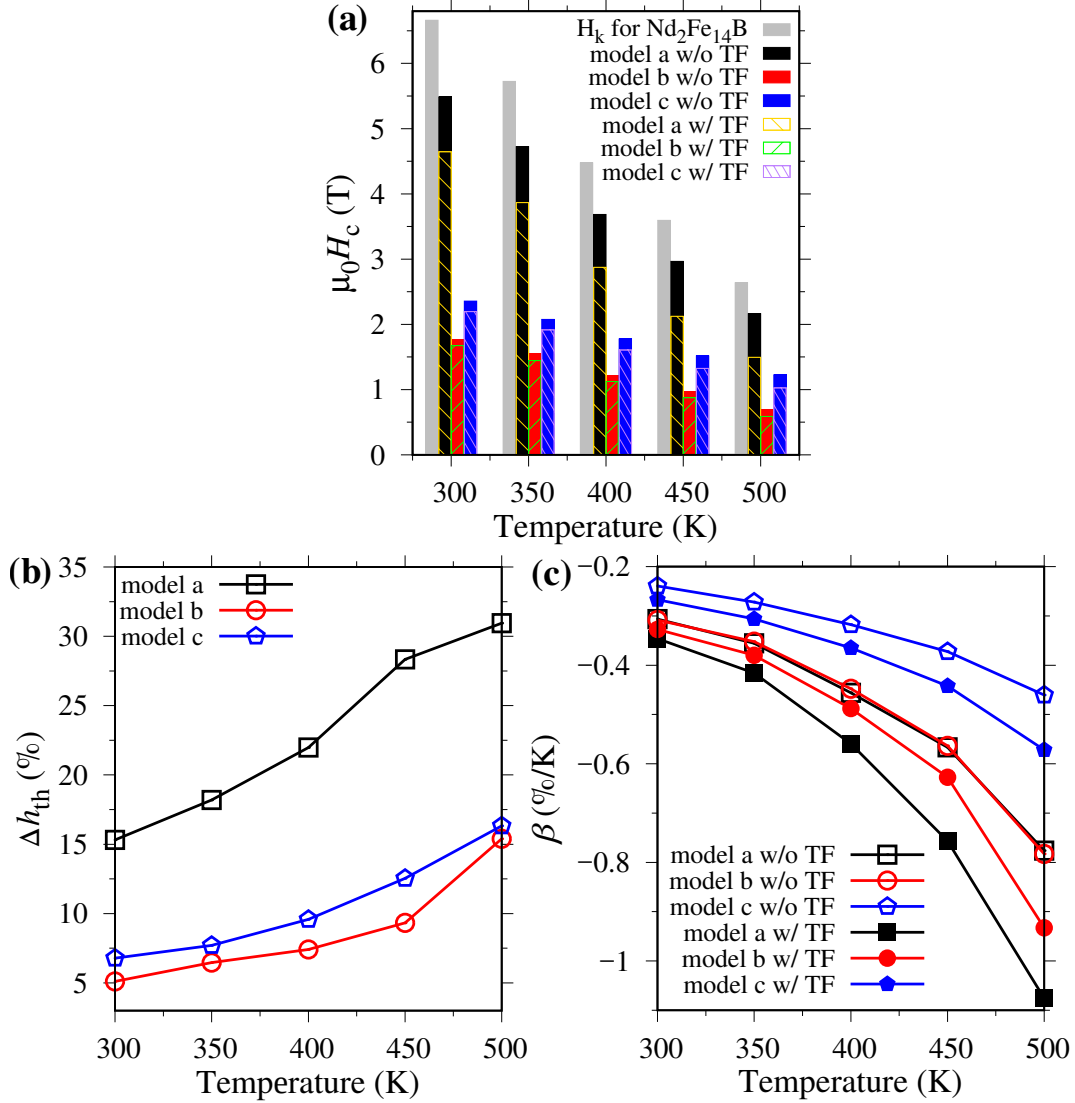
Figure 5.7: (a) Coercivity, (b) coercivity reduction ratio ($\Delta h_{th} = H_{th}/H_c^0$) by thermal fluctuations (TF), and (c) temperature coefficient of coercivity (β) as a function of temperature for three models. $\beta(T) = \frac{1}{H_c(T)} \frac{dH_c}{dT}$ in which $\frac{dH_c}{dT}$ is the fitted slope of curve H_c vs T. The defect layer is 3-nm-thick with an Fe+Co content around 60% [246]: $\mu_0 M_s^d = 1$ T, $A_e^d = 6.2$ pJ/m, $K_1^d = 0$ MJ/m^3. The hard shell is 4.5-nm-thick $(Nd_{0.53}Dy_{0.47})_2Fe_{14}B$ with temperature dependent magnetic properties from [365].

to the experimental measurement of the ferromagnetic grain boundary (GB) phase that is demonstrated to contain an Fe+Co content of about 60% [246]. Since the change in M_s of Fe and Co within 300–500 K is negligible [366] and the recent experimental measurement shows not too much change in the magnetization of GB phase at low temperatures [61] , M_s^d of the defect layer with the main composition as Fe+Co is reasonably assumed to be temperature independent within 300–500 K. The Dy-rich hard shell is set as 4.5-nm-thick with a composition of $(Nd_{0.53}Dy_{0.47})Fe_{14}B$ whose temperature dependent magnetic properties can be readily extracted from the experimental measurements [365].

Figure 5.6 shows the typical magnetization reversal curves and the corresponding magnetic states in the three models at 400 K. It can be found from Figure 5.6(a) that, without thermal fluctuations the reversal curves are smooth, while they fluctuates when temperature induced thermal fluctuations are considered. The coercivity is also obviously reduced by thermal fluctuations. Figure 5.6(b) shows the separate contributions to the magnetization reversal from the $Nd_2Fe_{14}B$ core, GB defect layer, and Dy-doped hard shell for models b and c. It is clear that magnetization reversal in GB defect layer is much faster in model b without hard shell than that in model c with a hard shell. The thermal fluctuations also induce faster magnetization reversal in GB defect layer. In model c, the hard shell is directly exchange coupled to the GB defect layer and thus is magnetically reversed faster than the $Nd_2Fe_{14}B$ core. At the coercivity point, the total magnetization in core, GB, and shell is reversed instantly. The representative magnetic states during the magnetization reversal process at the coercivity point are shown in Figure 5.6(c). It can be seen that the magnetic reversal starts at a corner or edge of the grain due to the inhomogeneous stray field therein [74, 367]. The thermal fluctuations make the magnetization contour fluctuate in Figure 5.6(c), and add additional fields to induce premature reversal at a corner or edge under even lower external field. It can be seen from Figs. 5.6(c) that the soft GB layer in models b and c is magnetically reversed firstly, followed by the expansion of reversed domains and the propagation of domain walls. This phenomenon is compatible with the exchange-spring behavior [130, 333, 368].

Figure 5.7 presents a quantitative analysis to reveal the influence of thermal fluctuations on both the coercivity and its temperature coefficient β for the three models. As expected, the coercivity rapidly decreases with the increasing temperature, mainly due to the quick decrease of anisotropy field. For the pure $Nd_2Fe_{14}B$ dodecahedral grain (model a) at different temperatures, it can be found from Figure 5.7(a) that the thermal fluctuations induced coercivity reduction ($\mu_0 H_{th}$) is around 0.8 T. This 0.8 T reduction of coercivity agrees well with the previous calculation results for a similar grain by Bance et al. [253, 289], who used the elastic band method or string method to obtain the energy barrier and then determined the thermally activated coercivity. This agreement indicates that our simulation results based on the stochastic LL equation is credible. In contrast, for models b and c, $\mu_0 H_{th}$ is smaller, around 0.1 and 0.2 T, respectively.

According to the so-called phenomenological 'global model' proposed by Givord et al. [293, 369, 370],

$$\mu_0 H_{\text{th}} = \frac{25k_{\text{B}}T}{vM_{\text{s}}}, \qquad (5.4)$$

in which v is the activation volume. Accordingly, $\mu_0 H_{\text{th}}$ (proportional to $1/v$) decreases with increasing v. In fact, by using Equation 5.4 and $\mu_0 H_{\text{th}}$ determined from Figure 5.7(a), v can be calculated, as shown the case of $\mu_0 M_{\text{s}}^{\text{d}} = 1$ T in Figure 5.8. It can be seen that the defect layer leads to a remarkably increased v which is reduced by adding the hard shell. v is found to decrease in the order: model b > model c > model a, in accordance with the previous study using the energy barrier method [253]. Therefore, the dependence of v on the model microstructure features could be intrinsically responsible for the different reduction of coercivity by thermal fluctuations ($\mu_0 H_{\text{th}} = 0.8$, 0.2, and 0.1 T for model a, c, and b, respectively) in the three models.

The coercivity reduction ratio by thermal fluctuations is defined as $\Delta h_{\text{th}} = H_{\text{th}}/H_{\text{c}}^0$ in which H_{c}^0 is the coercivity without thermal fluctuations. It can be seen clearly from Figure 5.7(b) that Δh_{th} increases with the temperature, indicating the stronger intensity of thermal fluctuations at higher temperatures. H_{c}^0 is deduced to be proportional to $v^{-2/3}$ [370] and H_{th} to v^{-1}, so Δh_{th} is proportional to $v^{-1/3}$. v decreases in the order: model b > model c > model a. Therefore, at the same temperature Δh_{th} is the highest in model a and lowest in model b. For example, Δh_{th} increases from 15.3%, 5.1%, and 6.8% at 300 K to 31%, 15.4%, and 16.4% at 500 K for model a, b, and c, respectively.

The temperature coefficient of coercivity, β, is a very important parameter for the performance evaluation of Nd-Fe-B magnets at high temperatures. Here β is calculated by $\beta(T) = \frac{1}{H_{\text{c}}}\frac{\text{d}H_{\text{c}}}{\text{d}T}$ [371]. Since the curve H_{c} vs T is found to be almost linear, $\frac{\text{d}H_{\text{c}}}{\text{d}T}$ is estimated by linearly fitting H_{c} vs T curve. Figure 5.7(c) presents β as a function of temperature for all the three models. β is found to decrease with the increasing temperature. At 300 K, β is around -0.24 to -0.35%/K. A typical value of β for the hot-deformed Nd-Fe-B magnets and commercial Nd-Fe-B sintered magnets at room temperature is about -0.48 and -0.6%/K, respectively [72, 80]. These β values are smaller than our calculated ones, possibly owing to the ideally simplified microstructure in our simulations. In addition, it is clear in Figure 5.7(c) that thermal fluctuations further decreases β and thus makes Nd-Fe-B magnets with lower thermal stability. For example, thermal fluctuations reduce β by 0.04 and 0.19%/K for model a at 300 and 450 K, respectively. At 500 K, the reduction of β by thermal fluctuations is 0.3, 0.16, and 0.11%/K for model a, b, and c, respectively.

5.4.3 Influence of defect layer

In Nd-Fe-B magnets, the ferromagnetic thin grain boundaries or surface defects are found to be the weak region where the magnetization reversal occurs at a low external magnetic field. This weak region is important microstructure feature for Nd-Fe-B magnets, and is
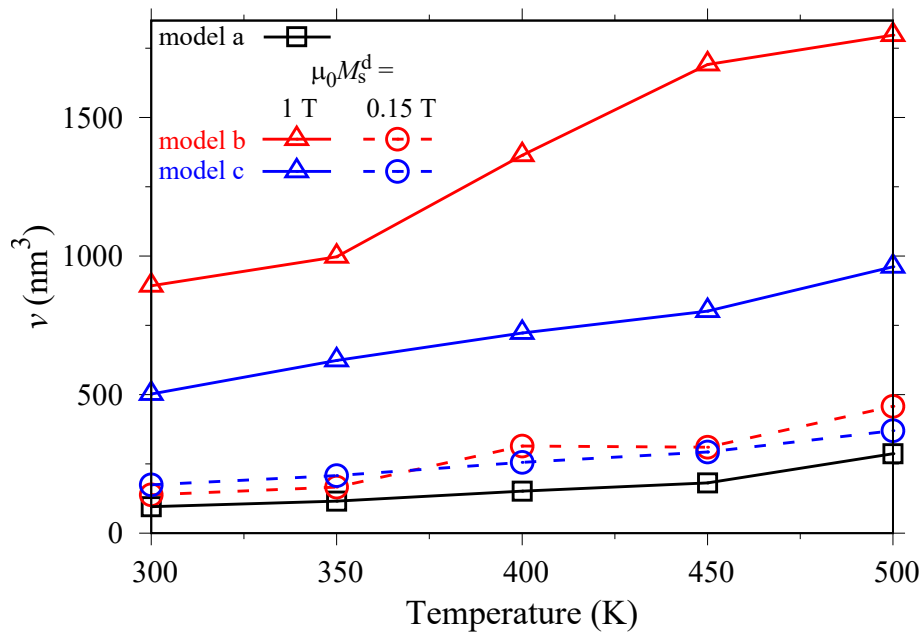
Figure 5.8: Temperature dependent activation volume (v) for different models with very strong magnetization ($\mu_0 M_s^{\mathrm{d}} = 1$ T) and very weak magnetization ($\mu_0 M_s^{\mathrm{d}} = 0.15$ T) in the defect layer. The hard shell thickness in model c is 4.5 nm.
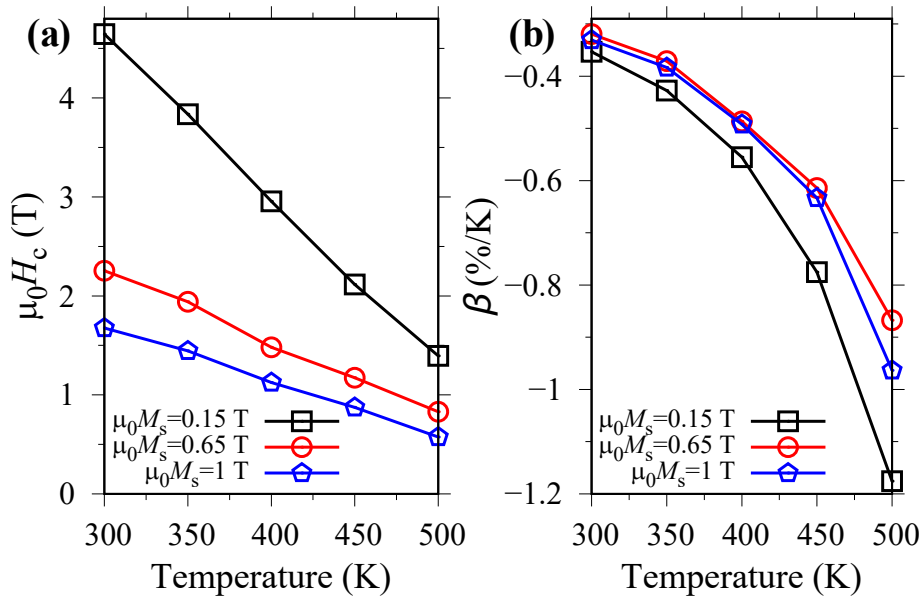
Figure 5.9: (a) Coercivity ($\mu_0 H_{\mathrm{c}}$) and (b) temperature coefficient of coercivity (β) in model b (Figure 5.2) with different defect-layer property.

often modeled as a soft defect layer covering the grain. Its influence on the coercivity at high temperatures will be computationally explored here.

According to the results of model b with thermal fluctuations in Figure 5.7(a), the introduction of a 3-nm-thick defect layer can significantly reduce the coercivity by 2.9 and 2.4 T at 300 and 350 K, respectively. In contrast, the coercivity reduction is only 1.3 and 0.9 T at 450 and 500 K, respectively. This implies that the defect layer has much stronger influence on coercivity at lower temperatures. In addition, the defect layer can significantly decrease the influence of thermal fluctuations on coercivity (Figure 5.7(b)), and increase the thermal stability (curves with thermal fluctuations in Figure 5.7(c)). The enhanced thermal stability and the reduced influence of thermal fluctuations in model b when compared to model a, are mainly attributed to the large activation volume which is induced by the defect layer in model b, as shown in Figure 5.8 and the above discussions based on Equation 5.4. The significantly reduced coercivity in model b is owing to the zero magnetocrystalline anisotropy of the defect layer. Consequently, the defect layer seems like a double-edged sword (increasing the thermal stability while decreasing the coercivity) which could be possibly harnessed for a balance between coercivity and thermal stability.

Figure 5.9 presents the effect of defect-layer magnetization ($\mu_0 M_s^d$) on H_c and β. According to the experimentally measured magnetization of grain boundary in Nd-Fe-B magnets [168, 246], defect layers with strong ($\mu_0 M_s^d = 1$ T), moderate ($\mu_0 M_s^d = 0.65$ T), and weak ($\mu_0 M_s^d = 0.15$ T) magnetization are considered. The corresponding exchange stiffness is estimated by $A_e^d \sim \epsilon (\mu_0 M_s^d)^2$ with the material constant $\epsilon = 5.41$ pJ/m/T^2 which is calculated from the experimental results of α-Fe [246]. It is evident in Figure 5.9(a) that weaker magnetization in the defect layer leads to higher coercivity, while faster decrease of coercivity with respect to temperature. This finding is in accordance with the micromagnetic theoretical analysis, i.e., in the case of defect layer thickness (3 nm here) less than the domain wall width (Figure 5.4(c)), both the nucleation and depinning field are inverse proportional to $\mu_0 M_s^d$ [333, 372]. From the temperature coefficient results in Figure 5.9(b), it is found that weak magnetization ($\mu_0 M_s^d = 0.15$ T) in the defect layer leads to lower thermal stability than strong ($\mu_0 M_s^d = 1$ T) and moderate ($\mu_0 M_s^d = 0.65$ T) magnetization. The difference in β values for the case of $\mu_0 M_s^d = 1$ and 0.65 T is not significant. These results indicate that an increase of defect-layer magnetization above a certain value (e.g. 0.65 T here) will reduce H_c as usual, but will not considerably influence β.

The defect-layer magnetization is also shown to influence the activation volume in Figure 5.8. In both models b and c, the introduction of strong magnetization ($\mu_0 M_s^d = 1$ T) in the defect layer increases the activation volume by several times. In contrast, a weak magnetization of $\mu_0 M_s^d = 0.15$ T only slightly enhances the activation volume.

124
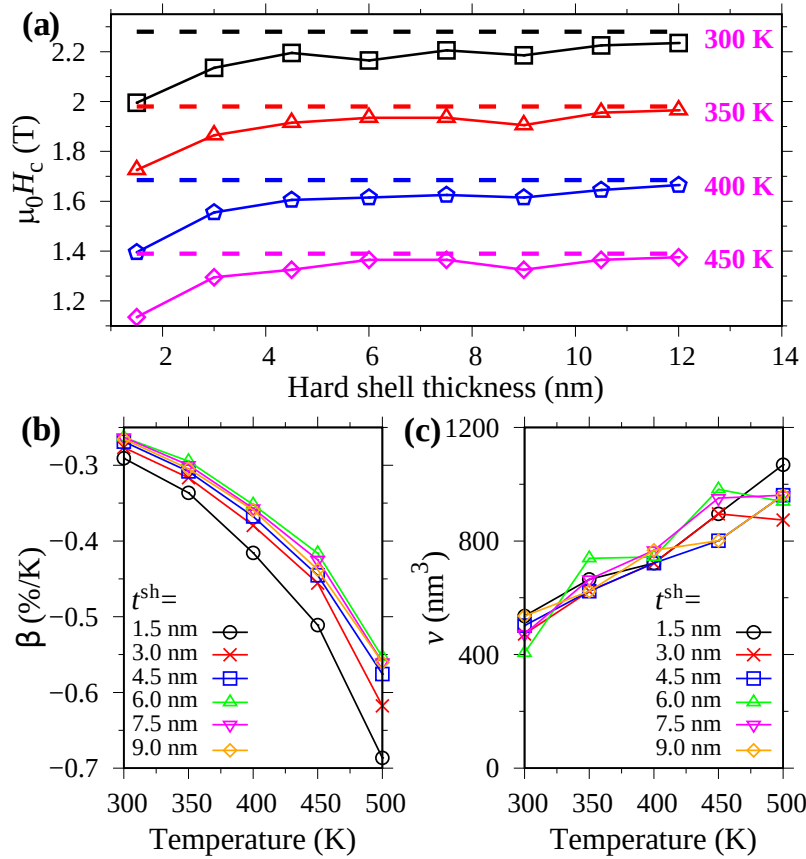
Figure 5.10: (a) Coercivity, (b) temperature coefficient of coercivity (β), and (c) activation volume (v) as a function of the hard shell thickness (t^{sh}) in model c (Figure 5.2) at different temperatures. Dashed lines in (a) correspond to the results when the core takes the same properties as the shell and $t^{\mathrm{sh}} = 4.5$ nm. The magnetic properties of 3-nm-thick defect layer: $\mu_0 M_{\mathsf{s}}^{\mathsf{d}} = 1$ T, $A_{\mathsf{e}}^{\mathsf{d}} = 6.2$ pJ/m, $K_1^{\mathsf{d}} = 0$ MJ/m^3 [246].

5.4.4 Influence of hard shell

It is expected that Dy substitution near grain surfaces effectively enhances coercivity. This idea has been realized by the grain boundary diffusion of Dy to form a hard shell around the grain surface [53, 68, 160, 347]. So the Dy-rich hard shell is another important microstructure feature for high-performance Nd-Fe-B magnets, as illustrated in Figure 5.2(c). Currently it is still essential for Nd-Fe-B magnets used at high temperatures.

As shown the results of model c in Figure 5.7(a), adding a 4.5-nm-thick $(\mathrm{Nd}_{0.53}\mathrm{Dy}_{0.47})_2\mathrm{Fe}_{14}\mathrm{B}$ hard shell enhances the coercivity by ~ 0.5 T when compared to model b only with a 3-nm-thick defect layer. But the 4.5-nm-thick shell cannot fully cancel out the reduction of coercivity from the 3.5-nm-thick defect layer. In addition, the hard shell remarkably

enhances β and thus the thermal stability (Figure 5.7(c)), in accordance with the strategy of designing the high-temperature Nd-Fe-B magnets by adding Dy.

As for the activation volume v in Figure 5.8, in the case of strong defect-layer magnetization ($\mu_0 M_s^d = 1$ T), adding a 4.5-nm-thick hard shell approximately reduces v by half. However, if the defect-layer magnetization is very weak (e.g. $\mu_0 M_s^d = 0.15$ T), the hard shell shows no significant influence on v (circle markers in Figure 5.8). This suggests that decreasing the defect-layer magnetization and meanwhile adding the hard shell not only appreciably increase the coercivity, but also suppress the thermal fluctuations induced coercivity reduction.

Figure 5.10 shows the dependence of coercivity, thermal stability, and activation volume on the shell thickness (t^{sh}). The dashed line in Figure 5.10(a) shows the coercivity when the core is assumed to have the same properties as the shell, corresponding to the limit of a very thick shell. In Figure 5.10(a), the coercivity is firstly improved by increasing t^{sh} and then saturates toward the dashed line at around $t^{sh} = 6 - 8$ nm. Similarly, the temperature coefficient of coercivity increases with t^{sh} and does not change significantly after t^{sh} exceeds 6-8 nm, as shown in Figure 5.10(b). The activation volume in Figure 5.10(c) is found to not remarkably change with t^{sh}, indicating a weak dependence of the thermal fluctuations induced coercivity reduction on the hard shell thickness. These results imply that a shell thickness of $t^{sh} = 6 - 8$ nm is enough to achieve the maximum coercivity enhancement and thermal stability, and adding Dy into the core (e.g. Dy alloying in the initial sintered magnets before grain boundary diffusion) is not indispensable.

5.5 Summary

In summary of this chapter, a multiscale computational scheme integrating atomistic spin model (ASM) and micromagnetic simulations is proposed to calculate the coercivity of Nd-Fe-B permanent magnets at high temperatures. Using the ASM Hamiltonian constructed for $Nd_2Fe_{14}B$, ASM simulations are carried out to obtain the temperature-dependent saturated magnetization $M_s(T)$, magnetocrystalline anisotropy $K_1(T)$, and exchange stiffness constant $A_e(T)$ at high temperatures. The calculated $M_s(T)$, $K_1(T)$, and $A_e(T)$ are demonstrated to coincide with the experimental measurement.

Taking the ASM results as input, finite-temperature micromagnetic simulations using the stochastic LL equation are performed to calculate the magnetic reversal, thermal activation volume v, thermal fluctuations induced coercivity reduction H_{th} and its ratio Δh_{th}, and coercivity H_c and its temperature coefficient β in pure $Nd_2Fe_{14}B$ and $Nd_2Fe_{14}B$ grain with surface defect layer or Dy-rich hard shell. Specifically, the stepwise external field and the step time for calculating the magnetic reversal curves are optimized.

It is found that apart from the anisotropy field decreasing with temperature, the thermal fluctuations further reduce H_c by 5–10% and β by 0.02–0.1%/K. The defect layer with strong magnetization (e.g. 1 T) is demonstrated to result in a remarkably increased v (which

can be reduced by adding the Dy-rich hard shell) and significantly decrease H_c, while suppress the influence of thermal fluctuations and thus reduce H_{th} and Δh_{th}.

It is also revealed that even though the presence of Dy-rich hard shell cannot fully cancel out the reduction of coercivity from the defect layer, a 4.5-nm-thick $(Nd_{0.53}Dy_{0.47})_2Fe_{14}B$ shell enhances H_c by 0.5 T and considerably improves the thermal stability. Both H_c and β are found to saturate at a Dy-rich shell thickness of 6–8 nm. A even thicker shell or Dy alloying into the core prior to grain boundary diffusion is not essential.

The multiscale scheme and the calculation results in this chapter are useful for the design of high-performance Nd-Fe-B permanent magnets used at high temperatures in terms of microstructure engineering.

6 Microstructural effects in rare-earth free exchange-spring magnets by micromagnetic simulations

6.1 Introduction

Rare-earth free permanent magnets have been attracting more and more attentions. Due to the recent and ongoing supply chain vulnerability and price volatility of rare-earth metals, there is a continuous risk of a shortage of rare-earth elements (especially for Dy and Tb) [373]. Developing rare-earth free permanent magnets that possess properties comparable to (or better than) (Nd,Dy)-Fe-B permanent magnets is a long cherished dream of researchers all around the world.

The best available hard magnetic materials ($\kappa = \sqrt{K_1/(\mu_0 M_\mathrm{s}^2)} \gg 1$) usually have lower saturation magnetization but higher coercivity than many soft magnetic materials ($\kappa \ll 1$). The theoretical limit for the maximum energy product of a magnet is $(BH)_\mathrm{max} = \mu_0 M_\mathrm{s}^2/4$. This limit seems to only depend on M_s, but is subjected to the conditions: remanence equaling to M_s and nucleation field larger than $M_\mathrm{s}/2$. This means that high $(BH)_\mathrm{max}$ can only be achieved in magnet with both high magnetization and magnetocrystalline anisotropy constant. Therefore, it is naturally proposed to make composite magnets consisting of hard magnetic materials for providing a high coercivity and soft magnetic materials for providing a high saturation magnetization. Following this idea, the so-called exchange-spring magnets are proposed 20 years ago [333, 368, 374, 375].

The idea of exchange-spring magnets would make it possible to fabricate a super magnet with an energy product exceeding that in Nd-Fe-B magnets. If the size of the soft grains is sufficiently small, i.e., less than about twice of the domain wall width of the hard phase, the coercivity of the hard phase can be preserved [375]. Some recent reports have challenged this criterion and show continuous decrease in nucleation field even for smaller size of soft phase [376, 377].

Especially, nanostructured two-phase systems, which are composed of small soft magnetic grains that are strongly exchange-coupled to a hard magnetic phase, could result in remarkable high energy products. For instance, multilayer films of Sm-Co/Fe [378] and Sm-Co/Fe-Co [379] were reported to have $(BH)_\mathrm{max}$ higher that in SmCo$_5$ single phase. Mi-

cromagnetic simulations predict $(BH)_{\max}$ of an anisotropic nanocomposite $Nd_2Fe_{14}B/\alpha$-Fe system exceeding 700 kJ/m^3 [380], which is never achieved experimentally in the type of bulk or thin-film nanocomposites [381–383]. In spite of the continuing efforts, the exchange-spring Nd-Fe-B magnets in the bulk form seem infeasible to achieve the comparable performance of sintered or hot-pressed Nd-Fe-B magnets in the short term. One difficulty is that processing methods for good texturing require high temperatures which result in coarser grains and weaker effective exchange coupling [384].

More importantly, the exchange-spring-magnet principle provides a feasible route to synthesize rare-earth free permanent magnets which possess magnetic performance comparable to the commercialized rare-earth based magnets. Among the soft magnetic phases, magnetite (Fe_3O_4) and soft spinel cubic ferrite (MFe_2O_4, M = Co, Fe, Mn) powders are of general interests owing to their low cost, high saturation magnetization, and high chemical stability [385, 386]. Among the hard materials investigated so far, strontium ferrites or hexaferrites have attracted intensive attentions since they possess high chemical stability, large availability, low production cost and good magnetic properties [386].

In this chapter, motivated by and in cooperation with the experimental research [387, 388], two rare-earth free exchange-spring magnets, i.e., α''-$Fe_{16}N_2/SrAl_2Fe_{10}O_{19}$ composite [387] and MnBi/FeCo bilayer [388], are investigated by micromagnetic simulations with a focus on the microstructural effects on their magnetic properties. In particular, a new multiscale scheme is proposed to determining the interface exchange parameter for the MnBi/FeCo system. Here, Al-doped Sr-hexaferrite $SrAl_2Fe_{10}O_{19}$ particles in the sub-microscale and low temperature phase of MnBi films are typical hard magnetic materials. FeCo films are typical soft magnetic materials. However, α''-$Fe_{16}N_2$ nanoscale particles, which are synthesized via a two-step route developed by Dirba et al. [389], are of relatively high magnetocrystalline anisotropy energy and are more like semi-hard magnetic materials.

6.2 Effect of microstructural features in α''-Fe$_{16}$N$_2$/SrAl$_2$Fe$_{10}$O$_{19}$ composite

The soft phase in exchange-spring magnets is mainly to increase the magnetization, but negatively affects coercivity and energy product. Semi-hard magnetic materials as soft phase could potentially stabilize the coercivity, since they possess a much higher magnetocrystalline anisotropy energy than the ideally soft phases whose magnetocrystalline anisotropy is neglectable. The use of semi-hard magnetic materials in exchange-spring magnets is intriguing for the development of rare-earth free permanent magnets.

α''-$Fe_{16}N_2$ nanoparticles are demonstrated to be typical semi-hard phase [389]. The nanoparticles are synthesized by the nitrogenation in an ammonia flow of pure-phase α-Fe nanoparticles that are produced by the reduction of iron oxides at a hydrogen pressure of 53 MPa a low temperature of 483 K. They possess semi-hard magnetic properties with
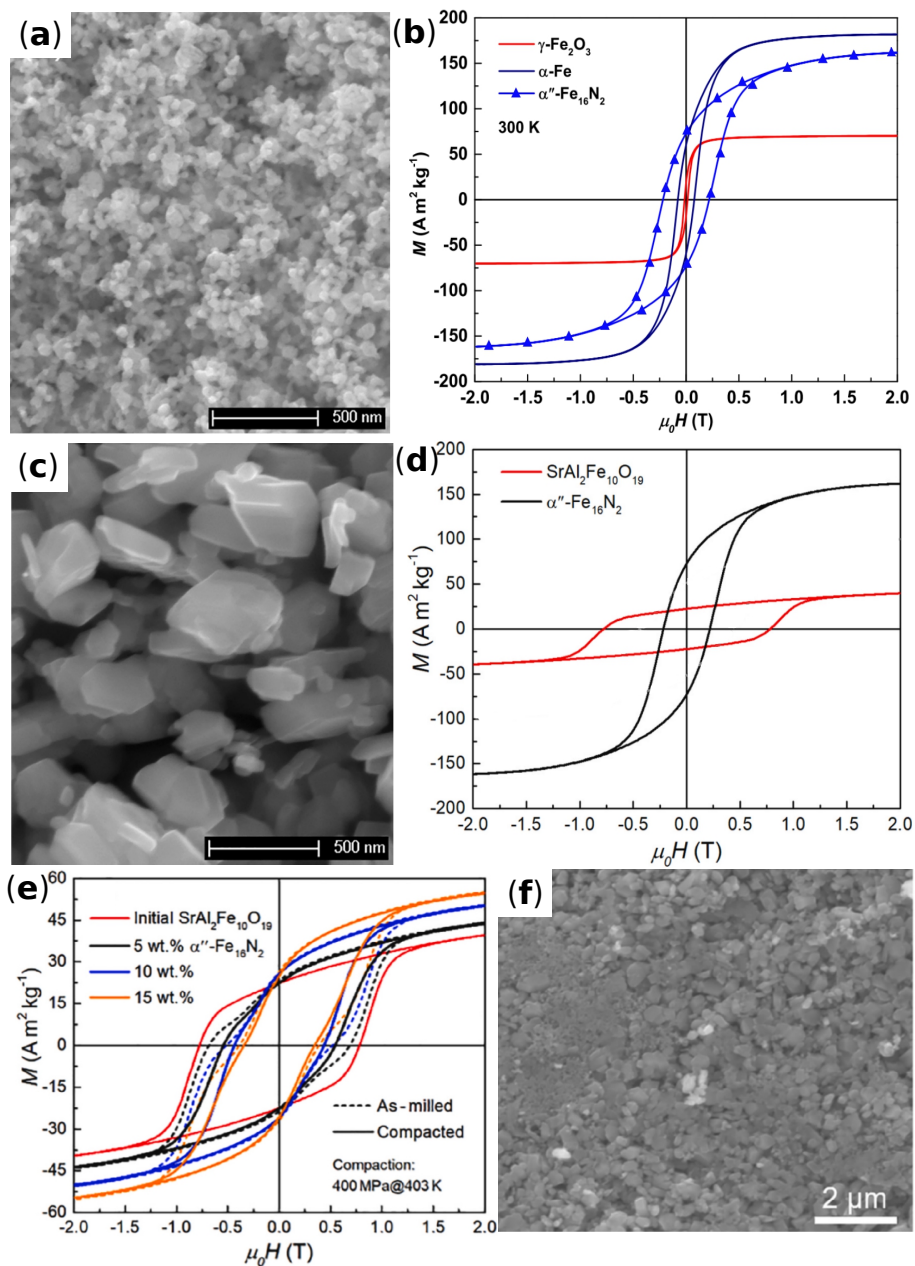
Figure 6.1: (a) Morphology of α''-$Fe_{16}N_2$ nanoparticles [389]. (b) Hysteresis of γ-Fe_2O_3, α-Fe, and α''-$Fe_{16}N_2$ at 300 K [389]. (c) Morphology of $SrAl_2Fe_{10}O_{19}$ particles [387]. (d) Hysteresis of α''-$Fe_{16}N_2$ and $SrAl_2Fe_{10}O_{19}$ powders [387]. (e) Hysteresis of as-milled and consolidated α''-$Fe_{16}N_2$/$SrAl_2Fe_{10}O_{19}$ magnet samples for different α''-$Fe_{16}N_2$ weight fractions [387]. (f) Morphology of consolidated α''-$Fe_{16}N_2$/$SrAl_2Fe_{10}O_{19}$ magnet [387].

magnetization saturation M_s = 162 Am^2/kg and coercivity $\mu_0 H_c$ = 0.22 T at room temperature, and Curie temperature T_c = 634 K [389]. The morphology and typical hysteresis of α''-Fe$_{16}$N$_2$ nanoparticles are shown in Figure 6.1(a) and (b). It can be seen that α''-Fe$_{16}$N$_2$ possesses a magnetization saturation close to α-Fe, but its coercivity is nearly three times as large as that in α-Fe. These intriguing magnetic properties together with the lost-cost and abundant Fe and N elements make α''-Fe$_{16}$N$_2$ nanoparticles as promising phases for the rare-earth free exchange-spring magnets. SrAl$_2$Fe$_{10}$O$_{19}$, which is doped with Al and thus possesses significantly enhanced coercivity but lower magnetization [390], is used as the hard phase. It is low-price for the application in nanocomposite magnets. The morphology and hysteresis of SrAl$_2$Fe$_{10}$O$_{19}$ powders are shown in Figure 6.1(c) and (d). It is clear that SrAl$_2$Fe$_{10}$O$_{19}$ particles are in the scale of sub-micro meter.

Figure 6.1(e) presents the hysteresis of the as-milled and compacted (at 403 K) samples with different loading of α''-Fe$_{16}$N$_2$ nanoparticles. It is found that the addition of α''-Fe$_{16}$N$_2$ gives rise to an notable increase in saturation magnetization and a slight increase in remanence. However, the coercivity is remarkably reduced and the square shape of the demagnetization curves is deteriorated significantly. This unfavorable features will not lead to an enhancement in $(BH)_{max}$. In addition, from Figure 6.1(f) which shows the morphology of the consolidated α''-Fe$_{16}$N$_2$/SrAl$_2$Fe$_{10}$O$_{19}$ composite, it is found that the magnets are simply slightly pressed powders with high porosity, loose interfaces, and poor mechanical stability [389]. Consequently, the nanoscale exchange-coupling between these two phases are not realized in this consolidated magnet, and the hysteresis loops apparently exhibit a two-step switching behavior.

Although the experimental results by Dirba et al. [389] do not show the increase of $(BH)_{max}$ by combining semi-hard α''-Fe$_{16}$N$_2$ and hard SrAl$_2$Fe$_{10}$O$_{19}$, they motivate theoretical studies to explore which kind of microstructural features could be important for guiding the future experimental endeavor to increase the performance of exchange-spring α''-Fe$_{16}$N$_2$/SrAl$_2$Fe$_{10}$O$_{19}$ composite. For this purpose the micromagnetic simulations were carried out in this subsection.

6.2.1 Simulation details

In order to unravel the possible microstructural factors which could influence the magnetic properties of α''-Fe$_{16}$N$_2$/SrAl$_2$Fe$_{10}$O$_{19}$ composite, micromagnetic simulations were conducted by using OOMMF [286]. The used material parameters are listed in Table 6.1. These two materials possess uniaxial anisotropy. With these parameters, the magnitude of the ratio $\kappa = \sqrt{K_1/(\mu_0 M_s^2)}$ for α''-Fe$_{16}$N$_2$ and SrAl$_2$Fe$_{10}$O$_{19}$ is estimated as 0.89 (not $\ll$ 1) and 2.38, respectively. Therefore, SrAl$_2$Fe$_{10}$O$_{19}$ is hard phase, whereas α''-Fe$_{16}$N$_2$ is not exactly a soft phase and should be a semi-hard phase with κ between 0.5 and 1 [148]. Whether the criterion for soft/hard exchange-spring magnets also holds for the semi-hard/hard cases should be further studied by micromagnetic simulations.

Table 6.1: Magnetic parameter of α''-Fe$_{16}$N$_2$ and SrAl$_2$Fe$_{10}$O$_{19}$ used in micromagnetic simulations.

	α''-Fe$_{16}$N$_2$	SrAl$_2$Fe$_{10}$O$_{19}$
$\mu_0 M_s$ (T)	1.23 [387]	0.23 [387]
K_1 (MJ/m^3)	0.96 [391]	0.238 [392]
A_e (pJ/m)	7 [389]	6 [393]

The exchange length ($\sqrt{2A_e/(\mu_0 M_s^2)}$) and domain wall width ($\pi\sqrt{A_e/K_1}$) are estimated as 3.4 and 8.5 nm for α''-Fe$_{16}$N$_2$, respectively, and 16.9 and 15.8 nm for SrAl$_2$Fe$_{10}$O$_{19}$, respectively. The finite-difference cell size in OOMMF should be less than the minimum of these values and is thus set as 2 nm. The exchange strength A_{int} between these two materials is usually difficult to determine experimentally and is varied to investigate its influence on the magnetic properties of composite. For calculating the hysteresis and reversal process under external magnetic field, Oxs_MinDriver and Oxs_CGEvolve in OOMMF are used, i.e., the conjugate gradient minimizer with no preconditioning. Parallel calculations based on OpenMP are used.

6.2.2 Quasi-1D simulation for size influence of α''-Fe$_{16}$N$_2$

Though the soft phase favors the increase in saturation magnetization, it could significantly decrease the coercivity. If the size of the soft phase is too large, the inhomogeneous distribution of the magnetization caused by reversible rotations in the soft magnetic phase will account for the reduction of coercivity. If the size of the soft magnetic phases l_s is less than twice of the domain wall width of the hard magnetic phase [394], .i.e,

$$l_s < 2\pi\sqrt{A_e/K_1^{\mathrm{h}}} \tag{6.1}$$

and the exchange between soft and hard phases is relatively strong, exchange interactions could suppress the reversible rotation of the magnetization in the soft magnetic phase. In this case, exchange coupling between the soft and hard magnetic phase override the effect of strong demagnetizing fields. Thus the inhomogenous magnetic state can be avoided and the coercivity remains remarkably high [375].

The domain wall width of typical hard phases is around several to tens of nanomaters. This requires that the size of soft phases should also be in the nanoscale, leading to serious experimental challenges in the fabrication of exchange-spring magnets in the bulk type. In addition, for the case of semi-hard phase α''-Fe$_{16}$N$_2$, the criterion for the size of semi-hard

phase changes to [394]

$$l_s < 2\pi \sqrt{A_e/\left(K_1^h - K_1^s\right)} \tag{6.2}$$

which indicates that the length-scale requirement of semi-hard phases are slightly more relaxed. For instance, in the case of $K_1^h = 0.238$ MJ/m^3 and $K_1^s = 0$ for purely soft phase, the
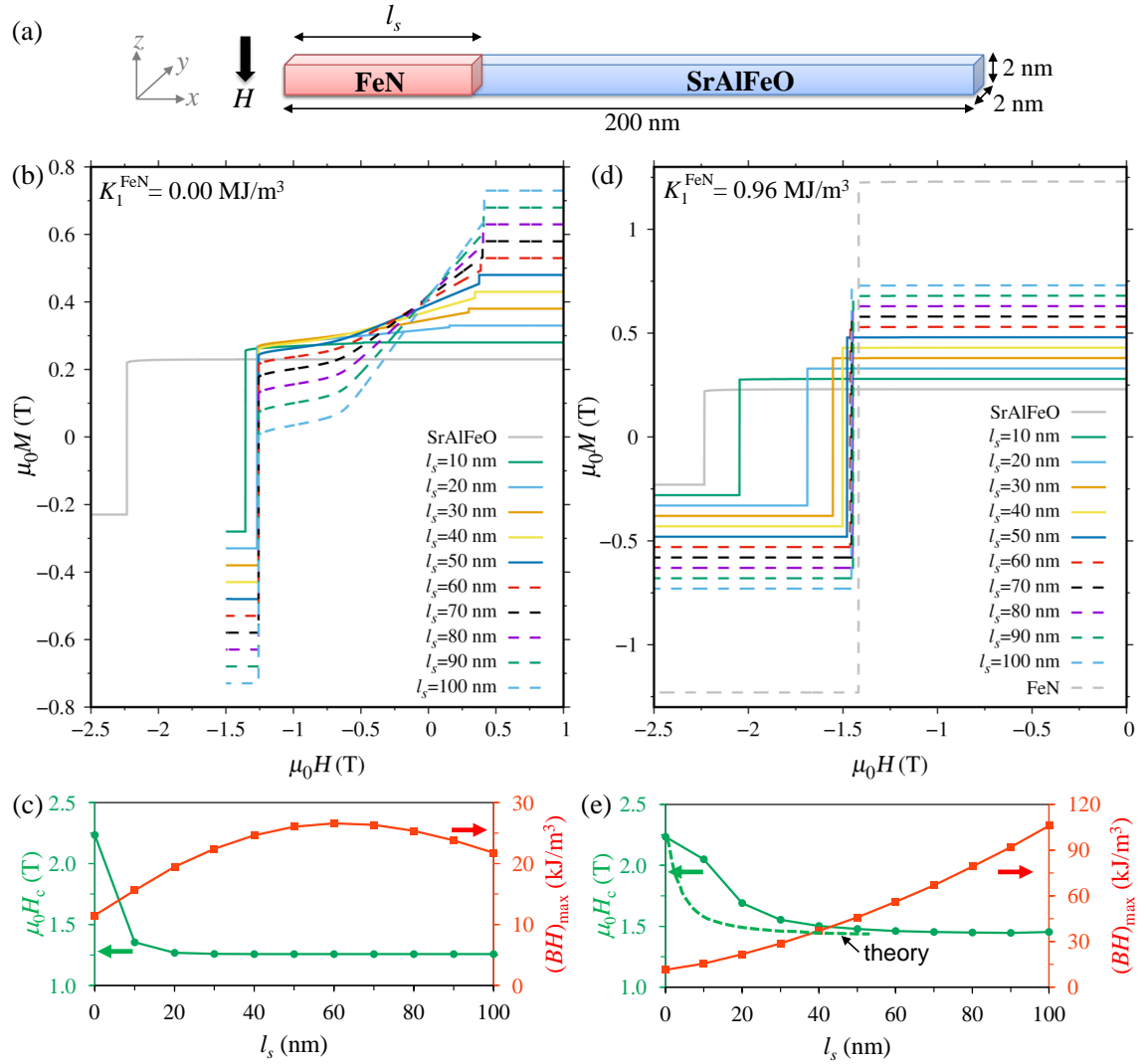
Figure 6.2: Micromagnetic simulation results of a quasi-1D geometry. (a) Illustration of the quasi-1D geometry with the length of FeN as l_s nm and the length of SrAlFeO as $(200-l_s)$ nm. The uniaxial easy axis is set along z direction. The reversal curves, coercivity and $(BH)_{max}$ as a function of l_s for (b) (c) $K_1^{FeN} = 0.00$ MJ/m^3 and (d) (e) $K_1^{FeN} = 0.96$ MJ/m^3. The theoretical curve in (e) is calculated by Equation 6.4. FeN: α''-Fe$_{16}$N$_2$; SrAlFeO: SrAl$_2$Fe$_{10}$O$_{19}$.

critical size is 31.5 nm. If a semi-hard phase is used, e.g., $K_1^s = 0.1$ MJ/m^3, the critical size is increased to 41.4 nm. The increase of the critical size can make the practical production and handling of the material slightly easy.

However, for the α''-Fe$_{16}$N$_2$/SrAl$_2$Fe$_{10}$O$_{19}$ composite here, the semi-hard phase even possesses a much higher K_1 than the hard phase, as shown in Table 6.1. This means that $K_1^h < K_1^s$ in the denominator of Equation 6.2, thus leading to a negative number under the square root and the invalidness of Equation 6.2. In addition, the pining field H_p expressed as [376]

$$H_p = \frac{2\left(A_e^h K_1^h - A_e^s K_1^s\right)}{\left(\sqrt{A_e^h M_s^h} + \sqrt{A_h^h M_s^h}\right)^2} \tag{6.3}$$

also turns out to be negative, implying that the pinning here disappears, and the nucleation is the dominant coercivity mechanism. Therefore, the α''-Fe$_{16}$N$_2$/SrAl$_2$Fe$_{10}$O$_{19}$ composite is an elusive system beyond the ability of the previous theoretical models.

In order to elucidate the discrepancy from the theoretical criterion in Equation 6.2 caused by the semi-hard phase, micromagnetic simulations are performed on a quasi-1D geometry shown in Figure 6.2(a). The geometry is similar to the 1D model in the early theoretical study of hard/ soft exchange-spring magnets [368]. The exchange between SrAl$_2$Fe$_{10}$O$_{19}$ and α''-Fe$_{16}$N$_2$ is set as a harmonic mean, i.e., 4.67 pJ/m. The 1D geometry is 200 nm long, with the length of α''-Fe$_{16}$N$_2$ as l_s. The influence of l_s on the demagnetization curve, coercivity, and $(BH)_{max}$ is examined. To be consistent with the previous theoretical study [368] and the requirement of Equation 6.2, as a first step we assume α''-Fe$_{16}$N$_2$ as a perfectly soft phase (i.e. $K_1^{FeN} = 0$). The results are presented in Figure 6.2(b) and (c). The demagnetization curve in Figure 6.2(b) exhibits a notable kink (indicator of poor exchange coupling) when l_s approaches 20–30 nm, which is consistent with the theoretical estimation of $2\delta_B \approx 31.5$ nm for α''-Fe$_{16}$N$_2$. Accordingly, as shown in Figure 6.2(c), the coercivity rapidly decreases with l_s and remains constant after $l_s \geq 30$ nm, while $(BH)_{max}$ reaches its maximum at $l_s = 50$–70 nm. These results are reasonable, since the perfectly soft phase satisfies the requirement of the previous theory of exchange-spring magnets.

In contrast, for the semi-hard α''-Fe$_{16}$N$_2$ phase examined here, the previous theory does not work. As shown in Figure 6.2(d), the demagnetization curves maintain the rectangular shape despite of l_s, indicating the coherent behavior and thus strong exchange coupling of the two phases. It can be also found in Figure 6.2(e) that the coercivity slowly decreases with l_s and remains almost unchanged after $l_s \geq 60$ nm. In the analytical model that describes the relation between l_s and nucleation field H_n [376], one has

$$l_s = \frac{2\sqrt{A_e^s/K_1^s}}{\sqrt{H_n/H_K^s - 1}} \arctan \sqrt{\frac{A_e^h K_1^h(1 - H_n/H_K^h)}{A_e^s K_1^s(H_n/H_K^s - 1)}} \tag{6.4}$$
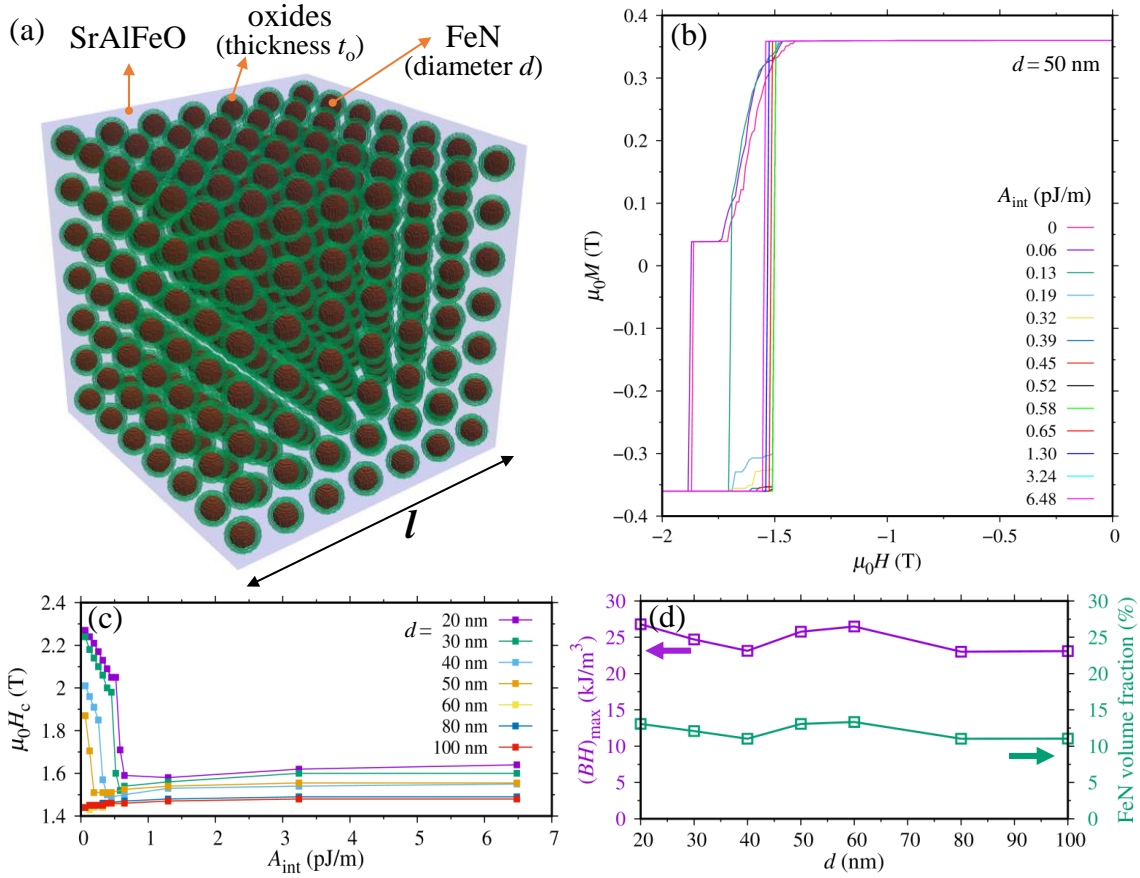
Figure 6.3: (a) Illustration of the micromagnetic model microstructure of α''-Fe$_{16}$N$_2$/SrAl$_2$Fe$_{10}$O$_{19}$ composite with l around 560 nm. (b) Demagnetization curves under different interface exchange (A_{int}) between α''-Fe$_{16}$N$_2$ and SrAl$_2$Fe$_{10}$O$_{19}$ (d = 50 nm, t_{o}=0). (c) Coercivity as functions of d and A_{int} (t_{o} = 0). (d) $(BH)_{\mathrm{max}}$ and α''-Fe$_{16}$N$_2$ volume fraction as a function of d (irrespective of A_{int}, t_{o} = 0).

in which $H_{\mathrm{K}}^{\mathrm{h}}$ and $H_{\mathrm{K}}^{\mathrm{s}}$ are the nucleation fields of hard and semi-hard phases, respectively. Here, from the demagnetization curves of pure α''-Fe$_{16}$N$_2$ and SrAl$_2$Fe$_{10}$O$_{19}$ in Figure 6.2(d), $\mu_0 H_{\mathrm{K}}^{\mathrm{h}}$ and $\mu_0 H_{\mathrm{K}}^{\mathrm{s}}$ are estimated as 2.23 and 1.42 T, respectively. Then Equation 6.4 can be plotted as the theoretical curve in Figure 6.2(e). It can be found that the micromagnetic simulation results follow the same trend as the theoretical prediction by Equation 6.4. Both show saturation behavior after $l_s \geq 50 - 60$ nm.

In Figure 6.2(e), $(BH)_{\mathrm{max}}$ always increases with l_s. Therefore, in this ideal model there is no optimal l_s for a strong exchange coupling and a maximum $(BH)_{\mathrm{max}}$. It should be noted that even though the simple 1D model does not consider microstructural features, it indeed reflects the prominent difference between hard/soft and hard/semi-hard nanocomposites.
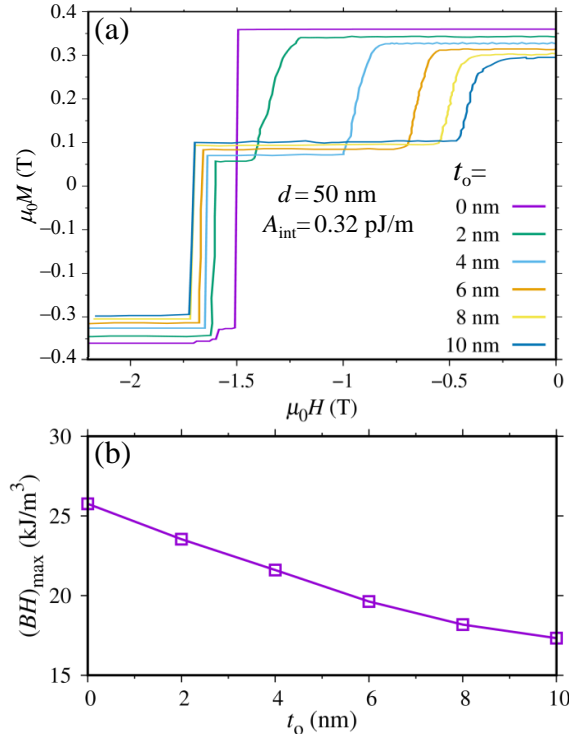
Figure 6.4: (a) Demagnetization curves and (b) $(BH)_{\text{max}}$ by micromagnetic simulations with different oxides thickness t_{o} (d = 50 nm, A_{int} = 0.32 pJ/m).

6.2.3 Role of interface exchange, diameter, oxide-layer thickness, and volume fraction of α''-Fe$_{16}$N$_2$

Even though the combination of semi-hard α''-Fe$_{16}$N$_2$ and hard SrAl$_2$Fe$_{10}$O$_{19}$ is expected to give rise to a high-performance exchange-spring magnet, the experimental attempts of producing bulk composite magnets show that these two phases are poorly exchange coupled and enhancing $(BH)_{\text{max}}$ is not achieved [387]. In order to understand the discrepancy between the expected and experimental results, micromagnetic simulations based on ideal microstructure models are carried out. The goal is not to reproduce the experimental results, but to computationally elucidate which microstructural features should be tailored to improve the specific magnetic properties of interests. The significance of micromagnetic simulation results in this subsection is helpful to assist the experimentations to improve the performance of α''-Fe$_{16}$N$_2$/SrAl$_2$Fe$_{10}$O$_{19}$ composite by microstructure engineering.

There are multiple factors in experiments influencing the magnetic properties of the prepared composites. In order to elucidate the possible role of different microstructural features on the magnetic properties of the α''-Fe$_{16}$N$_2$/SrAl$_2$Fe$_{10}$O$_{19}$ composites, we have carried out micromagnetic simulations of the ideal model microstructure shown in Figure 6.3(a), where evenly distributed α''-Fe$_{16}$N$_2$ spherical nanoparticles are embedded in SrAl$_2$Fe$_{10}$O$_{19}$
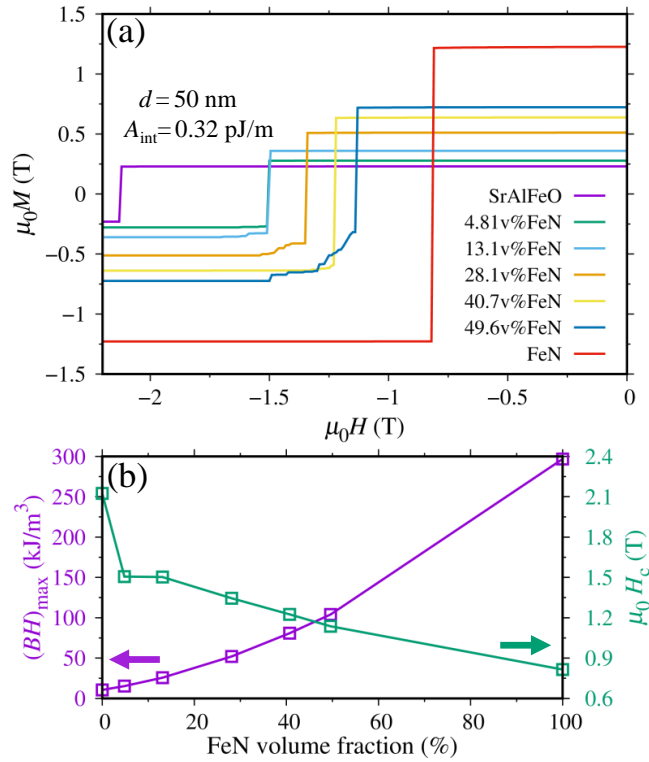
Figure 6.5: (a) Demagnetization curves and (b) $(BH)_{max}$ and coercivity by micromagnetic simulations with different volume fractions of α''-Fe$_{16}$N$_2$ (d = 50 nm, A_{int} = 0.32 pJ/m, t_o = 0).

matrix. Emphasis is put on the role the interface exchange (A_{int}) between α''-Fe$_{16}$N$_2$ and SrAl$_2$Fe$_{10}$O$_{19}$ and the diameter (d) and the volume fraction of α''-Fe$_{16}$N$_2$ nanoparticles. The oxides are found to exist on the surfaces of α''-Fe$_{16}$N$_2$ nanoparticles [389], so the surface oxide layer thickness (t_o) should be also considered.

In simulations, the surface oxides with a thickness of t_o is assumed to have zero magnetocrystalline anisotropy and a saturation magnetization which is half of that in the pure α''-Fe$_{16}$N$_2$ nanoparticle. Figure 6.3(b) presents the typical demagnetization curves for d = 50 nm and different A_{int}, from which it can be seen that two phases are magnetically reversed simultaneously when A_{int} reaches a critical value (e.g. 0.2 pJ/m here). As shown in Figure 6.3(c), the coercivity rapidly decreases with A_{int} for d = 20–50 nm and remains almost constant when d exceeds 60 nm. This is exactly consistent with the results in Figure 6.2(e). In addition, the critical A_{int} for the occurrence of the coercivity plateau decreases with the increasing d. This suggests that small α''-Fe$_{16}$N$_2$ nanoparticles and small interface exchange favor high coercivity, and an interface exchange in the order of 0.01 and 0.1 pJ/m is possibly enough.

The $(BH)_{max}$ calculated from the similar demagnetization curves in Figure 6.3(b) is

found nearly independent of A_{int}, but correlated to d and thus the volume fraction of α''-Fe$_{16}$N$_2$ nanoparticles, as shown in Figure 6.3(d). In addition, the demagnetization curves in Figure 6.4(a) and $(BH)_{\text{max}}$ in Figure 6.4(b) imply the significant influence of surface oxide thickness.

The role of volume fraction of α''-Fe$_{16}$N$_2$ nanoparticles is depicted in Figure 6.5(a) and (b). It is obvious that $(BH)_{\text{max}}$ increases with volume fraction of α''-Fe$_{16}$N$_2$ nanoparticles, while the coercivity decreases with it. There is a trade-off between the coercivity and $(BH)_{\text{max}}$ of the composite. It should be mentioned that the pure α''-Fe$_{16}$N$_2$ bulk (i.e. 100% volume fraction) in Figure 6.5(b) with the highest $(BH)_{\text{max}}$ is an ideal case but not practically achievable, due to the low coercivity and the poor form of nanoparticles.

The micromagnetic simulations suggest that d and A_{int} are decisive factors for the coercivity. $d \leq 50$ nm and A_{int} in the order of 0.01–0.1 pJ/m enable coercivity enhancement. Reducing surface oxidation and increasing α''-Fe$_{16}$N$_2$ volume fraction would play a decisive role in enhancing the $(BH)_{\text{max}}$.

6.3 Effect of interface roughness and FeCo thickness in MnBi/FeCo bilayer

Bulk-type exchange-spring magnets are usually produced by a nanodispersed composite in bulk processing, as an typical example of α''Fe$_{16}$N$_2$/SrAl$_2$Fe$_{10}$O$_{19}$ composite shown in Section 6.2. However, the microstructural complexities in the composites with randomly distributed nanoparticles often make it difficult to control the microstructure and to identify the factors that affect the reversal process. In contrast, film-type exchange-spring magnets have a simple structure with clear interfaces, which are amenable to a wider variety of microscopic characterization tools than that in nanocomposites. As a model system, the film structure possibly provides the opportunity to reveal the magnetization reversal processes and establish the microstructure-properties relationship [395].

In this section, micromagnetic simulations are performed on the MnBi/FeCo bilayer which is a typical rare-earth free exchange-spring thin-film magnets. The simulations are motivated by the experimental work by Sabet et al., [388] who deposited exchange coupled MnBi/FeCo bilayer onto quartz glass substrates in a dc magnetron sputtering system. The low temperature phase of MnBi is of a high magnetocrystalline anisotropy around several MJ/m^3 [396] and of a low saturation magnetization around 0.714 MA/m [397], making it a candidate as the rare-earth free hard phase. FeCo as a soft phase is of high saturation magnetization. The combination of MnBi and FeCo is promising to yield an exchange-spring magnets with superior properties.

However, experimental results indicate that MnBi/FeCo bilayers does not show enhanced magnetic performance. The hysteresis loops of MnBi/FeCo bilayers apparently exhibit two-

step switching behavior, with the first shoulder in the demagnetization curve corresponding to switching of the magnetically softer FeCo phase and the second one to the magnetically harder MnBi, as shown in Figure 6.6 [388]. This indicates a poor exchange coupling between MnBi and FeCo. In this regard, micromagnetic simulations are carried out to investigate the influence of two typical microstructural features, i.e., interface roughness and FeCo layer thickness. The target is not to reproduce the experimentally measured hysteresis loops.

6.3.1 Simulation details

Micromagnetic simulations were performed within a simplified model to investigate the mechanism of exchange coupling in MnBi/FeCo magnets by using the OOMMF code [286]. In the micromagnetic model, the thicknesses of the hard MnBi and soft FeCo layers (initially) are set as 40 and 0.5–8 nm, respectively. The lateral size is chosen as 8×8 nm^2 and an in-plane periodic boundary condition is applied. The model was discretized by 0.4 nm $\times$ 0.4 nm $\times$ 0.1 nm cuboid cells. Magnetic reversal curves are calculated by setting the initial magnetization along a positive z axis and changing the external magnetic field along z axis from positive to negative values.

Another important issue is the determination of interface exchange parameters (A_{int}) for micromagnetic simulations in OOMMF. The determination of A_{int} in the micromagnetic framework from the DFT-determined J_{int} is nontrivial. In most of the literature on the micromagnetic simulations of exchange-coupled magnets, the parameter A_{int} is chosen to be the same as the value in the bulk material, or to be artificially modulated to study its influence on the exchange-coupled behavior. Indeed, the equations of Equations 4.25 and 4.26 in [130] present a way to estimate the effective exchange between grains. But
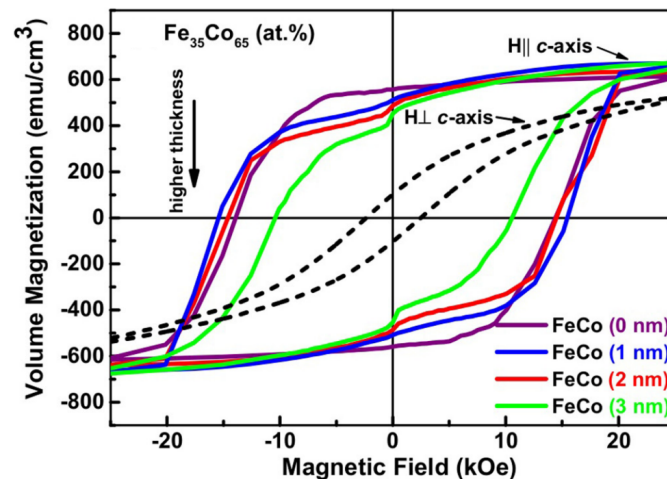
Figure 6.6: Experimentally measured magnetization hysteresis loops at 300 K for MnBi/FeCo bilayers with different FeCo thicknesses from 0 to 3 nm [388].
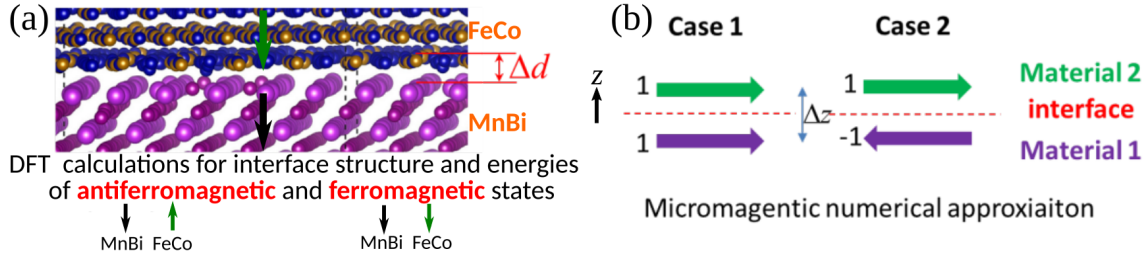
Figure 6.7: (a) MnBi/FeCo energies in the ferromagnetic and antiferromagnetic states and average interface distance Δd determined from DFT calculations by Moradabadi [388]. (b) Two magnetization configurations for the estimation of micromagnetic parameter A_{int}.

how to combine these equations with DFT results still remains to be explored. In other words, even though one has obtained the interlayer or interface exchange coupling energy from DFT calculations, the reasonable transfer of the DFT results to the continuum micromagnetic simulations (i.e., the parameter A_{int}) is not that easy. For the bulk materials, we can estimate the continuum or macroscopic exchange parameters A_{e} by calculating the domain wall width and magnetocrystalline anisotropy constant through the combination of DFT calculations and atomistic spin model simulations, as shown in Chapter 3. But for the interface case, the parameter A_{int} is unattainable by using this way.

In this section, considering the current difficulties in physically bridging first-principles results and micromagnetic interface exchange parameter A_{int}, as a compromise an alternative method is attempted. A_{int} is estimated by using the DFT results and the definition of continuum exchange energy in OOMMF code in the viewpoint of numerical implementation and energy equivalence. The DFT calculations can determine the average interface distance and the interface exchange coupling energy J_{int} expressed as the energy difference between ferromagnetic and antiferromagnetic states, as shown in Figure 6.7(a). J_{int} with one interface of area S is calculated as

$$J_{\mathrm{int}} = \frac{E^{\mathrm{AFM}} - E^{\mathrm{FM}}}{S} \tag{6.5}$$

in which E^{AFM} and E^{FM} are DFT-calculated energies of antiferromagnetic and ferromagnetic states, respectively. It should be noted that this expression of J_{int} is widely used to estimate the interface exchange coupling energy by using the DFT results as input, as shown in other exchange-spring magnetic system [198, 337].

In order to illustrate the method in numerical micromagnetics, the two cases with parallel and antiparallel magnetization are considered, as shown in Figure 6.7(b). According to the micromagnetic OOMMF code, the exchange energy density contribution in the cell i is

Table 6.2: Micromagnetic parameters for hard MnBi and soft FeCo phases [396, 398].

	MnBi	FeCo
$\mu_0 M_s$ (T)	0.81	2.47
K_1 (MJ/m^3)	1.86	0.0
A_e (pJ/m)	8	10

Table 6.3: Interface exchange parameter A_{int} and interface exchange coupling energy (J_{int} from DFT results by Moradabadi [388]) of MnBi/FeCo bilayer system.

Bilayer system	J_{int} (J/m^2)	A_{int} (pJ/m)
MnBi(001)/crystalline Fe$_3$Co$_5$(111)	0.129	5.4
MnBi(001)/disordered Fe$_3$Co$_5$(110)	0.082	1.9

numerically implemented as [286]

$$E_i = \sum_{j \in N_i} A_{ij} \frac{\mathbf{m}_i \cdot (\mathbf{m}_i - \mathbf{m}_j)}{\Delta_{ij}^2} \tag{6.6}$$

in which $\mathbf{m}_i$ is the magnetization unit vector of cell i, Δ_{ij} is the distance between cells i and j, and A_{ij} is the exchange constant between cells i and j. Therefore, the micromagnetic exchange energy density difference in the two cases in Figure 6.7(b) can be numerically approximated as

$$\Delta E = \frac{2A_{int}}{\Delta z^2} \tag{6.7}$$

in which Δz is the cell size along z direction. This energy density difference is assumed to equal to that from the DFT calculations, i.e.,

$$\frac{2A_{int}}{\Delta z^2} = \frac{J_{int}}{\Delta d} \quad \Rightarrow \quad A_{int} = \frac{J_{int} \Delta z^2}{2\Delta d} \tag{6.8}$$

in which Δd is the average interface distance measured from the crystal structures after relaxation from DFT calculations, as shown in Figure 6.7(a). It should be mentioned that the Equation 6.8 is not a physical expression, but a result of the numerical approximation of the treatment of exchange energy in micromagnetic OOMMF code. $\Delta z = 0.1$ nm is also not a physical length, but a numerical discretization size along the thickness direction of the extremely thin FeCo film (0–6 nm).

In the layered structure, DFT calculations are performed to obtain the interface exchange

coupling energy (J_{int}) in MnBi(001)/crystalline Fe$_3$Co$_5$(111) and MnBi(001)/disordered Fe$_3$Co$_5$(110) interfaces by Moradabadi [388]. Using the above methodology and the DFT results from Moradabadi [388], the micromagnetic parameters are determined and listed in Tables 6.2 and 6.3.

6.3.2 Effect of interface roughness

Since the microstructure of the experimental MnBi/FeCo bilayer samples are extremely complicated which usually cannot be fully included in simulations, the simplified models and the qualitative information on the exchange behavior are aimed. The simplified model with an in-plane size 8 nm$\times$8 nm, 40 nm thick MnBi, and 2 nm thick Fe$_3$Co$_5$ is shown in Figure 6.8(a). Periodic boundary conditions are applied in the $x-y$ plane. The external magnetic field is applied along z axis from 2.5 T to –2.5 T.

Experimental microscopic characterizations have shown that the interface between MnBi and FeCo is not exactly flat or sharp and is rather rough [388]. Therefore, apart from the interface exchange coupling energy, the interface roughness should also be a critical factor that can influence the interfacial exchange coupled behavior. Figure 6.8(b) presents the morphology of the interfacial roughness that is implemented in micromagnetic simulations. The interfacial roughness is modeled by introducing randomly distributed dents into the MnBi surface. The deepest depth of these dents is set around 0.4 nm.

MnBi/Fe$_3$Co$_5$ model systems with crystalline Fe$_3$Co$_5$(111) orientation and disordered Fe$_3$Co$_5$(110) orientation are studied. The following four cases are considered.

(1) The interface is perfect and flat. The associated interface exchange parameter for crystalline Fe$_3$Co$_5$(111) orientation is $A_{\mathrm{int}}^{(111)} = 5.4$ pJ/m and for disordered Fe$_3$Co$_5$(110) orientation is $A_{\mathrm{int}}^{(110)} = 1.9$ pJ/m. The demagnetization curves by micromagnetic simulations are presented in Figure 6.8(c).

(2) The interface is rough, with the roughness modeled in Figure 6.8(b). The associated interface exchange parameter A_{int} is the same as that in the case (1). The demagnetization curves by micromagnetic simulations are presented in Figure 6.8(d).

(3) The rough interface is the same as that in the case (2), but the interface exchange parameters are reduced by 70%, i.e., $A_{\mathrm{int}}^{(111)} = 1.62$ pJ/m and $A_{\mathrm{int}}^{(110)} = 0.57$ pJ/m. The demagnetization curves by micromagnetic simulations are presented in Figure 6.8(e).

(4) The rough interface is the same as that in the case (2), but the interface exchange parameters are reduced by 90%, i.e., $A_{\mathrm{int}}^{(111)} = 0.54$ pJ/m and $A_{\mathrm{int}}^{(110)} = 0.19$ pJ/m. The demagnetization curves by micromagnetic simulations are presented in Figure 6.8(f).

It should be noted that the simulated magnetic reversal curves in Figure 6.8(c)-(f) do not show the kinks that are observed in the measured hysteresis loops of the experimental samples in Figure 6.6 [388]. The possible reason is that the simplified model does

not include the complicated microstructure in the real experimental samples, or that the residual in-plane magnetization component of the hard magnetic phase is ignored in the micromagnetic simulations. Therefore, the kinks in the simulated reversal curves will not
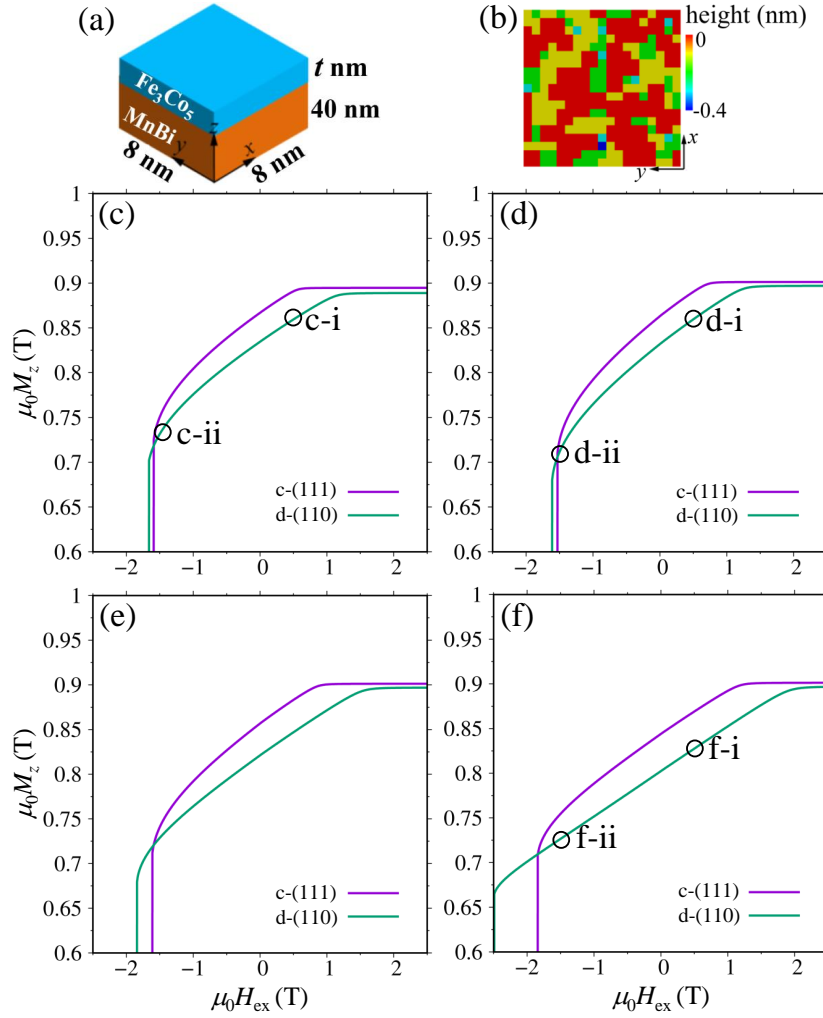
Figure 6.8: (a) Micromagnetic model geometry with in-plane periodic boundary condition (t = 2 nm). (b) Interfacial roughness of MnBi with a maximum dent height of 0.4 nm. Micromagnetic simulation results of demagnetization curves for (c) no interface roughness with A_{int} value listed in Table 6.3, (d) interface roughness with the same A_{int} as in (c), (e) interface roughness with A_{int} reduced to 30% of that in (d), and (f) interface roughness with A_{int} reduced to 10% of that in (d). c-(111) and d-(110) denote MnBi/Fe$_3$Co$_5$ model system with crystalline FeCo(111) and disordered FeCo(110), respectively. The external magnetic field $\mu_0 H_{ex}$ is applied along the z direction.
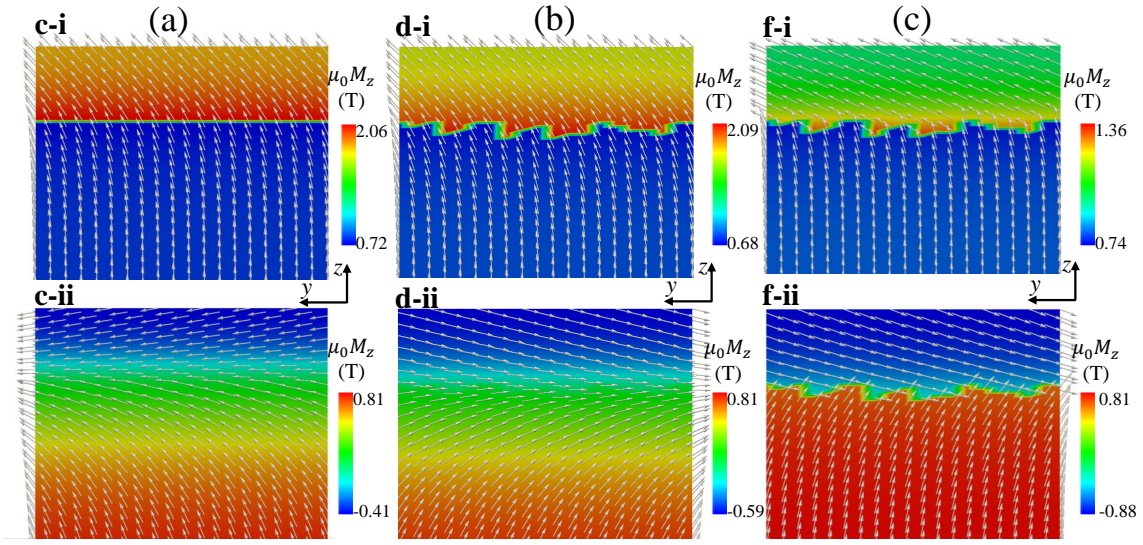
Figure 6.9: (a) (b) (c) Magnetic configurations (yz surfaces at $x = 0$) corresponding to the marked circles in reversal curves in Figure 6.8(c), (d), (f), respectively.

be focused to analyze the interface exchange behavior in MnBi/FeCo bilayers.

The magnetic configuration and its evolution around the interface of MnBi/disordered $Fe_3Co_5(110)$ model system at different external fields are examined, as shown in Figure 6.9 corresponding to the markers in Figure 6.8(c), (d) and (f). When the interface is assumed to be perfect and $A_{int}^{(110)} = 1.9$ pJ/m from Table 6.3 is used, the magnetization vectors near the interface in FeCo tend to rotate coherently with those in MnBi, as shown in Figure 6.9(a). This indicates a strong interface exchange coupling.

If a rough interface is assumed and $A_{int}^{(110)}$ remains the same, Figure 6.8(b) still suggests strong interface exchange coupling. But the interface magnetization vectors are much easier to be reversed. This can be verified by comparing the distribution of magnetization z component ($\mu_0 M_z$). For example, at $\mu_0 H_{ex} = 0.5$ T, the model with rough interface shows a minimum $\mu_0 M_z$ ($\mu_0 M_z^{min}$) of 0.68 T around the interface (d-i of Figure 6.9(b)), but the model without roughness shows a little higher $\mu_0 M_z^{min}$ (c-i of Figure 6.9(a)). The premature reversal in c-i and c-ii of Figure 6.9(b) could be attributed to the local higher demagnetization field induced by the sharp corners or irregularities in the rough interface [74, 165, 363]. Accordingly, the simulated coercivity in Figure 6.8(d) is also slightly smaller than that in Figure 6.8(c).

If the interface is rough and the interface exchange parameter is reduced by 70%, i.e., $A_{int}^{(110)} = 0.57$ pJ/m, the shape of demagnetization curve in Figure 6.8(e) is similar to that in Figure 6.8(d). But the reversal process starts much early and the coercivity is a little higher.

If the interface roughness is thought as defects that significantly reduce the interface

exchange parameter by 90%, i.e., $A_{\text{int}}^{(110)} = 0.19$ pJ/m, magnetic reversal curve presents a straight line, as shown in Figure 6.8(f). From the magnetic configuration in Figure 6.9(c), it can be also found that the magnetization vectors around the interface cross each other and the magnetization in FeCo almost rotates freely, indicating very poor interface exchange coupling.

It can be concluded from Figures 6.8 and 6.9 that even though the interface exchange coupling strength evaluated from DFT calculations of ideal interface structure provides useful insight into the atomic or compositional design of MnBi/FeCo bilayer magnets, the interface roughness or irregularity could also be critical since it can induce locally premature reversal and thus deteriorate the interface exchange coupling.

6.3.3 Effect of FeCo thickness

Figure 6.10(a), (b), and (c) summarizes the dependence of demagnetization curves on the FeCo thickness in MnBi(001)/disordered Fe$_3$Co$_5$(110) bilayers without roughness and $A_{\text{int}}^{(110)} = 1.9$ pJ/m, with roughness and $A_{\text{int}}^{(110)} = 1.9$ pJ/m, and with roughness and $A_{\text{int}}^{(110)} = 0.19$ pJ/m, respectively.

In the case of no interface roughness and $A_{\text{int}}^{(110)} = 1.9$ pJ/m in Figure 6.10(a), when the FeCo thickness is above 1 nm, magnetic reversal notably occurs even in the positive external field. This is due to the competition between the exchange field exerted by the hard MnBi layer and the demagnetization field within FeCo layer. Since FeCo layer is of extremely high saturation magnetization, its magnetization tends to lie in the plane in order to reduce the demagnetization energy. If the FeCo layer is thin (e.g. $t \leq 1$ nm), the exchange field exerted by the hard MnBi layer is enough to overcome the demagnetization field within FeCo layer and hold the FeCo magnetization out of plane in the presence of zero or even negative external field. However, if FeCo layer is thick (e.g. $t \geq 2$ nm), the exchange field is incapable of holding all the magnetization in FeCo layer out of plane. So the FeCo magnetization is spontaneously reversed towards in plane even when a positive external field is applied. In the case of interface roughness and the same $A_{\text{int}}^{(110)} = 1.9$ pJ/m in Figure 6.10(b), the phenomena are similar. But the FeCo magnetization is already reversed at zero external field when $t = 1$ nm. This premature reversal is due to the interface roughness that induces local demagnetization field to favor the reversal.

When the interface roughness reduces $A_{\text{int}}^{(110)}$ to 0.19 pJ/m in Figure 6.10(c), the exchange field is so weak that the FeCo magnetization is spontaneously reversed towards in plane even when $t = 0.5$ nm. For $t \geq 1$ nm, the demagnetization curves are more like straight lines, implying extremely weak exchange coupling between MnBi and FeCo. This indicates that interface roughness induced $A_{\text{int}}^{(110)}$ reduction could require a much thinner FeCo layer for a well exchange coupling.

The influence of both interface roughness and FeCo thickness on coercivity H_{c} and energy

146
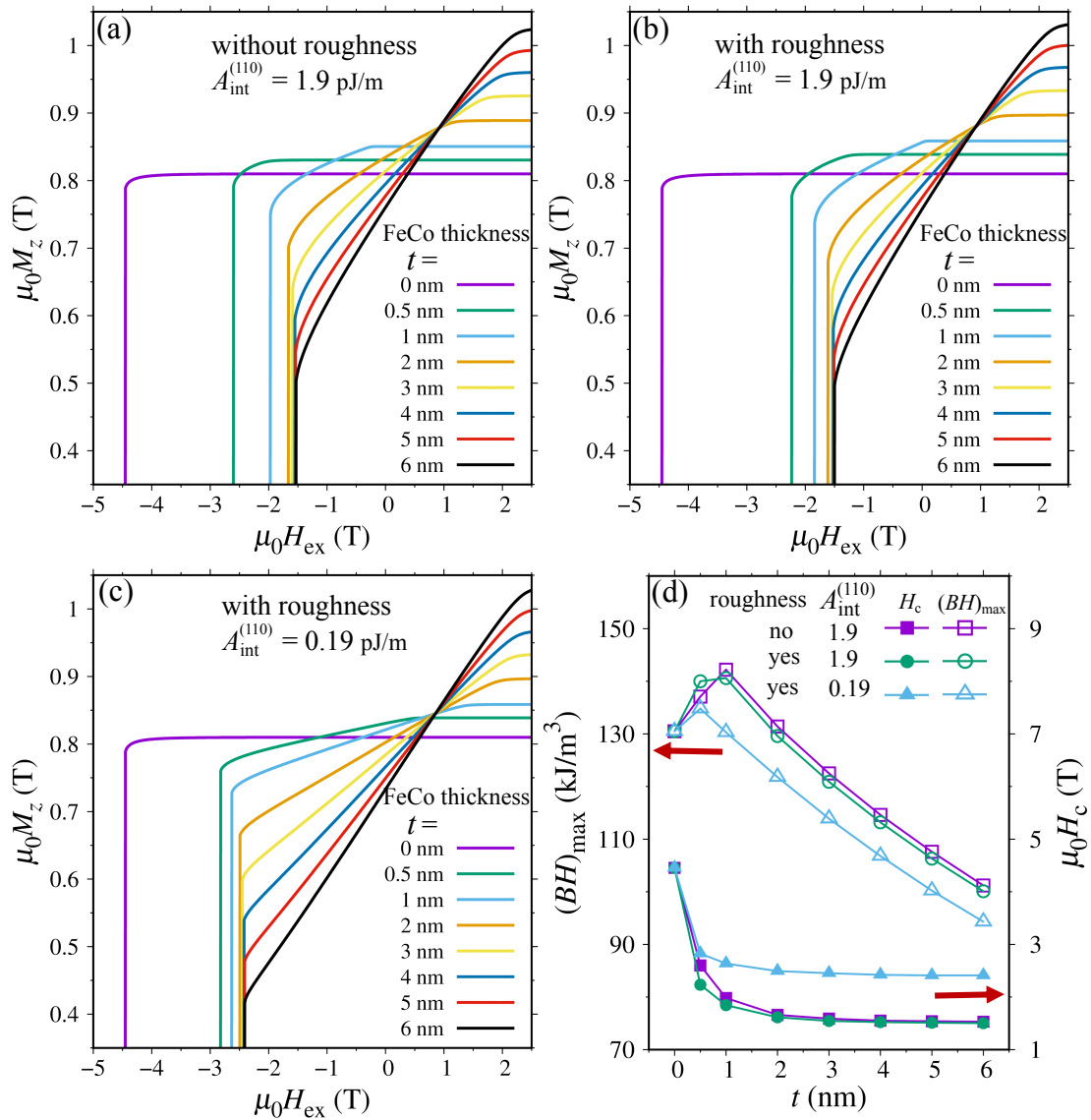
Figure 6.10: Micromagnetic simulation results of demagnetization curves in MnBi(001)/disordered Fe$_3$Co$_5$(110) bilayers including (a) no interface roughness with $A_{\text{int}}^{(110)}$ = 1.9 pJ/m, (b) interface roughness with the same $A_{\text{int}}^{(110)}$ as in (a), (c) interface roughness with $A_{\text{int}}^{(110)}$ reduced to 10% of that in (a). (d) Coercivity and $(BH)_{\text{max}}$ as a function of FeCo thickness in MnBi(001)/disordered FeCo(110) bilayers.

product $(BH)_{\text{max}}$ is summarized in Figure 6.10(d). It can be found that H_{c} decreases with the increasing FeCo thickness. This is expected since soft phase usually reduces the coercivity. The case with interface roughness and reduced $A_{\text{int}}^{(110)}$ = 0.19 pJ/m possesses the highest

H_c, which is governed by hard MnBi due to the weak exchange coupling. For a constant $A_{\text{int}}^{(110)} = 1.9$ pJ/m, both H_c and $(BH)_{\text{max}}$ is sightly higher in the case without interface roughness than with roughness. As for the energy product, $(BH)_{\text{max}}$ reaches its maximum at $t = 1$ and 0.5 nm for $A_{\text{int}}^{(110)} = 1.9$ and 0.19 pJ/m, respectively. The maximum $(BH)_{\text{max}}$ achieved in $A_{\text{int}}^{(110)} = 1.9$ pJ/m is larger than that in $A_{\text{int}}^{(110)} = 0.19$ pJ/m. This suggests that if the interface roughness significantly reduces the interface exchange parameter by 90%, a high coercivity but a low energy product (maximum at $t = 0.5$ nm) will be obtained. If the strong interface exchange coupling can be kept irrespective of the interface roughness, a low coercivity but a much higher energy product (maximum at $t = 1$ nm) could be obtained. A 1-nm thick FeCo layer and an interface exchange parameter around 2 pJ/m could improve the energy product by 10% when compared to the pure MnBi layer.

6.4 Summary

In summary, for the rare-earth free exchange-spring α''-Fe$_{16}$N$_2$/SrAl$_2$Fe$_{10}$O$_{19}$ composite magnet, it is revealed by micromagnetic simulations that the previous theory for the magnetically hard/soft-phase composites, i.e., the critical size of soft phase is twice the domain wall width of the hard phase, does not work for the hard/semi-hard-phase composite in this chapter. The α''-Fe$_{16}$N$_2$ nanoparticle diameter and interface exchange are decisive for the coercivity. The α''-Fe$_{16}$N$_2$ nanoparticle diameter is suggested to be less than 50 nm. The α''-Fe$_{16}$N$_2$/SrAl$_2$Fe$_{10}$O$_{19}$ interface exchange in the order of 0.01–0.1 pJ/m enables the coercivity enhancement. Less surface oxides and higher volume fraction of α''-Fe$_{16}$N$_2$ nanoparticles are very important for enhancing the $(BH)_{\text{max}}$ of the composite.

For the rare-earth free exchange-spring MnBi/FeCo bilayer, we proposed a compromising scheme to calculate the interface exchange parameter from DFT calculations. It enables a reasonably parameterized micromagnetic simulations. Results demonstrate that the interface roughness between the hard MnBi and soft FeCo layers as well as the soft FeCo layer thickness governs the effectiveness of exchange coupling. The interface roughness could significantly reduce the interface exchange strength and thus result in weak exchange coupling in MnBi/FeCo bilayer and premature reversal in soft FeCo layer. The coercivity of MnBi/FeCo bilayer decreases with the increasing thickness of FeCo layer, while $(BH)_{\text{max}}$ reaches a maximum at an FeCo-layer thickness around 1 and 0.5 nm for the strong (around 2 pJ/m) and weak (around 0.2 pJ/m) interface exchange, respectively. The $(BH)_{\text{max}}$ could be improved by 10% (compared to the pure MnBi layer), when FeCo layer is 1-nm thick and the interface exchange parameter is around 2 pJ/m.

7 Conclusions and outlook

7.1 Conclusions

To conclude, the thesis presents the multiscale simulations for the calculation of intrinsic and extrinsic properties of permanent magnets including Nd-Fe-B magnets as well as rare-earth free exchange-spring α''-$Fe_{16}N_2$/$SrAl_2Fe_{10}O_{19}$ composite and MnBi/FeCo bilayer. A multiscale computational scheme integrating DFT calculations, atomistic spin model (ASM) simulations, and micromagnetic simulations (stochastic Landau–Lifshitz equation for finite temperatures) is proposed to calculate: (1) the zero-temperature intrinsic properties including atomic magnetic moment μ_s, interatomic exchange interactions J_{ij}, and atomic magnetocrystalline anisotropy k_i or crystal-field energy $\mathcal{H}_{cf}$; (2) the finite-temperature intrinsic properties including saturation magnetization $M_s(T)$, exchange stiffness constant $A_e(T)$ and its anisotropy, effective magnetocrystalline anisotropy constants $K_i^{eff}(T)$, and Néel/Bloch domain wall width $\delta_w(T)$; (3) the extrinsic properties including microstructure dependent interface exchange coupling strength J_{int}, magnetization reversal mechanism, coercivity H_c and energy product $(BH)_{max}$ with or without the consideration of finite-temperature fluctuations.

The ASM simulations provoke a scale bridge between electronic-level DFT calculations and microstructure-level micromagnetic simulations, enabling a holistic computational framework which covers and integrates electronic, atomistic, and microstructural information in the simulation of magnetic materials. The mapping from ASM simulation results to macroscopically magnetic quantities should be based on the currently available or newly established continuum models.

For the intrinsic properties of $Nd_2Fe_{14}B$ main phase in Nd-Fe-B permanent magnets, the multiscale framework yields the temperature dependent $M_s(T)$, $A_e(T)$, $K_i^{eff}(T)$, and $\delta_w(T)$ of $Nd_2Fe_{14}B$, which match well with the experimental measurements. The spin reorientation phenomenon at low temperature is also well predicted. Specifically, the bulk exchange stiffness in $Nd_2Fe_{14}B$ is found to be intrinsically anisotropic (i.e., depend on the crystallographic axis) and its value along c axis is lower than along a/b axis.

For the extrinsic properties of Nd-Fe-B permanent magnets including the typical microstructural feature of grain boundary (GB), the "double anisotropy" phenomenon regarding to GB is discovered. In addition to the anisotropy in GB composition or magnetization, the

interface exchange coupling strength (J_{int}) between $Nd_2Fe_{14}B$ and GB is also confirmed to be strongly anisotropic. Even if the GB $Fe_xNd_{1\text{-}x}$ has the same composition, J_{int} for (100) interface is much higher than that for (001) interface. The exchange anisotropy is shown to obviously influence the coercivity of Nd-Fe-B magnets, inspiring the design of high-performance Nd-Fe-B permanent magnets by tailoring exchange.

For the extrinsic properties of Nd-Fe-B permanent magnets including the typical microstructural feature of soft defect layer and/or Dy-rich hard shell, finite-temperature micromagnetic simulations with ASM simulations results as input are performed. It is demonstrated that in addition to the decrease of anisotropy field with temperature, the thermal fluctuations further reduce coercivity by 5–10% and its temperature coefficient by 0.02–0.1%/K in the presence of a defect layer. The defect layer with strong magnetization (e.g. 1 T) is shown to significantly decrease coercivity, but suppress the influence of thermal fluctuations. Both coercivity and its temperature coefficient can be increased by adding the Dy-rich hard shell, but saturate at a shell thickness around 6–8 nm after which further increasing the shell thickness or adding Dy into the core is not essential.

For the extrinsic properties of rare-earth free exchange-spring magnets, i.e., α''-$Fe_{16}N_2$/$SrAl_2Fe_{10}O_{19}$ composite and MnBi/FeCo bilayer, the influence of diverse microstructural features are explored by micromagnetic simulations. It is found that for semi-hard α''-$Fe_{16}N_2$, the criterion that the critical size of soft phase is twice the domain wall width of hard phase is invalid. For improving coercivity, the α''-$Fe_{16}N_2$ nanoparticle diameter and the interface exchange are suggested to be less than 50 nm and around 0.01–0.1 pJ/m, respectively. Reducing surface oxidation and increasing α''-$Fe_{16}N_2$ volume fraction are mandatory for the $(BH)_{\text{max}}$ enhancement. In MnBi/FeCo bilayer, the interface roughness induced interface-exchange strength reduction would lead to premature reversal in the soft FeCo layer and thus inferior magnetic performance. 1-nm thick FeCo layer and interface exchange around 2 pJ/m could improve the $(BH)_{\text{max}}$ by 10% (compared to the pure MnBi layer).

The multiscale strategy presented in this thesis is valuable for simulating permanent magnets across the electronic, atomistic, and micro/continuum scales and correlating the extrinsic properties with the intrinsic properties and microstructural features. The results obtained by multiscale simulations in this thesis are beneficial for the multilevel understanding of microstructural effects on the magnetic properties at both the atomic level and microscopic level, as well as for the design of high-performance permanent magnets by microstructure engineering.

7.2 Outlook

Based on the experience and lessons learned from the studies in this thesis, the following issues are sill open and remained to be resolved or explored in the near future.

(1) The atomisctic spin model of $Nd_2Fe_{14}B$ has to be extended for its usage in other

rare-earth permanent magnet system. In this thesis, the total magnetization is assumed to be collinear to the Fe magnetization in $Nd_2Fe_{14}B$. This assumption is correct for $Nd_2Fe_{14}B$, but it raises a serious error in evaluating magnetocrystalline anisotropy of other $R_2Fe_{14}B$ systems in which R magnetization is highly non-collinear to Fe magnetization. For instance, $Dy_2Fe_{14}B$ possesses a strong non-collinearity effect which remarkably influences the temperature dependence of its magnetocrystalline anisotropy [309, 399, 400]. Therefore, some modifications of the atomisctic spin model including the non-collinearity effect are essential. In addition, the non-monotonic variation of magnetocrystalline anisotropy with temperature is observed experimentally for some $R_2Fe_{14}B$-type magnets (e.g. $Y_2Fe_{14}B$ [401]). It is recently proposed that atomistic spin model simulations that include contributions from competing two-ion and single-ion anisotropies are able to reproduce the observed non-monotonic behavior [401].

(2) The idea of tuning interface exchange has already been proposed to design exchange-spring nanocomposite magnets, but its application to sintered and hot-pressed rare-earth permanent magnets is less-focused (except for the control of GB for an exchange decoupling) and the related theoretical guidance (especially in terms of nanostructure and atomic-level engineering) is still not well established. An alternative strategy based on the tuning of exchange parameters via the nanostructure and atomic-level engineering will be a potentially feasible avenue for the design of high-performance rare-earth permanent magnets. Theoretical foundations of the tuning-exchange strategy should be developed. However, the accurate and efficient theoretical calculation of interatomic exchange parameters, especially the exchange among atoms in the interfacial vicinity, is still of difficulty.

(3) The multiscale approach in this thesis is a hierarchical scheme, i.e., performing calculation by a set of different computational tools sequentially and transferring parameters from one smaller scale to another larger scale. A concurrent scheme with scale transition in local regions of interests (e.g., nanoscale sub-phase, nanoscale GB, etc.) is more realistic. A concurrent multiscale model using an atomistic spin model in the $Nd_2Fe_{14}B$/GB or sub-phase interfacial vicinity and a micromagnetic approach in the interior of $Nd_2Fe_{14}B$ grains and GB phase should be developed. The model and the associated efficient algorithm have to be numerically implemented for a convenient usage.

(4) The finite-temperature micromagnetic simulations based on stochastic Landau–Lifshitz equations suffer from the issue of time scale when they are applied to calculate the coercivity with the consideration of thermal fluctuations. The time scale in simulation is in the order of nanosecond, whereas the coercivity is experimentally measured in the time scale of second. The method of applying a stepwise external field to calculate hysteresis at finite temperatures in this thesis should be compared to other methods. For example, one can combine the micromagnetic simulations without thermal fluctuations and the nudged elastic band method to obtain the energy barrier as a function of external field, as introduced in Subsection 2.3.3. One can also apply a series of constant fields for a sufficiently long time

to induce magnetization switching and then calculate the relaxation time. In this way, the energy barrier as a function of switching field or the switching field as a function of time can be derived [402–404]. The results from these different methods should be compared.

Bibliography

[1]   R. J. Parker. *Advances in permanent magnetism*. Wiley-VCH, 1990.

[2]   W. Gilbert. *De magnete*. Courier Corporation, 1958.

[3]   G. C. Hadjipanayis and A. Kim. "Domain wall pinning versus nucleation of reversed domains in R-Fe-B magnets". In: *Journal of Applied Physics* 63.8 (1988), pp. 3310–3315.

[4]   K. Honda and S. Saitô. "On K. S. magnet steel". In: *Physical Review* 16.6 (1920), p. 495.

[5]   T. Mishima. "Nickel-aluminum steel for permanent magnets". In: *Ohm* 19 (1932), p. 353.

[6]   R. A. McCurrie. "The structure and properties of alnico permanent magnet alloys". In: *Handbook of ferromagnetic materials* 3 (1982), pp. 107–188.

[7]   H. Forestier and G. Guiot-Guillain. "A new series of ferromagnetic bodies: the ferrites of rare earths". In: *Comptes Rendus* (1950). URL: www.osti.gov/biblio/4424375.

[8]   H. Stäblein. "Hard ferrites and plastoferrites". In: *Handbook of Ferromagnetic Materials* 3 (1982), pp. 441–602.

[9]   H. Kojima. "Fundamental properties of hexagonal ferrites with magnetoplumbite structure". In: *Handbook of Ferromagnetic Materials* 3 (1982), pp. 305–391.

[10]   A. S. Nowick. *Rare Earth Permanent Magnets*. Academic Press Inc, 1973. ISBN: 978-0-12-515450-5.

[11]   M. G. Benz and D. L. Martin. "Cobalt-samarium permanent magnets prepared by liquid phase sintering". In: *Applied Physics Letters* 17.4 (1970), p. 176.

[12]   A. E. Ray and S. Liu. "Recent progress in 2:17-type permanent magnets". In: *Journal of Materials Engineering and Performance* 1.2 (1992), pp. 183–191.

[13]   D. Sander et al. "The 2017 magnetism roadmap". In: *Journal of Physics D: Applied Physics* 50.36 (2017), p. 363001.

[14]   M. Sagawa et al. "Permanent magnet materials based on the rare earth-iron-boron tetragonal compounds". In: *IEEE Transactions on Magnetics* 20.5 (1984), pp. 1584–1589.

[15]   S. Hirosawa et al. "Magnetization and magnetic anisotropy of $R_2Fe_{14}B$ measured on single crystals". In: *Journal of Applied Physics* 59.3 (1986), pp. 873–879.

[16] Y. Matsuura et al. "Phase diagram of the Nd-Fe-B ternary system". In: *Japanese Journal of Applied Physics* 24.8A (1985), p. L635.

[17] M. Sagawa et al. "Nd–Fe–B permanent magnet materials". In: *Japanese Journal of Applied Physics* 26.6R (1987), p. 785.

[18] D. Givord, H. S. Li, and R. P. De La Bâthie. "Magnetic properties of $Y_2Fe_{14}B$ and $Nd_2Fe_{14}B$ single crystals". In: *Solid State Communications* 51.11 (1984), pp. 857–860.

[19] J. J. Croat et al. "High-energy product Nd-Fe-B permanent magnets". In: *Applied Physics Letters* 44.1 (1984), pp. 148–149.

[20] J. J. Croat et al. "Pr-Fe and Nd-Fe-based materials: a new class of high-performance permanent magnets". In: *Journal of Applied Physics* 55.6 (1984), pp. 2078–2082.

[21] N. C. Koon et al. "Magnetic properties of $R_2Fe_{14}B$ single crystals". In: *Journal of Applied Physics* 57.8 (1985), pp. 4091–4093.

[22] Y. Yang et al. "REE recovery from end-of-Life NdFeB pPermanent magnet scrap: a critical review". In: *Journal of Sustainable Metallurgy* 3.1 (2016), pp. 122–149.

[23] K. P. Skokov and O. Gutfleisch. "Heavy rare earth free, free rare earth and rare earth free magnets - vision and reality". In: *Scripta Materialia* 154 (2018), pp. 289–294.

[24] J. F. Liu, P. Vora, and M. Walmer. "Overview of recent progress in Sm-Co based magnets". In: *Journal of Iron and Steel Research International* 13.SUPPL.1 (2006), pp. 319–323.

[25] D. B. De Mooij and K. H. Buschow. "Some novel ternary $ThMn_{12}$-type compounds". In: *Journal of the Less Common Metals* 136.2 (1988), pp. 207–215.

[26] K. Ohashi et al. "Magnetic properties of Fe-rich rare-earth intermetallic compounds with a $ThMn_{12}$ structure". In: *Journal of Applied Physics* 64.10 (1998), p. 5714.

[27] Y. Hirayama et al. "$NdFe_{12}N_x$ hard-magnetic compound with high magnetization and anisotropy field". In: *Scripta Materialia* 95.1 (2015), pp. 70–72.

[28] A. M. Gabay and G. C. Hadjipanayis. "Recent developments in RFe_{12}-type compounds for permanent magnets". In: *Scripta Materialia* 154 (2018), pp. 284–288.

[29] K. Strnat et al. "A family of new cobalt-base permanent magnet materials". In: *Journal of Applied Physics* 38.3 (1967), pp. 1001–1002.

[30] S. Sugimoto. "Current status and recent topics of rare-earth permanent magnets". In: *Journal of Physics D: Applied Physics* 44.6 (2011), p. 064001.

[31] K. Yamazaki and Y. Fukushima. "Effect of eddy-current loss reduction by magnet segmentation in synchronous motors with concentrated windings". In: *IEEE Transactions on Industry Applications* 47.2 (2011), pp. 779–788.

[32] D. G. Dorrell et al. "A review of the design issues and techniques for radial-flux brushless surface and internal rare-earth permanent-magnet motors". In: *IEEE Transactions on Industrial Electronics* 58.9 (2010), pp. 3741–3757.

[33] H. J. Kim, C. S. Koh, and P. S. Shin. "A new anisotropic bonded NdFeB permanent magnet and its application to a small DC motor". In: *IEEE Transactions on Magnetics* 46.6 (2010), pp. 2314–2317.

[34] C. Chen, M. H. Walmer, and S. Liu. "Thermal stability and the effectiveness of coatings for Sm-Co 2:17 high-temperature magnets at temperatures up to 550 °C". In: *IEEE Transactions on Magnetics* 40.4 (2004), pp. 2928–2930.

[35] C. H. Chen et al. "Fully dense bulk nanocomposites of $(Sm_{1-x}Gd_x)_2(Co_{1-y}Fe_y)_{17} + (Co,Fe)$ with high coercivity and high Curie temperature". In: *IEEE Transactions on Magnetics* 40.4 (2004), pp. 2937–2939.

[36] O. Gutfleisch et al. "Evolution of magnetic domain structures and coercivity in high-performance SmCo 2:17-type permanent magnets". In: *Acta Mater* 54 (2006), p. 997.

[37] D. Hinz et al. "Hot deformed (Nd,Pr)(Fe,Co)B magnets for low-temperature applications". In: *Journal of Magnetism and Magnetic Materials* 272 (2004), E321–E322.

[38] T. S. Chin. "Permanent magnet films for applications in microelectromechanical systems". In: *Journal of Magnetism and Magnetic Materials* 209.1-3 (2000), pp. 75–79.

[39] K. M. Krishnan. *Fundamentals and Applications of Magnetic Materials*. Oxford University Press, 2016.

[40] J. M. Coey. "Permanent magnets: plugging the gap". In: *Scripta Materialia* 67.6 (2012), pp. 524–529.

[41] M. Sagawa et al. "New material for permanent magnets on a base of Nd and Fe". In: *Journal of Applied Physics* 55.6 (1984), pp. 2083–2087.

[42] J. J. Croat et al. "Pr-Fe and Nd-Fe-based materials: a new class of high-performance permanent magnets (invited)". In: *Journal of Applied Physics* 55.6 (1984), pp. 2078–2082.

[43] O. Gutfleisch et al. "Magnetic materials and devices for the 21st century: stronger, lighter, and more energy efficient". In: *Advanced Materials* 23.7 (2011), pp. 821–842.

[44] J. F. Herbst. "$R_2Fe_{14}B$ materials: intrinsic properties and technological aspects". In: *Reviews of Modern Physics* 63.4 (1991), p. 819.

[45] H. Sepehri-Amin et al. "High-coercivity ultrafine-grained anisotropic Nd–Fe–B magnets processed by hot deformation and the Nd–Cu grain boundary diffusion process". In: *Acta Materialia* 61.17 (2013), pp. 6622–6634.

[46] R. W. Lee. "Hot-pressed neodymium-iron-boron magnets". In: *Applied Physics Letters* 46.8 (1985), pp. 790–791.

[47] L. Liu et al. "Coercivity of the Nd–Fe–B hot-deformed magnets diffusion-processed with low melting temperature glass forming alloys". In: *Journal of Magnetism and Magnetic Materials* 412 (2016), pp. 234–242.

[48] J. Fidler and J. Bernardi. "Transmission electron microscope characterization of cast and hot-worked R-Fe-B: Cu (R= Nd, Pr) permanent magnets". In: *Journal of Applied Physics* 70.10 (1991), pp. 6456–6458.

[49] F. Vial et al. "Improvement of coercivity of sintered NdFeB permanent magnets by heat treatment". In: *Journal of Magnetism and Magnetic Materials* 242 (2002), pp. 1329–1334.

[50] M. Seeger et al. "Magnetic and microstructural properties of sintered FeNdB-based magnets with Ga and Nb additions". In: *Journal of Magnetism and Magnetic Materials* 138.3 (1994), pp. 294–300.

[51] A. Yan et al. "Magnetic and microstructural properties of sintered FeNdB-based magnets with W, Mo and Nb additions". In: *Journal of Alloys and Compounds* 257.1-2 (1997), pp. 273–277.

[52] H. Sepehri-Amin et al. "Grain boundary and interface chemistry of an Nd–Fe–B-based sintered magnet". In: *Acta Materialia* 60.3 (2012), pp. 819–830.

[53] H. Sepehri-Amin, T. Ohkubo, and K. Hono. "The mechanism of coercivity enhancement by the grain boundary diffusion process of Nd–Fe–B sintered magnets". In: *Acta Materialia* 61.6 (2013), pp. 1982–1990.

[54] T. T. Sasaki et al. "Formation of non-ferromagnetic grain boundary phase in a Ga-doped Nd-rich Nd–Fe–B sintered magnet". In: *Scripta Materialia* 113 (2016), pp. 218–221.

[55] L. Liang et al. "Coercivity enhancement of Dy-free Nd–Fe–B sintered magnets by intergranular adding $Ho_{63.4}Fe_{36.6}$ alloy". In: *Journal of Magnetism and Magnetic Materials* 397 (2016), pp. 139–144.

[56] M. Soderžnik et al. "Magnetization reversal of exchange-coupled and exchange-decoupled Nd-Fe-B magnets observed by magneto-optical Kerr effect microscopy". In: *Acta Materialia* 135 (2017), pp. 68–76.

[57] H. Kronmüller and T. Schrefl. "Interactive and cooperative magnetization processes in hard magnetic materials". In: *Journal of Magnetism and Magnetic Materials* 129.1 (1994), pp. 66–78.

[58] J. Liu et al. "Effect of Nd content on the microstructure and coercivity of hot-deformed Nd–Fe–B permanent magnets". In: *Acta Materialia* 61.14 (2013), pp. 5387–5399.

[59] Y. Murakami et al. "Magnetism of ultrathin intergranular boundary regions in Nd–Fe–B permanent magnets". In: *Acta Materialia* 71 (2014), pp. 370–379.

[60] T. Kohashi et al. "Magnetism in grain-boundary phase of a NdFeB sintered magnet studied by spin-polarized scanning electron microscopy". In: *Applied Physics Letters* 104.23 (2014), p. 232408.

[61] T. Nakamura et al. "Direct observation of ferromagnetism in grain boundary phase of Nd-Fe-B sintered magnet using soft x-ray magnetic circular dichroism". In: *Applied Physics Letters* 105.20 (2014), p. 202404.

[62] H. Sepehri-Amin et al. "Coercivity enhancement of hydrogenation–disproportionation–desorption–recombination processed Nd–Fe–B powders by the diffusion of Nd–Cu eutectic alloys". In: *Scripta Materialia* 63.11 (2010), pp. 1124–1127.

[63] K. Hono and H. Sepehri-Amin. "Strategy for high-coercivity Nd–Fe–B magnets". In: *Scripta Materialia* 67.6 (2012), pp. 530–535.

[64] H. Sepehri-Amin, S. Hirosawa, and K. Hono. "Advances in Nd-Fe-B based permanent magnets". In: *Handbook of Magnetic Materials*. Vol. 27. Elsevier, 2018, pp. 269–372.

[65] W.-H. Cheng et al. "The magnetic properties, thermal stability and microstructure of Nd–Fe–B/Ga sintered magnets prepared by blending method". In: *Journal of Magnetism and Magnetic Materials* 234.2 (2001), pp. 274–278.

[66] L. Liu et al. "Coercivity enhancement of hot-deformed Nd-Fe-B magnets by the eutectic grain boundary diffusion process using $Nd_{62}Dy_{]20}Al_{18}$ alloy". In: *Scripta Materialia* 129 (2017), pp. 44–47.

[67] J. Fliegans et al. "Revisiting the demagnetization curves of Dy-diffused Nd-Fe-B sintered magnets". In: *Journal of Magnetism and Magnetic Materials* 520 (2021), p. 167280.

[68] K. Hirota et al. "Coercivity enhancement by the grain boundary diffusion process to Nd–Fe–B sintered magnets". In: *IEEE Transactions on Magnetics* 42.10 (2006), pp. 2909–2911.

[69] S. Bance et al. "Grain-size dependent demagnetizing factors in permanent magnets". In: *Journal of Applied Physics* 116.23 (2014), p. 233903.

[70] R. Ramesh and K. Srikrishna. "Magnetization reversal in nucleation controlled magnets. I. Theory". In: *Journal of Applied Physics* 64.11 (1988), pp. 6406–6415.

[71] R. Ramesh, G. Thomas, and B. M. Ma. "Magnetization reversal in nucleation controlled magnets. II. Effect of grain size and size distribution on intrinsic coercivity of Fe-Nd-B magnets". In: *Journal of Applied Physics* 64.11 (1988), pp. 6416–6423.

[72] J. Liu et al. "Grain size dependence of coercivity of hot-deformed Nd–Fe–B anisotropic magnets". In: *Acta Materialia* 82 (2015), pp. 336–343.

[73] H. Sepehri-Amin et al. "Micromagnetic simulations on the grain size dependence of coercivity in anisotropic Nd–Fe–B sintered magnets". In: *Scripta Materialia* 89 (2014), pp. 29–32.

[74] M. Yi, O. Gutfleisch, and B.-X. Xu. "Micromagnetic simulations on the grain shape effect in Nd-Fe-B magnets". In: *Journal of Applied Physics* 120.3 (2016), p. 033903.

[75] J. Li et al. "Coercivity and its thermal stability of NdFeB hot-deformed magnets enhanced by the eutectic grain boundary diffusion process". In: *Acta Materialia* 161 (2018), pp. 171–181.

[76] A. S. Kim, F. Camp, and T. Lizzi. "Hydrogen induced corrosion mechanism in NdFeB magnets". In: *Journal of Applied Physics* 79.8 (1996), pp. 4840–4842.

[77] S. Okamoto et al. "Temperature-dependent magnetization reversal process and coercivity mechanism in Nd-Fe-B hot-deformed magnets". In: *Journal of Applied Physics* 118.22 (2015), p. 223903.

[78] S. Mohakud et al. "Temperature dependence of the threshold magnetic field for nucleation and domain wall propagation in an inhomogeneous structure with grain boundary". In: *Physical Review B* 94.5 (2016), p. 054430.

[79] T. Yomogita et al. "Temperature and field direction dependences of first-order reversal curve (FORC) diagrams of hot-deformed Nd-Fe-B magnets". In: *Journal of Magnetism and Magnetic Materials* 447 (2018), pp. 110–115.

[80] H. Sepehri-Amin et al. "Microstructure and temperature dependent of coercivity of hot-deformed Nd–Fe–B magnets diffusion processed with Pr–Cu alloy". In: *Acta Materialia* 99 (2015), pp. 297–306.

[81] K. Strnat et al. "A family of new cobalt-base permanent magnet materials". In: *Journal of Applied Physics* 38.3 (1967), p. 1001.

[82] K. H. Buschow and A. S. Van Der Goot. "Intermetallic compounds in the system samarium-cobalt". In: *Journal of the Less Common Metals* 14.3 (1968), pp. 323–328.

[83] K. Kumar. "RETM$_5$ and RE$_2$TM$_{17}$ permanent magnets development". In: *Journal of Applied Physics* 63.6 (1988), R13.

[84] M. Kalter et al. "A new model for the coercivity mechanism of Sm$_2$(Co,Fe,Cu,Zr)$_{17}$ magnets". In: *IEEE Transactions on Magnetics* 32.5 (1996), pp. 4815–4817.

[85] B. Das et al. "Anisotropy and orbital moment in Sm-Co permanent magnets". In: *Physical Review B* 100.2 (2019), pp. 44–46.

[86] O. Gutfleisch et al. "Evolution of magnetic domain structures and coercivity in high-performance SmCo 2:17-type permanent magnets". In: *Acta Materialia* 54.4 (2006), pp. 997–1008.

[87] L. Rabenberg, R. K. Mishra, and G. Thomas. "Microstructures of precipitation-hardened SmCo permanent magnets". In: *Journal of Applied Physics* 53.3 (1998), p. 2389.

[88] M. Duerrschnabel et al. "Atomic structure and domain wall pinning in samarium-cobalt-based permanent magnets". In: *Nature Communications* 8 (2017), p. 54.

[89] R. Skomski. "Domain-wall curvature and coercivity in pinning type Sm-Co magnets". In: *Journal of Applied Physics* 81.8 (1998), p. 5627.

[90] J. M. Coey. "Hard magnetic materials: a perspective". In: *IEEE Transactions on Magnetics* 47.12 (2011), pp. 4671–4681.

[91] D.-T. Zhang et al. "Microstructure and magnetic properties of SmCo$_5$ sintered magnets". In: *Rare Metals* 39.11 (2020), pp. 1295–1299.

[92] S. Foner et al. "Magnetic properties of cobalt-samarium with a 24-MG Oe energy product". In: *Applied Physics Letters* 20.11 (2003), p. 447.

[93] A. Riley. "The microstructure of SmCo$_5$ sintered magnet material". In: *Journal of the Less Common Metals* 44 (1976), pp. 307–317.

[94] K. H. Buschow. "Permanent magnet materials based on tetragonal rare earth compounds of the type RFe$_{12-x}$M$_x$". In: *Journal of Magnetism and Magnetic Materials* 100.1-3 (1991), pp. 79–89.

[95] B. Fuquan et al. "Phase formation and magnetic properties of YFe$_{12-x}$Nb$_x$ ($x = 0.70 - 0.90$) compounds". In: *Journal of Magnetism and Magnetic Materials* 290-291 (2005), pp. 1192–1194.

[96] D. P. F. Hurley and J. M. D. Coey. "Gas-phase interstitially modified intermetallics R(Fe$_{11}$Ti)Z$_{1-\delta}$: I. Magnetic properties of the series R(Fe$_{11}$Ti)C$_{1-\delta}$: R = Y, Nd, Sm, Gd, Tb, Dy, Ho, Er, Tm, Lu". In: *Journal of Physics: Condensed Matter* 4.25 (1992), pp. 5573–5584.

[97] Y. C. Yang et al. "Magnetic and crystallographic properties of novel Fe-rich rare-earth nitrides of the type RTiFe$_{11}$N1-δ (invited)". In: *Journal of Applied Physics* 70.10 (1991), pp. 6001–6005.

[98] T. Miyake et al. "First-principles study of magnetocrystalline anisotropy and magnetization in NdFe$_{12}$, NdFe$_{11}$Ti, and NdFe$_{11}$TiN". In: *Journal of the Physical Society of Japan* 83.4 (2014), pp. 10–13.

[99] A. M. Schönhöbel et al. "Intrinsic magnetic properties of SmFe$_{12-x}$V$_x$ alloys with reduced V-concentration". In: *Journal of Alloys and Compounds* 786 (2019), pp. 969–974.

[100] Y. Hirayama et al. "Intrinsic hard magnetic properties of Sm(Fe$_{1-x}$Co$_x$)$_{12}$ compound with the ThMn$_{12}$ structure". In: *Scripta Materialia* 138 (2017), pp. 62–65.

[101] W. Körner, G. Krugel, and C. Elsässer. "Theoretical screening of intermetallic ThMn$_{12}$-type phases for new hard-magnetic compounds with low rare earth content". In: *Scientific Reports* 6 (2016), p. 24686.

[102] R. W. McCallum et al. "Practical aspects of modern and future permanent magnets". In: *Annual Review of Materials Research* 44 (2014), pp. 451–477.

[103] C. A. Julien and F. G. Jones. "Alpha-sub-gamma phase in alnico 8 alloys". In: *Journal of Applied Physics* 36.3 (1965), pp. 1173–1174.

[104] H. Zeng et al. "Structure and magnetic properties of ferromagnetic nanowires in self-assembled arrays". In: *Physical Review B* 65.13 (2002), p. 134426.

[105] J. J. Went et al. "Hexagonal iron-oxide compounds as permanent-magnet materials". In: *Physical Review* 86.3 (1952), pp. 424–425.

[106] L. H. Lewis et al. "Inspired by nature: investigating tetrataenite for permanent magnet applications". In: *Journal of Physics Condensed Matter* 26.6 (2014).

[107] P. Rani et al. "Magnetism and magnetocrystalline anisotropy of tetragonally distorted L1$_0$-FeNi: N alloy". In: *Journal of Alloys and Compounds* 835 (2020), p. 155325.

[108] M. Kotsugi et al. "Novel magnetic domain structure in iron meteorite induced by the presence of L1$_0$-FeNi". In: *Applied Physics Express* 3 (2010), p. 013001.

[109] L. Néel et al. "Magnetic properties of an iron - nickel single crystal ordered by neutron bombardment". In: *Journal of Applied Physics* 35.3 (1964), pp. 873–876.

[110] S. Goto et al. "Synthesis of single-phase L1$_0$-FeNi magnet powder by nitrogen insertion and topotactic extraction". In: *Scientific Reports* 7 (2017), p. 13216.

[111] Q. Lin et al. "Towards synthetic L1$_0$-FeNi: detecting the absence of cubic symmetry in laser-ablated Fe-Ni nanoparticles". In: *Applied Surface Science* 567 (2021), p. 150664.

[112] K. H. Jack. "The occurrence and the crystal structure of α''-iron nitride; a new type of interstitial alloy formed during the tempering of nitrogen-martensite". In: *Proceedings of the Royal Society of London. Series A. Mathematical and Physical Sciences* 208.1093 (1951), pp. 216–224.

[113] J. P. Wang. "Environment-friendly bulk Fe$_{16}$N$_2$ permanent magnet: review and prospective". In: *Journal of Magnetism and Magnetic Materials* 497 (2019), p. 165962.

[114] K. Mikio and W. Kunio. "Temperature dependence of coercivity ofmanganese-bismuth (MnBi) particles". In: *Japanese Journal of Applied Physics* 14 (1975), pp. 893–894.

[115] N. V. Rama Rao, A. M. Gabay, and G. C. Hadjipanayis. "Anisotropic fully dense MnBi permanent magnet with high energy product and high coercivity at elevated temperatures". In: *Journal of Physics D: Applied Physics* 46.6 (2013), pp. 58–62.

[116] D. T. Zhang et al. "Structural and magnetic properties of bulk MnBi permanent magnets". In: *Journal of Applied Physics* 109.7 (2011), 07A722.

[117] C. Müller et al. "Constitution of Mn-Al-(Cu, Fe, Ni or C) alloys near the magnetic τ phase". In: *Zeitschrift Fur Metallkunde* 88 (1997), pp. 620–624.

[118] A. Vishina et al. "High-throughput and data-mining approach to predict new rare-earth free permanent magnets". In: *Physical Review B* 101.9 (2020), p. 094407.

[119] Q. Gao et al. "Designing rare-earth free permanent magnets in heusler alloys via interstitial doping". In: *Acta Materialia* 186 (2020), pp. 355–362.

[120] C. Shen et al. "Designing of magnetic MAB phases for energy applications". In: *Journal of Materials Chemistry A* 9.13 (2021), pp. 8805–8813.

[121] C. Kittel. *Introduction to Solid State Physics*. Wiley-VCH, 1996.

[122] P. Kittel. "Orbital resupply of liquid helium". In: *Journal of Spacecraft and Rockets* 23.4 (1986), pp. 391–396.

[123] S. Miyashita et al. "Perspectives of stochastic micromagnetism of Nd$_2$Fe$_{14}$B and computation of thermally activated reversal process". In: *Scripta Materialia* 154 (2018), pp. 259–265.

[124] M. A. Ruderman and C. Kittel. "Indirect exchange coupling of nuclear magnetic moments by conduction electrons". In: *Physical Review* 96 (1 1954), pp. 99–102.

[125] K. Yosida. "Magnetic properties of Cu-Mn alloys". In: *Physical Review* 106 (5 1957), pp. 893–898.

[126] T. Kasuya. "A theory of metallic ferro- and antiferromagnetism on Zener's model". In: *Progress of Theoretical Physics* 16.1 (July 1956), pp. 45–57.

[127] N. W. Ashcroft and N. D. Mermin. *Solid state physics*. Cengage Learning, 1976.

[128] K. Moorjani and J. M. D. Coey. *Magnetic glasses*. North Holland, 1984.

[129] J. M. Yeomans. *Statistical mechanics of phase transitions*. Clarendon Press, 1992.

[130] R. Skomski. "Nanomagnetics". In: *Journal of physics: Condensed matter* 15.20 (2003), R841.

[131] F. Bloch. "Zur theorie des ferromagnetismus". In: *Zeitschrift für Physik* 61.3-4 (1930), pp. 206–219.

[132] E. Ising. "Beitrag zur theorie des ferromagnetismus". In: *Zeitschrift für Physik* 31.1 (1925), pp. 253–258.

[133] S. G. Brush. "History of the Lenz-Ising model". In: *Reviews of Modern Physics* 39.4 (1967), p. 883.

[134] S. Hirosawa. "Current status of research and development toward permanent magnets free from critical elements". In: *Journal of the Magnetics Society of Japan* 39.3 (2015), pp. 85–95.

[135] T. Yoshioka and H. Tsuchiura. "Site-specific magnetic anisotropies in $R_2Fe_{14}B$ systems". In: *Applied Physics Letters* 112.16 (2018), p. 162405.

[136] J. M. D. Coey. *Rare-earth iron permanent magnets*. 54. Oxford University Press, 1996.

[137] R. Skomski and J. M. D. Coey. *Permanent Magnetism*. Bristol, 1999.

[138] G. H. O. Daalderop, P. J. Kelly, and M. F. H. Schuurmans. "First-principles calculation of the magnetocrystalline anisotropy energy of iron, cobalt, and nickel". In: *Physical Review B* 41.17 (1990), pp. 11919–11937.

[139] S. Hirosawa. "Development of industrial nanocomposite permanent magnets: a review". In: *Transactions of the Magnetics Society of Japan* 4.4-1 (2004), pp. 101–112.

[140] R. Aragón. "Cubic magnetic anisotropy of nonstoichiometric magnetite". In: *Physical Review B* 46 (9 1992), pp. 5334–5338.

[141] H. Shenker. "Magnetic anisotropy of cobalt ferrite ($Co_{1.01}Fe_{2.00}O_{3.62}$) and nickel cobalt ferrite ($Ni_{0.72}Fe_{0.20}Co_{0.08}Fe_2O_4$)". In: *Physical Review* 107.5 (1957), pp. 1246–1249.

[142] R. S. Turtelli et al. "Co-ferrite – a material with interesting magnetic properties". In: *IOP Conference Series: Materials Science and Engineering* 60 (2014), p. 012020.

[143] A. Shan et al. "Phase formations and magnetic properties of single crystal nickel ferrite ($NiFe_2O_4$) with different morphologies". In: *CrystEngComm* 17.7 (2015), pp. 1603–1608.

[144] Z. X. Tang et al. "Size-dependent magnetic properties of manganese ferrite fine particles". In: *Journal of Applied Physics* 69.8 (1991), pp. 5279–5281.

[145] R. F. Pearson. "The magnetocrystalline anisotropy of cobalt-substituted manganese ferrite". In: *Proceedings of the Physical Society* 74.5 (1959), pp. 505–512.

[146] S. A. Oliver et al. "Structure and magnetic properties of magnesium ferrite fine powders". In: *Scripta Metallurgica et Materiala* 33.10-11 (1995), pp. 1695–1701.

[147] V. A. M. Brabers et al. "Magnetic anisotropy of magnesium ferrous ferrites". In: *Journal of Magnetism and Magnetic Materials* 15-18 (1980), pp. 545–546.

[148] R. Skomski and J. M. Coey. "Magnetic anisotropy - How much is enough for a permanent magnet?" In: *Scripta Materialia* 112 (2016), pp. 3–8.

[149] H. Kronmüller. "Theory of nucleation fields in inhomogeneous ferromagnets". In: *Physica Status Solidi (B)* 144.1 (1987), pp. 385–396.

[150] H. Kronmüller, K. D. Durst, and M. Sagawa. "Analysis of the magnetic hardening mechanism in RE-FeB permanent magnets". In: *Journal of Magnetism and Magnetic Materials* 74.3 (1988), pp. 291–302.

[151] D. Givord, M. Rossignol, and V. M. T. S. Barthem. "The physics of coercivity". In: *Journal of Magnetism and Magnetic Materials* 258 (2003), pp. 1–5.

[152] J. M. D. Coey and P. A. I. Smith. "Magnetic nitrides". In: *Journal of Magnetism and Magnetic Materials* 200.1-3 (1999), pp. 405–424.

[153] W. F. Brown. "Virtues and weaknesses of the domain concept". In: *Reviews of Modern Physics* 17.1 (1945), pp. 15–19.

[154] M. A. Pinto. "Brown paradox of micromagnetic theory (abstract)". In: *Journal of Applied Physics* 69.8 (1998), p. 4856.

[155] E. C. Stoner and E. P. Wohlfarth. "A mechanism of magnetic hysteresis in heterogeneous alloys". In: *Philosophical Transactions of the Royal Society of London. Series A, Mathematical and Physical Sciences* 240.826 (1948), pp. 599–642.

[156] S. Bance et al. "Micromagnetics of shape anisotropy based permanent magnets". In: *Journal of Magnetism and Magnetic Materials* 363 (2014), pp. 121–124.

[157] S. Erokhin and D. Berkov. "Optimization of nanocomposite materials for permanent magnets: micromagnetic simulations of the effects of intergrain exchange and the shapes of hard grains". In: *Physical Review Applied* 7.1 (2017), p. 014011.

[158] K. Uestuener, M. Katter, and W. Rodewald. "Dependence of the mean grain size and coercivity of sintered Nd–Fe–B magnets on the initial powder particle size". In: *IEEE Transactions on Magnetics* 42.10 (2006), pp. 2897–2899.

[159] H. Nakamura et al. "Magnetic properties of extremely small Nd-Fe-B sintered magnets". In: *IEEE Transactions on Magnetics* 41.10 (2005), pp. 3844–3846.

[160] S. Sawatzki et al. "Grain boundary diffusion in nanocrystalline Nd-Fe-B permanent magnets with low-melting eutectics". In: *Acta Materialia* 115 (2016), pp. 354–363.

[161] K. Loewe et al. "Grain boundary diffusion of different rare earth elements in Nd-Fe-B sintered magnets by experiment and FEM simulation". In: *Acta Materialia* 124 (2017), pp. 421–429.

[162]   Y. Tatetsu, S. Tsuneyuki, and Y. Gohda. "First-principles study of the role of Cu in improving the coercivity of Nd-Fe-B permanent magnets". In: *Physical Review Applied* 6 (6 2016), p. 064029.

[163]   Y. Toga, T. Suzuki, and A. Sakuma. "Effects of trace elements on the crystal field parameters of Nd ions at the surface of $Nd_2Fe_{14}B$ grains". In: *Journal of Applied Physics* 117.22 (2015), p. 223905.

[164]   G. Hrkac et al. "Impact of different Nd-rich crystal-phases on the coercivity of Nd-Fe-B grain ensembles". In: *Scripta Materialia* 70.1 (2014), pp. 35–38.

[165]   M. Yi et al. "Multiscale examination of strain effects in Nd-Fe-B permanent magnets". In: *Physical Review Applied* 8.1 (2017), p. 014011. eprint: `1611.08940`.

[166]   T. G. Woodcock et al. "Understanding the microstructure and coercivity of high performance NdFeB-based magnets". In: *Scripta Materialia* 67.6 (2012), pp. 536–541.

[167]   H. Sepehri-Amin et al. "Grain boundary and interface chemistry of an Nd–Fe–B-based sintered magnet". In: *Acta Materialia* 60.3 (2012), pp. 819–830.

[168]   G. A. Zickler and J. Fidler. "Nanocompositional electron microscopic analysis and role of grain boundary phase of isotropically oriented Nd-Fe-B magnets". In: *Advances in Materials Science and Engineering* 2017 (2017), p. 1461835.

[169]   K. Niitsu et al. "Magnetization measurements for grain boundary phases in Ga-doped Nd-Fe-B sintered magnet". In: *Journal of Alloys and Compounds* 752 (2018), pp. 220–230.

[170]   C. Kittel. "Physical Theory of Ferromagnetic Domains". In: *Review of Modern Physics* 21 (4 1949), pp. 541–583.

[171]   H. Kronmuller, H. Kronmüller, and M. Fähnle. *Micromagnetism and the microstructure of ferromagnetic solids*. Cambridge university press, 2003.

[172]   J. L. Tsai et al. "Magnetoresistance study in thin zig zag NiFe wires". In: *Journal of Applied Physics* 91.10 (2002), pp. 7983–7985.

[173]   R. Skomski, H.-P. Oepen, and J. Kirschner. "Micromagnetics of ultrathin films with perpendicular magnetic anisotropy". In: *Physical Review B* 58.6 (1998), p. 3223.

[174]   R. Skomski. "Finite-temperature behavior of anisotropic two-sublattice magnets". In: *Journal of Applied Physics* 83.11 (1998), pp. 6724–6726.

[175]   H. J. Kersten, H. L. Miller, and G. F. Smith. "Stimulative effects of x-rays on plants". In: *Plant Physiology* 18.1 (1943), p. 8.

[176]   P. Gaunt. "Magnetic viscosity and thermal activation energy". In: *Journal of Applied Physics* 59.12 (1986), pp. 4129–4132.

[177]   J. Zhou et al. "Sm–Co–Cu–Ti high-temperature permanent magnets". In: *Applied Physics Letters* 77.10 (2000), pp. 1514–1516.

[178]   K. Hono and H. Sepehri-Amin. "Prospect for HRE-free high coercivity Nd-Fe-B permanent magnets". In: *Scripta Materialia* 154 (2018), pp. 277–283.

[179] P. Hohenberg and W. Kohn. "Inhomogeneous electron gas". In: *Physical Review* 136 (3B 1964), B864–B871.

[180] W. Kohn and L. J. Sham. "Self-consistent equations including exchange and correlation effects". In: *Physical Review* 140 (4A 1965), A1133–A1138.

[181] A. D. Becke. "A new mixing of Hartree–Fock and local density-functional theories". In: *The Journal of Chemical Physics* 98.2 (1993), p. 1372.

[182] V. I. Anisimov and O. Gunnarsson. "Density-functional calculation of effective Coulomb interactions in metals". In: *Physical Review B* 43.10 (1991), pp. 7570–7574.

[183] U. von Barth and L. Hedin. "A local exchange-correlation potential for the spin polarized case. i". In: *Journal of Physics C: Solid State Physics* 5.13 (1972), pp. 1629–1642.

[184] M. M. Pant and A. K. Rajagopal. "Theory of inhomogeneous magnetic electron gas". In: *Solid State Communications* 10.12 (1972), pp. 1157–1160.

[185] I. A. Campbell. "Indirect exchange for rare earths in metals". In: *Journal of Physics F: Metal Physics* 2.3 (1972), pp. L47–L50.

[186] S. S. Jaswal. "Electronic structure and magnetism of $R_2\mathrm{Fe}_{14}\mathrm{B}$ (R=Y,Nd) compounds". In: *Physical Review B* 41 (14 1990), pp. 9697–9700.

[187] C. Gao et al. "Observation of the asphericity of 4f-electron density and its relation to the magnetic anisotropy axis in single-molecule magnets". In: *Nature Chemistry* 12.2 (2020), pp. 213–219.

[188] M. Weinert, R. E. Watson, and J. W. Davenport. "Total-energy differences and eigenvalue sums". In: *Physical Review B* 32.4 (1985), p. 2115.

[189] X. Wang et al. "Validity of the force theorem for magnetocrystalline anisotropy". In: *Journal of Magnetism and Magnetic Materials* 159 (1996), pp. 337–341.

[190] N. Drebov et al. "Ab initio screening methodology applied to the search for new permanent magnetic materials". In: *New Journal of Physics* 15.12 (2013), p. 125023.

[191] K. H. Buschow, J. W. De Vries, and R. C. Thiel. "Note on the crystal-field-induced magnetic anisotropy in $R_2\mathrm{Fe}_{14}\mathrm{B}$ compounds and other rare-earth-based permanent magnet materials". In: *Journal of Physics F: Metal Physics* 15.4 (1985), pp. L93–L97.

[192] H. Tsuchiura et al. "First-principles calculations of magnetic properties for analysis of magnetization processes in rare-earth permanent magnets". In: *Science and Technology of Advanced Materials* 22.1 (2021), pp. 748–757.

[193] M. T. Hutchings. "Point-charge calculations of energy levels of magnetic ions in crystalline electric fields". In: *Solid State Physics* 16 (1964), pp. 227–273.

[194] P. Novák and J. Kuriplach. "Calculation of crystal-field parameters in the RNi_5 (R=rare earth) system". In: *Physical Review B* 50.4 (1994), pp. 2085–2089.

[195] H. Tsuchiura, T. Yoshioka, and P. Novak. "First-principles calculations of crystal field parameters of Nd ions near surfaces and interfaces in Nd-Fe-B magnets". In: *IEEE Transactions on Magnetics* 50.11 (2014), p. 2105004.

[196] S. Tanaka et al. "First-principles calculation of crystal field parameters of Dy ions substituted for Nd in Nd-Fe-B magnets". In: *Journal of Physics: Conference Series* 266.1 (2011), pp. 8–13.

[197] T. Suzuki, Y. Toga, and A. Sakuma. "Effects of deformation on the crystal field parameter of the Nd ions in $Nd_2Fe_{14}B$". In: *Journal of Applied Physics* 115.17 (2014), 17A703.

[198] M. Yamada et al. "Crystal-field analysis of the magnetization process in a series of $Nd_2Fe_{14}B$-type compounds". In: *Physical Review B* 38.1 (1988), p. 620.

[199] A. J. Freeman and J. P. Desclaux. "Dirac-Fock studies of some electronic properties of rare-earth ions". In: *Journal of Magnetism and Magnetic Materials* 12.1 (1979), pp. 11–21.

[200] A. J. Freeman and R. E. Watson. "Theoretical investigation of some magnetic and spectroscopic properties of rare-earth ions". In: *Physical Review* 127.6 (1962), p. 2058.

[201] K. Hummler and M. Fähnle. "Full-potential linear-muffin-tin-orbital calculations of the magnetic properties of rare-earth-transition-metal intermetallics. II. $Nd_2Fe_{14}B$". In: *Physical Review B* 53.6 (1996), pp. 3290–3295.

[202] T. Yoshioka, H. Tsuchiura, and P. Novák. "Crystal field parameters with Wannier functions: application to $Nd_2Fe_{14}B$ systems". In: *Materials Research Innovations* 19 (2015), S4–S8.

[203] H. Moriya, H. Tsuchiura, and A. Sakuma. "First principles calculation of crystal field parameter near surfaces of $Nd_2Fe_{14}B$". In: *Journal of Applied Physics* 105.7 (2009), 07A740.

[204] R. F. L. Evans et al. "Atomistic spin model simulations of magnetic nanomaterials". In: *Journal of Physics: Condensed Matter* 26.10 (2014), p. 103202.

[205] D. A. Garanin. "Self-consistent Gaussian approximation for classical spin systems: Thermodynamics". In: *Physical Review B* 53 (17 1996), pp. 11593–11605.

[206] D. Šabani, C. Bacaksiz, and M. V. Milošević. "Ab initio methodology for magnetic exchange parameters: generic four-state energy mapping onto a Heisenberg spin Hamiltonian". In: *Physical Review B* 102 (1 2020), p. 014457.

[207] A. Jacobsson et al. "Exchange parameters and adiabatic magnon energies from spin-spiral calculations". In: *Physical Review B* 88 (13 2013), p. 134427.

[208] A. I. Liechtenstein, M. I. Katsnelson, and V. A. Gubanov. "Exchange interactions and spin-wave stiffness in ferromagnetic metals". In: *Journal of Physics F: Metal Physics* 14.7 (1984), pp. L125–L128.

[209] A. I. Liechtenstein et al. "Local spin density functional approach to the theory of exchange interactions in ferromagnetic metals and alloys". In: *Journal of Magnetism and Magnetic Materials* 67.1 (1987), pp. 65–74.

[210] V. P. Antropov, M. I. Katsnelson, and A. I. Liechtenstein. "Exchange interactions in magnets". In: *Physica B: Condensed Matter* 237-238 (1997), pp. 336–340.

[211] E. F. Bertaut. "Lattice theory of spin configuration". In: *Journal of Applied Physics* 33.3 (1962), pp. 1138–1143.

[212] M. Ležaić et al. "Exchange interactions and local-moment fluctuation corrections in ferromagnets at finite temperatures based on noncollinear density-functional calculations". In: *Physical Review B* 88.13 (2013), p. 134403.

[213] P. Kurz. "Non-collinear magnetism at surfaces and in ultrathin films". PhD Thesis. RWTH Aachen, 2001.

[214] A. Terasawa et al. "Efficient algorithm based on Liechtenstein method for computing exchange coupling constants using localized basis set". In: *Journal of the Physical Society of Japan* 88.11 (2019), p. 114706.

[215] H. Ebert. *A spin polarized relativistic Korringa-Kohn-Rostoker (SPR-KKR) code for calculating solid state properties: user's guide*. Tech. rep. München: Universität München, 2017.

[216] Y. Toga et al. "Monte Carlo analysis for finite-temperature magnetism of $Nd_2Fe_{14}B$ permanent magnet". In: *Physical Review B* 94.17 (2016), p. 174433.

[217] V. Heine. "Electronic structure from the point of view of the local atomic environment". In: *Solid State Physics*. 1980, pp. 1–127.

[218] W. M. Temmerman. "On the generalization of the impurity problem". In: *Journal of Physics F: Metal Physics* 12.3 (1982), pp. L25–L29.

[219] M. J. Han, T. Ozaki, and J. Yu. "Electronic structure, magnetic interactions, and the role of ligands in Mn_n (n=4,12) single-molecule magnets". In: *Physical Review B* 70.18 (2004), p. 184421.

[220] Y. Gohda. "First-principles determination of intergranular atomic arrangements and magnetic properties in rare-earth permanent magnets". In: *Science and Technology of Advanced Materials* 22.1 (2021), pp. 113–123.

[221] H. Ebert, D. Ködderitzsch, and J. Minár. "Calculating condensed matter properties using the KKR-Green's function method—recent developments and applications". In: *Reports on Progress in Physics* 74.9 (2011), p. 096501.

[222] D. C. Jiles. *Introduction to Magnetism and Magnetic Materials*. Boca Raton: CRC Press, 1998.

[223] K. Schwarz et al. "Electronic and magnetic structure of BCC Fe-Co alloys from band theory". In: *Journal of Physics F: Metal Physics* 14.11 (1984), pp. 2659–2671.

[224] B. Skubic et al. "A method for atomistic spin dynamics simulations: implementation and examples". In: *Journal of physics: condensed matter* 20.31 (2008), p. 315203.

[225] L. D. Landau and E. Lifshitz. "On the theory of the dispersion of magnetic permeability in ferromagnetic bodies". In: *Physikalische Zeitschrift der Sowjetunion* 8 (1935), p. 153.

[226] M. Yi and B.-X. Xu. "A constraint-free phase field model for ferromagnetic domain evolution". In: *Proceedings of the Royal Society A* 470.2171 (2014), p. 20140517.

[227] W. F. Brown Jr. "Thermal fluctuations of a single-domain particle". In: *Physical Review* 130.5 (1963), p. 1677.

[228] R. F. L. Evans et al. "Stochastic form of the Landau-Lifshitz-Bloch equation". In: *Physical Review B* 85.1 (2012), p. 014433.

[229] S. Miyashita et al. "Atomistic theory of thermally activated magnetization processes in $Nd_2Fe_{14}B$ permanent magnet". In: *Science and Technology of Advanced Materials* 22.1 (2021), pp. 658–682.

[230] S. C. Westmoreland et al. "Multiscale model approaches to the design of advanced permanent magnets". In: *Scripta Materialia* 148 (2018), pp. 56–62.

[231] H. Tsuchiura, T. Yoshioka, and P. Novák. "Bridging atomistic magnetism and coercivity in Nd-Fe-B magnets". In: *Scripta Materialia* 154 (2018), pp. 248–252.

[232] J. L. García-Palacios and F. J. Lázaro. "Langevin-dynamics study of the dynamical properties of small magnetic particles". In: *Physical Review B* 58.22 (1998), pp. 14937–14958.

[233] M. D'Aquino et al. "Midpoint numerical technique for stochastic Landau-Lifshitz-Gilbert dynamics". In: *Journal of Applied Physics* 99.8 (2006), 08B905.

[234] D. V. Berkov and N. L. Gorn. "Thermally activated processes in magnetic systems consisting of rigid dipoles: equivalence of the Ito and Stratonovich stochastic calculus". In: *Journal of Physics: Condensed Matter* 14.13 (2002), pp. L281–L287.

[235] N. Metropolis et al. "Equation of state calculations by fast computing machines". In: *The Journal of Chemical Physics* 21.6 (1953), pp. 1087–1092.

[236] P. Asselin et al. "Constrained Monte Carlo method and calculation of the temperature dependence of magnetic anisotropy". In: *Physical Review B* 82.5 (2010), p. 054415.

[237] W. F. Brown Jr. "Micromagnetics: successor to domain theory?" In: *Journal de Physique et Le Radium* 20.2–3 (1959), pp. 101–104.

[238] J. Fischbacher et al. "Micromagnetics of rare-earth efficient permanent magnets". In: *Journal of Physics D: Applied Physics* 51.19 (2018), p. 193002.

[239] H. Barkhausen. "Two phenomena revealed with the help of new amplifiers". In: *Physikalische Zeitschrift* 29.6 (1919), pp. 401–403.

[240] K. J. Sixtus and L. Tonks. "Propagation of large Barkhausen discontinuities". In: *Physical Review* 37.8 (1931), p. 930.

[241] P. Weiss. "L'hypothèse du champ moléculaire et la propriété ferromagnétique". In: *Journal of Theoretical and Applied Physics* 6.1 (1907), pp. 661–690.

[242] F. Bitter. "On inhomogeneities in the magnetization of ferromagnetic materials". In: *Physical review* 38.10 (1931), p. 1903.

[243] W. F. Brown Jr. "The effect of dislocations on magnetization near saturation". In: *Physical Review* 60.2 (1941), p. 139.

[244] G. Hrkac et al. "The role of local anisotropy profiles at grain boundaries on the coercivity of $Nd_2Fe_{14}B$ magnets". In: *Applied Physics Letters* 97.23 (2010), p. 232511.

[245] P. Toson, G. A. Zickler, and J. Fidler. "Do micromagnetic simulations correctly predict hard magnetic hysteresis properties?" In: *Physica B: Condensed Matter* 486 (2016), pp. 142–150.

[246] G. Zickler et al. "A combined TEM/STEM and micromagnetic study of the anisotropic nature of grain boundaries and coercivity in Nd-Fe-B magnets". In: *Advances in Materials Science and Engineering* 2017 (2017), p. 6412042.

[247] W. Scholz et al. "Scalable parallel micromagnetic solvers for magnetic nanostructures". In: *Computational Materials Science* 28.2 (2003), pp. 366–383.

[248] J. Fidler and T. Schrefl. "Micromagnetic modelling - The current state of the art". In: *Journal of Physics D: Applied Physics* 33.15 (2000), R135.

[249] T. Fischbacher et al. "A systematic approach to multiphysics extensions of finite-element-based micromagnetic simulations: Nmag". In: *IEEE Transactions on Magnetics* 43.6 (2007), pp. 2896–2898.

[250] A. Vansteenkiste et al. "The design and verification of MuMax3". In: *AIP Advances* 4.10 (2014), p. 107133.

[251] P. Cordones. "Micromagnetic models for high-temperature magnetization dynamics". PhD Thesis. Universidad Autonoma de Madrid, 2015.

[252] R. Chang et al. "FastMag: Fast micromagnetic simulator for complex magnetic structures (invited)". In: *Journal of Applied Physics* 109.7 (2011), p. 07D358.

[253] S. Bance, J. Fischbacher, and T. Schrefl. "Thermally activated coercivity in core-shell permanent magnets". In: *Journal of Applied Physics* 117.17 (2015), 17A733.

[254] S. Bance et al. "Influence of defect thickness on the angular dependence of coercivity in rare-earth permanent magnets". In: *Applied Physics Letters* 104.18 (2014), p. 182408.

[255] H. Sepehri-Amin et al. "Micromagnetic simulations on the grain size dependence of coercivity in anisotropic Nd–Fe–B sintered magnets". In: *Scripta Materialia* 89 (2014), pp. 29–32.

[256] J. Fujisaki et al. "Micromagnetic simulation of the orientation dependence of grain boundary properties on the coercivity of Nd-Fe-B sintered magnets". In: *AIP Advances* 6.5 (2016), p. 056028.

[257] B. D. Cullity and C. D. Graham. *Introduction to Magnetic Materials*. Hoboken, New Jersey: Wiley-IEEE Press, 2008.

[258] T. L. Gilbert. "A phenomenological theory of damping in ferromagnetic materials". In: *IEEE Transactions on Magnetics* 40.6 (2004), pp. 3443–3449.

[259] D. A. Garanin. "Fokker-Planck and Landau-Lifshitz-Bloch equations for classical ferromagnets". In: *Physical Review B* 55.5 (1997), p. 3050.

[260] N. Kazantseva et al. "Towards multiscale modeling of magnetic materials: Simulations of FePt". In: *Physical Review B* 77.18 (2008), p. 184428.

[261] K. Binder, H. Rauch, and V. Wildpaner. "Monte Carlo calculation of the magnetization of superparamagnetic particles". In: *Journal of Physics and Chemistry of Solids* 31.2 (1970), pp. 391–397.

[262] E. Şaşıoğlu et al. "Exchange interactions and temperature dependence of magnetization in half-metallic Heusler alloys". In: *Physical review B* 72.18 (2005), p. 184415.

[263] M. D. Kuz'min. "Shape of temperature dependence of spontaneous magnetization of ferromagnets: quantitative analysis". In: *Physical Review Letters* 94.10 (2005), p. 107204.

[264] A. Jakobsson et al. "First-principles calculations of exchange interactions, spin waves, and temperature dependence of magnetization in inverse-Heusler-based spin gapless semiconductors". In: *Physical Review B* 91.17 (2015), p. 174439.

[265] M. Pajda et al. "Ab initio calculations of exchange interactions, spin-wave stiffness constants, and Curie temperatures of Fe, Co, and Ni". In: *Physical Review B* 64.17 (2001), p. 174402.

[266] U. Atxitia et al. "Multiscale modeling of magnetic materials: Temperature dependence of the exchange stiffness". In: *Physical Review B* 82.13 (2010), p. 134440.

[267] D. Böttcher, A. Ernst, and J. Henk. "Temperature-dependent Heisenberg exchange coupling constants from linking electronic-structure calculations and Monte Carlo simulations". In: *Journal of Magnetism and Magnetic Materials* 324.4 (2012), pp. 610–615.

[268] R. Moreno et al. "Temperature-dependent exchange stiffness and domain wall width in Co". In: *Physical Review B* 94.10 (2016), p. 104433.

[269] Y. Toga et al. "Anisotropy of exchange stiffness based on atomic-scale magnetic properties in the rare-earth permanent magnet $Nd_2Fe_{14}B$". In: *Physical Review B* 98.5 (2018), p. 054418.

[270] C. Zener. "Classical theory of the temperature dependence of magnetic anisotropy energy". In: *Physical Review* 96.5 (1954), p. 1335.

[271] Y. Millev and M. Fähnle. "Temperature dependence of magnetic anisotropy and magnetostriction". In: *Physical Review B* 51.5 (1995), p. 2937.

[272] J. B. Staunton et al. "Temperature dependence of magnetic anisotropy: An ab initio approach". In: *Physical Review B* 74.14 (2006), p. 144411.

[273] A. Buruzs et al. "Ab initio theory of temperature dependence of magnetic anisotropy in layered systems: applications to thin Co films on Cu (100)". In: *Physical Review B* 76.6 (2007), p. 064417.

[274] R. Sasaki, D. Miura, and A. Sakuma. "Theoretical evaluation of the temperature dependence of magnetic anisotropy constants of $Nd_2Fe_{14}B$: Effects of exchange field and crystal field strength". In: *Applied Physics Express* 8.4 (2015), p. 043004.

[275] H. Tsukahara et al. "Large-scale micromagnetics simulations with dipolar interaction using all-to-all communications". In: 6.5 (2016), p. 056405.

[276] J. Fischbacher et al. "Nonlinear conjugate gradient methods in micromagnetics". In: 7.4 (2017), p. 045310.

[277] T. Tanaka et al. "Speeding up micromagnetic simulation by energy minimization with interpolation of magnetostatic field". In: 53.6 (2017), pp. 1–4.

[278] C. M. Pfeiler et al. "Computational micromagnetics with Commics". In: *Computer Physics Communications* 248 (2020), p. 106965.

[279] C. Abert et al. "Magnum.fe: A micromagnetic finite-element simulation code based on FEniCS". In: *Journal of Magnetism and Magnetic Materials* 345 (2013), pp. 29–35.

[280] J. Leliaert and J. Mulkers. "Tomorrow's micromagnetic simulations". In: *Journal of Applied Physics* 125.18 (2019), p. 180901.

[281] M. J. Donahue and D. G. Porter. "Exchange energy formulations for 3D micromagnetics". In: *Physica B: Condensed Matter* 343.1-4 (2004), pp. 177–183.

[282] M. J. Donahue. "A variational approach to exchange energy calculations in micromagnetics". In: *Journal of Applied Physics* 83.11 (1998), pp. 6491–6493.

[283] J. H. J. van Opheusden and E. M. C. M. Reuvekamp. "Computer simulation of a thin magnetic film with vertical anisotropy". In: *Journal of Magnetism and Magnetic Materials* 88 (1990), pp. 247–259.

[284] R. D. McMichael et al. "Comparison of magnetostatic field calculation methods on two-dimensional square grids as applied to a micromagnetic standard problem". In: *Journal of Applied Physics* 85.8 (1999), pp. 5816–5818.

[285] J. Leliaert et al. "Adaptively time stepping the stochastic Landau-Lifshitz-Gilbert equation at nonzero temperature: Implementation and validation in MuMax3". In: *AIP Advances* 7.12 (2017), p. 125010.

[286] M. Donahue and D. Porter. *OOMMF software package*. URL: math.nist.gov/oommf.

[287] M.-A. Bisotti et al. "Fidimag – A finite difference atomistic and micromagnetic simulation package". In: *Journal of Open Research Software* 6.1 (2018), p. 22.

[288] L. Lopez-Diaz et al. "Micromagnetic simulations using Graphics Processing Units". In: *Journal of Physics D: Applied Physics* 45.32 (2012), p. 323001.

[289] S. Bance et al. "Thermal activation in permanent magnets". In: *JOM* 67.6 (2015), pp. 1350–1356.

[290] J. Fischbacher et al. "On the limits of coercivity in permanent magnets". In: *Applied Physics Letters* 111.7 (2017), p. 072404.

[291] R. Dittrich et al. "A path method for finding energy barriers and minimum energy paths in complex micromagnetic systems". In: *Journal of Magnetism and Magnetic Materials* 250 (2002), pp. 12–19.

[292] W. E, W. Ren, and E. Vanden-Eijnden. "Simplified and improved string method for computing the minimum energy paths in barrier-crossing events". In: *The Journal of Chemical Physics* 126.16 (2007), p. 164103.

[293] D. Givord et al. "Magnetic viscosity in Nd-Fe-B sintered magnets". In: *Journal of Magnetism and Magnetic Materials* 67.3 (1987), pp. L281–L285.

[294] D. Givord, P. Tenaud, and T. Viadieu. "Angular dependence of coercivity in sintered magnets". In: *Journal of Magnetism and Magnetic Materials* 72.3 (1988), pp. 247–252.

[295] X. B. Liu and Z. Altounian. "The partitioning of Dy and Tb in NdFeB magnets: a first-principles study". In: *Journal of Applied Physics* 111.7 (2012), 07A701.

[296] T. Helbig et al. "Experimental and computational analysis of magnetization reversal in (Nd, Dy)-Fe-B core shell sintered magnets". In: *Acta Materialia* 127 (2017), pp. 498–504.

[297] S. Hirosawa, M. Nishino, and S. Miyashita. "Perspectives for high-performance permanent magnets: applications, coercivity, and new materials". In: *Advances in Natural Sciences: Nanoscience and Nanotechnology* 8.1 (2017), p. 013002.

[298] R. F. L. Evans et al. "Atomistic spin dynamics and temperature dependent properties of $Nd_2Fe_{14}B$". In: *8th Joint European Magnetic Symposia, 21-26 August, 2016* ().

[299] M. Nishino et al. "Atomistic-model study of temperature-dependent domain walls in the neodymium permanent magnet $Nd_2Fe_{14}B$". In: *Physical Review B* 95.9 (2017), p. 094429.

[300] O. Eriksson et al. *Atomistic spin dynamics: Foundations and applications*. Oxford university press, 2017.

[301] "Finite-temperature dynamical and static properties of Nd magnets studied by an atomistic modeling". In: *AIP Advances* 11.2 (2021), p. 025102.

[302] R. J. Elliott and K. W. H. Stevens. "The theory of magnetic resonance experiments on salts of the rare earths". In: *Proceedings of the Royal Society of London. Series A. Mathematical and Physical Sciences* 218.1135 (1953), pp. 553–566.

[303] Y. Miura, H. Tsuchiura, and T. Yoshioka. "Magnetocrystalline anisotropy of the Fe-sublattice in $Y_2Fe_{14}B$ systems". In: *Journal of Applied Physics* 115.17 (2014), 17A765.

[304] H. Yoon et al. "Reliability and applicability of magnetic-force linear response theory: numerical parameters, predictability, and orbital resolution". In: *Physical Review B* 97.12 (2018), p. 125132.

[305] T. J. Kim, H. Yoon, and M. J. Han. "Calculating magnetic interactions in organic electrides". In: *Physical Review B* 97.21 (2018), p. 214431.

[306] S. W. Jang et al. "Charge density functional plus U theory of $LaMnO_3$: Phase diagram, electronic structure, and magnetic interaction". In: *Physical Review B* 98.12 (2018), p. 125126.

[307] A. Szilva et al. "Interatomic exchange interactions for finite-temperature magnetism and nonequilibrium spin dynamics". In: *Physical Review Letters* 111.12 (2013), p. 127204.

[308] Y. O. Kvashnin et al. "Microscopic origin of Heisenberg and non-Heisenberg exchange interactions in ferromagnetic bcc Fe". In: *Physical Review Letters* 116.21 (2016), p. 217202.

[309] D. Miura and A. Sakuma. "Non-collinearity effects on magnetocrystalline anisotropy for $R_2Fe_{14}B$ magnets". In: *Journal of the Physical Society of Japan* 88.4 (2019), pp. 1–9.

[310] K. D. Durst and H. Kronmüller. "Determination of intrinsic magnetic material parameters of $Nd_2Fe_{14}B$ from magnetic measurements of sintered $Nd_{15}Fe_{77}B_8$ magnets". In: *Journal of Magnetism and Magnetic Materials* 59.1-2 (1986), pp. 86–94.

[311] D. Givord, H. S. Li, and R. Perrier de la Bǎthie. "Magnetic properties of $Y_2Fe_{14}B$ and $Nd_2Fe_{14}B$ single crystals". In: *Solid State Communications* 88.11-12 (1993), pp. 907–910.

[312] A. V. Ruban et al. "Atomic and magnetic configurational energetics by the generalized perturbation method". In: *Physical Review B* 70.12 (2004), p. 125115.

[313] J. Staunton et al. "The static, paramagnetic, spin susceptibility of metals at finite temperatures". In: *Journal of Physics F: Metal Physics* 16.11 (1986), p. 1761.

[314] R. F. L. Evans, U. Atxitia, and R. W. Chantrell. "Quantitative simulation of temperature-dependent magnetization dynamics and equilibrium properties of elemental ferromagnets". In: *Physical Review B* 91.14 (2015), p. 144425.

[315] R. Bastardis et al. "Unified decoupling scheme for exchange and anisotropy contributions and temperature-dependent spectral properties of anisotropic spin systems". In: *Physical Review B* 86.9 (2012), p. 094415.

[316] O. Yamada et al. "Magnetocrystalline anisotropy in $Nd_2Fe_{14}B$ intermetallic compound". In: *Journal of Magnetism and Magnetic Materials* 54 (1986), pp. 585–586.

[317] Y. G. Pastushenkov, A. Forkl, and H. Kronmüller. "Temperature dependence of the domain structure in $Fe_{14}Nd_2B$ single crystals during the spin-reorientation transition". In: *Journal of Magnetism and Magnetic Materials* 174.3 (1997), pp. 278–288.

[318] Y. G. Pastushenkov et al. "The magnetic domain structure of $Fe_{14}Nd_2B$ single crystals between 135 and 4 K and the low-temperature magnetization reversal process in Fe-Nd-B permanent magnets". In: *Journal of Magnetism and Magnetic Materials* 196 (1999), pp. 856–858.

[319] Y. Sun and C. Beckermann. "Sharp interface tracking using the phase-field equation". In: *Journal of Computational Physics* 220.2 (2007), pp. 626–653.

[320] A. Hubert and R. Schäfer. *Magnetic domains: the analysis of magnetic microstructures*. Springer Science & Business Media, 2018.

[321] K. Ono et al. "Observation of spin-wave dispersion in Nd-Fe-B magnets using neutron Brillouin scattering". In: *Journal of Applied Physics* 115.17 (2014), 17A714.

[322] Y. Zhu and M. R. McCartney. "Magnetic-domain structure of $Nd_2Fe_{14}B$ permanent magnets". In: *Journal of Applied Physics* 84.6 (1998), pp. 3267–3272.

[323] S. J. Lloyd, J. C. Loudon, and P. A. Midgley. "Measurement of magnetic domain wall width using energy-filtered Fresnel images". In: *Journal of Microscopy* 207.2 (2002), pp. 118–128.

[324] M. Beleggia et al. "Quantitative domain wall width measurement with coherent electrons". In: *Journal of Magnetism and Magnetic Materials* 310.2 (2007), pp. 2696–2698.

[325] L. S. Campana et al. "Spectral-density method for classical systems: Heisenberg ferromagnet". In: *Physical Review B* 30.5 (1984), p. 2769.

[326] R.-C. Peng et al. "Switching the chirality of a magnetic vortex deterministically with an electric field". In: *Materials Research Letters* 6.12 (2018), pp. 669–675.

[327] S. P. Bennett et al. "Magnetic order multilayering in FeRh thin films by He-ion irradiation". In: *Materials Research Letters* 6.1 (2017), pp. 106–112.

[328] O. Rivin et al. "Evidence for ferromagnetic ordering in the MAX phase $(Cr_0.96Mn_{0.04})_2GeC$". In: *Materials Research Letters* 5.7 (2017), pp. 465–471.

[329] T. Ohkubo et al. "Faceted shell structure in grain boundary diffusion-processed sintered Nd–Fe–B magnets". In: *Journal Alloy and Compounds* 617 (2014), pp. 884–892.

[330] W. F. Li et al. "Distribution of Dy in high-coercivity (Nd,Dy)–Fe–B sintered magnet". In: *Acta Materialia* 59.8 (2011), pp. 3061–3069.

[331] D. Wu et al. "Magnetic domain switching in Nd–Fe–B sintered magnets with superior magnetic properties". In: *Materials Research Letters* 6.4 (2018), pp. 255–260.

[332] T. G. Woodcock et al. "Atomic-scale features of phase boundaries in hot deformed Nd–Fe–Co–B–Ga magnets infiltrated with a Nd–Cu eutectic liquid". In: *Acta Materialia* 77 (2014), pp. 111–124.

[333] R. Skomski and J. M. D Coey. "Giant energy product in nanostructured two-phase magnets". In: *Physical Review B* 48.21 (1993), p. 15812.

[334] G. C. Hadjipanayis, L. Withanawasam, and R. F. Krause. "Nanocomposite $R_2Fe_{14}B/\alpha$-Fe permanent magnets". In: *IEEE Transactions on Magnetics* 31.6 (1995), pp. 3596–3601.

[335] D. Haskel et al. "Atomic origin of magnetocrystalline anisotropy in $Nd_2Fe_{14}B$". In: *Physical Review Letters* 95.21 (2005), p. 217207.

[336] D. Ogawa et al. "Evaluation of interlayer exchange coupling in α-Fe(100)/Nd_2Fe_{14}B(001) films". In: *Journal of the Korean Physical Society* 63.3 (2013), pp. 489–492.

[337] Y. Toga et al. "First principles study on interfacial electronic structures in exchange-spring magnets". In: *Journal of Physics: Conference Series* 266 (2011), p. 012046.

[338] D. Ogawa et al. "Negative exchange coupling in $Nd_2Fe_{14}B(100)/\alpha$-Fe interface". In: *Applied Physical Letters* 107.10 (2015), p. 102406.

[339] N. Umetsu, A. Sakuma, and Y. Toga. "First-principles study of interface magnetic structure in $Nd_2Fe_{14}B$/(Fe,Co) exchange spring magnets". In: *Physical Review B* 93.1 (2016), p. 014408.

[340] Q. Gong et al. "Calculating temperature-dependent properties of $Nd_2Fe_{14}B$ permanent magnets by atomistic spin model simulations". In: *Physical Review B* 99.21 (2019), p. 214409.

[341] Q. Gong, M. Yi, and B.-X. Xu. "Multiscale simulations toward calculating coercivity of Nd-Fe-B permanent magnets at high temperatures". In: *Physical Review Materials* 3.8 (2019), p. 084406.

[342] A. Sakuma et al. "Magnetism of Nd-Fe films as a model of grain boundary phase in Nd-Fe-B permanent magnets". In: *Applied Physical Express* 9.1 (2015), p. 013002.

[343] Y. Xiao et al. "The effects of various alloying elements on modifying the elevated temperature magnetic properties of sintered Nd-Fe-B magnets". In: *Journal of Applied Physics* 63.8 (1988), pp. 3516–3518.

[344] L. Q. Yu et al. "Production for high thermal stability NdFeB magnets". In: *Journal of Magnetism and Magnetic Materials* 320.8 (2008), pp. 1427–1430.

[345] M. H. Ghandehari. "Reactivity of Dy_2O_3 and Tb_4O_7 with $Nd_{15}Fe_{77}B_8$ powder and the coercivity of the sintered magnets". In: *Applied Physics Letters* 48.8 (1986), pp. 548–550.

[346] X. G. Cui et al. "Effect of Dy_2O_3 intergranular addition on thermal stability and corrosion resistance of Nd–Fe–B magnets". In: *Intermetallics* 55 (2014), pp. 118–122.

[347] K. Löewe et al. "Temperature-dependent Dy diffusion processes in Nd–Fe–B permanent magnets". In: *Acta Materialia* 83 (2015), pp. 248–255.

[348] T. Oikawa et al. "Large-scale micromagnetic simulation of Nd-Fe-B sintered magnets with Dy-rich shell structures". In: *AIP Advances* 6.5 (2016), p. 056006.

[349] J. Thielsch et al. "Dependence of coercivity on length ratios in sub-micron $Nd_2Fe_{14}B$ particles with rectangular prism shape". In: *Journal of Applied Physics* 114.22 (2013), p. 223909.

[350] R. Fischer et al. "Grain-size dependence of remanence and coercive field of isotropic nanocrystalline composite permanent magnets". In: *Journal of Magnetism and Magnetic Materials* 153.1-2 (1996), pp. 35–49.

[351] G. Henkelman, B. P. Uberuaga, and H. Jónsson. "A climbing image nudged elastic band method for finding saddle points and minimum energy paths". In: *The Journal of Chemical Physics* 113.22 (2000), pp. 9901–9904.

[352] M. F. Carilli, K. T. Delaney, and G. H. Fredrickson. "Truncation-based energy weighting string method for efficiently resolving small energy barriers". In: *The Journal of Chemical Physics* 143.5 (2015), p. 054105.

[353] Q. Du and L. Zhang. "A constrained string method and its numerical analysis". In: *Communications in Mathematical Sciences* 7.4 (2009), pp. 1039–1051.

[354] A. Samanta and E. Weinan. "Optimization-based string method for finding minimum energy path". In: *Communications in Computational Physics* 14.2 (2013), pp. 265–275.

[355]   W. Ren and E. Vanden-Eijnden. "A climbing string method for saddle point search". In: *The Journal of Chemical Physics* 138.13 (2013), p. 134105.

[356]   W. Scholz, T. Schrefl, and J. Fidler. "Micromagnetic simulation of thermally activated switching in fine particles". In: *Journal of Magnetism and Magnetic Materials* 233.3 (2001), pp. 296–304.

[357]   T. Schrefl et al. "Computational micromagnetics: prediction of time dependent and thermal properties". In: *Journal of Magnetism and Magnetic Materials* 226 (2001), pp. 1213–1219.

[358]   D. V. Berkov. "Fast switching of magnetic nanoparticles: Simulation of thermal noise effects using the Langevin dynamics". In: *IEEE Transactions on Magnetics* 38.5 (2002), pp. 2489–2495.

[359]   V. Tsiantos et al. "The effect of the cell size in Langevin micromagnetic simulations". In: *Journal of Magnetism and Magnetic Materials* 242 (2002), pp. 999–1001.

[360]   E. Martinez et al. "Micromagnetic simulations with thermal noise: Physical and numerical aspects". In: *Journal of Magnetism and Magnetic Materials* 316.2 (2007), pp. 269–272.

[361]   E. Martínez et al. "Minimizing cell size dependence in micromagnetics simulations with thermal noise". In: *Journal of Physics D: Applied Physics* 40.4 (2007), p. 942.

[362]   R. Cardias et al. "The Bethe-Slater curve revisited; new insights from electronic structure theory". In: *Scientific Reports* 7 (2017), p. 4058.

[363]   W. Rave, K. Ramstöck, and A. Hubert. "Corners and nucleation in micromagnetics1". In: *Journal of Magnetism and Magnetic Materials* 183.3 (1998), pp. 329–333.

[364]   H. Oezelt et al. "Full-spin-wave-scaled stochastic micromagnetism for mesh-independent simulations of ferromagnetic resonance and reversal". In: *npj Computational Materials* 8 (2022), p. 35.

[365]   M. Sagawa et al. "Dependence of coercivity on the anisotropy field in the $Nd_2Fe_{14}B$-type sintered magnets". In: *Journal of Applied Physics* 61.8 (1987), pp. 3559–3561.

[366]   J. Crangle and G. M. Goodman. "The magnetization of pure iron and nickel". In: *Proceedings of the Royal Society A* 321.1547 (1971), pp. 477–491.

[367]   T. Schrefl, J. Fidler, and H. Kronmüller. "Nucleation fields of hard magnetic particles in 2D and 3D micromagnetic calculations". In: *Journal of Magnetism and Magnetic Materials* 138.1-2 (1994), pp. 15–30.

[368]   E. F. Kneller and R. Hawig. "The exchange-spring magnet: a new material principle for permanent magnets". In: *IEEE Transactions on Magnetics* 27.4 (1991), pp. 3588–3560.

[369]   D. Givord, P. Tenaud, and T. Viadieu. "Coercivity mechanisms in ferrites and rare earth transition metal sintered magnets ($SmCo_5$, Nd-Fe-B)". In: *IEEE Transactions on Magnetics* 24.2 (1988), pp. 1921–1923.

[370] D. Givord et al. "Experimental approach to coercivity analysis in hard magnetic materials". In: *Journal of Magnetism and Magnetic Materials* 83.1-3 (1990), pp. 183–188.

[371] S. Liu and G. E. Kuhl. "Temperature coefficients of rare earth permanent magnets". In: *IEEE Transactions on Magnetics* 35.5 (1999), pp. 3271–3273.

[372] H. Kronmüller and D. Goll. "Micromagnetic theory of the pinning of domain walls at phase boundaries". In: *Physica B: Condensed Matter* 319.1-4 (2002), pp. 122–126.

[373] L. H. Lewis and F. Jiménez-Villacorta. "Perspectives on permanent magnetic materials for energy conversion and power generation". In: *Metallurgical and Materials Transactions A* 44.S1 (2013), pp. 2–20.

[374] R. Coehoorn, D. de Mooij, and C. de Waard. "Meltspun permanent magnet materials containing Fe_3B as the main phase". In: *Journal of Magnetism and Magnetic Materials* 80.1 (1989), pp. 101–104.

[375] T. Schrefl, H. Kronmüller, and J. Fidler. "Exchange hardening in nano-structured two-phase permanent magnets". In: *Journal of Magnetism and Magnetic Materials* 127.3 (1993), pp. L273–L277.

[376] G. P. Zhao and X. L. Wang. "Nucleation, pinning, and coercivity in magnetic nanosystems: an analytical micromagnetic approach". In: *Physical Review B* 74.1 (2006), pp. 2–5.

[377] G. P. Zhao et al. "Coercivity mechanisms in nanostructured permanent magnets". In: *Chinese Physics B* 28.7 (2019), p. 077505.

[378] V. Neu et al. "Fully epitaxial, exchange coupled $SmCo_5$/Fe multilayers with energy densities above 400 kJ/m^3". In: *IEEE Transactions on Magnetics* 48.11 (2012), pp. 3599–3602.

[379] J. Zhang et al. "Sm(Co,Cu)$_5$/Fe exchange spring multilayer films with high energy product". In: *Applied Physics Letters* 86.12 (2005), p. 122509.

[380] H. Fukunaga and H. Nakamura. "Micromagnetic approach for relationship between nanostructure and magnetic properties of nanocomposite magnets". In: *Scripta Materialia* 44.8-9 (2001), pp. 1341–1345.

[381] S. Hirosawa, H. Kanekiyo, and T. Miyoshi. "Unusual effects of Ti and C additions on structural and magnetic properties of Nd–Fe–B nanocomposite magnets in a B-rich and Nd-poor composition range". In: *Journal of Magnetism and Magnetic Materials* 281.1 (2004), pp. 58–67.

[382] W.-B. Cui, Y. K. Takahashi, and K. Hono. "$Nd_2Fe_{14}B$/FeCo anisotropic nanocomposite films with a large maximum energy product". In: *Advanced Materials* 24.48 (2012), pp. 6530–6535.

[383] H. Sepehri-Amin et al. "Development of high coercivity anisotropic Nd-Fe-B/Fe nanocomposite powder using hydrogenation disproportionation desorption recombination process". In: *Acta Materialia* 175 (2019), pp. 276–285.

[384] M. J. Kramer et al. "Prospects for non-rare earth permanent magnets for traction motors and generators". In: *JOM* 64.7 (2012), pp. 752–763.

[385] K. P. Remya et al. "Exchange spring magnetic behavior in $BaFe_{12}O_{19}/Fe_3O_4$ nanocomposites". In: *Journal of Magnetism and Magnetic Materials* 406 (2016), pp. 233–238.

[386] M. Petrecca et al. "Optimizing the magnetic properties of hard and soft materials for producing exchange spring permanent magnets". In: *Journal of Physics D: Applied Physics* 54.13 (2021).

[387] I. Dirba et al. "Synthesis and magnetic properties of bulk α''-$Fe_{16}N_2$/ $SrAl_2Fe_{10}O_{19}$ composite magnets". In: *Journal of Magnetism and Magnetic Materials* 518 (2021), p. 167414.

[388] S. Sabet et al. "Impact of interface structure on magnetic exchange coupling in $MnBi/Fe_xCo_{1-x}$ bilayers". In: *Physical Review B* 98.17 (2018), p. 174440.

[389] I. Dirba et al. "Synthesis, morphology, thermal stability and magnetic properties of α''-$Fe_{16}N_2$ nanoparticles obtained by hydrogen reduction of γ-Fe_2O_3 and subsequent nitrogenation". In: *Acta Materialia* 123 (2017), pp. 214–222.

[390] F. Rhein et al. "Enhancement of coercivity and saturation magnetization of Al^{3+} substituted M-type Sr-hexaferrites". In: *Journal of Alloys and Compounds* 690 (2017), pp. 979–985.

[391] T. Ogawa et al. "Challenge to the synthesis of α''-$Fe_{16}N_2$ compound nanoparticle with high saturation magnetization for rare earth free new permanent magnetic material". In: *Applied Physics Express* 6.7 (2013), p. 073007.

[392] D. J. De Bitetto. "Anisotropy Fields in Hexagonal Ferrimagnetic Oxides by Ferrimagnetic Resonance". In: *Journal of Applied Physics* 35.12 (1964), pp. 3482–3487.

[393] J. M. D. Coey. *Magnetism and Magnetic Materials*. Cambridge University Press, 2001.

[394] R. Skomski, G. C. Hadjipanayis, and D. J. Sellmyer. "Graded permanent magnets". In: *Journal of Applied Physics* 105.7 (2009), pp. 1–4.

[395] J. S. Jiang and S. D. Bader. "New thin film permanent magnets". In: *Materials Science and Technology* 17.12 (2001), pp. 1491–1499.

[396] S. Sabet et al. "Low-Temperature phase c-axis oriented manganese bismuth thin films with high anisotropy grown from an alloy $Mn_{55}Bi_{45}$ target". In: *IEEE Transactions on Magnetics* 53.4 (2017).

[397] J. Park et al. "Electronic structure and maximum energy product of MnBi". In: *Metals* 4.3 (2014), pp. 455–464.

[398] T. H. Rana et al. "Micromagnetism of MnBi:FeCo thin films". In: *Journal of Physics D: Applied Physics* 49.7 (2016), p. 075003.

[399] Y. B. Kim and H. M. Jin. "Sublattice anisotropy constants of $Dy_2Fe_{14}B$ and $Tb_2Fe_{14}B$ at 4.2 K". In: *Journal of Magnetism and Magnetic Materials* 189.2 (1998), pp. 251–254.

[400] M. Ito et al. "Calculations of the magnetic properties of $R_2M_{14}B$ intermetallic compounds (R=rare earth, M=Fe,Co)". In: *Journal of Magnetism and Magnetic Materials* 400 (2016), pp. 379–383.

[401] R. Cuadrado et al. "First principles and atomistic calculation of the magnetic anisotropy of $Y_2Fe_{14}B$". In: *Journal of Applied Physics* 130.2 (2021), p. 023901.

[402] P. J. Flanders and M. P. Sharrock. "An analysis of time-dependent magnetization and coercivity and of their relationship to print-through in recording tapes". In: *Journal of Applied Physics* 62.7 (1987), pp. 2918–2928.

[403] M. P. Sharrock. "Time dependence of switching fields in magnetic recording media (invited)". In: *Journal of Applied Physics* 76.10 (1994), pp. 6413–6418.

[404] S. Okamoto. "Experimental approaches for micromagnetic coercivity analysis of advanced permanent magnet materials". In: *Science and Technology of Advanced Materials* 22.1 (2021), pp. 124–134.

Publications and Presentations

Publications

1. **Q Gong**, M Yi, RFL Evans, BX Xu, O Gutfleisch. Calculating temperature-dependent properties of permanent magnets by atomistic spin model simulations. *Physical Review B*, 2019, 99 (21), 214409.

2. **Q Gong**, M Yi, BX Xu. Multiscale simulations toward calculating coercivity of Nd-Fe-B permanent magnets at high temperatures. *Physical Review Materials*, 2019, 3 (8), 084406.

3. **Q Gong**, M Yi, RFL Evans, O Gutfleisch, BX Xu. Anisotropic exchange in Nd–Fe–B permanent magnets. *Materials Research Letters*, 2020, 8 (3), 89–96.

4. **Q Gong**, M Yi, BX Xu. Electric field induced magnetization reversal in magnet/insulator nanoheterostructure. *International Journal of Smart and Nano Materials*, 2020, 11 (3), 298–309.

5. S Sabet, A Moradabadi, S Gorji, M Yi, **Q Gong**, MH Fawey, E Hildebrandt. Impact of interface structure on magnetic exchange coupling in bilayers. *Physical Review B*, 2018, 98 (17), 174440.

6. I Dirba, M Mohammadi, F Rheina, **Q Gong**, M Yi, BX Xu, M Krispin, O Gutfleisch. Synthesis and magnetic properties of bulk a''-$Fe_{16}N_2$/$SrAl_2Fe_{10}O_{19}$ composite magnets. *Journal of Magnetism and Magnetic Materials*, 2021, 518, 167414.

Presentations

1. **Q Gong**, M Yi, BX Xu. Multiscale simulations on properties of Nd-Fe-B magnets at elevated temperatures. *2018 Rare Earth Permanent Magnets and Advanced Magnetic Materials and Their Applications (REPM 2018)*, Bejjing, Aug 26-30, 2018.

2. **Q Gong**, M Yi, BX Xu. Micromagnetic simulations on Ce-doped Nd-Fe-B permanent magnets. *MANA 2018 - Micromagnetics: Analysis, Numerics, Applications*, Vienna, Nov 8-9, 2018.

3. **Q Gong**, M Yi, BX Xu. Calculating coercivity at finite temperatures by micromagnetic simulations: a comparative study. *12th International Symposium on Hysteresis Modeling and Micromagnetics (HMM2019)*, Heraklion, Crete, May 19-22, 2019.

Curriculum Vitae

M.Sc. Qihua Gong,
Born on the July 09, 1990 in Hunan, China

Education

Apr 2017 - now	Doctoral study in Materials Science **Technische Universität Darmstadt, Germany** Doctoral thesis: Calculating intrinsic and extrinsic properties of permanent magnets by multiscale simulations
Sep 2014 - Mar 2017	Master study in Chemistry **Master of Science** **Beihang University (BUAA), Beijing, China** Master thesis: Quantitative study of *in-situ* mechanical behavior of low-dimensional nanomaterials
Sep 2009 - Jul 2013	Bachelor study in Chemical Engineering and Technology **Bachelor of Engineering** **Hunan Institute of Engineering, Hunan, China**
Sep 2006 - Jul 2009	High school **The Second High School of Hengyang, Hunan, China**